



THE HONG KONG
POLYTECHNIC UNIVERSITY

香港理工大學

Pao Yue-kong Library

包玉剛圖書館

Copyright Undertaking

This thesis is protected by copyright, with all rights reserved.

By reading and using the thesis, the reader understands and agrees to the following terms:

1. The reader will abide by the rules and legal ordinances governing copyright regarding the use of the thesis.
2. The reader will use the thesis for the purpose of research or private study only and not for distribution or further reproduction or any other purpose.
3. The reader agrees to indemnify and hold the University harmless from and against any loss, damage, cost, liability or expenses arising from copyright infringement or unauthorized usage.

IMPORTANT

If you have reasons to believe that any materials in this thesis are deemed not suitable to be distributed in this form, or a copyright owner having difficulty with the material being included in our database, please contact lbsys@polyu.edu.hk providing details. The Library will look into your claim and consider taking remedial action upon receipt of the written requests.

**SMALL STRAIN STIFFNESS OF A
COMPACTED CLAY WITH DIFFERENT
INITIAL STRUCTURES UNDER CYCLIC
THERMO-HYDRO-MECHANICAL LOADS**

BENTIL OBED TAKYI

PhD

The Hong Kong Polytechnic University

2023

The Hong Kong Polytechnic University

Civil and Environmental Engineering Department

**Small Strain Stiffness of a Compacted Clay with
Different Initial Structures Under Cyclic Thermo-
Hydro-Mechanical Loads**

Bentil Obed Takyi

**A thesis submitted in partial fulfilment of the requirements for the
degree of Doctor of Philosophy**

March 2023

CERTIFICATE OF ORIGINALITY

I hereby declare that this thesis is my work and that, to the best of my knowledge and belief, it reproduces no material previously published or written, nor material that has been accepted for the award of any other degree or diploma, except where due acknowledgement has been made in the text.

_____ (Signed)

BENTIL OBED TAKYI (Name of student)

ABSTRACT

Lateritic soils are chemically weathered materials extensively distributed in tropical and subtropical regions like Asia (India and China), West Africa (Ghana and Nigeria) and South America (Brazil). They have a high sesquioxide (iron and aluminium oxides) content that leads to considerable particle aggregations and affect soil microstructure. The aggregated structures have been shown to significantly affect the mechanical properties of lateritic soils differently from other soils, including their shear strength and compressibility. For instance, due to mechanical and thermal action, the possible loosely bonded particle aggregations may disintegrate into smaller particles. This feature makes it challenging to use their particle size distribution, index properties (e.g., plasticity index) and soil classification to solely predict their geotechnical engineering performance, giving it unique engineering qualities compared to other soils. Compacted lateritic soils are commonly used backfill material in the parts of the world mentioned above due to their favourable material properties. In the past studies of lateritic soils, researchers focused on their mechanical behaviour at large strains (above 1%), such as shear strength and dilatancy. The small strain stiffness has not been well studied especially when the soil is unsaturated and anisotropic, which is crucial for accurately predicting ground movement and geotechnical structures' serviceability limit state. Furthermore, lateritic soils in many geotechnical structures (e.g., pavements, railway embankments and energy geotechnical structures) experience complex working conditions, like daily and seasonal variations of temperature and suction. Therefore, there is an urgent need to improve the fundamental understanding of the small strain stiffness behaviour of unsaturated lateritic soils, considering the influence of compaction-induced anisotropy, soil microstructure and thermo-hydro-mechanical loading.

This study aims to reveal the small strain stiffness characteristics of compacted lateritic soils, which are widely used in geotechnical construction, along various thermo-hydro-mechanical paths. The principal objectives are to (1) obtain the complete set of cross-anisotropic elastic parameters and reveal the influence of initial microstructure on the evolution of stiffness anisotropy at saturated and isothermal conditions; (2) investigate the coupled effects of suction and initial microstructure on the stiffness characteristics of unsaturated specimens over a wide suction range; (3) reveal the influence of temperature and thermal cycles on the elastic shear modulus of saturated and unsaturated specimens; (4) develop a semi-empirical thermo-hydro-mechanical model for the small strain stiffness and apply it in the pavement analysis for investigating the influence of suction and thermal effects on the pavement performance.

To meet these objectives, this study tested a lateritic clay at saturated and unsaturated conditions. The specimens were compacted at different water contents and densities to produce various as-compacted microstructures and then tested along various thermo-hydro-mechanical paths. Both vertically and horizontally cut specimens were used to investigate the anisotropy of stiffness. Several advanced apparatuses were used in the testing, including a new temperature-controlled oedometer equipped with bender elements, a new suction and temperature-controlled triaxial apparatus with local strain measurements, bender elements and double-cell total volume change measurements. Soil suctions in the low (below 300 kPa) and high (above 4 MPa) ranges were controlled using the axis translation and vapour equilibrium techniques, respectively. In addition, a temperature range of 5 to 60°C was considered. The ranges of suction and temperature were selected with reference to some field monitoring studies on subgrade soils, which showed that temperature and suction fluctuate widely up to a depth of 2 meters. Moreover, microstructural analysis was used to interpret experimental results providing a linkage between micro and macro soil behaviour.

The experimental results at saturated conditions reveal that in comparison to other clays, the lateritic clay exhibits a lower dependency of shear modulus to confining pressure, a higher shear modulus at the same confining pressure and its stiffness degrades rapidly with strain. Due to its large-size aggregated microstructure caused by cladding of particles, the lateritic clay behaves like granular material, and the commonly utilized relationships between stiffness parameters and plasticity index does not fit well for lateritic clay. Additionally, the elastic shear modulus in the vertical plane is fairly higher than in the horizontal plane, and the anisotropy evolves during shearing. A complete set of cross-anisotropic stiffness parameters for effective and total stress analysis were obtained.

At unsaturated conditions, the shear stiffness increases non-linearly with increasing suction. The incremental rate reduces when suction increases. The non-linear response of the increment in stiffness and suction was observed for all different mean net stresses. This non-linearity occurs because of the effects of particle aggregation and water retention behaviour. More importantly, the degree of anisotropy during shearing is affected by suction and net stress.

Temperature-controlled tests at saturated and unsaturated conditions consistently reveal that soil shear modulus is smaller after heating at a given stress and suction. The thermal effects can be attributed to the reduction of interparticle force while heating saturated clay, according to the double layer theories. The reduction in the air-water surface tension between particles

and aggregates is another mechanism for unsaturated soil. Moreover, the reduction in shear modulus upon heating varies in magnitude and depends on the measuring plane, suggesting a potential thermally induced anisotropy. Furthermore, the shear modulus increases by 12% and 16% after four thermal cycles for overconsolidated and normally consolidated specimens, respectively, probably due to soil densification and particle rearrangement during the heating-cooling cycles.

The new results from the experimental study are useful for calibrating constitutive models and evaluating the serviceability of earth structures made of lateritic soils. Taking pavement as one example, a series of numerical simulations were carried out using KENPAVE software to investigate the influence of suction and temperature on rutting prediction and fatigue cracking. An increase in subgrade modulus due to suction causes was found to reduce rutting more than twice the damage caused by fatigue cracking. Similarly, the damage resulting from thermal effects on subgrade modulus is relatively higher for rutting than fatigue cracking.

ACKNOWLEDGEMENTS

Most importantly, I am eternally grateful to God Almighty for the knowledge He bestowed upon me and the grace He gave me, which has enabled me to endure the peaks and valleys during my PhD research study.

I wish to take this opportunity to express my sincere gratitude to the following people from whom, for different reasons, I derived great benefits during my study.

I am deeply thankful to my supervisor, Professor Chao Zhou, for his constructive guidance throughout my research. Specifically, I am grateful for his review and helpful feedback, as well as my research colleagues, who were kind enough to review my thesis later and provide additional input for interpreting my results.

I would also like to thank my co-supervisor, Prof. Jianhua Yin, for providing the advanced test devices in our soil lab. Many thanks to Prof. John McCartney from the University of California San Diego, Prof. Sergio Lourenco from the University of Hong Kong, and Prof. Zhenyu YIN from the Hong Kong Polytechnic University for their precious time and great efforts as the external examiners and the committee chairman.

Many thanks go to the technician in the soil mechanics laboratory at HK PolyU, Mr Kit, for ensuring that the soil mechanics laboratory is in order. My sincere gratitude goes to the technician Civil Engineering workshop, Mr David, for his exceptional work and great attempts to assist me in designing and modifying most of the various equipment I used in the HK PolyU soil mechanics laboratory.

I am deeply grateful to my research colleagues, past and present, for their kind help and discussions on my research in various ways. Special thanks to Daniel Preprah-Manu for his inspiring discussions, motivations, and support and for sharing the joys and frustrations on several issues related to my research study.

Finally, I would like to express my utmost gratitude to my family and friends for their endless love, encouragement and support throughout my study.

TABLE OF CONTENTS

Abstract.....	iv
Acknowledgements	vii
Table of contents	viii
List of tables.....	xiv
List of figures.....	xv
List of plates.....	xxi
CHAPTER 1 INTRODUCTION.....	1
1.1 Background of this research	1
1.2 Objectives and research strategy	4
1.3 Layout of thesis	6
CHAPTER 2 LITERATURE REVIEW.....	10
2.1 Basic unsaturated soil mechanism	10
2.1.1 Stress State for Unsaturated Soils.....	10
2.1.2 Suction in unsaturated soils	11
2.1.3 Common techniques for suction control.....	11
2.1.4 Mechanical effects of suction in unsaturated soils	13
2.2 Stiffness characteristics of soils under working conditions	14
2.2.1 Small-strain shear modulus of saturated and unsaturated soils	14
2.2.2 Effects of soil microstructure on small strain shear behaviour.....	17
2.2.3 Anisotropy of soil behaviour	19
2.2.4 Cyclic shear behaviour of saturated and unsaturated soils	20
2.3 Thermal effects on soil behaviour	22
2.3.1 Volume change response under thermal loading.....	22
2.3.2 Thermal-induced pore water pressure	22
2.3.3 Thermal effects on yield stress	22

2.3.4 Thermal effects on normally consolidated line (NCL) and critical state line (CSL).....	23
2.3.5 Thermal effects on small strain behaviour.....	23
2.4 Modelling stiffness of saturated and unsaturated soils	24
2.5 The use of unsaturated soil mechanics in pavement engineering.....	27
2.5.1 Methods of pavement performance analysis	28
CHAPTER 3 SOIL PROPERTIES, SPECIMEN PREPARATION METHODS AND TESTING SYSTEMS	49
3.1 Lateritic soil tested in this study.....	49
3.1.1 Basic properties	49
3.1.2 Mineralogy and chemical composition of the tested lateritic soil	49
3.2 Specimen preparation using different compaction methods	50
3.3 Microstructural analysis	51
3.3.1 Scanning electron microscope	51
3.3.2 Mercury intrusion porosimetry	51
3.4 Water retention behaviour of compacted specimens	52
3.5 Testing equipment and apparatus.....	53
3.5.1 Bender element electrical components for measuring shear wave velocity....	53
3.5.2 Double-cell triaxial apparatus for testing unsaturated soil at room temperature	54
3.5.3 A new temperature-controlled oedometer with bender elements	54
3.5.4 A new temperature- and suction-controlled triaxial apparatus.....	55
CHAPTER 4 ANISOTROPIC STIFFNESS AT SATURATED CONDITIONS FROM VERY SMALL TO LARGE STRAINS.....	70
4.1 Theoretical consideration, testing programme and testing procedures	70
4.1.1 Theoretical consideration.....	70
4.1.2 Testing programme	71
4.1.3 Testing procedures.....	72

4.2 Complete set of cross-anisotropic stiffness parameters for effective and total stress analysis	74
4.2.1 Anisotropic elastic shear modulus during isotropic compression	74
4.2.2 Consolidated-drained shear response	76
4.2.3 Consolidated-undrained shear behaviour	78
4.2.4 Complete stiffness and strength parameters for effective and total stress analysis	78
4.2.5 Discussion on the relationship between PI and stiffness degradation	79
4.3 Influence of compaction-induced fabric on the evolution of anisotropic moduli	80
4.3.1 Influence of compaction density on the stiffness evolution during compression	80
4.3.2 Influence of compaction water content on the stiffness evolution during compression	80
4.3.3 Stiffness anisotropy of different compacted soil fabric	81
4.4 Summary	83
CHAPTER 5 LOW SUCTION EFFECTS ON SOIL STIFFNESS UNDER MONOTONIC LOADING	99
5.1 Theoretical considerations of unsaturated soil stiffness.....	99
5.1.1 Soil stiffness at very small strains	99
5.1.2 Stiffness degradation with strain	101
5.2 Testing programmes and procedures for suction-controlled triaxial shear tests	102
5.2.3 Testing programme	102
5.2.4 Testing procedures	102
5.3 Interpretations of strength and dilatancy behaviour of unsaturated specimens	103
5.4 Small strain stiffness of unsaturated specimens	105
5.5 Anisotropic strength and dilatancy of unsaturated lateritic soil.....	107

5.6 Anisotropic small strain stiffness during drained shearing.....	108
5.7 Verification of small strain stiffness and stiffness degradation with strain	110
5.8 Summary	111
CHAPTER 6 HIGH SUCTION EFFECTS ON STIFFNESS UNDER MONOTONIC AND CYCLIC LOADING.....	128
6.1 Testing programme for high on both monotonic and cyclic shear behaviour ..	128
6.1.1 Monotonic shear behaviour	128
6.1.2 Cyclic shear behaviour	129
6.2 High suction effects on the pore size distribution	130
6.3 Interpretations of monotonic shear behaviour	131
6.3.1 Stress-strain response.....	131
6.3.2 Shearing-induced dilatancy	131
6.3.3 Influence of compaction water contents on peak and critical state strengths	132
6.3.4 Effects of high suction on small strain stiffness for same compaction water content.....	132
6.3.5 Discussion about the stiffness behaviour based on microstructures.....	133
6.4 Interpretations of cyclic shear behaviour.....	134
6.4.1 Influence of deviator stress on resilient modulus	134
6.4.2 Influence of suction and stress on resilient modulus.....	135
6.4.3 Accumulated plastic strain.....	137
6.5 Summary	138
CHAPTER 7 CYCLIC THERMAL EFFECTS ON SOIL STIFFNESS AT SATURATED AND UNSATURATED CONDITIONS.....	162
7.1 Testing programme and procedures.....	162
7.1.1 Temperature-controlled oedometer apparatus at saturated conditions	162
7.1.2 Temperature- and suction-controlled tests at saturated and unsaturated conditions.....	163
7.2 Thermal effect under one-dimensional stress conditions.....	164

7.2.1 Influence of temperature on the elastic shear modulus during one-dimensional compression	164
7.2.2 Effects of thermal cycles on the elastic shear modulus at different stress states	164
7.3 Thermal and suction effects under isotropic stress conditions.....	166
7.3.1 Influence of temperature on G_0 at different suctions under isotropic stress condition	166
7.3.2 Effects of suction on the G_0 at different temperatures.....	167
7.4 Discussion about cyclic thermal effects on soil stiffness.....	168
7.4.1 Discussion on the existing formulations for temperature-dependent G_0	168
7.4.2 Discussion on the existing formulations for temperature-dependent G_0	169
7.4.3 A semi-empirical equation for temperature-dependent modulus of saturated and unsaturated soils.....	170
7.4.4 Potential applications of temperature-dependent G_0 in the geotechnical analysis	171
7.5 Summary	172
CHAPTER 8 PAVEMENT PERFORMANCE ANALYSIS	191
8.1 Pavement performance analysis.....	191
8.1.1 Pavement performance analysis using KENPAVE.....	191
8.1.2 Numerical model and input parameters	191
8.2 Equations for calculating rutting and fatigue cracking.....	192
8.2.3 Rutting Prediction.....	192
8.2.4 Fatigue Cracking.....	194
8.3 Numerical programme.....	195
8.4 Analysis of numerical results.....	196
8.4.1 Stress and strain distribution under the pavement at constant suction	196
8.4.2 Suction effects on compressive strain and rutting	197
8.4.1 Suction effects on horizontal strain and fatigue cracking.....	197

8.4.2 Thermal effects on compressive strain and rutting.....	198
8.4.3 Thermal effects on horizontal strain and fatigue cracking	199
8.5 Summary	199
CHAPTER 9 CONCLUSIONS AND RECOMMENDATIONS FOR FURTHER WORK	
211	
9.1 Conclusions.....	211
9.1.1 Anisotropic stiffness of a saturated compacted lateritic clay from very small to large strains	211
9.1.2 Low suction effects soil stiffness under monotonic loading	212
9.1.3 High suction effects on the stiffness under monotonic shearing	213
9.1.4 High suction effects on the stiffness under cyclic shearing.....	214
9.1.5 Thermal and suction effects on elastic shear modulus of compacted lateritic clay	215
9.1.6 Pavement performance analysis	215
9.2 Recommendations for Further work	216
9.2.1 Recommendations for experimental study	216
9.2.2 Recommendations for modelling and analysis	217
APPENDIX.....	218
Derivation of cross-anisotropic elastic constants	218
REFERENCES.....	219

LIST OF TABLES

<i>Table 3.1 Physical properties of lateritic soils</i>	57
<i>Table 4.1 Testing programme for cross-anisotropic elastic parameters of a saturated lateritic clay</i>	84
<i>Table 4.2 Testing programme for compaction structure on anisotropic elastic stiffness of a saturated lateritic clay</i>	84
<i>Table 4.3 Cross-anisotropic elastic parameters</i>	85
<i>Table 4.4 Summary of fitting parameters on effects of compaction state on the anisotropic elastic stiffness</i>	85
<i>Table 5.1 Test programme for investigating suction effects on stiffness characteristics</i> 112	
<i>Table 5.2 Test programme for investigating the coupled influence of anisotropy and suction</i>	113
<i>Table 5.3 Summary of measured and calculated parameters</i>	114
<i>Table 6.1 High suction effect on monotonic behaviour at small strains</i>	140
<i>Table 6.2 Effects of initial compaction water content on cyclic behaviour</i>	140
<i>Table 6.3 High suction effect on cyclic behaviour at small strains</i>	141
<i>Table 6.4 Soil state after suction-induced desiccation via VET</i>	141
<i>Table 7.1 Testing programme for constant temperature loading and unloading one-dimensional stress</i>	174
<i>Table 7.2 Testing programme for thermal cycles on G_0 at constant one-dimensional stress</i>	174
<i>Table 7.3 Testing programme for coupled suction and thermal effects on G_0 at constant stress</i>	175
<i>Table 7.4 Soil states at suction and thermal equilibrium</i>	176
<i>Table 7.5 Calibrated fitting parameters for the proposed semi-empirical equation</i>	177
<i>Table 8.1 Modulus parameters for subgrade layer</i>	201

LIST OF FIGURES

<i>Figure 1.1 Stiffness degradation curve (Atkinson and Sallfors 1991; Mair 1993; Sawangsuriya 2012)</i>	7
<i>Figure 1.2 Interaction of geotechnical infrastructures and environment</i>	8
<i>Figure 1.3 Research strategy adopted in this study</i>	9
<i>Figure 2.1 Axis-translation device for measuring negative pore-water pressures (Hilf 1956)</i>	30
<i>Figure 2.2 Principle of osmotic technique (Blatz et al. 2008; Ng and Menzies 2007b)</i> ..	31
<i>Figure 2.3 Application of vapour equilibrium technique in a desiccator (Tang and Cui 2005, Blatz et al. 2008)</i>	32
<i>Figure 2.4 Pore water distribution in unsaturated soil lo</i>	33
<i>Figure 2.5 Representation of measurement technique of bender element (Ingale et al. 2017)</i>	34
<i>Figure 2.6 Arrangement of bender elements for measuring stiffness anisotropy (Ng and Yung 2008b)</i>	35
<i>Figure 2.7 Influence of matric suction on initial shear modulus of an unsaturated compacted silty sand (a) at OMC (b) wet side of OMC (Mancuso et al. 2002)</i>	36
<i>Figure 2.8 Influence of wetting and drying on the initial shear modulus of an unsaturated soil (Ng et al. 2009)</i>	37
<i>Figure 2.9 Influence of suction on strain-dependent shear modulus (Xu 2011)</i>	38
<i>Figure 2.10 Comparison of normalised shear modulus degradation of unsaturated loess with design curves (Ng et al. 2017b)</i>	38
<i>Figure 2.11 Typical stress-strain of subgrade soil under cyclic loading-unloading (O'reilly and Brown 1992)</i>	39
<i>Figure 2.12 Effects of stress and suction on resilient modulus (a) light compaction (b) heavy compaction (Sivakumar et al. 2013)</i>	40
<i>Figure 2.13 Influence of stress and high suction state on resilient modulus (Banerjee et al. 2020)</i>	41
<i>Figure 2.14 Volume change of saturated Bangkok clay during heating and cooling cycle at different OCRs (Abuel-Naga et al. 2007)</i>	42
<i>Figure 2.15 Volume changes of two fine-grained soils during heating/cooling cycles</i>	43
<i>Figure 2.16 Thermal effects on preconsolidation of Lulea clay (Eriksson 1989)</i>	43

Figure 2.17 Secant Young's modulus of a saturated Kaolin (Cekerevac and Laloui 2004)	44
Figure 2.18 Normalised secant shear modulus of clay at different temperatures (Ghahremannejad 2003a)	45
Figure 2.19 Secant shear modulus of compacted silt at different temperatures (Zhou et al. 2015a)	45
Figure 2.20 Small strain shear modulus of compacted silt at different temperatures (Vahedifard et al. 2020)	46
Figure 2.21 Typical cross-section of various pavement structures (Brown 1996)	47
Figure 2.22 Pavement failure modes (a) fatigue cracking (b) rutting (Brown 1996)	48
Figure 3.1 Particle size distribution of soil	58
Figure 3.2 Standard Proctor compaction curve of soil	58
Figure 3.3 X-ray diffractometer results and mineralogy in the lateritic clay (Ng et al. 2019c)	59
Figure 3.4 Specimen preparation for vertical and horizontal cut specimen	59
Figure 3.5 SEM image of lateritic soil	60
Figure 3.6 Typical pore size distribution of lateritic soil with changes in suction (Akinniyi 2019)	61
Figure 3.7 Predicted soil water retention of a lateritic soil	61
Figure 3.8 Schematic diagram of a double-cell triaxial apparatus equipped with local strain measurements (after Chen et al. (2018))	62
Figure 3.9 Schematic diagram of a temperature-controlled oedometer equipped with bender elements	63
Figure 3.10 Schematic diagram of triaxial apparatus with temperature control and bender element set-up	64
Figure 4.1 Relationship between (a) small-strain shear modulus (G_0) and mean effective stress (b) Parameter A and (c) Parameter n for G_0 (Atkinson 2000)	87
Figure 4.2 SEM image of (a) Lateritic soil (b) CDT	88
Figure 4.3 Shear behaviour from drained tests at effective confining stress of 50 and 200 kPa (a) stress-strain and (b) volumetric response	89
Figure 4.4 Drained small strain stiffness behaviour (a) Stiffness degradation (b) Evolution of stiffness anisotropy	90
Figure 4.5 Relationship between small strain Young's modulus and mean effective stress	91

Figure 4.6 Shear behaviour from undrained tests at effective confining stress of 50 and 200 kPa (a) stress-strain and (b) pore pressure change (c) stress path.....	92
Figure 4.7 Small strain stiffness behaviour.....	93
Figure 4.8 Unified critical state in $q - p'$ space.....	93
Figure 4.9 Summary of the relationship between PI and degradation with design curves by Vardanega and Bolton (2013).....	94
Figure 4.10 Variations of $G_{0(hh)}$ during isotropic compression for specimen with initial compaction water content of (a) 16.5%, (b) 19.5% and (c) 22.5%.....	95
Figure 4.11 Variations of $G_{0(hv)}$ during isotropic compression for specimen with initial compaction water content of (a) 16.5%, (b) 19.5% and (c) 22.5%.....	96
Figure 4.12 Anisotropic shear stiffness at different compaction water content (a) 90% and (b) 95% MDD.....	97
Figure 4.13 SEM of specimens at compaction water content of (a) 16% (b) 19 and 22%.....	98
Figure 5.1 Stress path for suction effects on small to large strain behaviour of soil under monotonic loading.....	115
Figure 5.2 Stress-strain behaviour of unsaturated compacted lateritic soil at (a) 50 and (b) 200 kPa mean net stress.....	116
Figure 5.3 Effects of mean net stress on stress strain behaviour at a particular suction of (a) 0 kPa (b) 10 kPa and (c) 150 kPa.....	117
Figure 5.4 Volume change response of unsaturated compacted lateritic soil at (a) 50 and (b) 200 kPa mean net stress.....	118
Figure 5.5 Influence of mean net stress on volumetric response at a particular suction of (a) 0 kPa (b) 10 kPa and (c) 150 kPa.....	119
Figure 5.6 Small-strain stiffness of unsaturated compacted lateritic soil at (a) 50 kPa (b) 200 kPa mean net stress.....	120
Figure 5.7 Effects of mean net stress small strain stiffness at a particular suction.....	121
Figure 5.8 Specimen orientation and suction effects at 50 and 200 kPa mean net stress: (a), (b) stress-strain behaviour; (c), (d) volume change response.....	123
Figure 5.9 Specimen orientation and suction effects on small-strain stiffness at (a) 50 kPa (b) 200 kPa mean net stress.....	124
Figure 5.10 Suction effects on the evolution of stiffness anisotropy of compacted specimen.....	125

Figure 5.11 Comparison between measured and calculated E_0 at mean net stress of (a) 50 kPa; (b) 200 kPa	126
Figure 5.12 Summary of all measured degradation curves in comparison with design charts.....	127
Figure 6.1 Changes in gravimetric water content in desiccators for (a) K_2SO_4 (b) NaCl (c) LiCl	142
Figure 6.2 Pore size distribution of the lateritic specimen after various suction induced desiccation for different compaction water contents (a) w16, (b) w19 and (c) w22.	143
Figure 6.3 Comparison of suction of effects on inter-aggregate and intra-aggregate pore volume for different compaction water contents (a) w16, (b) w19 and (c) w22.....	144
Figure 6.4 Influence of compaction water content on stress-strain at (a) 40 MPa and (c)300 MPa	145
Figure 6.5 Effects of high suction on stress-strain for the compaction water content of (a) 16%, (b) 19% and (c) 22%	146
Figure 6.6 Influence of compaction water content on dilatancy at (a) 40 MPa and (b)300 MPa.....	147
Figure 6.7 Effects of high suction on dilatancy for the compaction water content of (a) 16%, (b) 19% and (c) 22%	148
Figure 6.8 Effects of compaction water content on peak and critical state strength after high suction-induced desiccation.....	149
Figure 6.9 Influence of compaction water content on small strain at (a) 40 MPa and (c)300 MPa.....	150
Figure 6.10 Effects of high suction on small stain stiffness for the compaction water content of (a) 16%, (b) 19% and (c) 22%.....	151
Figure 6.11 Influence of deviator stress on M_R when the compaction water content in 16.5% (a) 42 kPa and (b) 15 kPa	152
Figure 6.12 Influence of deviator stress on M_R when the compaction water content in 19.5% (a) 42 kPa and (b) 15 kPa	153
Figure 6.13 Influence of deviator stress on M_R when the compaction water content in 22.5% (a) 42 kPa and (b) 15 kPa	154
Figure 6.14 Effects of suction on M_R when the compaction water content in 16.5% (a) 42 kPa and (b) 15 kPa	155
Figure 6.15 Effects of suction on M_R when the compaction water content in 19.5% (a) 42 kPa and (b) 15 kPa	156

Figure 6.16 Effects of suction on M_R when the compaction water content is 22.5% (a) 42 kPa and (b) 15 kPa	157
Figure 6.17 Influence of mean net stress on M_R when $w = 16%$ at suctions of approximately (a) 4 (b) 40 (c) 300 MPa	158
Figure 6.18 Influence of cyclic stress on plastic strain accumulation at different compaction water contents (a) w_{16} , (b) w_{19} and (c) w_{22}	159
Figure 6.19 Influence of high suction on plastic strain accumulation at different compaction water contents (a) w_{16} , (b) w_{19} and (c) w_{22}	160
Figure 7.1 Thermo-mechanical paths (a) 1D compression at constant temperature (b) cyclic heating-cooling at constant stress	178
Figure 7.2 Stress path adopted for suction and thermal effects on G_0	179
Figure 7.3 Influence of temperature on one-dimensional compression.	180
Figure 7.4 Influence of temperature on elastic shear modulus.	180
Figure 7.5 Accumulation of cyclic thermal strains at vertical effective stresses of 50 kPa (overly consolidated) and 400 kPa (normally consolidated).....	181
Figure 7.6 Elastic shear modulus during cyclic heating and cooling at vertical effective stresses of (a) 50 kPa (overly consolidated) and (b) 400 kPa (normally consolidated).....	182
Figure 7.7 Effects of thermal cycles on the elastic shear modulus at vertical effective stresses of 50 kPa (overly consolidated) and 400 kPa (normally consolidated).....	183
Figure 7.8 Effects of temperature on (a) $G_{0(hh)}$ and (b) $G_{0(hv)}$ at various suctions (mean net stress = 50 kPa)	184
Figure 7.9 Effects of temperature on (a) $G_{0(hh)}$ and (b) $G_{0(hv)}$ at various suctions (mean net stress = 200 kPa)	185
Figure 7.10 Suction effects on the (a) $G_{0(hh)}$ and (b) $G_{0(hv)}$ at different temperatures (mean net stress = 50 kPa)	186
Figure 7.11 Suction effects on the (a) $G_{0(hh)}$ and (b) $G_{0(hv)}$ at different temperatures (mean net stress = 200 kPa)	187
Figure 7.12 Thermal induced anisotropy at various suctions.....	188
Figure 7.13 Comparison between measured and calculated temperature and suction-dependent G_0 of unsaturated lateritic clay (a) $G_{0(hv)}$ and (b) $G_{0(hh)}$	189
Figure 7.14 Comparison between measured and calculated temperature and suction-dependent G_0 of unsaturated silt (measured data from Vahedifard et al. (2020))	190
Figure 8.1 Flexible pavement adopted for performance prediction on lateritic soil subgrade.....	202

<i>Figure 8.2 Vertical stress distribution under the pavement (1) centre (2) edge (3) mid-point between the two wheels (note: compression is positive)</i>	<i>203</i>
<i>Figure 8.3 Radial stress distribution under the pavement (1) centre (2) edge (3) mid-point between the two wheels (note: compression is positive).....</i>	<i>203</i>
<i>Figure 8.4 Vertical compressive strain distribution under the pavement (1) centre (2) edge (3) mid-point between the two wheels (note: compression is positive)</i>	<i>204</i>
<i>Figure 8.5 Horizontal tensile strain distribution under the pavement (1) centre (2) edge (3) mid-point between the two wheels (note: compression is positive)</i>	<i>204</i>
<i>Figure 8.6 Vertical resilient strain profile with depth along the centreline of wheel loading</i>	<i>205</i>
<i>Figure 8.7 Calculated rutting depth versus the number of load applications.....</i>	<i>206</i>
<i>Figure 8.8 Horizontal strain profile with depth along the centreline of wheel loading.</i>	<i>206</i>
<i>Figure 8.9 Suction effects on fatigue cracking</i>	<i>207</i>
<i>Figure 8.10 Temperature effect on estimated vertical resilient strain profile</i>	<i>208</i>
<i>Figure 8.11 Thermal influence on calculated rutting depth versus the number of load applications (a) $s = 0$ kPa (b) $s = 150$ kPa</i>	<i>209</i>
<i>Figure 8.12 Thermal effects on tensile strain profile with depth along the centreline of wheel loading.....</i>	<i>210</i>
<i>Figure 8.13 Fatigue cracking with the number of load applications.</i>	<i>210</i>

LIST OF PLATES

<i>Plate 3.1 Dynamic compaction components</i>	65
<i>Plate 3.2 Static compaction with a triaxial loading frame</i>	65
<i>Plate 3.3 Carefully trimmed horizontal cut specimen</i>	66
<i>Plate 3.4 Double-cell triaxial apparatus</i>	66
<i>Plate 3.5 Cyclic triaxial apparatus</i>	67
<i>Plate 3.6 Temperature-controlled oedometer with the bender element setup</i>	68
<i>Plate 3.7 Set up of temperature and suction control triaxial apparatus</i>	69
<i>Plate 6.1 Suction imposed via Vapour equilibrium technique in desiccators</i>	161
<i>Plate 6.2 PoreMaster[®] mercury intrusion pore size analyser at HKUST</i>	161

CHAPTER 1 INTRODUCTION

1.1 Background of this research

Lateritic soils are chemically weathered materials widely distributed in tropical and subtropical areas like Asia (India and China), West Africa (Ghana and Nigeria) and South America (Brazil) (Gidigas 1976; Ng et al. 2019c). Compacted lateritic soils are used to construct many geotechnical structures, including foundations, embankments, retaining walls and pavements. Their high sesquioxide (iron and aluminium oxides) content leads to significant aggregation and has an impact on the soil microstructure (Blight 1991b; Gidigas 1976; Netterberg 2014). The mechanical characteristics of lateritic soils, such as their compressibility and shear strength, have been demonstrated to be significantly impacted by the aggregated structures (Fagundes and Rodrigues 2015; Futai and Almolda 2005; Ng et al. 2019c; Toll 2000; Zhang et al. 2016). The past studies of lateritic soils concentrated on their mechanical behaviour at large strains (above 1%), such as shear strength and dilatancy. The results can be used for analysing the ultimate limit state of geotechnical structures. However, it is difficult to accurately predict structures' serviceability limit state (i.e., their performance in working conditions). The problem is because the strain encountered by many geotechnical structures under the working conditions is within the small strain range (0.001–0.1%), as shown in Figure 1.1 (Atkinson and Salfors 1991; Mair 1993; Sawangsurriya 2012). An accurate prediction of the ground movements is crucial for some emerging geotechnical structures like the embankments for high-speed rail (HSR). Compared to conventional embankments, the allowable post-construction ground deformation of HSR embankments is much smaller (e.g., 15 mm in China National Standards). Excessive settlement may induce problems such as foundation serviceability issues at the Paris-Brussels-London line (Cui et al. 2004; Muñoz-Castelblanco et al. 2011). In addition, soil compaction can result in an inherent anisotropy (Jovičić and Coop 1998) that may lead to stiffness anisotropy, which could greatly affect ground movements (Cai et al. 2015). Thus, it is important to investigate the anisotropic stiffness of compacted lateritic soils with consideration of their initial structure, in order to improve the fundamental understanding of small strain behaviour of unsaturated lateritic soils in various geo-structures.

As Mitchell and Soga (2005) described, the structure of compacted soils is the combination of cementation and the arrangement of individual particles, their aggregates, and pores. This structure is affected by the compaction conditions in terms of the compaction water content and

density and the compaction method (i.e., static and dynamic compaction) (Alonso et al. 2013; Delage et al. 1996; Lambe 1958; Lambe 1962; Mitchell et al. 1965). So far, many studies have revealed that the compaction-induced structure significantly affects the engineering properties of saturated and unsaturated compacted soils. Most of these previous studies, however, focus on soil behaviour at large strains (above 1%), such as the strength and wetting collapse, as well as the changes in yield stress (Behbehani and McCartney 2022; Cokca et al. 2004; Çokça and Tilgen 2009; Delage et al. 1998; Mun and McCartney 2017; Sivakumar and Wheeler 2000; Toll 2000; Wheeler and Sivakumar 2000). With regards to strains below 1%, most studies on compacted soils measured the elastic stiffness (at strains less than 0.001%) (Hasan and Wheeler 2014; Heitor et al. 2013; Hoyos et al. 2015; Khosravi and McCartney 2011; Khosravi and McCartney 2012; Khosravi et al. 2018; Mancuso et al. 2002; Ng and Yung 2008b; Qian et al. 1993; Sawangsuriya et al. 2009b; Yang et al. 2008b) whereas very few of them have focused on soil behaviour at small strains, in particular, compaction-induced anisotropic small strain (i.e., between 0.001 to 1%) stiffness behaviour.

On the other hand, as illustrated in **Figure 1.2**, compacted soils are often unsaturated and subjected to various complex working conditions in the field. Taking compacted soils in the pavements and embankments as examples, they are subjected to daily and seasonal variations of temperature and suction, resulting from changes in water content, particularly at shallow depths. Based on field monitoring at given sites in Arkansas, McCartney and Khosravi (2013) found that up to a depth of 2 m, the suction and temperature of subgrade soils vary dramatically in a wide range of 0 to 10 MPa and 5 to 60°C, respectively. It is thus necessary to understand the influence of suction and temperature on the small strain stiffness of compacted soils.

To study suction effects on the small strain stiffness of unsaturated soils, some studies used soil specimens prepared at different gravimetric water contents or degrees of saturation (Qian et al. 1993; Wu et al. 1984) and the measurement of the post-specimen preparation suction (Sawangsuriya et al. (2008)). One problem with this approach is that the observed differences in tested specimens may be attributed to both suction and structure effects. Due to advances in laboratory testing over several decades, suction control techniques have been adopted. This method allows specimens to be prepared at a certain water content and subjected to suction control before evaluating the stiffness (Hoyos et al. 2015; Khosravi and McCartney 2011; Khosravi and McCartney 2012; Khosravi et al. 2010; Mancuso et al. 2002; Ng and Yung 2008b; Sawangsuriya et al. 2009b; Yang et al. 2008a; Yang et al. 2008b). In addition, most of the previous studies on suction-controlled effects on stiffness were limited to low suctions of less

than 1 MPa. Moreover, it should be noted that the subsequent changes in suction can alter the initial structure, such as the pore size distribution of the compacted soil (Romero 2013), and thus the soil stiffness. However, the coupled effects of suction and initial structure on soil stiffness are not fully understood.

Thermal effects on soil behaviour have attracted great attention in recent years because of their relevance to some emerging research areas like energy geo-structures (Laloui and Di Donna 2013; McCartney et al. 2016). Most of the previous studies focused on temperature effects on the shear strength, yielding and thermal strain of soil (Abuel-Naga et al. 2007; Cekerevac and Laloui 2004; Coccia and McCartney 2012; Ghahremannejad 2003b; Graham et al. 2001; Hueckel and Baldi 1990; Ng et al. 2017a; Ng et al. 2019b; Pan et al. 2020; Shanina and McCartney 2017). Moreover the studies by Coccia and McCartney (2012) and Shanina and McCartney (2017) are relevant to understanding stress-induced anisotropy effects on the thermal deformations of soils. Some valuable findings have been reported in the literature. For example, it is well recognized that the thermal strain of soil is greatly dependent on the overconsolidation ratio (OCR). Normally consolidated and slightly overconsolidated soils generally show irreversible contraction under heating and thus lead to thermal hardening. With increasing number of thermal cycles, there is an accumulation of plastic deformation at a decreasing rate (Campanella and Mitchell 1968; Di Donna and Laloui 2015). In contrast, heavily overconsolidated soil exhibits reversible expansion during the heating process. It has been also found that the yield stress decreases with an increase in temperature at overconsolidated state, which is commonly referred to as thermal softening (Cekerevac and Laloui 2004; Tang et al. 2008).

Regarding thermal effects on the stiffness of soils, there are minimal data in the literature, and the existing data comprises some contradictory findings. Cekerevac and Laloui (2004) determined the secant Young's modulus of a saturated Kaolin clay from the results of triaxial tests at an axial strain of 0.5%. They found that the secant Young's modulus increased with increasing temperature. Zhou et al. (2015a) observed that the secant shear modulus of silty soil at 60°C was consistently lower than that at 20°C in the strain range of 0.003% to 1%. The above two studies focused on the secant modulus rather than the elastic stiffness, an essential parameter in constitutive modelling and practical design. Recently, Vahedifard et al. (2020) measured the elastic shear modulus of silt using bender elements in a temperature-controlled triaxial. The elastic shear modulus decreased as soil temperature increased from 23 to 43°C. Their study mainly focused on unsaturated conditions, and the explanations of experimental

results were mainly based on thermal effects on the air-water surface tension. There are only two data points at the saturated condition; therefore, no solid conclusion can be drawn for saturated soils. Moreover, there is no study in the literature on the cyclic thermal effects on soil stiffness. Hence, there is a need to study the influence of temperature and thermal cycles on the stiffness of saturated and unsaturated soils. The results could be used to analyze the serviceability limit state of earthen structures under non-isothermal conditions and to improve the constitutive modelling. In addition, thermo-hydro-mechanical modelling of soil behaviour has attracted much attention (Abuel-Naga et al. 2009b; Graham et al. 2001; Hamidi et al. 2014; Hueckel and Baldi 1990; Zhou and Ng 2015a). The existing models do not consider thermal effects on the elastic stiffness behaviour due to the lack of experimental data, except the models reported by Graham et al. (2001) and Hamidi et al. (2014). Even though these two models have incorporated thermal effects on elasticity, the relevant formulations were not verified using experimental results.

Based on the above literature review, the small strain soil behaviour of compacted soils is essential for accurate and reasonable deformation assessment. There is an urgent need to improve the fundamental understanding of the small strain stiffness behaviour of compacted lateritic soils at saturated and unsaturated conditions, considering the influence of soil microstructure and thermo-hydro-mechanical loading. Aspects such as compaction-induced anisotropic stiffness and its evolution with suction at small strains, which has rarely been studied, must be investigated. Such investigations may lead to an improved understanding of the impact of suction on anisotropic soil stiffness. A wider range of suction needs to be considered to describe strain-dependent stiffness properties such as secant stiffness and resilient modulus measured under monotonic and cyclic loading, respectively. Moreover, investigating coupled suction and thermal effects on anisotropic stiffness will give more insights into unsaturated soil thermo-hydro-mechanical behaviour. Lastly, the focus being on lateritic clay soil is essential because it has distinct properties from other clays due to its high sesquioxide content. Its stiffness characteristics have not been well understood, especially when the soil is unsaturated and anisotropic.

1.2 Objectives and research strategy

This study aims to reveal the small strain stiffness characteristics of compacted lateritic soils along various thermo-hydro-mechanical paths. The principal objectives include the following:

1. To determine the complete set of cross-anisotropic elastic parameters for a saturated compacted lateritic clay and to reveal the influence of initial structure on the evolution of stiffness anisotropy.
2. To investigate the coupled effects of suction and initial microstructure on the stiffness characteristics of compacted specimens over a wide suction range.
3. To study the influence of temperature and thermal cycles on the elastic shear modulus of saturated and unsaturated compacted specimens.
4. To develop a semi-empirical model with an attempt to improve the modelling of soil behaviour at small strains (less than 1%) at various thermo-hydro-mechanical conditions and apply it in pavement analysis for investigating the influence of suction and thermal effects on rutting prediction and fatigue cracking.

This study tested a lateritic clay at saturated and unsaturated conditions to meet these objectives. The specimens were compacted at different water contents to produce various as-compacted microstructures and then tested along various thermo-hydro-mechanical paths. Both vertically and horizontally cut specimens were used to investigate the anisotropy of stiffness. Several advanced apparatuses were used in the testing, including a new temperature-controlled oedometer equipped with bender elements, a new suction and temperature-controlled triaxial apparatus with local strain measurements, bender elements and double-cell total volume change measurements. Soil suctions in the low (below 300 kPa) and high (above 4 MPa) ranges were controlled using the axis translation and vapour equilibrium techniques, respectively. In addition, a temperature range of 5 to 60°C was considered. The ranges of suction and temperature were selected with reference to some field monitoring studies on subgrade soils, which showed that temperature and suction fluctuate widely up to a depth of 2 meters. Moreover, microstructural analysis was used to interpret experimental results providing a linkage between micro and macro soil behaviour. Finally, a semi-empirical thermo-hydro-mechanical model was developed based on the results of the above tests and an existing equation (Zhou and Ng 2016). The interrelationships among these parts are illustrated in **Figure 1.3**.

1.3 Layout of thesis

This thesis consists of nine chapters, including an introduction in Chapter 1.

Chapter 2 presents a literature review of the thermo-hydro-mechanical behaviour of saturated and unsaturated soils, especially the small-strain behaviour.

Chapter 3 presents the soil properties, specimen preparation and test methods used.

In Chapter 4, the experimental results at saturated and room temperature conditions are reported and analysed. Particular attention is paid to the complete set of cross-anisotropic stiffness parameters from very small to large strains, which has not been reported in the literature for lateritic clays.

Chapters 5 analyses the results in the low suction range under monotonic loading. Suction effects on the small to large strain response, including discussion and proposal of semi-empirical equations for stiffness degradation of unsaturated soils.

Chapter 6 addresses the effects of high suction on both monotonic and cyclic shear behaviour, including the stress-strain relation, dilatancy, and degradation of shear modulus under monotonic shearing and resilient modulus under cyclic loads.

The 7th Chapter presents results about the coupled thermal and suction effects on elastic shear modulus.

Chapter 8 presents a simple pavement performance analysis using the new results from the previous chapters and discusses the possible influence of suction and temperature on rutting prediction and fatigue cracking.

Finally, Chapter 9 summarises the major conclusions drawn from this study. Some recommendations for further work are given.

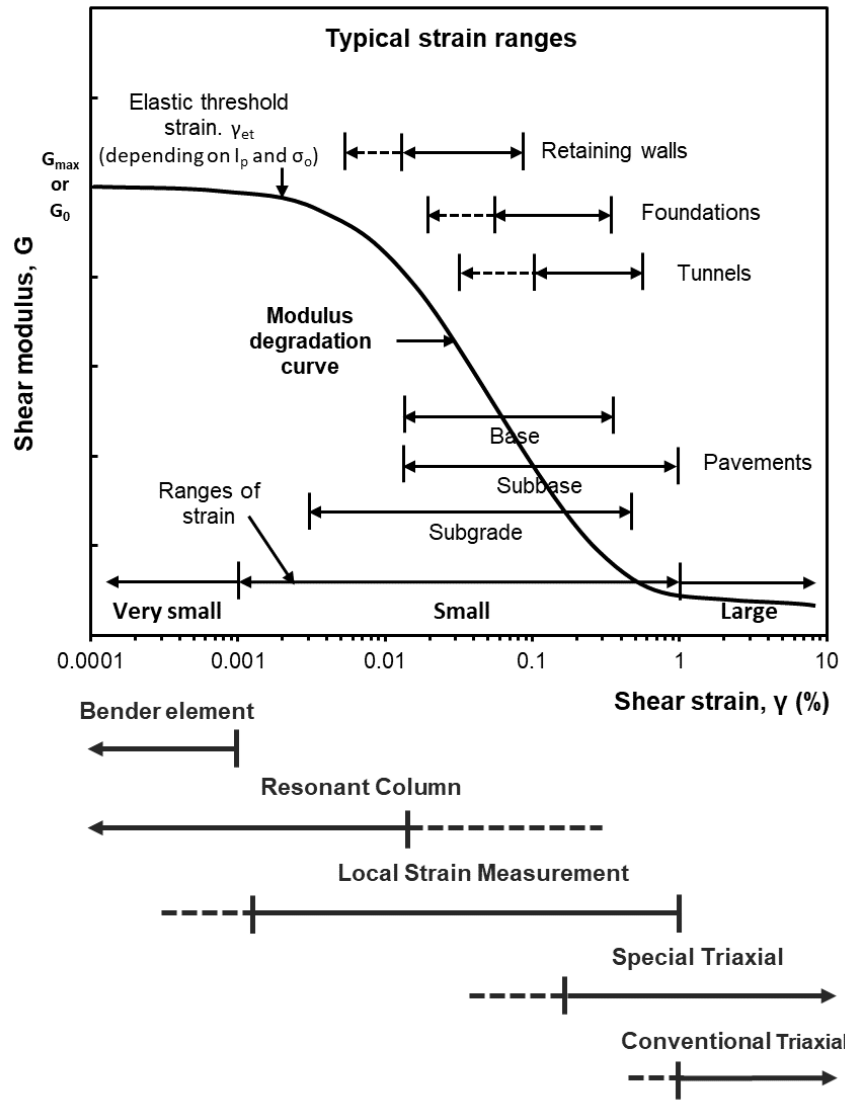


Figure 1.1 Stiffness degradation curve (Atkinson and Sallfors 1991; Mair 1993; Sawangsuriya 2012)

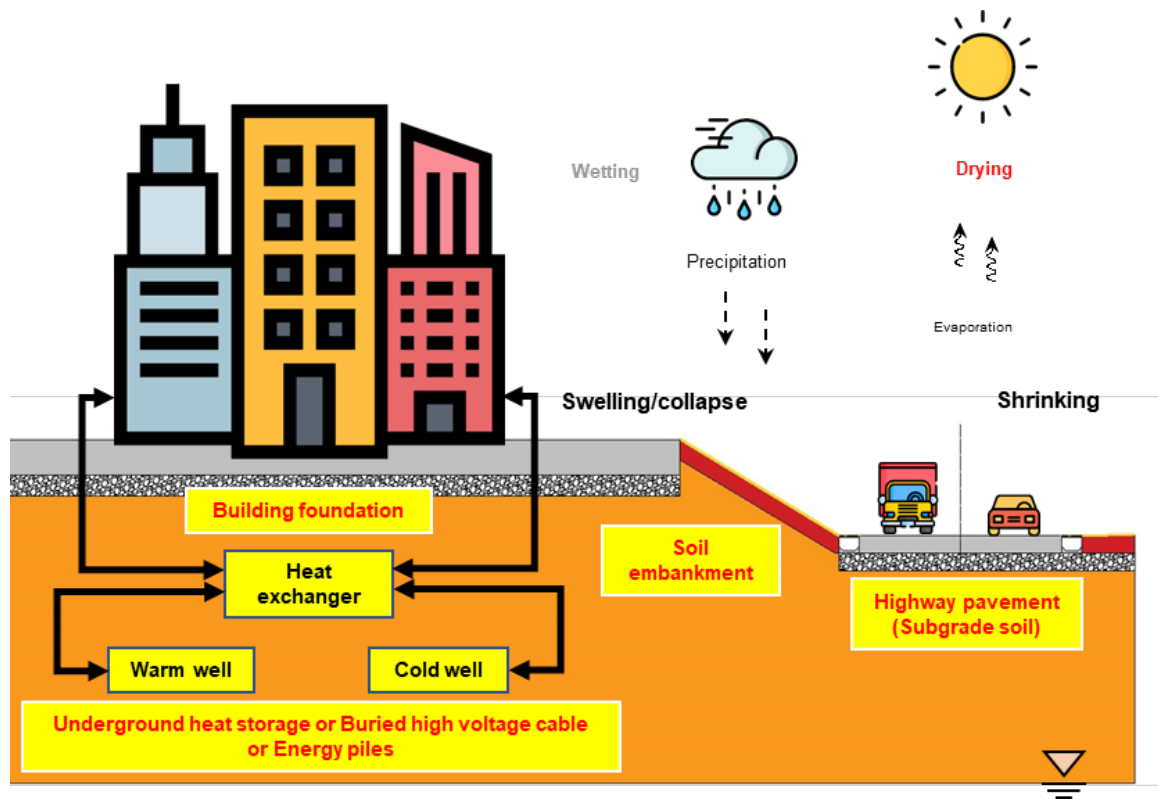


Figure 1.2 Interaction of geotechnical infrastructures and environment

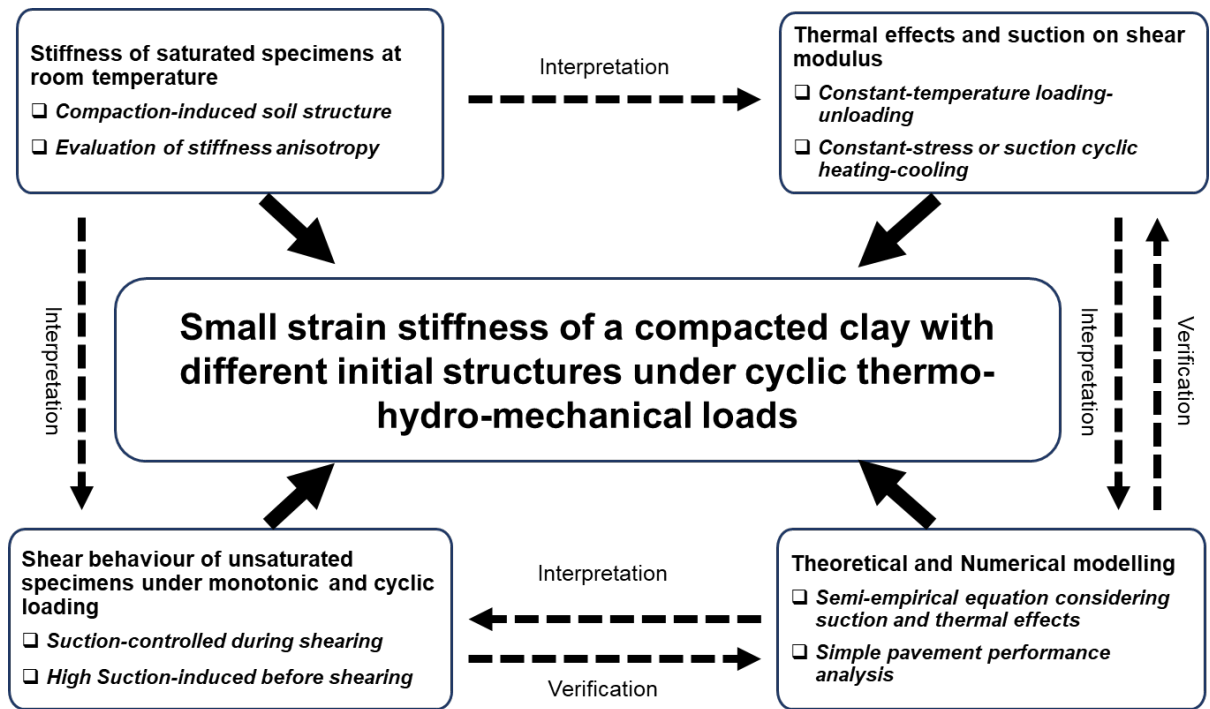


Figure 1.3 Research strategy adopted in this study

CHAPTER 2 LITERATURE REVIEW

2.1 Basic unsaturated soil mechanism

2.1.1 Stress State for Unsaturated Soils

According to [Fredlund and Morgenstern \(1977\)](#), an unsaturated soil consists of four phases: solid, water, air and an air-water interface called contractile skin ([Paddy 1969](#)). It is recognizable that the mechanical behaviour of an unsaturated soil is more complicated than a soil in completely saturated state. For a fully saturated soil, the effective stress variable, $\sigma' = \sigma - u_w$ is commonly used in soil mechanics as a stress state variable to which soil mechanical behaviour can be related ([Terzaghi 1936](#)). It is desirable that the concept of effective stress for saturated soils be extended to unsaturated soils. [Bishop \(1959\)](#) proposed a single-stress variable of effective stress, $\sigma' = \sigma - u_a + \chi(u_a - u_w)$ for unsaturated soils, he matric suction to consider the effect of capillary phenomenon. The effective stress parameter, χ , is a function of the degree of saturation and varies from 0 for dry soils to 1 for saturated soils. A number of researchers have also proposed similar expressions of effective stress ([Aitchison and Donald 1955](#); [Bishop and Blight 1963](#)), but the validity of Bishop's single variable effective stress for unsaturated soil has been questioned by some researchers due to its inability to provide a reasonable explanation for the collapse of unsaturated soils upon wetting ([Jennings and Burland 1962](#); [Jommi 2000](#)).

To overcome the limitations of the single variable effective stress theory, some researchers have proposed using two independent stress variables, net stress and matric suction, to describe the strength and deformation behaviour of unsaturated soils ([Bishop 1959](#); [Bishop and Blight 1963](#); [Coleman 1962](#)). This approach has been verified by null tests ([Fredlund and Morgenstern 1977](#)) and has become mainstream in unsaturated soil research. Recently, some researchers have used two variables, suction and the Bishop-type effective stress, to describe the behaviour of unsaturated soils ([Sheng et al. 2004](#); [Wheeler et al. 2003](#); [Zhao et al. 2009](#)).

However, there are limitations to using effective stress as a macroscopic stress variable in unsaturated soils. According to [Lu \(2008\)](#), matric suction is not a macroscopic stress variable in a Representative Elementary Volume (REV) of unsaturated soils, and a transfer function is necessary to scale it up to a macroscopic stress variable. The concept of suction stress has been introduced to also describe the effective stress as $\sigma' = \sigma - u_a + \sigma^s$ in partially saturated soil, and the expression of the transfer function has been provided by [Lu et al. \(2010\)](#). Additionally, the

effective degree of saturation (Alonso et al. 2013) needs to be considered, which includes the effect of water absorption action in soil pores, but it is difficult to determine macroscopically.

Detailed reviews and discussions of the effective stress state in relation to saturated and unsaturated soil behaviour can be found in the literature (Fredlund 2006; Fredlund and Rahardjo 1993; Lu et al. 2010; Nuth and Laloui 2008; Zhao et al. 2016).

2.1.2 Suction in unsaturated soils

For unsaturated soil, suction is considered one of the stress state variables in describing soil behaviour (Alonso et al. 1990; Fredlund and Rahardjo 1993; Gens et al. 2006; Wheeler et al. 2003). Edlefsen and Anderson (1943) describe soil suction as the free energy state of soil water, which can be estimated from the partial vapour pressure of pore water (Aitchison 1965a, 1965b) according to the thermodynamic theory as:

$$\psi_v = RT \frac{\rho_w}{\omega_v} \ln \left(\frac{p_v}{p_{v0}} \right) \quad (2.1)$$

where R is the universal gas constant; T is absolute temperature; ρ_w is the density of water; ω_v is the molecular mass of water; p_v is the partial pressure of pore-water p_{v0} is the partial pressure of water vapour in equilibrium with pure free water at given pressure and temperature; the ratio p_v/p_{v0} is commonly referred to as relative humidity (RH).

From the above equation, the suction estimated using the RH at isothermal conditions is referred to as total suction. The total suction comprises two components: matric suction ($u_a - u_w$) and osmotic suction (π). Matric suction, also sometimes referred to as negative of matric potential is caused by adsorptive forces between soil water and particles in addition to capillary forces at the air-water interface in the soil structure, whereas osmotic suction is caused primarily by dissolved salts or contaminants in the soil pore fluid (Baker and Frydman 2009; Krahn and Fredlund 1972; Lu 2016; Malaya and Sreedeeep 2012; Philip 1977; Tuller et al. 1999)

2.1.3 Common techniques for suction control

This section briefly reviews the different methods developed to control either matric or total suctions of unsaturated soils, including the axis-translation, osmotic, and vapour equilibrium techniques.

In geotechnical engineering, Hilf (1956) was perhaps the first to introduce the axis-translation technique to control or measure matric suction, as shown in Figure 2.1. The

procedure for measuring matric suction using the axis-translation technique is summarised in (Fredlund and Rahardjo 1993). This suction measurement is achieved by increasing the pore air pressure (u_a) to increase the pore water pressure (u_w). By the same quantity, the total pressure should be increased with pore air pressure so that the net stress does not change during this process. In the field, when the air pressure is generally equal to atmospheric pressure ($u_a = 0$), the value of matric suction is equal to the negative pore-water pressure. The axis-translation technique changes the origin of reference for the pore-water pressure from standard atmospheric conditions to the final air pressure in the chamber (Hilf 1956). Thus, cavitation in the water drainage system can be prevented by this technique. The matric suction of the soil is the difference between the air pressure in the chamber and the measured water pressure under the ceramic disk shown in **Figure 2.1** when the system is at equilibrium. The matric suction values range from 0 to 1500 kPa, depending on the air-entry value of the ceramic disk.

Soil scientists initiated the osmotic technique to control soil suction (Zur 1966). Geotechnical researchers then applied it for various soil testing, as summarised in Delage and Cui (2008). The phenomenon of osmosis is observed whenever a semi-permeable membrane separates a solvent and a solution, as shown in **Figure 2.2(a)**. Small-sized molecules and water can traverse the membrane, whereas the membrane limits large-sized molecules. The osmotic technique's application in geotechnical testing is achieved by placing a soil specimen in contact with a cellulosic semi-permeable membrane, as shown in **Figure 2.2(a)**. A solution is then circulated around the membrane. The membrane is usually permeable to water and ions in the soil but impermeable to large solution molecules and soil particles (Zur 1966). Because of the difference in solution concentration between specimen and solution, a difference in osmotic potential across the membrane is established. This causes drainage in the soil specimen and this potential is finally balanced by negative pore water pressure in the soil specimen. Zur (1966) showed that under equilibrium conditions, an analysis of water energy on both sides of a membrane demonstrates that matric suction in a soil specimen is equal to the osmotic pressure of the solution. The osmotic technique can apply a higher suction of up to 10 MPa (Delage et al. 1998). Polyethylene glycol (PEG) solution is commonly used in geotechnical testing, in the application of osmotic technique due to its safety and simplicity. The value of osmotic pressure or suction depends on the concentration of the PEG solution. A major problem of using the osmotic technique is the fragility of the membrane and its sensitivity to bacteria attack (Delage and Cui 2008).

Equation (2.1) shows that total suction of unsaturated soil can be induced by controlling relative humidity around the soil. This principle led to the development and successful application of the vapour equilibrium technique (VET) for experiments in geotechnical engineering (Blatz et al. 2008; Tang and Cui 2005; Tessier 1984). In VET, a soil specimen is set above an aqueous solution (e.g. saturated salt solution) in a sealed container (e.g. desiccator) **Figure 2.3**. The solution imposes a given RH , causing vapour exchange between the soil and solution until equilibrium, hence controlling the total suction in the soil. The equilibrium RH of some typical aqueous solutions can be found in Young (1967). Chemical compounds with different concentrations or various saturated salt solutions can be used as the aqueous solution. However, saturated salt solutions are advantageous because they can release or absorb more water without affecting the induced RH considerably. Besides using an aqueous solution to control RH , another method, such as mixing vapour-saturated gas with dry gas via a feedback system, can also be used in geotechnical testing. VET can apply or control much higher suctions, usually larger than 10 MPa and up to 1000 MPa.

2.1.4 Mechanical effects of suction in unsaturated soils

For an idealised unsaturated soil, the soil water comprises bulk water and meniscus water (**Figure 2.4**). The bulk water surrounds the particles or aggregates within interconnected pores without pore air. With the presence of air, meniscus water is created by the interaction between the air-water interface on the soil particle. Changes in pore water pressure within the bulk water affect both shear and normal forces at the particle contacts. On the other hand, pore water pressure in meniscus water affects only normal forces between soil particles (Wheeler and Karube 1996; Wheeler et al. 2003; Zhou et al. 2015a).

For completely saturated soil undergoing desaturation, an increase in suction will result in bulk water removal and replacement with air. With further removal of bulk water as suction increases, the amount of meniscus water increases in the soil matrix at the particle contacts. Moreover, the radius of the air-water interface of meniscus water reduces with an increase in suction and produces a larger normal inter-particle contact or capillary force (Fisher 1926; Lourenço et al. 2012) to stabilize the unsaturated soil. Thus, preventing slippage at particle contacts, with the capability to increase the shear resistance of the unsaturated soil. According to this phenomenon, suction influences the mechanical behaviour of unsaturated soil in two different mechanisms: firstly, by modifying the average skeleton force at particle contacts and secondly, by providing additional bonding forces (stabilisation effect) at particle contacts by meniscus water (Gallipoli et al. 2003; Wheeler and Karube 1996).

2.2 Stiffness characteristics of soils under working conditions

2.2.1 Small-strain shear modulus of saturated and unsaturated soils

Figure 1.1 shows representative shear modulus degradation with strain for soils in many geotechnical infrastructures. Moreover, the figure shows that the strain levels experienced by geotechnical engineering structures such as retaining walls, foundations, tunnels, and pavements under working conditions are within the small strain range (0.001–0.1%). The very-small-strain shear modulus (G_0) and the strain-dependent modulus degradation curve are fundamental properties used in predicting and analysing ground movements in geotechnical infrastructures subject to static and dynamic loadings.

The G_0 of soil is commonly measured by way of laboratory and field methods. Laboratory methods which G_0 can be assessed include bender element testing, resonant column testing, and advanced triaxial testing with local strain measurements.

The bender element testing technique is a commonly used method to determine G_0 in the laboratory. Bender element is a two-layer piezoelectric transducer which consists of two piezoceramic plates bonded together with conductive surfaces between them and on the outsides (**Figure 2.5 (a)**). It has an electro-mechanical transducer that deforms mechanically when an electrical voltage is applied, and it is able to produce an electrical output when subjected to mechanical deformation (Lee and Santamarina 2005). The wiring configuration (series or parallel) of a pair of bender elements and the direction of polarisation (same or opposite) determines its use as a transmitter or receiver of shear waves (**Figure 2.5 (b) and (c)**) and compressive waves (**Figure 2.5 (d) and (e)**) (Ingale et al. 2017).

If a pair of bender elements are inserted into opposite ends of a soil specimen where one is a shear wave transmitter and the other, a receiver. The knowledge of the travel distance and time can be used to estimate the shear wave velocity, hence the shear modulus using the following equation:

$$G_{0(ij)} = \rho V_{s(ij)}^2 = \rho(L_t / t)^2 \quad (2.2)$$

where $G_{0(ij)}$ is the very-small strain shear modulus, $V_{s(ij)}$ is the shear wave velocity, the travel length, L_t , and time, t .

Because of their simplicity and convenience, bender elements have been installed in various geotechnical laboratory apparatuses such as triaxial apparatus (Schultheiss 1981; Viggiani and Atkinson 1995), oedometer (Fam and Santamarina 1995; Zeng and Ni 1998) and resonant column apparatus (Fam et al. 2002; Yang and Gu 2013). More details about the configuration of bender elements in soil testing can be found in (Clayton 2011; Ingale et al. 2017; Lee and Santamarina 2005; Leong et al. 2009; Ng and Yung 2008b). Moreover, bender elements can also be positioned and orientated to generate horizontally propagated shear waves with horizontal and vertical polarisations, in addition, to vertically propagated shear waves with the horizontal polarisation of a single soil specimen (Figure 2.6). This allows for assessing the stiffness anisotropy of soils (Callisto and Rampello 2002; Lings et al. 2000b; Ng and Yung 2008b; Pennington et al. 1997).

Another major instrument capable of investigating the small strain behaviour of soils is the resonant column apparatus. This apparatus has been successfully used in soil dynamics to investigate the shear modulus (G) and damping ratio (D) of soils and weak rocks at very small strain levels and estimate the strain-dependent behaviour. The working principle is based on the torsional excitation of a cylindrical soil specimen to its fundamental mode of vibration and the measurement of the resonant frequency (f_r) and the peak amplitude of vibration once the fundamental mode of vibration of the soil column is achieved (ASTM 2007). The peak amplitude, which occurs at low levels of damping at the resonant frequency, is recorded. Given the mass polar moment of the drive head and top platen, the specimen mass and its dimensions, and assuming linear elasticity, the shear modulus of the soil is calculated (Clayton 2011).

Other researchers have used local strain measurement devices, such as linear variable differential transformers (LVDTs) (Clayton and Heymann 2001; Cuccovillo and Coop 1997; Jardine et al. 1984) or Hall effect sensors (Clayton and Khatrush 1986; Muñoz-Castelblanco et al. 2012; Ng and Zhou 2014; Sivakumar et al. 2013), which also allows for estimation of small strains. These are typically mounted on the mid-third of the specimen height. The use of these electronic sensors and computer-based data acquisition has allowed near-continuous records of displacement to be made, which is particularly important in the early stages of triaxial small-strain stiffness determination of saturated and unsaturated soils.

The investigation of the shear modulus of saturated soils has shown that the most significant factors that affect the small strain shear modulus include plasticity index, void ratio, confining stress, stress history and the recent stress state (Atkinson 2000; Clayton 2011;

Vucetic and Dobry 1991). With respect to unsaturated soils, early studies involved the soil specimen being prepared at different water content or degree of saturation. For example, Wu et al. (1984) through resonant column tests, found that soil has higher G_0 when it is in an unsaturated condition. Additionally, a change in G_0 was found to be more significant in soil with smaller particle sizes. The effects of unsaturated conditions on G_0 of coarse-grained soil became more pronounced with a decrease in void ratio and an increase in confining pressure (Qian et al. 1993; Sawangsurriya et al. 2008). In the studies by Wu et al. (1984) and Qian et al. (1993) there was increasing-decreasing trend in shear modulus with the degree of saturation, which can be related to the effects of soil structure.

Later on, matric suction was regarded as a stress state variable for unsaturated soils and used to describe the potential energy of soil-water interaction from capillary forces between soil particles and pore water and surface adsorptive forces. Subsequently, the effects of matric suction on G_0 were regarded.

Sawangsurriya et al. (2008) investigated a relationship between G_0 , soil suction, moisture content and compaction energy of compacted lean clay, silt and clayey sand at an as-compacted state. Bender elements and filter paper technique were employed for shear wave velocity and soil suction measurement, respectively. G_0 of the compacted soils depends primarily on matric suction and to a lesser degree of moulding water content and dry unit weight. Mancuso et al. (2002) investigated the G_0 behaviour of an unsaturated compacted silty sand. Compacted specimens at optimum and wet of optimum states were tested to analyse the effects of suction and fabric on soil behaviour. G_0 was measured after isotropic compression at constant suction. Greater values of G_0 were observed at high mean net stress as well as when suction increased. Vassallo et al. (2007) extended the work to G_0 of compacted clayey silt and included the effects of stress and suction history on G_0 . The applied stress paths are more complicated in which hydro-mechanical loading and unloading were involved. A large and growing body of literature has also reported that the G_0 of unsaturated soils increases significantly with an increase in suction in subgrade soils (Sawangsurriya et al. 2009b), completely decomposed tuff (CDT) (Ng and Yung 2008b) and compacted silty sand (Hoyos et al. 2015). The experimental results of Mancuso et al. (2002) are shown in **Figure 2.7**.

The influence of hydraulic hysteresis was shown by Ng et al. (2009). At a given suction, G_0 is consistently larger along the wetting path than along the drying path as shown in **Figure**

2.8. In most cases, the drying or wetting tests were conducted on the densely compacted specimen. Thus, drying induced contraction, whereas wetting led to slight swelling.

Biglari et al. (2012) found that G_0 of loosely compacted soil remained unchanged during wetting, owing to competing effects of hardening due to wetting-induced contraction and softening due to suction reduction. These studies were only focused on compacted soils and only G_0 is reported, the small-strain shear stiffness (G_{sec}) of unsaturated soil is overlooked.

Xu (2011) studied the strain-dependent shear modulus of an unsaturated compacted silt in an axis translation suction-control triaxial compression test. The suctions controlled in the study were 1, 150 and 300 kPa. As shown in **Figure 2.9**, the shear modulus is consistently larger at a higher suction. Similar studies on other soils for suction effects on the shear modulus degradation curve have been reported in the literature as well, but limited to a low suction range (Ng et al. 2016).

Ng et al. (2017b) observed steeper degradation curves towards lower plasticity index design curves at high suction (40 MPa) in an unsaturated fine-grained soil specimen (see **Figure 2.10**). The authors attributed it to suction-induced large silt–clay aggregations. This finding corroborates the findings of Vucetic and Dobry (1991), whose results show that the elastic threshold shear strains of clays are larger than sands. This implies that a steeper normalised degradation curve may be expected in deformable soils when the microstructural evolves from a fine-grained to a coarse-grained structure due to desiccation.

2.2.2 Effects of soil microstructure on small strain shear behaviour

Microstructural observations of soil particles and aggregations provide evidence used for interpreting the soil behaviour under various hydro-mechanical stress state conditions (Romero and Simms 2008). Compacted clayey soils form an aggregated fabric when compacted at the dry side or the optimum moisture content (Toll 2000) and are usually characterized by a dual pore size distribution (Li and Zhang 2009). The presence of aggregated fabric would influence the hydro-mechanical response of compacted soils.

To analyse the effects of fabric on the G_0 of unsaturated compacted soils, Mancuso et al. (2002) studied the evolution of G_0 of optimum and wet of optimum compacted silty sand specimens using a suction-controlled resonant column. Their results showed that the optimum compacted specimens had higher initial shear stiffness. Moreover, G_0 of the specimen with a higher compaction water content was less sensitive to suction. The results were mainly

attributed to the moulding water content and interpreted as the wet compaction inducing a weaker fabric than optimum compaction. Since the fabric is the arrangement of particles and voids, and if soils are brought to the same state through saturation, how then do we describe a fabric as weaker?

It was shown by [Heitor et al. \(2013\)](#) that apart from the moulding water content, the applied compacted energy governs the structure and matric suction of compacted soils. The study by [Heitor et al. \(2013\)](#) showed that an increase in energy corresponds to an increase in G_0 . However, and by the structure of the soil on the wet-side of the compaction plane, G_0 remains almost constant or decreases with the compaction energy. X-ray computed tomography (CT) scans were employed to observe structural changes of selected specimens upon compaction. Examining the aggregation changes associated with the increase in compaction energy, under constant water content ($w = 12.5\%$), are likely the reasons for the decrease in G_0 .

[Mendoza and Colmenares \(2006\)](#) observed that clay specimens prepared at a higher compaction water content exhibited higher initial Young's modulus (E_0), at suctions ranging from 100 kPa to 30 MPa. On the other hand, [Heitor et al. \(2015\)](#) reported that compaction water content has negligible effects on the shear wave velocity of sand during drying. However, during wetting, the specimen compacted at 2% dry of optimum exhibited slightly higher shear wave velocity than that compacted at 2% wet of optimum. It should be noted that these previous studies mainly focused on the effects of compaction water content on a single direction of G_0 with strains below 0.001%.

[Ng et al. \(2017b\)](#) studied the dynamic properties of loess at different initial states resulting from different specimen preparation techniques (i.e., reconstituted, recompacted, and intact) and their evolutions due to suction-induced desiccation. At the initial states, the specimen preparation technique has a negligible effect on the normalized modulus (G/G_0) while the influence becomes significant at a high suction of 40 MPa (see [Figure 2.10](#)). This is attributed to the microstructural evolution of specimens with different initial states that were subjected to suction-induced desiccation. Additionally, the elastic shear strain threshold decreases (i.e. reduction of elastic range) while shear modulus increases as suction reaches 40 MPa.

Most studies, over many decades, related to the small strain shear behaviour of soils have been focused on sedimentary soils or soils that are not formed from the laterization process (i.e., natural formation of iron nodules or cemented aggregates). However, residual soils with

cementing agents (sesquioxides) in the soil structure have shown differing soil behaviour and have been attributed to their very different structures (Macari and Hoyos 2003).

Pineda et al. (2014) investigated the effect of fabric and weathering intensity on the dynamic properties of undisturbed saturated residual and saprolitic soils via resonant column testing. The soil fabric studies were also performed based on SEM, MIP tests, and pore size distributions. It was concluded that the residual soil had greater initial shear stiffness than saprolitic soil. The residual soil had greater stiffness due to the presence of sesquioxides acting as cementing agents. In other words, there is likely expected a difference in the behaviour of chemically weathered soils compared to sedimentary soils.

2.2.3 Anisotropy of soil behaviour

Anisotropy often occurs in soils either inherently from the depositional process, specimen preparation or induced through stress or strain (Jovičić and Coop 1998). This results in anisotropic mechanical properties such as anisotropic small-strain stiffness. The small strain stiffness is highly related to the working performance of many geotechnical structures. Stiffness anisotropy has been reported in several natural soil deposits (Yimsiri and Soga 2011a) as well as compacted soils (Hasan 2016; Hasan and Wheeler 2014).

To determine the stiffness anisotropy of soils in the laboratory, several researchers measured the shear waves along different directions using bender elements (Callisto and Rampello 2002; Lings et al. 2000b; Ng and Yung 2008b; Pennington et al. 1997). Considering different positions and orientations, bender elements are used to generate horizontally propagated shear waves with horizontal and vertical polarisations and vertically propagated shear waves with the horizontal polarisation of a single soil specimen (Figure 2.6). Frequently, in the preparation of soil in the laboratory, 1-D compaction has often been used in the soil specimen preparation (Jotisankasa et al. 2009; Sun et al. 2015). This 1-D compaction process leads to anisotropic soil behaviour as reported by several authors (Cui and Delage 1996; Hasan and Wheeler 2014). Modelling and understanding of anisotropy are relevant to make reasonable predictions of ground movements by geotechnical construction in such soils (Schädlich and Schweiger 2013; Wongsaroj et al. 2007).

The stiffness anisotropy has been reported for several natural soil deposits for which most of them are clay soil deposits (Gasparre et al. 2007a; Gasparre et al. 2007b; Lings et al. 2000b; Yimsiri and Soga 2011b) and for reconstituted clays (Jovičić and Coop 1998) and on compacted soils (Hasan 2016; Hasan and Wheeler 2014; Kaewsong 2017).

However, anisotropic stiffness on compacted lateritic soils is rarely reported in the literature. Moreover, the anisotropic small-strain stiffness of compacted soils is potentially influenced by the compaction condition.

2.2.4 Cyclic shear behaviour of saturated and unsaturated soils

Subgrade soils undergo cyclic; loading and unloading from traffic, wetting and drying, heating and cooling, and coupled effects of suction and temperature. To prevent fatigue cracking in the flexible pavements – resilient modulus (M_R) and axial accumulated plastic strain, are the design parameters to be considered (Han and Vanapalli 2016; Ng et al. 2013). From a typical stress-strain of subgrade soil (Figure 2.11) (O'reilly and Brown 1992) resilient modulus is defined as the ratio of cyclic deviator stress (σ_d) to resilient strain (ϵ_r), from cyclic loading and unloading triaxial tests. The performance of the pavement depends on the integrity of the pavement layers. Accumulated deformation of subgrade soils under cyclic traffic loads plays a very important role in the performance of a pavement structure. To better design pavement structures, there is the need to estimate the resilient modulus of the subgrade soils subject to cyclic loading and unloading from the traffic loads, and also effects from environmental factors.

Lekarp et al. (2000) summarized the factors affecting the resilient modulus, which include stress level, stress history, soil density, grain size distribution (fines content and type of clay mineral), loading frequency and the number of load cycles and moisture content. Mechanistic-Empirical Pavement Design Guide (MEPDG) proposed a general empirical model to predict the variation of the resilient modulus with respect to the moisture content changes for both fine- and coarse-grained soils. This model did not consider the variable effects of environmental factors, and traffic loading. Other researchers have come up with various empirical models to predict the resilient modulus of subgrade soils, incorporating the effect of suction (Bilodeau and Doré 2012; Caicedo et al. 2009). However, most of these models also fail to consider the coupled effects of suction and principal stress rotation. McCartney and Khosravi (2013) stated that up to a depth of 2m in a pavement layer, the suction changes within a range from 0 to 1000 kPa. Soil suction in subgrade materials can be over 9 MPa, especially in prolonged dry conditions, which may be detrimental to the structure of the pavement (Puppala et al. 2011).

An advanced elastoplastic theory should be developed to interpret the cyclic behaviour of soils at various suctions from low to very high suction values. Additionally, a new elastoplastic model should be developed to model the effects of principal stress rotation on soil behaviour.

The consideration of principal stress rotation may be important in some cases such as pavement analysis because the rotation of principal stress takes place under cyclic traffic loads (Brown 1996). Blackmore et al. (2020) investigated the cyclic behaviour of a compacted clayey sand in triaxial and hollow cylinder apparatus. Specifically, they studied the influence of the degree of saturation on the resilient modulus in both triaxial and hollow cylinder apparatus. Their results show that the M_R increased significantly as the degree of saturation reduces. Similar trends were observed regardless of whether principal stress rotation was applied, when the samples were tested using the hollow cylinder apparatus.

The effects of suction on M_R of various subgrade materials have been reported by several researchers. While others measured the suction of the soil sample before and/or after testing (Blackmore et al. 2020; Khoury et al. 2011; Sawangsuriya et al. 2009a; Sivakumar et al. 2013; Zhang et al. 2019), others performed suction-controlled cyclic loading test (Ng et al. 2013; Yang et al. 2008a). Most of the aforementioned studies involving suction effects on cyclic behaviour were limited to a maximum suction close to 450 kPa.

Sivakumar et al. (2013) studied the influence of confining stress as well as water content on an unsaturated compacted clay. Repeated loading was performed on the compacted soil under constant mass conditions, whereas suction was measured using a psychrometer. From their results, an increase in resilient modulus was observed with an increasing water content up to nearly optimum water content, after which a considerable decrease of resilient modulus with increasing water content was observed.

Figure 2.12 shows an example of suction effects on M_R as reported by Sivakumar et al. (2013) at low suction, whereas Figure 2.13 shows the suction influence of M_R at a relatively high suction state (Banerjee et al. 2020). A continuous decrease in M_R with increasing deviator stress for the suction range considered has been reported (Banerjee et al. 2020; Ng et al. 2013; Sivakumar et al. 2013). Others reported a decrease in M_R with increasing deviator stress for the relatively lower suction and an increase in M_R with increasing deviator stress for the high suction (Kung et al. 2006; Yang et al. 2008a). Whether this may be related to the soil type or soil structure and suction effects is not fully understood.

Although, it is usually preferred that subgrade materials are compacted at optimum moisture conditions and usually 95% of their maximum dry density the exact achievement of the specific moisture content is challenging due to changes in water content during the construction and service period that practically unavoidable (Blackmore et al. 2020).

Moreover, high-suction states can alter the pore size distribution of soil (Cai et al. 2020), which may affect the M_R and the accumulation of plastic strain when a soil is subjected to cyclic loading. Therefore, there is a need to investigate the evolution of variable pore size distribution or soil structure or fabric and the influence of high suction on the resilient modulus and accumulation of plastic strain.

2.3 Thermal effects on soil behaviour

2.3.1 Volume change response under thermal loading

Figure 2.14 shows that the volumetric strain of soils subjected to thermal loading is dependent on the over-consolidation ratio (Abuel-Naga et al. 2007). With respect to volume change under drained conditions, normally consolidated soil would directly contract, slightly overconsolidated soil would first dilate and then contract, while only expansion is observed for highly overconsolidated soil during heating for saturated soils. On the other hand, there is almost linear elastic contraction during cooling. This is usually attributed to the thermal contraction of soil particles. In terms of cyclic heating and cooling, it was shown that with an increasing number of thermal cycles, there is an accumulation of plastic deformation at a decreasing rate or irreversible volume changes as shown in Figure 2.15 (Burghignoli et al. 1992; Campanella and Mitchell 1968; Di Donna and Laloui 2015; Vega and McCartney 2015). Despite that, remoulded clay expanded, whereas intact silt contracted under the cooling stage.

2.3.2 Thermal-induced pore water pressure

Several studies have revealed that under undrained conditions, the pore water pressure increased with an increasing temperature and reduced when the temperature decreased (Abuel-Naga et al. 2009a; Campanella and Mitchell 1968; Graham et al. 2001; Hueckel and Baldi 1990). Furthermore, there is a hysteresis response of pore water pressure during cyclic temperature changes as reported by Campanella and Mitchell (1968); (Mitchell et al. 1965). The pore water pressure during cooling was lower than during heating.

2.3.3 Thermal effects on yield stress

A considerable amount of literature has been published on the thermomechanical behaviour of loading under a constant temperature. Figure 2.16 shows that there is a decrease in yield stress with an increase in temperature, which is commonly referred to as “thermal softening of yield stress” (Cekerevac and Laloui 2004; Eriksson 1989; Tang and Cui 2005; Tidfors and Sällfors 1989). In the p-T plane, the yield stress forms a yield locus with

temperature (Eriksson 1989). This yield locus has been adopted in the development of thermomechanical constitutive models.

2.3.4 Thermal effects on normally consolidated line (NCL) and critical state line (CSL)

It has conclusively been shown that the NCL shifts downwards with an increasing temperature, in the $v - \ln p$ plane. Furthermore, NCLs at two different temperatures are almost parallel, which suggests that the plastic compressibility index λ is almost independent of temperature (Abuel-Naga et al. 2007; Cekerevac and Laloui 2004; Romero et al. 2003; Uchaipichat and Khalili 2009b). The CSL, in the $p - q$ plane, is also independent of temperature and the slope $M (= q_f / p_f)$ is a constant (Abuel-Naga et al. 2007; Cekerevac and Laloui 2004; Graham et al. 2001; Hueckel and Baldi 1990; Romero et al. 2003; Uchaipichat and Khalili 2009b) Results by (Uchaipichat and Khalili 2009b) from suction- and temperature-controlled conventional compression shear tests revealed the critical state line in the deviatoric stress versus mean stress plane is independent of temperature.

In the $v - \ln p$ plane, the CSL is a function of the temperature. Although, the slope $\lambda (= dv / d(\ln p))$ is a constant., the CSL shifts with temperature changes. At a given specific volume, the mean stress at the critical state decreases with increasing temperature (Lingnau et al. 1995; Uchaipichat and Khalili 2009b).

2.3.5 Thermal effects on small strain behaviour

Previous studies on the thermo-mechanical behaviour of soils investigated thermal effects on the volume change responses, yielding and shear strength. Little is known about thermal effects on soil behaviour at very small and small strains, at which stress paths may be within the yield surface. Cekerevac and Laloui (2004) determined the secant Young's modulus of a saturated Kaolin clay from the results of triaxial tests at an axial strain of 0.5%. They found that the secant Young's modulus increased with increasing temperature (Figure 2.17). Ghahremannejad (2003a) investigated the thermal effects on small strain behaviour on a saturated clay in a temperature-controlled triaxial apparatus, in which local strain measurement was used to measure small strains of soil specimens. It was found that the measured shear modulus degradation curve is strongly influenced by temperature. The measured secant shear modulus at a given strain is consistently smaller at a higher temperature (Figure 2.18). Although the experimental data is useful for developing and verifying small strain models, only saturated soil was tested without measuring of the maximum shear modulus, G_0 . Using a temperature and suction-controlled triaxial apparatus with small strain measurements. Zhou et

al. (2015a) investigated the effects of suction and temperature on the shear modulus (G_{sec}) of a compacted silty soil. From their experimental results (Figure 2.19), the shear modulus was lower at a higher temperature of 60°C than that at 20°C for the same suction. This was attributed to the decrease in surface tension when temperature increases. Therefore, causing weaker average skeleton stress and lower stabilisation effects on the soil. However, this study also did not involve the measurement of the maximum shear modulus, G_0 . Recently, Vahedifard et al. (2020) presented a model incorporating the thermal effects on small strain shear modulus of unsaturated soils, particularly those of unsaturated silty soils. The experiment on thermal effects on the small strain shear modulus of an unsaturated silty soil was carried out using a modified suction and temperature-controlled triaxial equipment with bender elements. It can be seen from Figure 2.20 that, the shear modulus decreased with an increase in temperature, for the same suction. Thermal effects on shear modulus were found to be more significant at higher suctions. Vahedifard et al. (2020) acknowledges that to validate their proposed model for temperature-dependent shear modulus more experimental tests for different soil types and wider ranges of suction and temperature are necessary.

Although the thermal effects on small-strain shear modulus are reported in the literature, it is very limited. For saturated soils, less is known about the factors that control the temperature effects on small-strain shear modulus. Because several parameters affect the shear modulus of various soils at different magnitudes, it is necessary to consider more experimental studies for shear moduli that incorporates a combination of some parameters such as structure, suction states, and temperature.

2.4 Modelling stiffness of saturated and unsaturated soils

As discussed above, several studies have shown and suggested that soils' small strain shear behaviour depends on soil mineralogy, structure, particle characteristics, void ratio, effective stress, and the degree of saturation (Clayton 2011; Heitor et al. 2013; Pineda et al. 2014). Several semi-empirical relationships have been established to predict the G_0 of soils by considering the stress conditions and saturation state.

The G_0 is related to a power function which is well fitted by a general equation proposed by (Hardin and Richart 1963; Hardin and Black 1966) and is expressed as:

$$G_{0(ij)} = AF(e)(p')^n \quad (2.3)$$

where $F(e)$ is a function of void ratio, p' is the current effective mean stress, A and n are material parameters. This equation can describe the G_0 of dry and fully saturated soils.

Over the past few decades, some semi-empirical equations for G_0 of unsaturated soils consider the effect of particle size, compaction energy, degree of saturation, matric suction, and hysteresis. (Heitor et al. 2013; Khosravi and McCartney 2012; Mancuso et al. 2002; Ng and Yung 2008b). For example, Ng and Yung (2008b) proposed a semi-empirical equation using mean net stress and suction to describe G_0 of unsaturated soils. Ng and Yung (2008b) proposed that G_0 of unsaturated soils can be expressed as a power function of net stress and suction:

$$G_{0(ij)} = C_{ij}^2 F(e) \left[\frac{(p - u_a)}{p_r} \right]^{2n} \left[1 + \frac{(u_a - u_w)}{p_r} \right]^{2b} \quad (2.4)$$

where $G_{0(ij)}$ is the very small strain shear modulus at the shear plane ij ; $C_{(ij)}$ is a function of the soil structure; $F(e)$ is a void ratio function; $(p - u_a)$ is mean net stress; p_r is reference stress; and $u_a - u_w$ is matric suction; n and b are fitting parameters. The effects of the degree of saturation are neglected in their equation.

Other researchers incorporated the effects of the degree of saturation in the estimating and interpreting of the G_0 of unsaturated soil (Khosravi and McCartney 2012; Sawangsurriya et al. 2009b), based on Bishop-type stress. The Bishop χ parameter was replaced by S_r to capture the dependence of G_0 on saturation and matric suction. The Bishop's stress was termed as the average skeleton stress (σ^*) (Wheeler et al. 2003).

$$\sigma^* = \sigma_{ij}^t - u_a + S_r(u_a - u_w) \quad (2.5)$$

Later, Alonso et al. (2010) proposed the use of an effective degree of saturation (S_r^e) based on soil microstructure. The effective degree of saturation is thus a measure of the freely available water filling the macropores in a scale that extends from 0, when all the water is stored in micropores, to 1, when the soil is fully saturated. Thus, G_{\max} of an unsaturated could be estimated from:

$$G_{\max} = A(p + S_r^e s) \quad (2.6)$$

where $S_r^e = (S_r)^a$, P is the mean net stress, S_r is the degree of saturation, s is the soil suction, A and a ($a \geq 1$) are material parameters. Nevertheless, a void ratio function was not explicitly included because all specimens in their study were prepared at the same void ratio, but different suction values (Ng et al. 2017b). It was shown by Ng et al. (2017b) that, the shear modulus of unsaturated soil depends on the inherent microstructure, soil suction, degree of saturation, and void ratio. The equation for determining G_{\max} then took the form:

$$G_{\max} = Af(e)(p + S_r^e s)^n \quad (2.7)$$

However, a major problem with some of the empirical equations mentioned above is that their fitting parameters have no solid physical meaning. Hence, it is not well related to the SWRC and soil properties of the unsaturated soils.

Dong et al. (2016a) proposed a new model for G_0 based on two conceptual mechanisms: material hardening/softening, which is considered using the degree of saturation as a variable, and interparticle contact forces carried by the soil skeleton, which is considered using the effective stress as a variable. The proposed model can be written as follows:

$$G_0 = A_0 \left(\frac{1}{S_e} \right)^\beta \cdot \left(\frac{\sigma}{P_{atm}} + 1 \right)^{\gamma_0} \quad (2.8)$$

where A_0 is an experimental fitting parameter having the same units as the small-strain shear modulus (typically MPa); When soil is saturated, $S_e = 1$ no external-confining stress is applied ($\sigma = 0$), and the suction stress is zero ($\sigma \neq \sigma^s = 0$); A_0 can be defined as the small-strain shear modulus of saturated soil without confinement; β = experimental fitting parameter; P_{atm} is a reference stress. The value of A_0 incorporates the effect of void ratio, particle interlocking, initial conditions, and stress history. The effective stress is assumed to primarily affect the shear modulus of unsaturated soils through the soil skeleton or network of particle contacts. The soil skeleton or network of particles could be attributed to the soil microstructure through the parameter A_0 . Therefore, the proposed unified model correlates well with the properties (e.g., SWRC and particle size) of the soils.

Given that thermal effects have additional effects on soil behaviour, ignoring the thermal effects on stiffness parameters of soil could underestimate soil deformation (non-conservative).

Although, some constitutive models have incorporated thermal effects on soil behaviour. (Abuel-Naga et al. 2009a; Graham et al. 2001; Hamidi et al. 2014; Hueckel and Baldi 1990; Zhou and Ng 2015a). These existing models do not consider thermal effects on the elastic stiffness behaviour due to the lack of experimental data, except the models reported by Graham et al. (2001) and Hamidi et al. (2014). The proposed temperature-dependent model by Graham et al. (2001) can be written as follows:

$$\left(\frac{G_T}{p'_{cons}} \right)_{oc} = \left(\frac{G_T}{p'_{cons}} \right)_{nc} [1 + C \ln(OCR)[1 + D(T - T_0)]] \quad (2.9)$$

where C and D are constants, and OCR is the overconsolidation ratio at the reference temperature T_0 . The subscripts oc and nc in **Equation (2.9)** represent overconsolidated and normally consolidated behaviour, respectively. Even though these two models reported by Graham et al. (2001) and Hamidi et al. (2014) have incorporated thermal effects on G_0 , the relevant formulations were not verified using experimental results.

2.5 The use of unsaturated soil mechanics in pavement engineering

Pavement structures vary greatly based on the type of vehicle to be accommodated, the wheel loads involved, and the volume of loads to be carried during a specific period. The cross-sections of various pavement types are shown in **Figure 2.21**, from the unpaved "gravel" roads to the heavy-duty flexible bituminous or concrete pavements (Brown 1996). Flexible pavement structures are constructed worldwide over a wide range of soil and topography. The foundation of flexible pavements usually involves a compacted granular material overlying compacted subgrade soil (Brown 1996). Lateritic soils have widely been used as subgrade materials for flexible pavements in tropical and sub-tropical areas, including Asia, South America and Africa (Netterberg 2014).

The entire pavement structure is subjected to repeated moving vehicles from pre- and post-construction traffic. Although several failure modes occur during the service life of pavements, in the design of flexible pavements, fatigue cracking and rutting (see **Figure 2.22**) are the common serviceability failure of major concern (Banerjee et al. 2020; Zhou 2014). Fatigue cracking at the bottom of the surface layer (usually made of concrete and asphalt layer). Rutting occurs by the accumulation of plastic strain at the top of the subgrade layer in the wheel path (Brown 1996). The above failure modes may be caused and enhanced by several reasons, such

as increased levels of traffic volume, deterioration of asphalt and concrete, deformation of unbound granular materials and differential settlement of subgrade soils (Brown 1997; Hveem 1955).

It is recommended by the AASHTO Mechanistic-Empirical Pavement Design Guide (MEPDG) (AASHTO 2008) and other researchers (Han and Vanapalli 2016; Ng et al. 2013) to utilise resilient modulus and axial accumulated plastic strain for characterising the subsoils of the flexible pavement structure (Banerjee et al. 2020; Mohammad et al. 1994).

It is well recognized that subgrade soils are often unsaturated and subjected to daily variations of water content and hence pore water pressure (suction) and temperature (Jin et al. 1994; McCartney and Khosravi 2013). Although some recent design guides have considered the effects of soil moisture on soil behaviour using empirical methods, the effects of temperature on subgrade soils are often ignored. Since, most of the current pavement design approaches do not take thermal effects on soil behaviour into account, despite the fact that extensive experimental data has already demonstrated that these effects are remarkable. The response of the soil specimen is generally evaluated at room temperature (AASHTO 2008). When the in-situ temperature is much higher than room temperature, soil deformation caused by traffic loads may be underestimated.

2.5.1 Methods of pavement performance analysis

The typical representation of flexible pavements is as elastic layered systems lying on a uniform semi-infinite halfspace. The contact pressure of the wheel load applied to the pavement surface is typically assumed to be the pressure in the vehicle tire. It is viewed as a uniform load distributed across a circular region. Because the flexible pavement is a multi-layered system the layered elastic theory was first developed by Burmister (1945) for three-layer systems more suitable for modelling pavements.

The pavement analysis has been solved using a number of linear elastic layered computer software over the years. The CHEVRON program the Chevron Research company created was one of the first (Warren and Dieckmann 1963). In order to roughly account for the nonlinear elastic granular base behaviour, Hwang and Witzak (1979) changed the program. They added it to the DAMA pavement design program for use by the Asphalt Institute.

Researchers from Shell created the computer program BISAR to calculate the response of multi-layer structures with linearly elastic material behaviour utilising Burmister's theory (De Jong 1979). When more than one dispersed circular load can be applied to the pavement,

BISAR examines several loading scenarios. Each layer can have a different elastic modulus, Poisson's ratio, and thickness depending on whether the interface exhibits slip or perfect bonding.

At the University of California, Berkeley, a widely known linear elastic layered system program was created (Kopperman et al. 1986). The ELSYM5 program runs on a microcomputer and can evaluate up to 5 layers as elastic systems under various wheel loads. The program superimposes different loads and computes the principal stresses, strains, and displacements at user-specified places, a feature all linear elastic programs share. Due to its ease of use in ordinary flexible pavement design, ELSYM5 has gained much popularity in the US, particularly among state transportation agencies.

Huang (2004) unveiled the computer software KENLAYER for the investigation of layered systems that are elastic and viscoelastic. The program, named after the University of Kentucky, uses flexible pavements as layered systems. Single, dual, dual-tandem, and dual-tridem wheels are all considered for the superposition of multiple wheel loading. Each layer of the system acts differently depending on whether it is linear, nonlinear, or viscoelastic Huang (2004). The damage is also considered in the study by breaking up a year into several periods and assigning each one a unique set of material attributes.

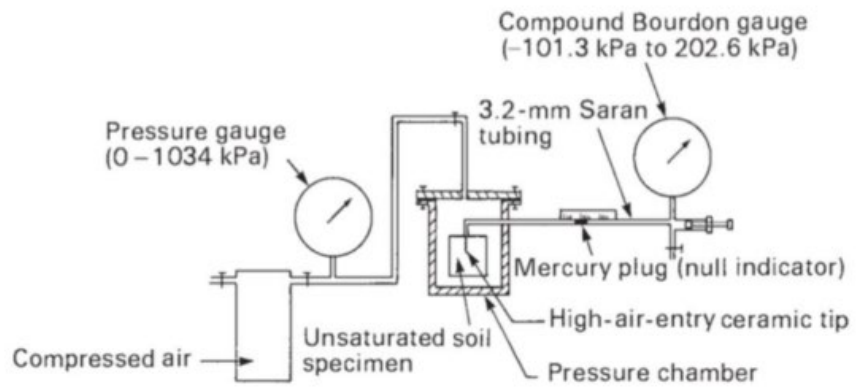
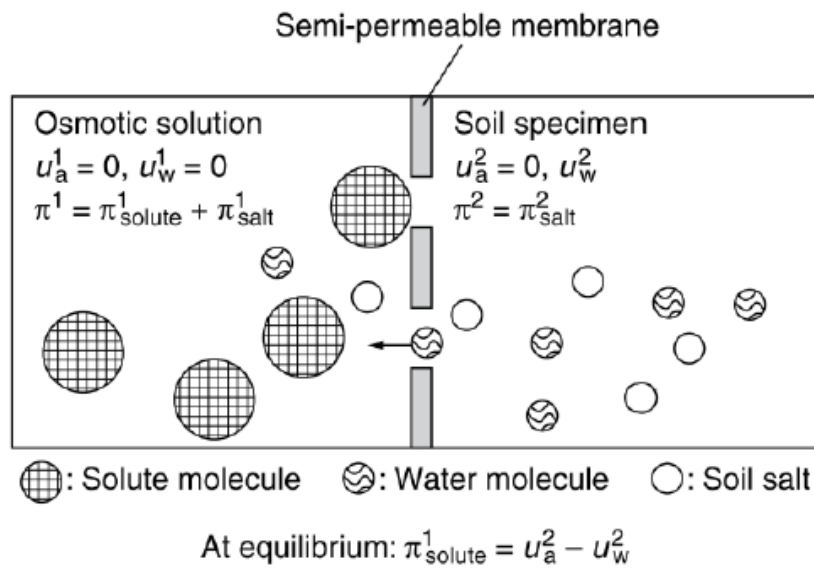
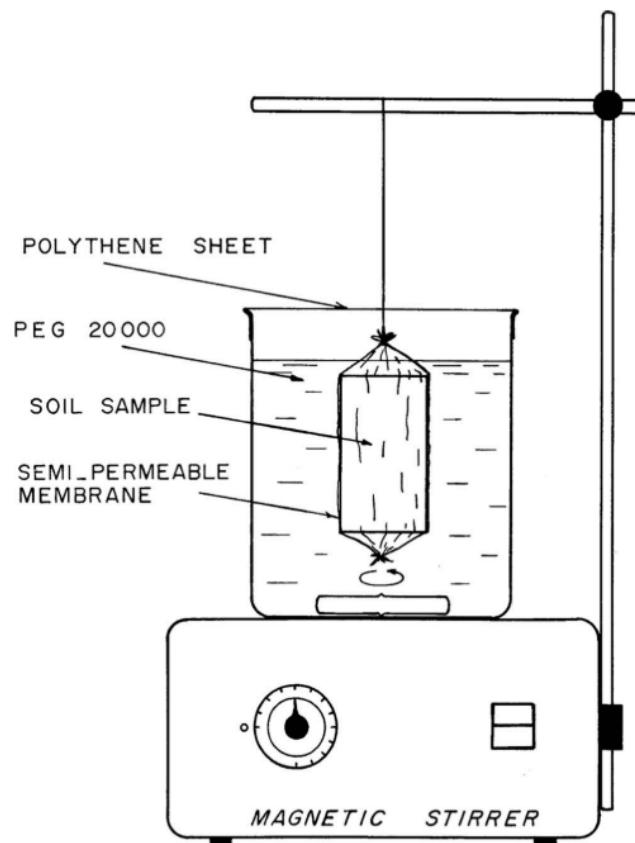


Figure 2.1 Axis-translation device for measuring negative pore-water pressures (Hilf 1956)



(a)



(b)

Figure 2.2 Principle of osmotic technique (Blatz et al. 2008; Ng and Menzies 2007b)

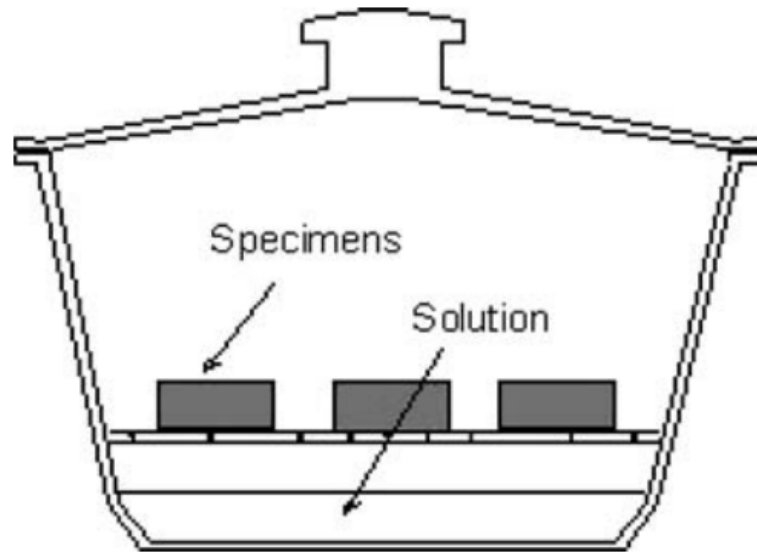


Figure 2.3 Application of vapour equilibrium technique in a desiccator (Tang and Cui 2005, Blatz et al. 2008)

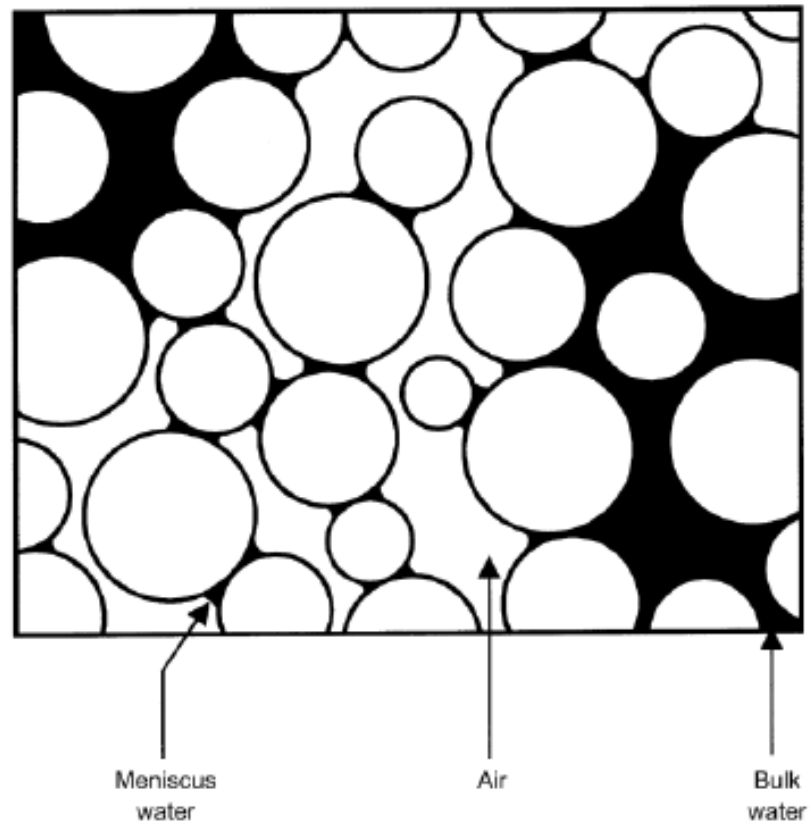


Figure 2.4 Pore water distribution in unsaturated soil lo

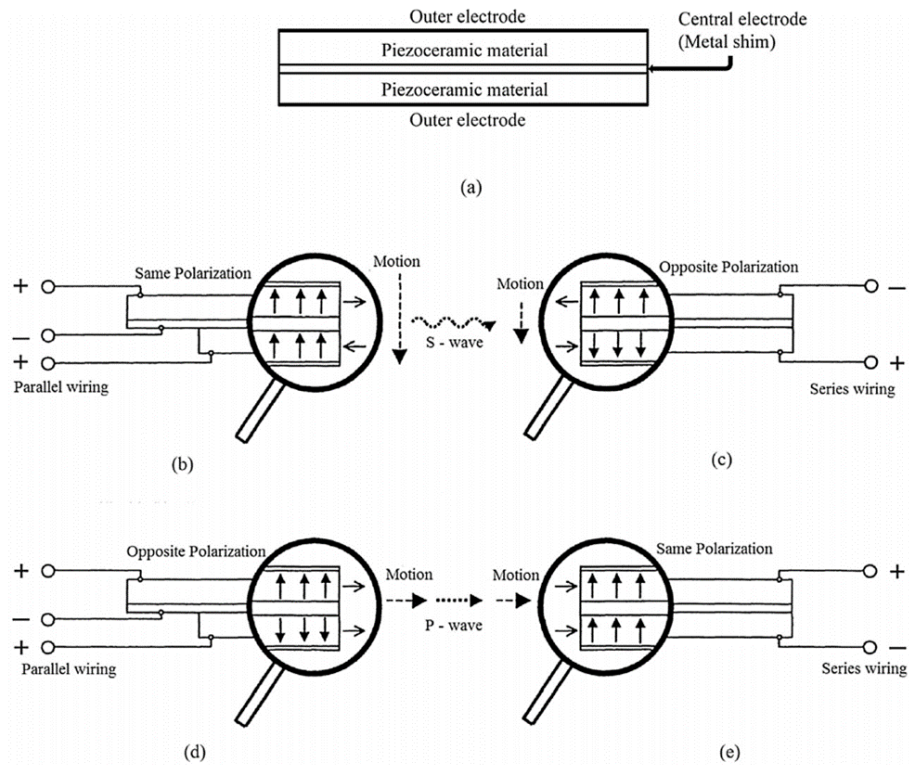


Figure 2.5 Representation of measurement technique of bender element (Ingale et al. 2017)

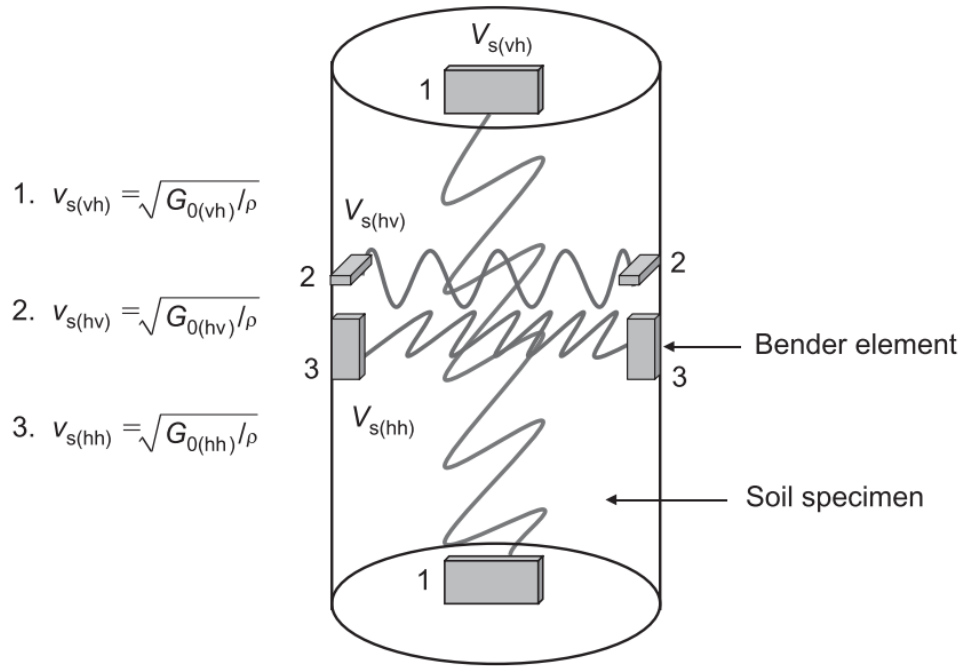


Figure 2.6 Arrangement of bender elements for measuring stiffness anisotropy (Ng and Yung 2008b)

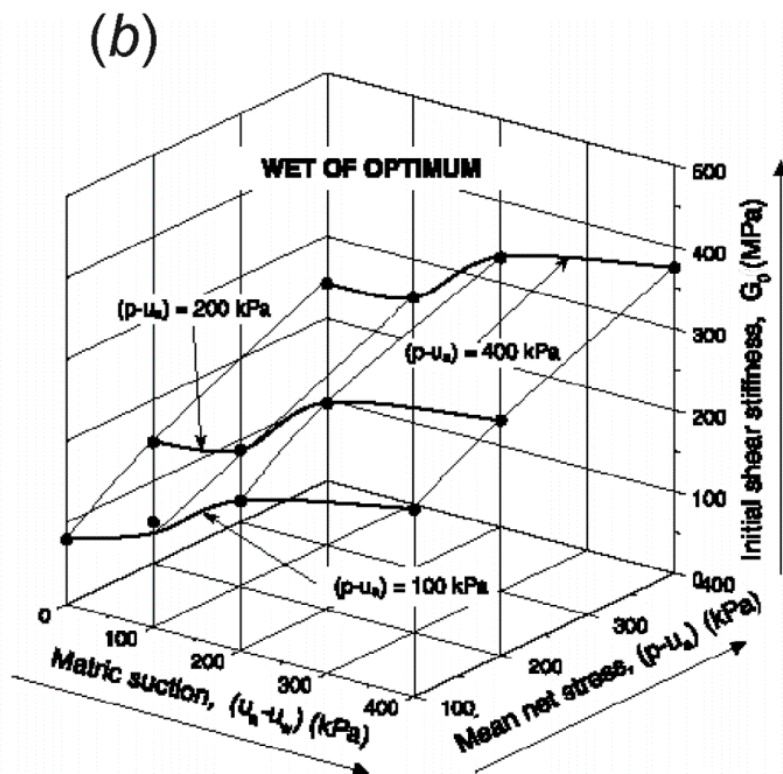
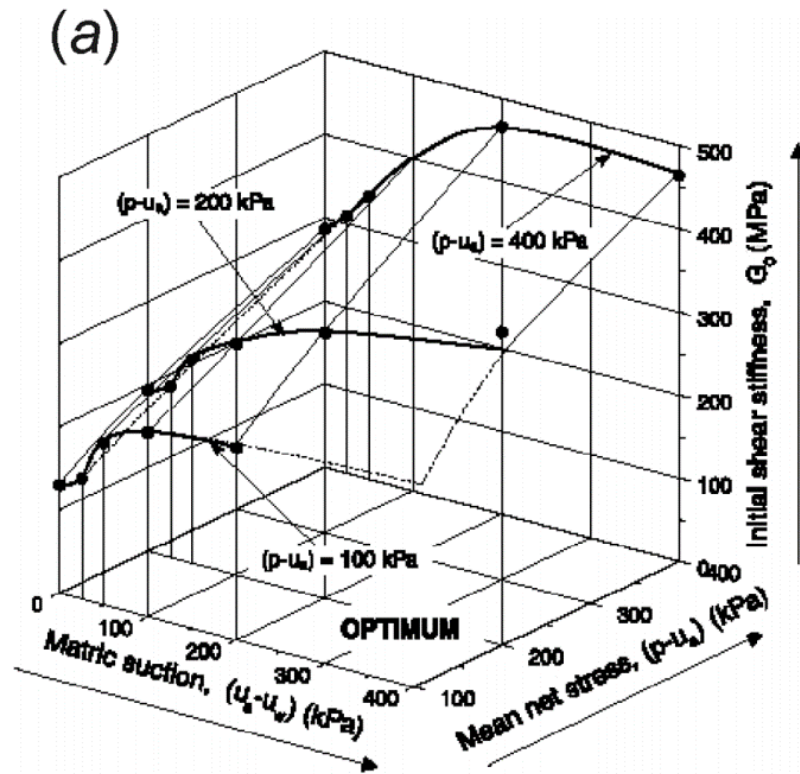


Figure 2.7 Influence of matric suction on initial shear modulus of an unsaturated compacted silty sand (a) at OMC (b) wet side of OMC (Mancuso et al. 2002)

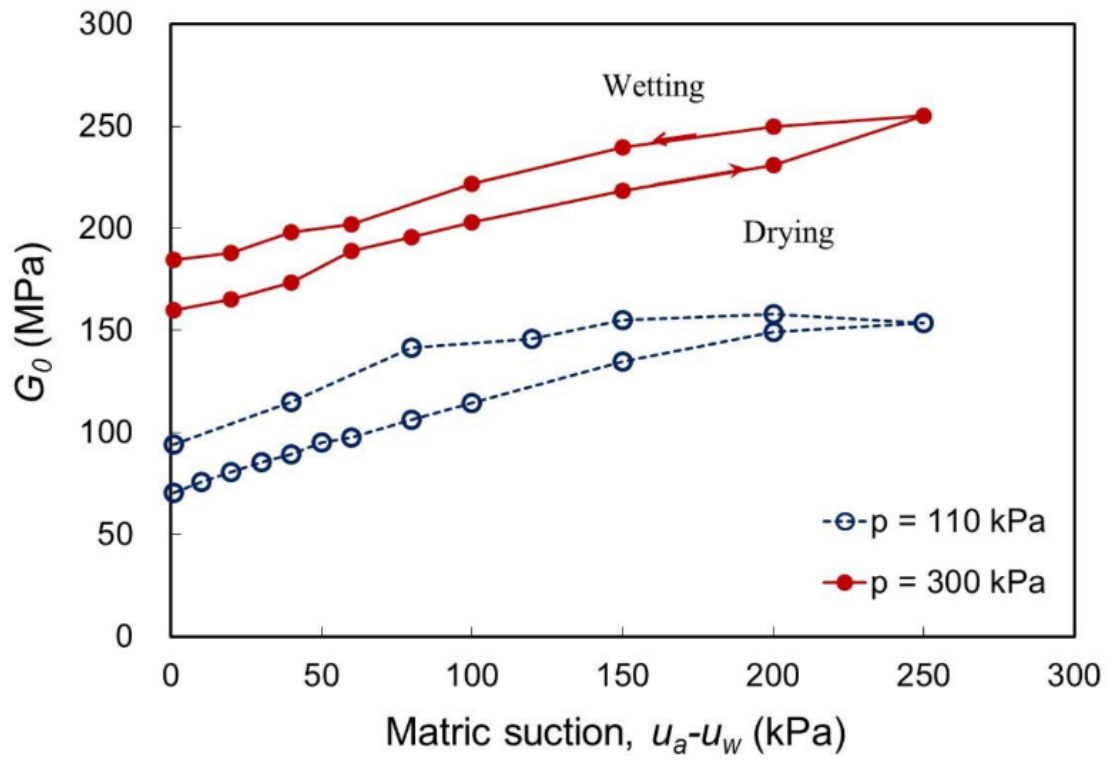


Figure 2.8 Influence of wetting and drying on the initial shear modulus of an unsaturated soil (Ng et al. 2009)

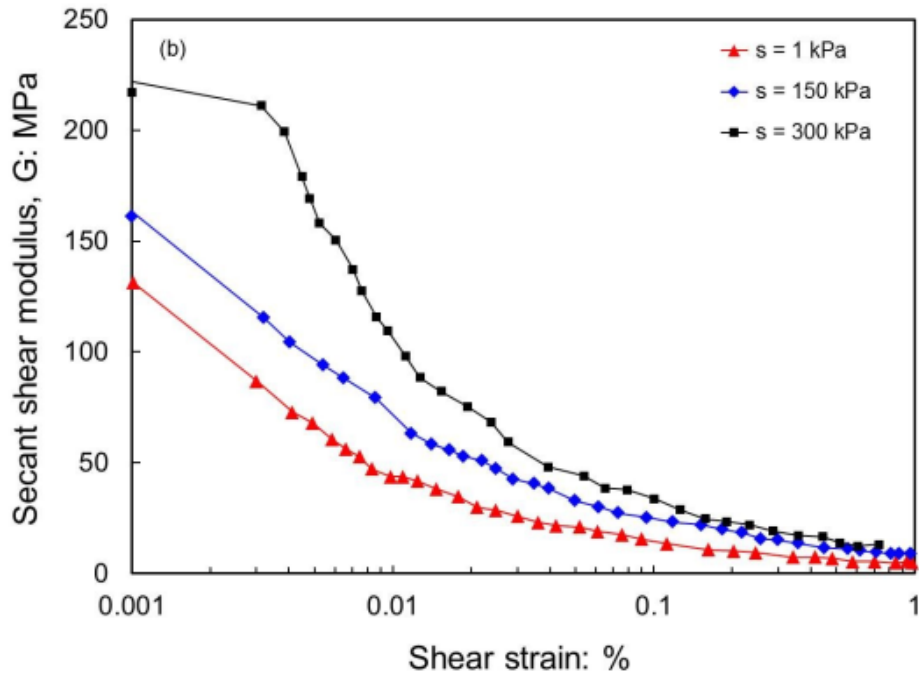


Figure 2.9 Influence of suction on strain-dependent shear modulus (Xu 2011)

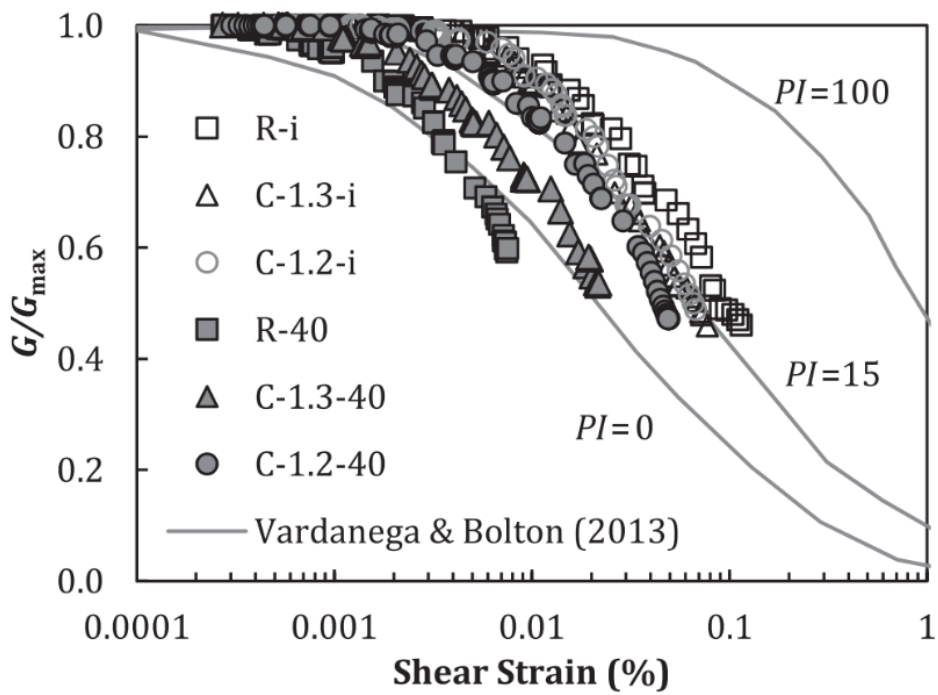


Figure 2.10 Comparison of normalised shear modulus degradation of unsaturated loess with design curves (Ng et al. 2017b)

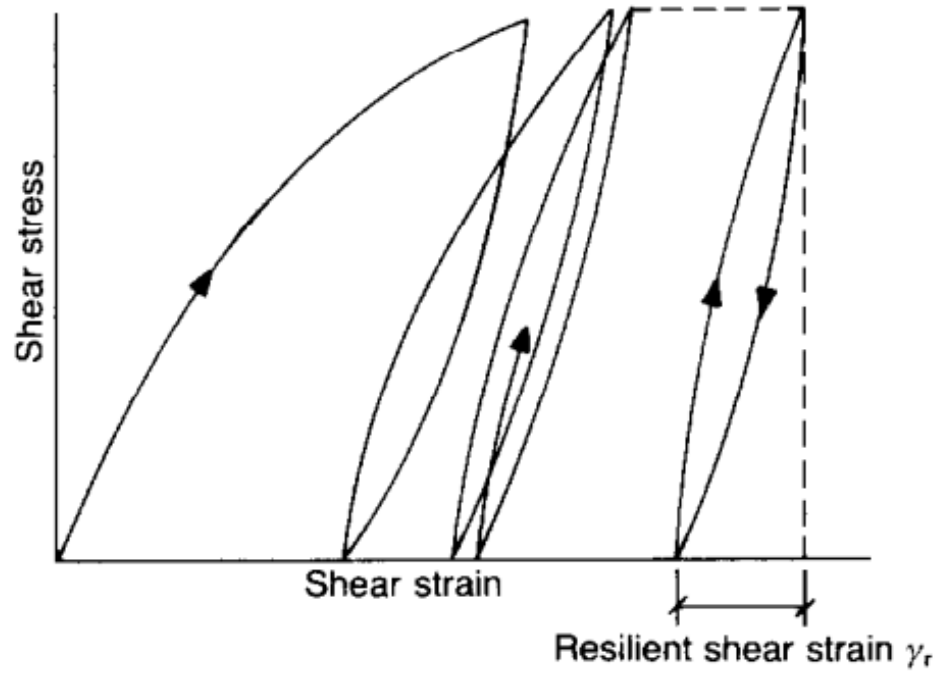


Figure 2.11 Typical stress-strain of subgrade soil under cyclic loading-unloading (O'reilly and Brown 1992)

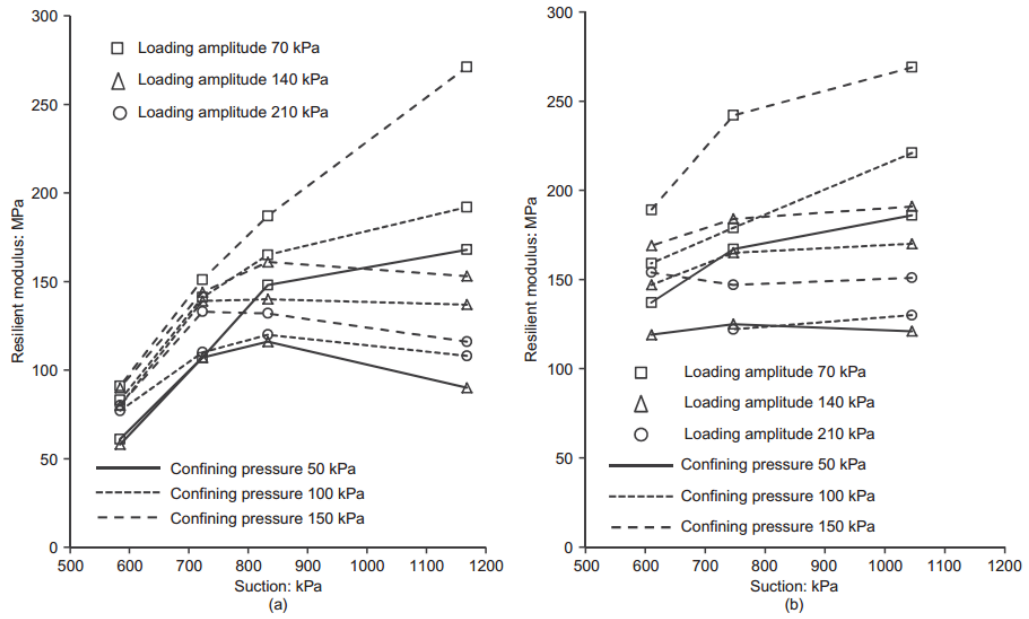


Figure 2.12 Effects of stress and suction on resilient modulus (a) light compaction (b) heavy compaction (Sivakumar et al. 2013)

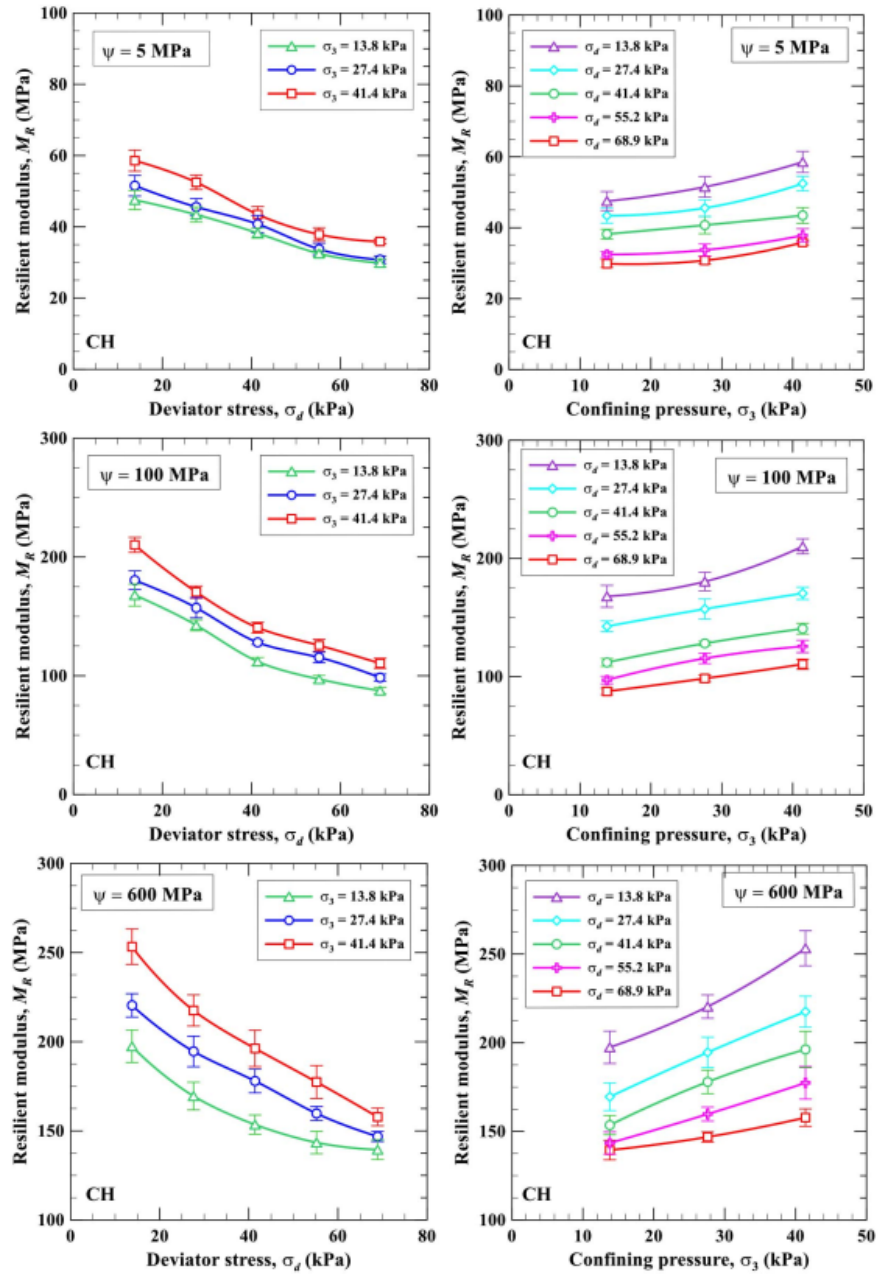


Figure 2.13 Influence of stress and high suction state on resilient modulus (Banerjee et al. 2020)

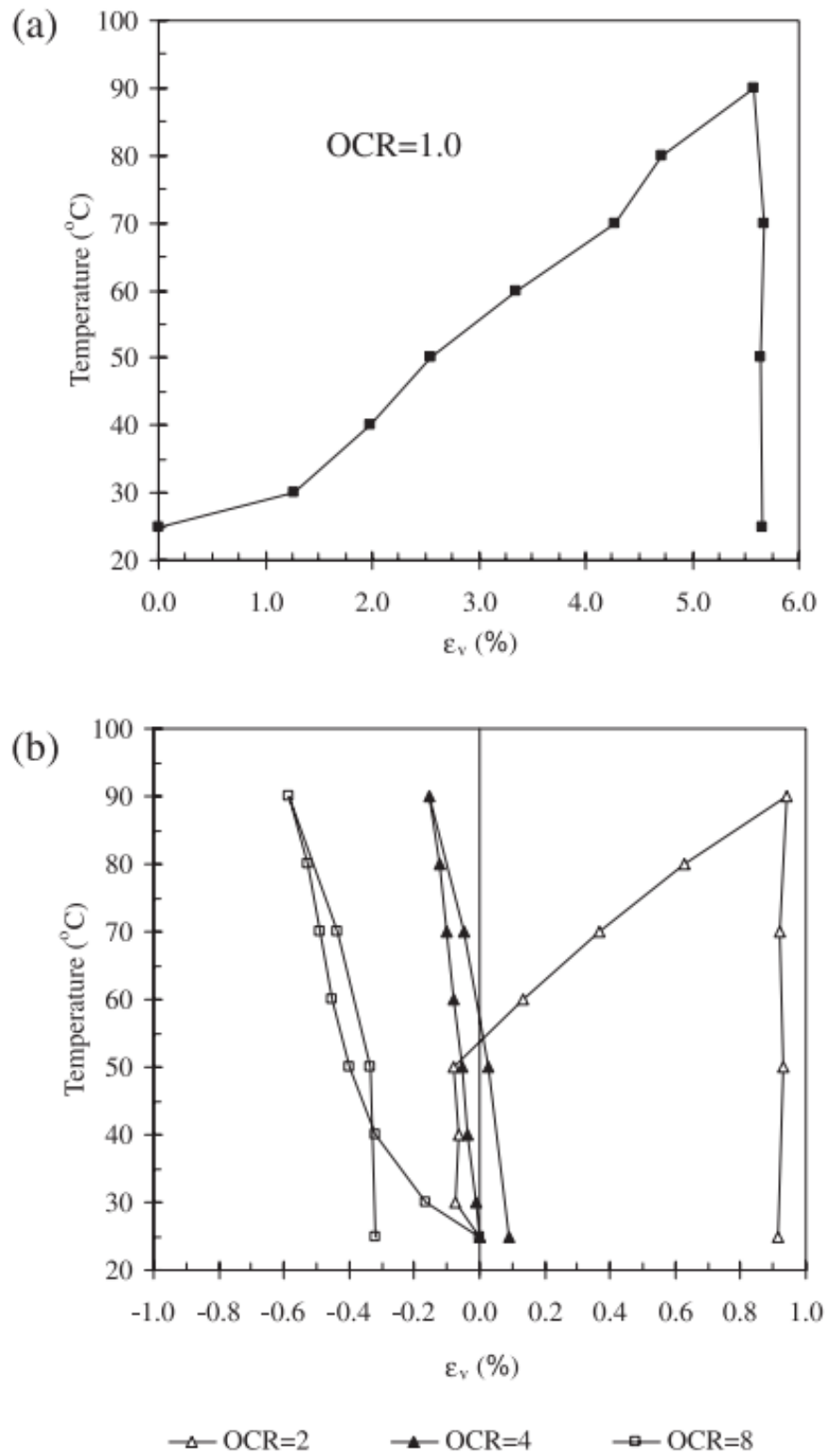


Figure 2.14 Volume change of saturated Bangkok clay during heating and cooling cycle at different OCRs (Abuel-Naga et al. 2007)

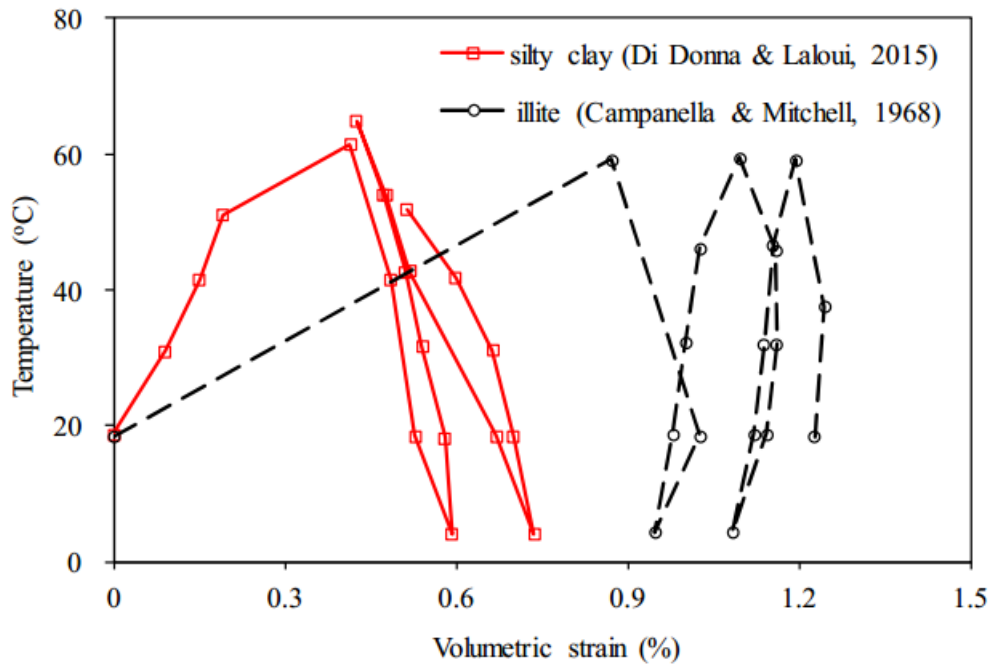


Figure 2.15 Volume changes of two fine-grained soils during heating/cooling cycles

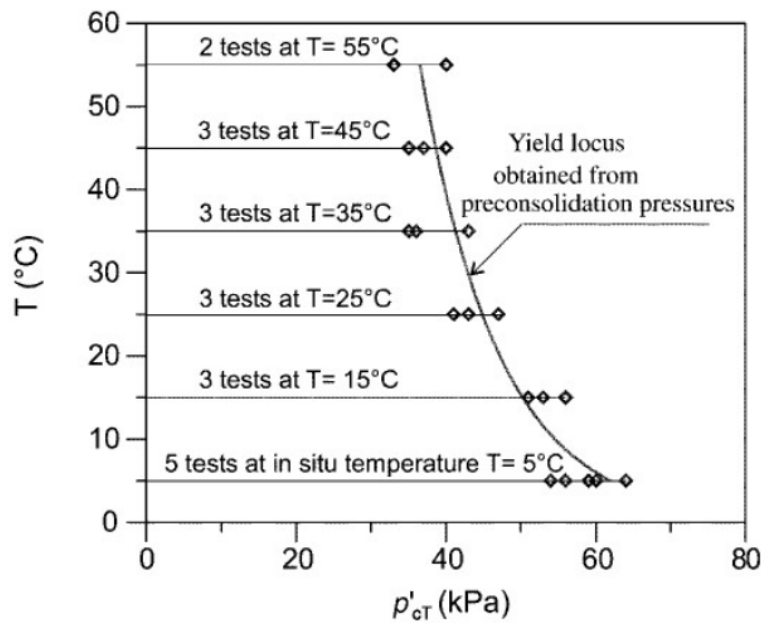


Figure 2.16 Thermal effects on preconsolidation of Lulea clay (Eriksson 1989)

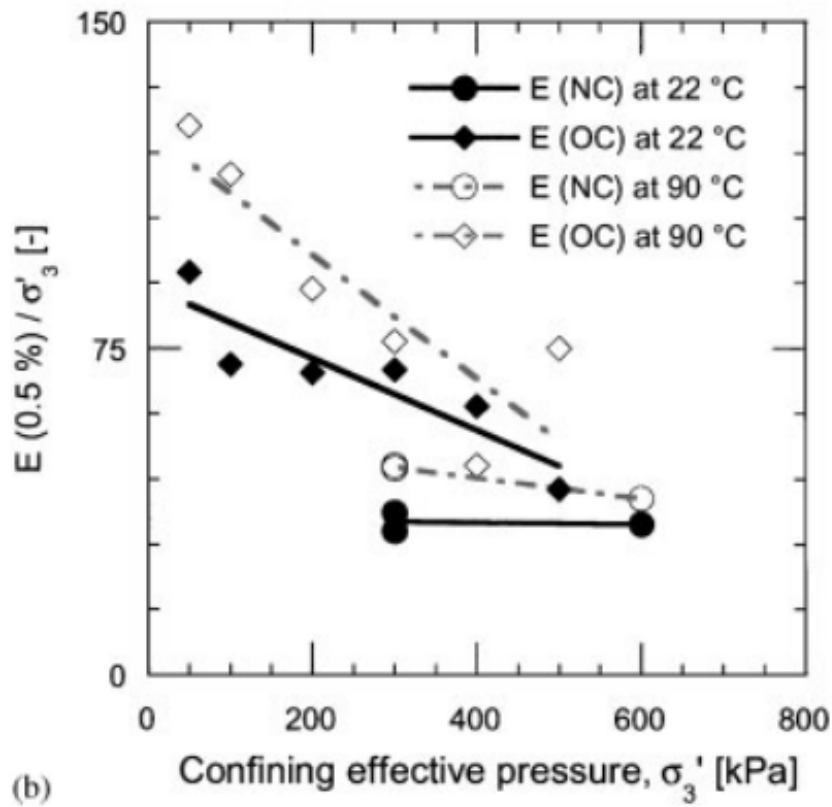
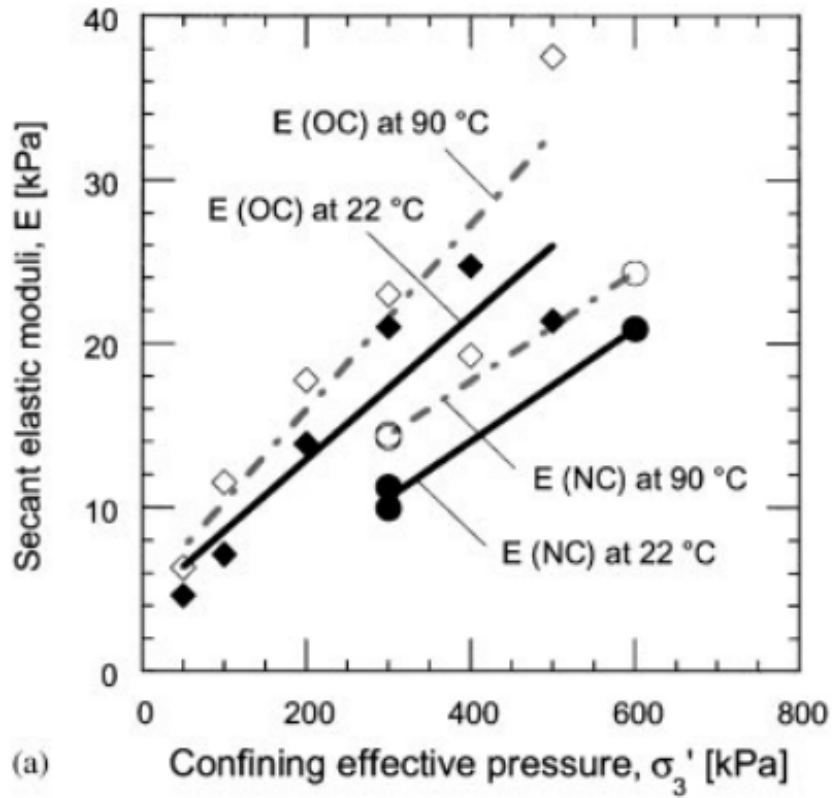


Figure 2.17 Secant Young's modulus of a saturated Kaolin (Cekerevac and Laloui 2004)

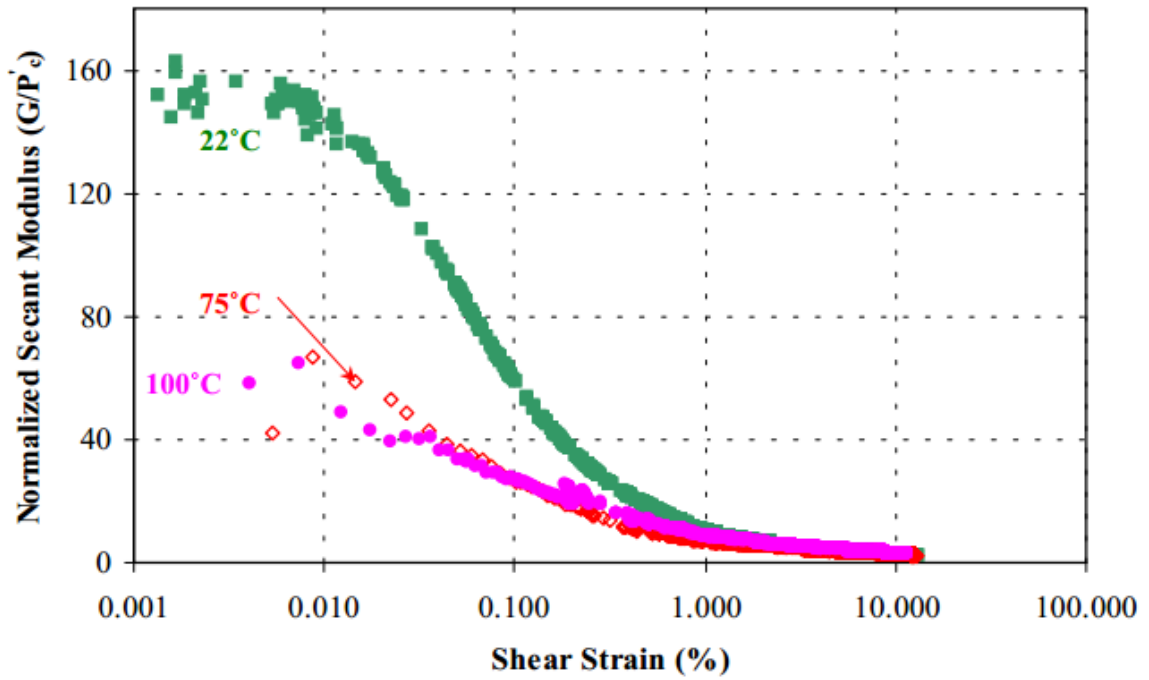


Figure 2.18 Normalised secant shear modulus of clay at different temperatures (Ghahremannejad 2003a)

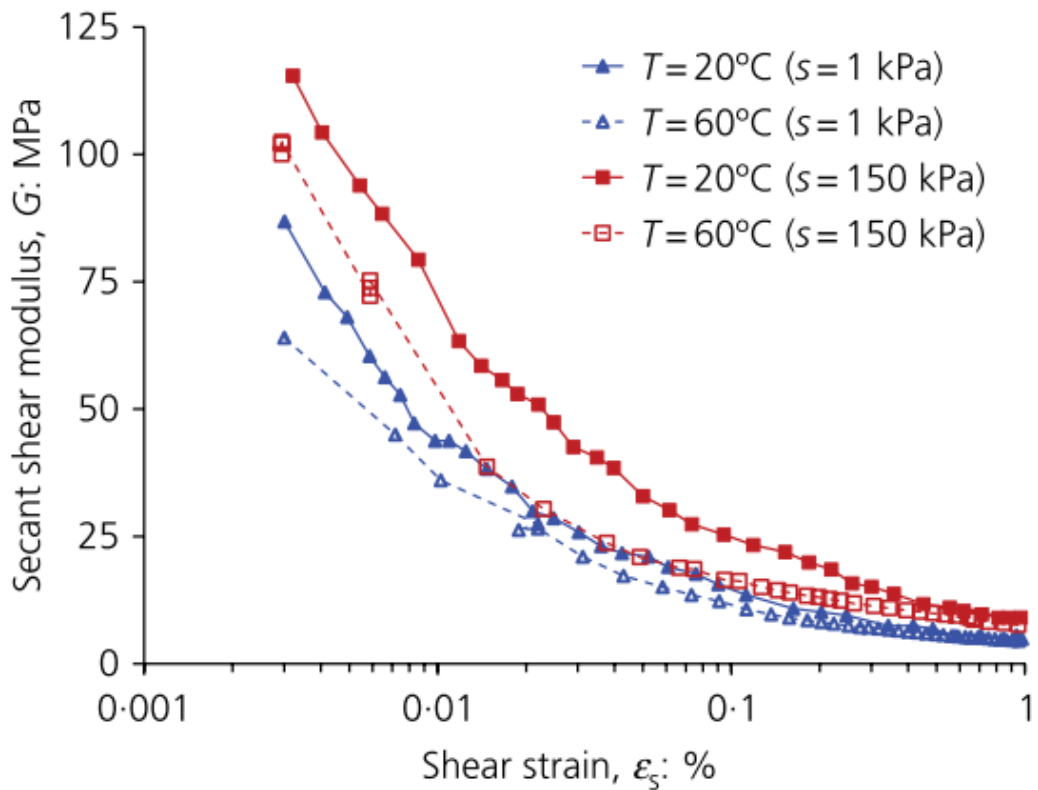


Figure 2.19 Secant shear modulus of compacted silt at different temperatures (Zhou et al. 2015a)

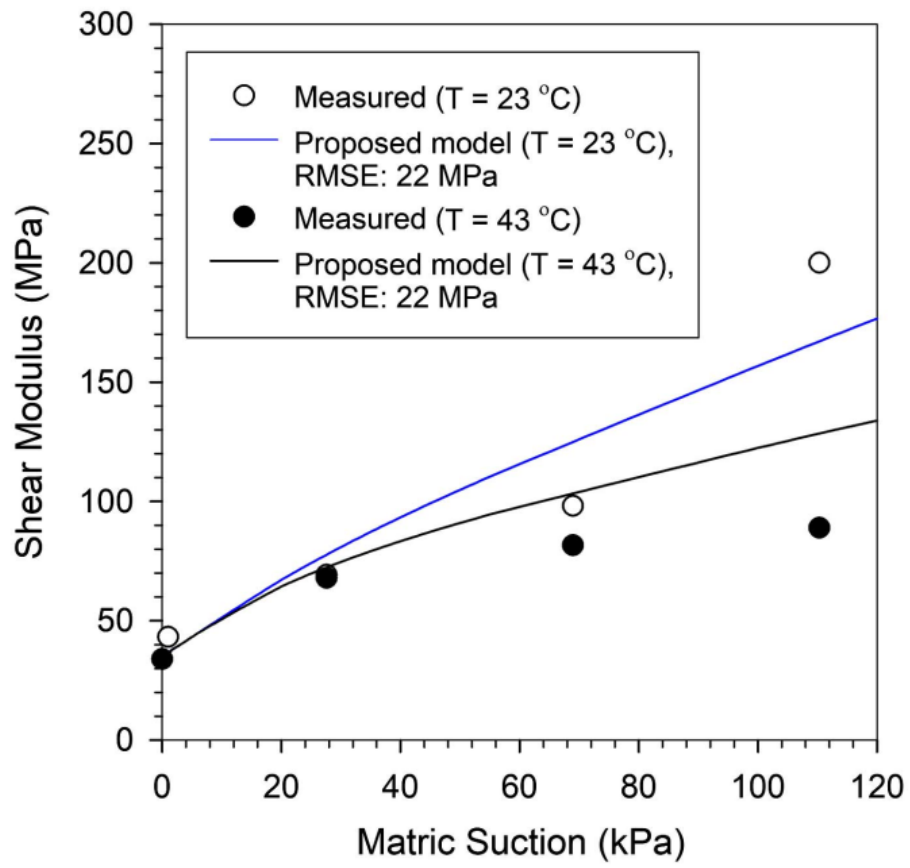


Figure 2.20 Small strain shear modulus of compacted silt at different temperatures (Vahedifard et al. 2020)

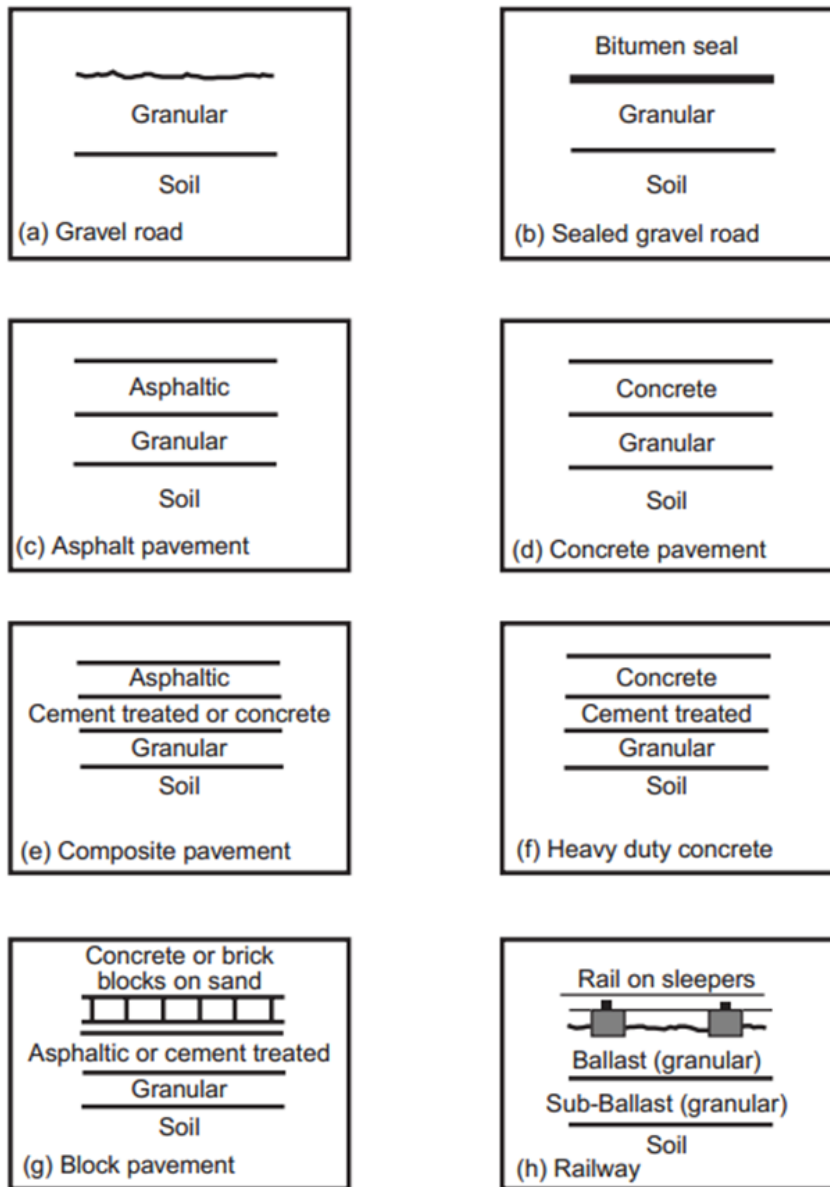
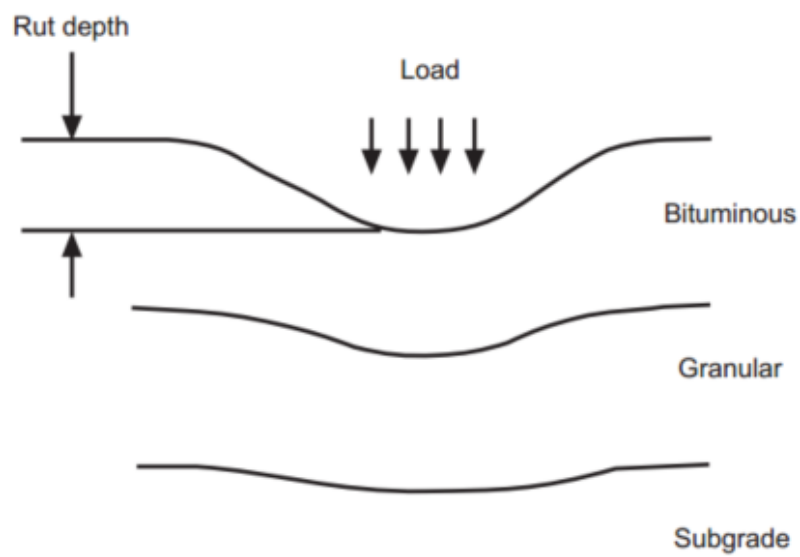


Figure 2.21 Typical cross-section of various pavement structures (Brown 1996)



(a)



(b)

Figure 2.22 Pavement failure modes (a) fatigue cracking (b) rutting (Brown 1996)

CHAPTER 3 SOIL PROPERTIES, SPECIMEN PREPARATION METHODS AND TESTING SYSTEMS

3.1 Lateritic soil tested in this study

3.1.1 Basic properties

Lateritic soils are highly weathered residual soils formed from a chemical weathering process common in tropical and sub-tropical climate regions. The chemical weathering process often leads to the leaching out of silica and the increasing concentration of iron and aluminium sesquioxides. This process is referred to as laterization. The formation of lateritic soils occurs directly or almost directly on the parent rock, making it possible for laterite and lateritic soils to retain some of the characteristics of the parent rocks. The process of laterization results in the formation of iron nodules or cemented aggregates, owing to the different polarity of the surface charges of clay and sesquioxides. Particle aggregations formed are weakly cemented & are known to break down into finer particles due to thermal and mechanical working (Airey et al. 2012; Blight 1991a; Gidigasu 1976; Netterberg 2014)

The soil investigated in this study is a lateritic soil taken from a 1.5 to 2-meter depth from a site in Ibadan, in the southwest of Nigeria. This lateritic soil is formed from a granite parent rock. **Figure 3.1** shows the particle size distribution of the lateritic soils, which was determined by the dry sieve and hydrometer analyses. Particle size distributions for the soil samples were determined using [ASTM \(2017b\)](#) and [ASTM \(2017c\)](#) with and without using a dispersant designated for wet and dry sieving. The figure shows that the particle size of the soil changed from granular to fine materials. The change between the wet and dry sieving curves illustrates the fine particle aggregation of both soil samples. The sand, silt, and clay contents are 42%, 30% and 28% from the wet sieving, respectively. The soil is classified as lean clay (CL) with low plasticity according to the Unified Classification System ([ASTM 2017a](#)).

Figure 3.2 shows the compaction curve of the soil obtained from the standard Proctor compaction test ([BSI 1990](#)). The optimum water content is about 19.5%, and the maximum dry density is 1.70 g/cm³. More results are summarized in **Table 3.1**.

3.1.2 Mineralogy and chemical composition of the tested lateritic soil

The mineral and chemical composition of the lateritic soil studied was investigated through X-ray diffraction (XRD) and X-ray fluorescence (XRF) tests, respectively. XRD results shown

in [Figure 3.3](#) confirmed the presence of quartz, hematite, kaolinite and goethite as the main mineral components in the soil ([Ng et al. 2019c](#)). From the XRF results, the soil contains a significant amount of sesquioxides. The soil contains iron sesquioxide of 10%, with aluminium sesquioxide of 28%. According to the definition proposed by [Netterberg \(2014\)](#), the soil can be described as lateritic soil because the cementing material content (iron and aluminium sesquioxides) is between 20 to 50%. Other criteria, such as the silica-sesquioxide ratio, are also used to classify soils, in which for a lateritic soil, the value of this ratio should fall in the range of 1.33 to 2 ([Lyon-Associates and BRRRI 1971](#)). According to this criterion, the soil tested in this study is lateritic with a silica-sesquioxide ratio of 1.72.

3.2 Specimen preparation using different compaction methods

The disturbed soil samples were broken down into smaller lumps by a rubber pestle and then oven-dried at 50°C for 24 hours. The oven-dried soil sample was passed through a 2 mm aperture sieve. After that, the soil sample was placed in the oven at a temperature of 50°C for 24 hours for additional drying. The oven-dried soil sample was gradually moistened and mixed with de-aired water using a sprayer, targeting a specific moisture content. Soil specimen was either dynamically or statically compacted in a compaction mould at a required dimension depending on the sample size required by the apparatus to be used. [Plate 3.1](#) shows the tools used for dynamic compaction. The static compaction was performed using a WF loading machine as shown in [Plate 3.2](#) at a speed of 2 mm/min and by adopting under compaction method proposed by [Ladd \(1978\)](#).

This research investigated two compacted soil specimen orientations (i.e., vertically and horizontally cut specimens) and their schematic diagram is shown in [Figure 3.4](#). The vertically cut specimen was directly prepared in the cylindrical mould using dynamic compaction. A box mould was used to compact a block specimen for the horizontally cut specimen. Following compaction, the specimen was rotated 90°, and a cylindrical specimen with a height and diameter comparable to the vertically cut specimen was carefully trimmed from the block specimen. All specimens were prepared at a moisture content of 19.5%, targeting 95% of the maximum dry density from the standard Proctor compaction, to ensure that the specimens were equivalent. Depending on the specimen orientation, the dynamic compaction was performed using a rotary hammer attached to a circular or square compaction plate. The boundary conditions (i.e., circular or square moulds) may affect the specimen quality. Large specimens

were prepared and used in this study to minimise the boundary effects. The diameter and height of each specimen were approximately 100 and 200 mm, respectively.

The process of compaction can induce structural features that differ from those found in natural lateritic clay produced by chemical weathering. One-dimensional compaction, in particular, may alter the orientation of particles and aggregations, resulting into cross-anisotropy. Additionally, the specimens were compacted in five layers to achieve a target density, which could result in inhomogeneous soil properties and layering effects that may impact the degree of cross-anisotropy measured. To address this issue, the surface of each preceding layer was carefully scarified before adding and compacting the subsequent soil layer to ensure proper interconnection between the layers and minimize any layering effects.

A proving ring attached to the loading machine was used to monitor the static pressure applied to the soil specimen during compaction. The initial dimensions of the specimen are measured by a calliper (readable to 0.01 mm) for height and diameter. The initial weight of the specimen was measured by a digital balance (readable to 0.01g).

3.3 Microstructural analysis

3.3.1 Scanning electron microscope

A scanning electron microscope was used to observe the soil microstructure of the initial as-compacted soil. These microstructural investigations were done to identify how water influences the particle aggregations of the different lateritic soil used in this study.

Moreover, a MIP test was conducted on the NL to identify the pore size distribution of the as-compacted specimen. As shown in [Figure 3.5](#), the as-compacted lateritic specimens mainly consist of an aggregation of fines, which could be attributed to the presence of iron and aluminium sesquioxides from the laterization process ([Airey et al. 2012](#); [Zhang et al. 2016](#)). As [Zhang et al. \(2016\)](#) discussed, iron oxides provide cementation effects, alternatively described as cladding. Cladding is simply a covering or coating on a structure or material.

3.3.2 Mercury intrusion porosimetry

Mercury intrusion porosimetry was used to quantitatively describe the microstructure of the compacted lateritic soils. [Figure 3.6](#) shows the evolution of pore size distribution of the compacted lateritic soil from Nigeria when suction is increased from 0 kPa to 150 kPa [Akinniyi \(2019\)](#). The sample at zero suction represents compacted lateritic soil that was saturated in a

desiccator. It was ensured that there was no volume change. For 50 kPa suction, back pressure was used to equalize the as-compacted soil suction to 50 kPa in a suction-controlled apparatus. The sample at 150 kPa suction represents the as-compacted sample, with an initial suction of 150 kPa measured via the null test axis translation technique. It is obvious that the unsaturated compacted NL soils show a bimodal pore size distribution.

The pore size distribution at zero suction has one peak occurring at a pore radius of 30 μm and another peak occurring at 0.25 μm . With an increase in suction to 50 kPa, the pore radius in the inter-aggregate zone at peak value increases to 60 μm , whereas the pore radius in the intra-aggregate zone at peak value increases to 0.30 μm . Further increase in suction to 150 kPa causes the pore radius in the inter-aggregate zone at peak value to increase to 100 μm , whereas the pore radius in the intra-aggregate zone at peak value seems to remain unchanged. It is shown in the figure that an increase in suction to 150 kPa caused a decrease in the volume of intra-aggregate pores (micropores). Moreover, the figure shows that an increase in suction also increased the pore diameter of the inter-aggregate pores (macropores). The reduction of intra-aggregate pore volume accompanied by an increase in inter-aggregate pore diameter implies shrinkage of the larger aggregates of the soil (see SEM image in [Figure 3.5](#)) with an increase in suction.

3.4 Water retention behaviour of compacted specimens

Based on the bimodal pore size distribution presented in the previous section, the water retention curve (WRC) predicted using the model proposed by [Cheng et al. \(2019\)](#). [Figure 3.6](#) shows the computed WRC in a suction range of 0 to 100 MPa. The WRC exhibits a clear dual porosity feature with significant water in the intra-aggregate pores. A dual-porosity water retention behaviour has been reported for other lateritic soils ([Cai et al. 2020](#); [Otálvaro et al. 2016](#); [Sun et al. 2016](#)).

The soil microstructure is likely to influence the measured drying SWRC. Because lateritic soils are highly aggregated, their microstructure is characterised by inter-aggregate and intra-aggregate pores. With such a microstructure, the WRC of lateritic soils may suggest a bimodal pore size distribution with the presence of a plateau ([Miguel and Bonder 2012](#)). There is usually a low air entry value of such lateritic clay soil ([Ng et al. 2020c](#)). The low value of AEV depict the dominance of inter-aggregate pores during drying. This is due to fine particle aggregation or cladding of particles, typical of lateritic soils. The WRC showed a sudden decrease in degree

of saturation following AEV suction, implying that the macropores were desaturated and the suction reached 10 kPa. With an increase in the suction from 50 to 1000 kPa, a small decrease in degree of saturation with an increase in suction was observed. Although the inter-aggregate pores may have desaturated, the intra-aggregate pores are likely to hold water. The water in the intra-aggregate pores may not contribute significantly to the mechanical behaviour of the unsaturated lateritic clay soils. A bimodal retention curve is expected, which is typical of tropical highly weathered soils containing aggregated particles uncemented or cemented by iron oxides linked by clay bridges (Carvalho and Leroueil 2000; Futai and Almelda 2005).

3.5 Testing equipment and apparatus

Suction and temperature-controlled tests are usually very time-consuming, so several apparatuses are used in this study to carry out parallel tests. They are briefly introduced in the following paragraphs.

3.5.1 Bender element electrical components for measuring shear wave velocity

The bender element electrical system utilised in this study includes the following key components: a function generator (Agilent 33220A), a piezo amplifier (Piezo Driver, Model EPA- 104, Piezo System Inc.) and an oscilloscope (Agilent DSO5014A). With the oscilloscope's convenient USB and computer connection cable ports, you can easily store and access important data.

A sine wave pulse of 5V was input in a wavefunction generator through a piezo amplifier, which is capable of up to 20 times voltage amplification to the transmitter bender elements. Hence the excitation voltage of 100V peak to peak was applied to the bender element. This voltage is below the maximum voltage capacity of the bender element used to prevent it from depolarization. The input frequency of 15 kHz was utilised. This input frequency was chosen based on the typical frequency used by other researchers in the literature (Lee and Santamarina 2005; Leong et al. 2009). An oscilloscope, which is connected to the bender elements, is used to log the transmitted and received waves signals. To determine the travel time from the bender element signals, the peak-to-peak technique is adopted because it is simple and capable of producing consistent results (Clayton 2011).

Bender elements can be used to measure the shear wave velocity. It is then used to deduce the elastic shear modulus ($G_{0(vh)}$) using the following equation:

$$G_{0(vh)} = \rho V_{(vh)}^2 \quad (3.1)$$

where ρ = bulk density of the soil; and V_{vh} = vertically propagated shear wave velocity with the horizontal polarisation of the soil.

3.5.2 Double-cell triaxial apparatus for testing unsaturated soil at room temperature

A double-cell triaxial equipment developed by [Chen et al. \(2018\)](#) was utilized for testing saturated and unsaturated tests at room temperature. [Plate 3.4](#) depicts a picture of the double-cell triaxial apparatus. [Liu et al. \(2020\)](#) and [Chen et al. \(2018\)](#) provide more information on this device. This apparatus was used to carry out suction-controlled, consolidated drained and undrained shear tests. The device comprises an outer cell, an inner cell connected to an automatic volume change device and an internal load cell to measure the deviator stress of the specimen. In addition, the equipment incorporates internal LVDTs to measure the local deformation of specimens at the midpoint of their height with an accuracy of about 0.001% strain. A pressure/volume controller with a high-precision LVDT is used to monitor the inner cell's volume change; thus, the volumetric deformation of the specimen is determined. Before starting the tests, the LVDTs, pressure transducers, and load cells attached to a datalogger are calibrated. [Figure 3.8](#) shows a schematic diagram of the double-cell triaxial apparatus.

3.5.3 A new temperature-controlled oedometer with bender elements

Several researchers have used a thermal oedometer to investigate soil deformation under heating and cooling ([Abuel-Naga et al. 2007](#); [Ng et al. 2017a](#); [Ng et al. 2019b](#)). However, the elastic shear modulus has not been simultaneously measured during the heating and cooling of the soil. The elastic shear modulus is an important parameter for analysing the serviceability of geo-materials and structures. Therefore, it is valuable and useful to investigate the thermal effects on shear modulus since many energy geo-structures and ground, such as energy piles, tunnels. Soils around high-voltage cables also experience prolonged temperature changes ([Hueckel and Baldi 1990](#); [Mitchell et al. 1982](#)).

To investigate the thermal effects on the elastic shear modulus of a saturated lateritic clay, a new temperature-controlled oedometer was developed. Different from the conventional oedometer, this new oedometer is larger and contains a groove to accommodate a pair of bender elements in the top cap and base to measure the shear wave velocity in the vertical direction. [Figure 3.9](#) shows a schematic diagram of the thermal oedometer with the bender element setup. The temperature control system comprises a spiral copper coil that circulates heated or cooled

water from a temperature control system (i.e., SD07R-20-A12E) manufactured by PolyScience. A thermocouple was installed inside the oedometer to monitor soil temperature during thermal loading. To minimize the heat loss, an insulating material was used to wrap the oedometer apparatus. From a calibration test performed with three thermocouples (i.e., one positioned in the middle of the specimen, one at the edge of the specimen and the last one in the water surrounding the oedometer specimen ring), 3-6 hours are sufficient to achieve a steady and uniform temperature within the soil specimen, depending on the temperature path. At thermal equilibrium, the accuracy of temperature is $\pm 0.1^\circ\text{C}$. In addition, bender elements can be used to measure the shear wave velocity. It is then used to deduce the elastic shear modulus in the vertical plane ($G_{0(vh)}$).

3.5.4 A new temperature- and suction-controlled triaxial apparatus

This study developed a new suction and temperature-controlled triaxial apparatus equipped with bender elements and local strain measurements to investigate the coupled effects of temperature and suction on elastic stiffness.

Figure 3.10 shows a schematic diagram of the new testing system. **Plate 3.7** shows the final set-up with the bender element electrical components. The temperature control system is identical to what was used previously for the thermal oedometer described in the previous section. Similarly, the temperature is controlled by circulating heated or cooled water through a spiral copper coil around the soil specimen. A thermocouple was installed inside the triaxial cell close to the soil specimen to monitor the soil temperature and estimate the thermal equilibrium state of the soil. During testing, an insulating material was used to wrap the triaxial apparatus to reduce the thermal energy loss, as shown in **Plate 3.7**.

Suction (i.e., matric suction) control is achieved in this apparatus using the axis translation technique (Hilf 1956). The pore-air pressure u_a is applied at the top of the soil specimen through a coarse porous stone. A filter paper is placed between the porous stone and the soil specimen to prevent blockage of the voids of the porous stone by soil particles. The pore water pressure u_w is applied at the base of the specimen through a high air entry ceramic disk. The high air-entry value ceramic disk permits water passage but prevents free airflow from the specimen to the water pressure control or drainage system connected underneath it. In addition, a diffused air volume indicator, air pressure control and a high air entry ceramic disk were used at the base pedestal.

Moreover, the stress-path triaxial apparatus has bender element probes to measure horizontally propagated shear wave velocity with vertical polarization v_{hv} and horizontally transmitted shear wave velocity with horizontal polarization, hence measures v_{hh} . This allows for estimating the anisotropic elastic or very small strain shear moduli $G_{0(hv)}$ and $G_{0(hh)}$, respectively. Hence, the stiffness anisotropy can be evaluated by the stiffness ratio $G_{0(hh)} / G_{0(hv)}$. Detailed description of the bender element probe can be found in [Ng et al. \(2004\)](#) and [Ng et al. \(2009\)](#).

Two local LVDT transducers inserted in a fixing mount were fitted in the middle third of the specimen to measure local axial displacements. Moreover, one LVDT transducer, with the help of a pair of yokes attached to the middle of the specimen, was used for the radial displacements of the soil specimen ([Chen et al. 2020](#)). The fixing mount pads of the LVDT are directly attached to the membrane of the soil specimen using adhesive.

Table 3.1 Physical and chemical properties of lateritic soils

Index property	Value
Atterberg limits	
Liquid limit	47
Plasticity index	21
Particle size distribution (%)	
Sand fraction	42
Silt fraction	30
Clay fraction	28
Standard Proctor compaction	
Optimum moisture content (%)	19.5
Maximum dry density (g/cm ³)	1.70
Classification	
Unified Soil Classification System (ASTM 2017)	Sandy lean clay (CL)
Main chemical composition (%)	
SiO ₂	60
Fe ₂ O ₃	10
Al ₂ O ₃	28

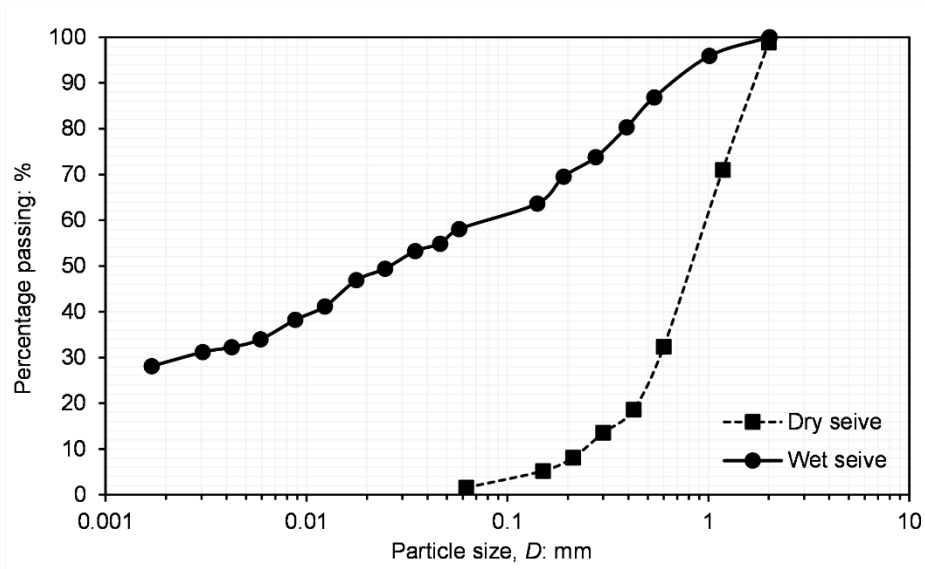


Figure 3.1 Particle size distribution of soil

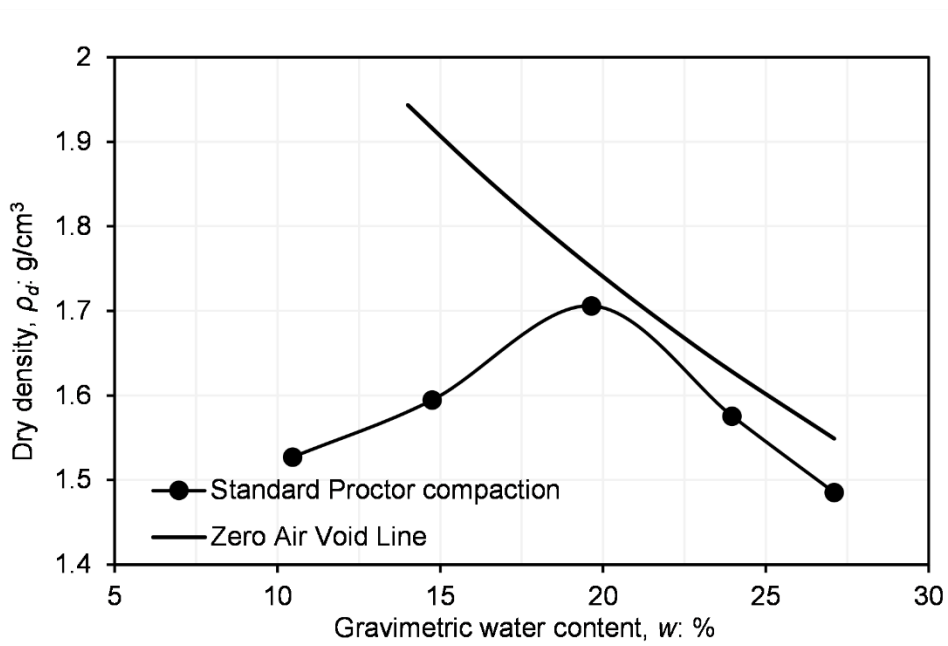


Figure 3.2 Standard Proctor compaction curve of soil

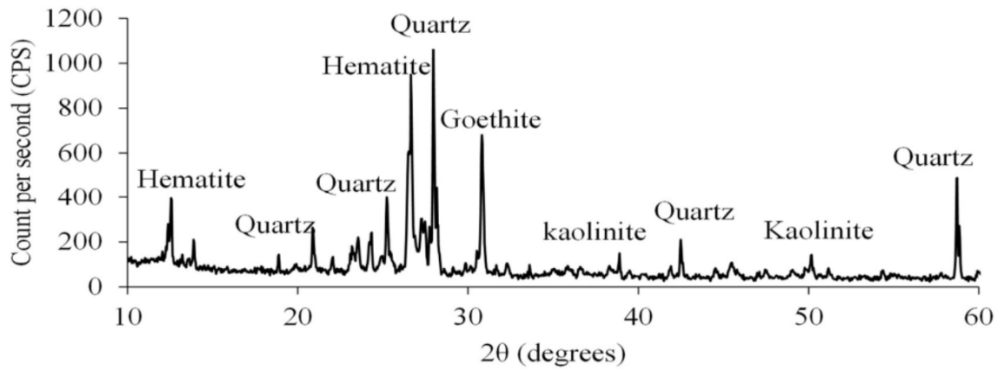


Figure 3.3 X-ray diffractometer results and mineralogy in the lateritic clay (Ng et al. 2019c)

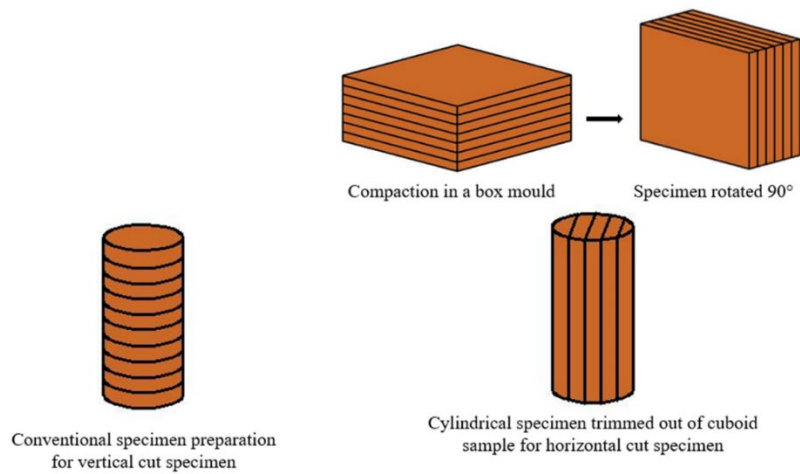


Figure 3.4 Specimen preparation for vertical and horizontal cut specimen

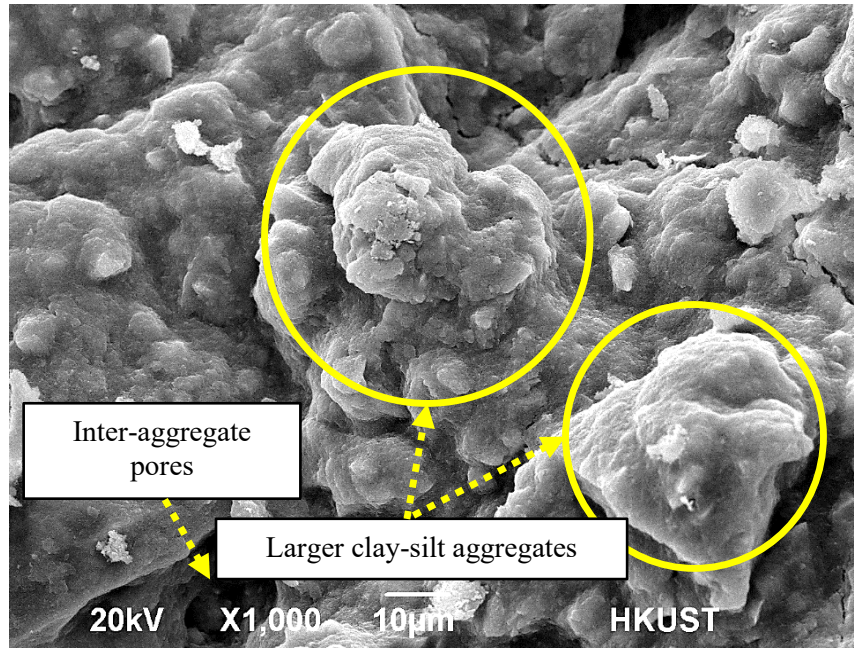


Figure 3.5 SEM image of lateritic soil

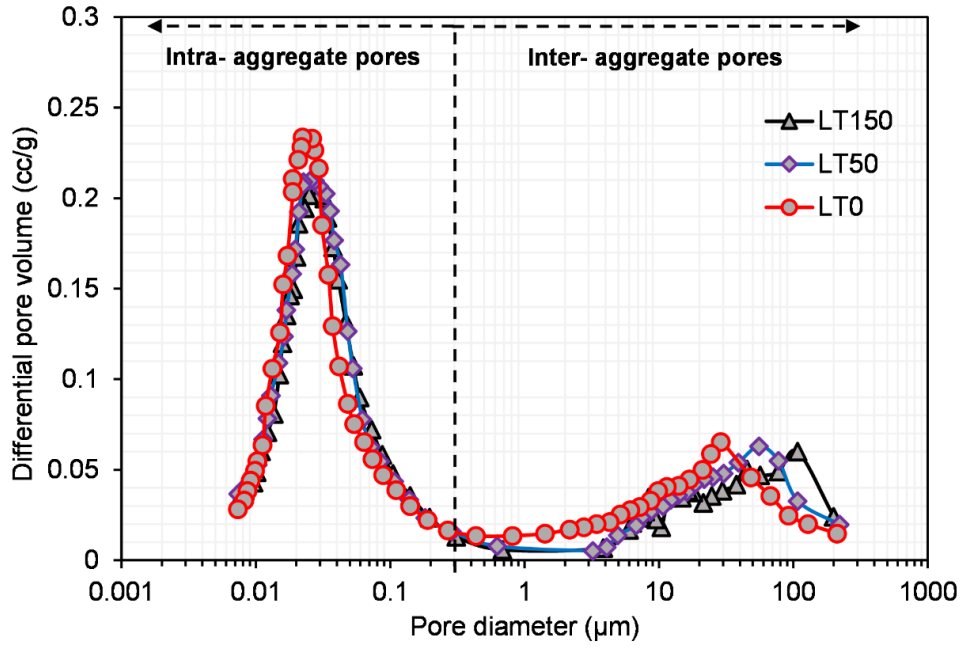


Figure 3.6 Typical pore size distribution of lateritic soil with changes in suction (Akinniyi 2019)

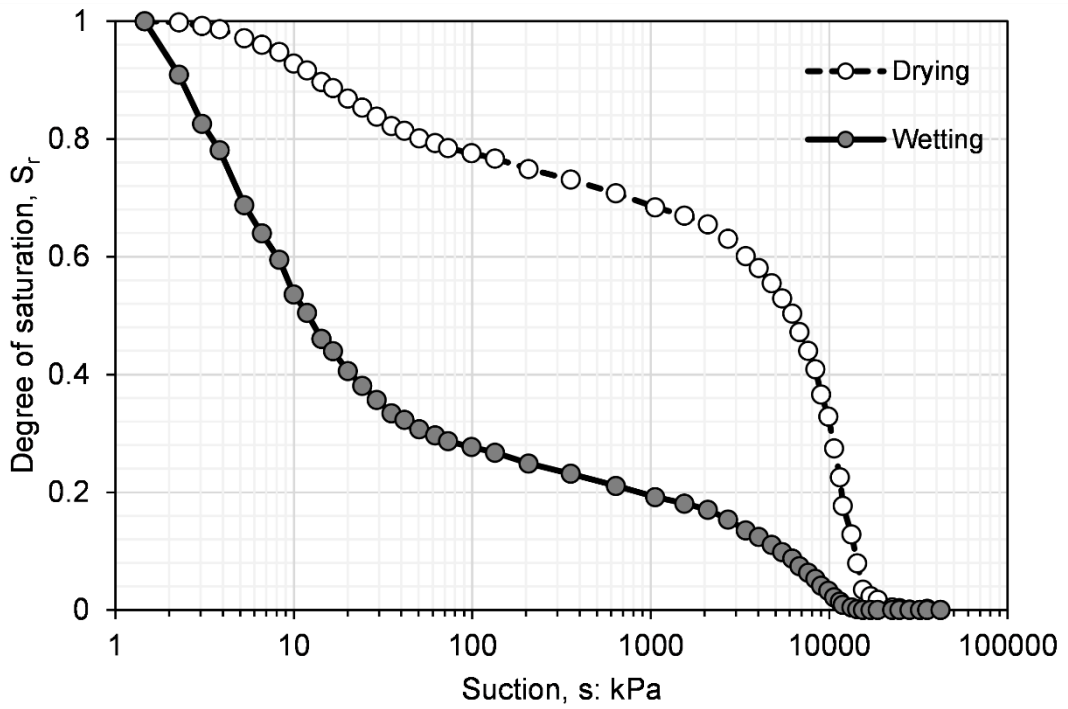


Figure 3.7 Predicted soil water retention of a lateritic soil

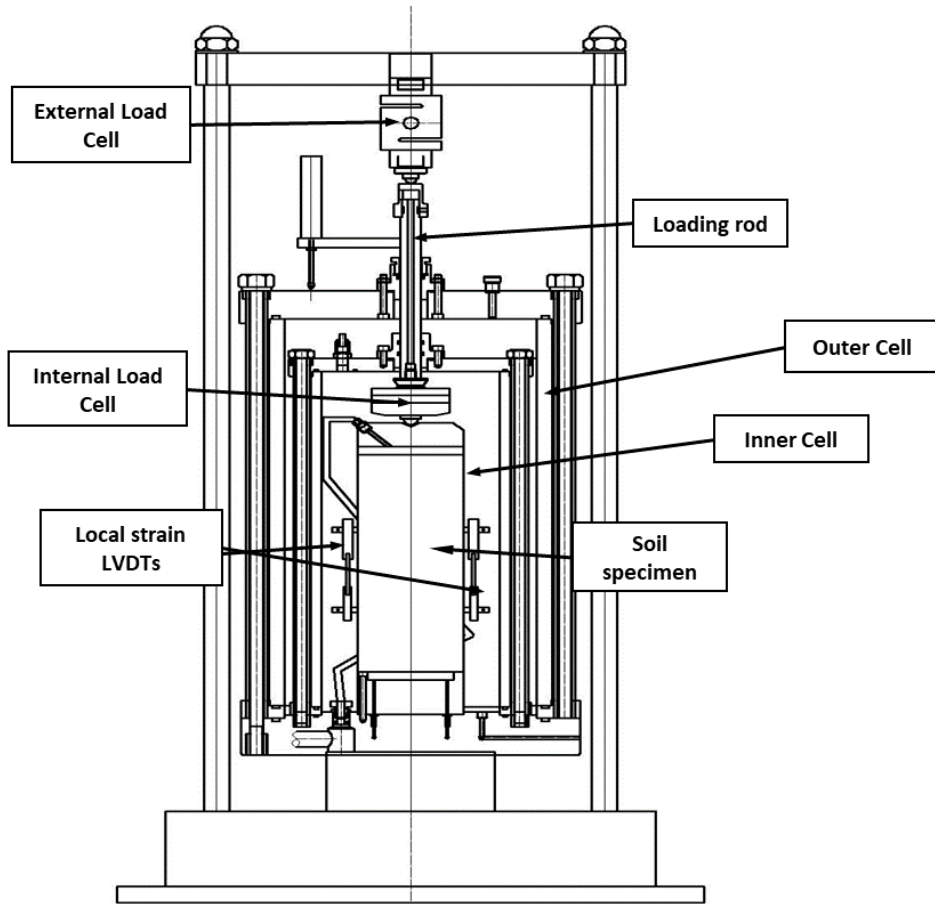


Figure 3.8 Schematic diagram of a double-cell triaxial apparatus equipped with local strain measurements (after [Chen et al. \(2018\)](#))

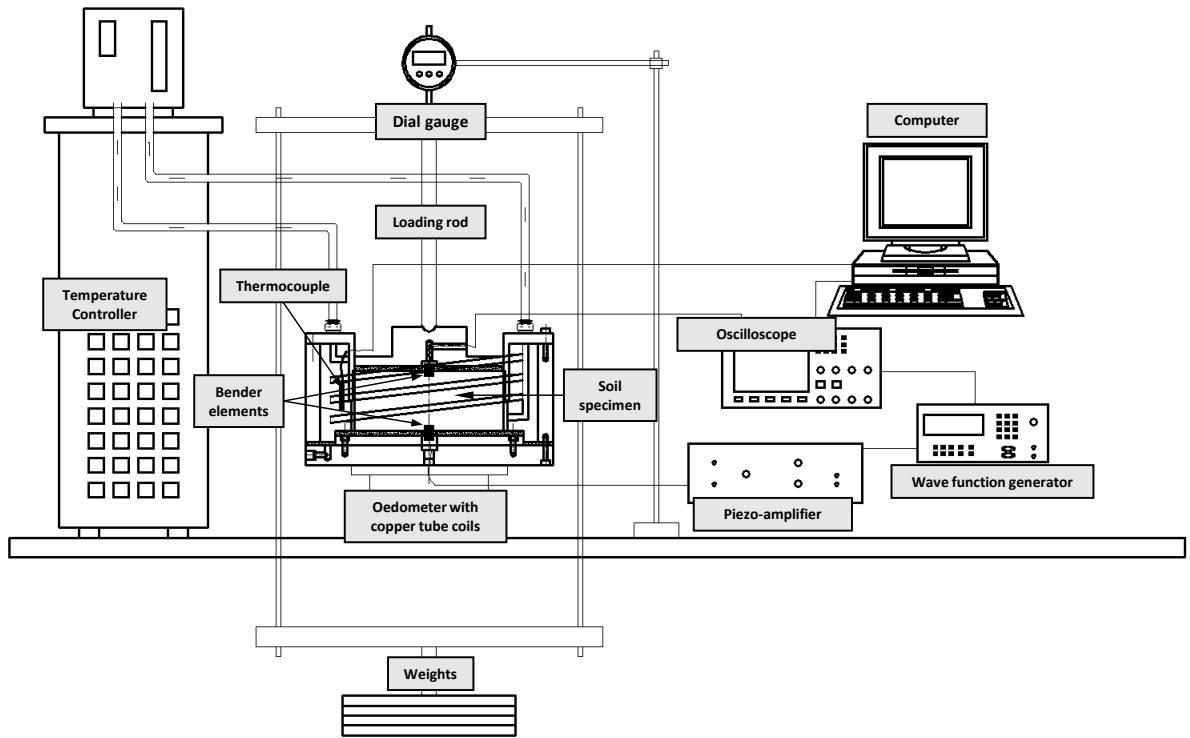


Figure 3.9 Schematic diagram of a temperature-controlled oedometer equipped with bender elements

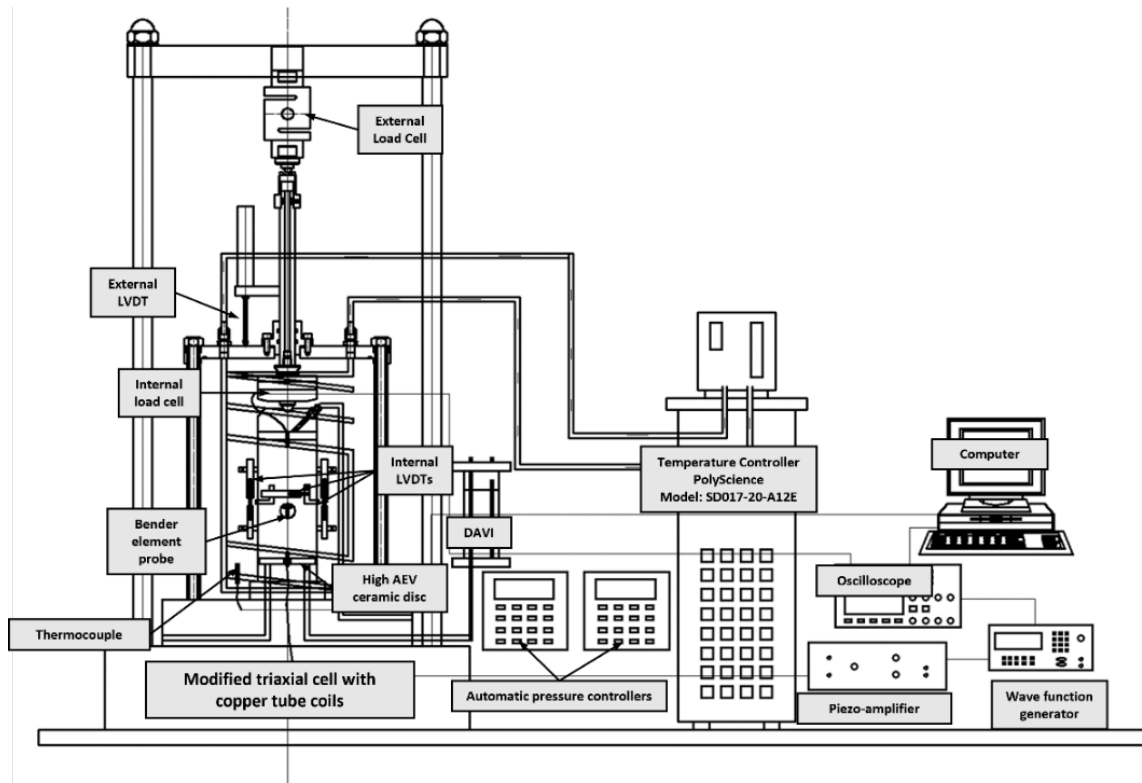


Figure 3.10 Schematic diagram of triaxial apparatus with temperature control and bender element set-up

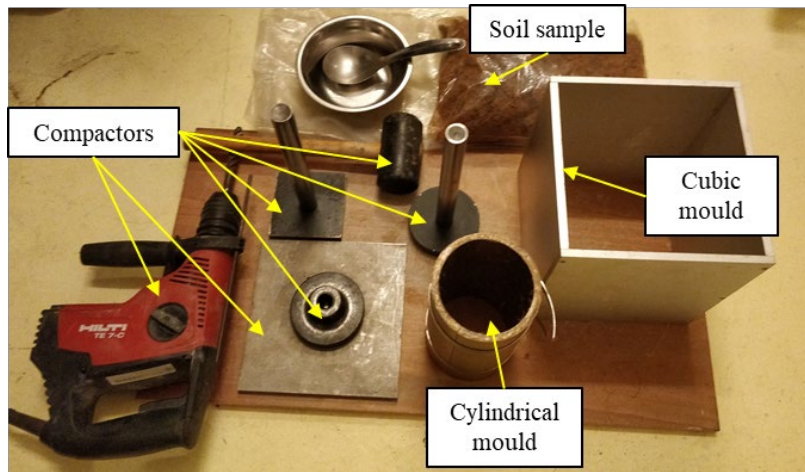


Plate 3.1 Dynamic compaction components

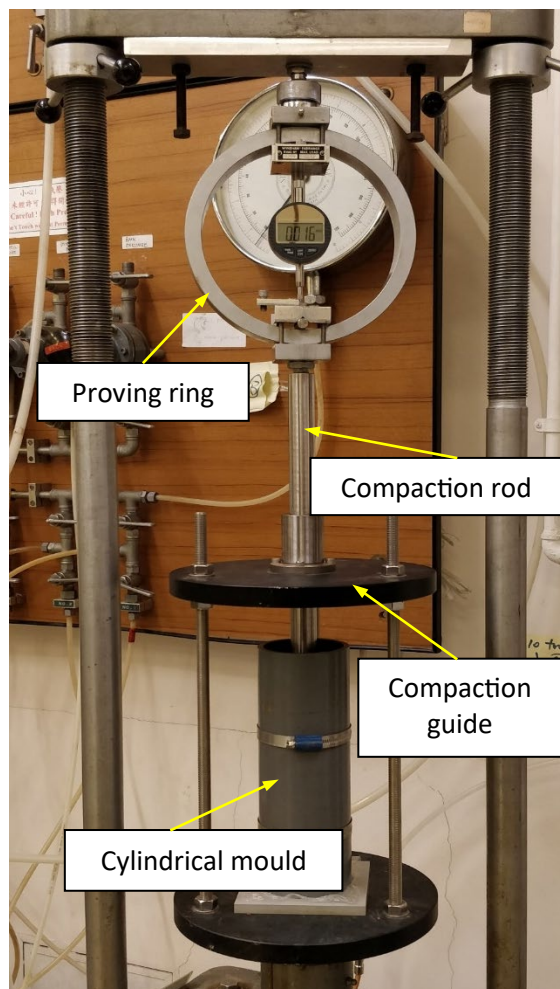


Plate 3.2 Static compaction with a triaxial loading frame



Plate 3.3 Carefully trimmed horizontal cut specimen

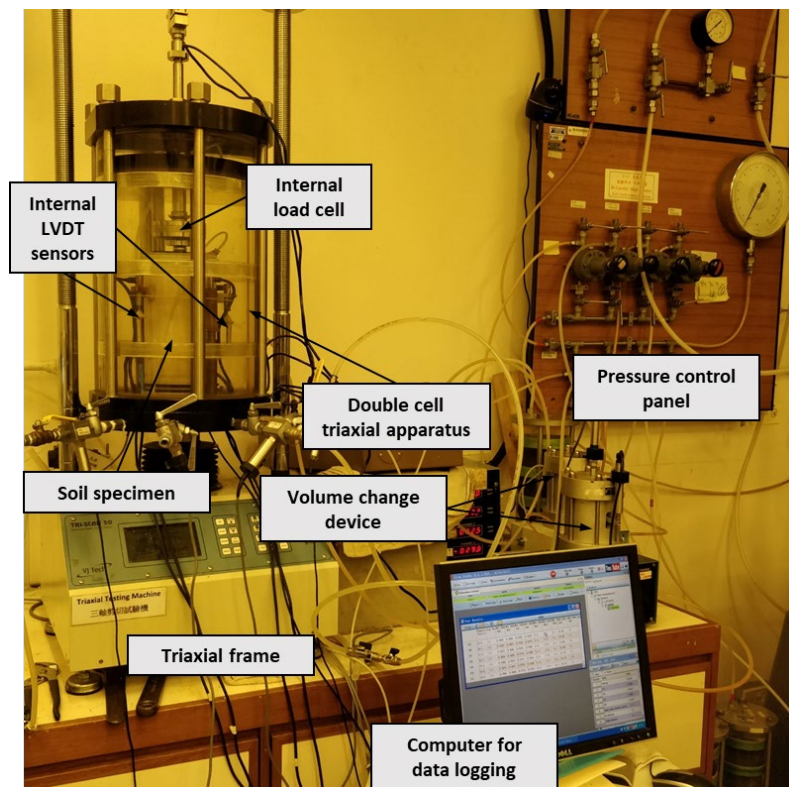


Plate 3.4 Double-cell triaxial apparatus

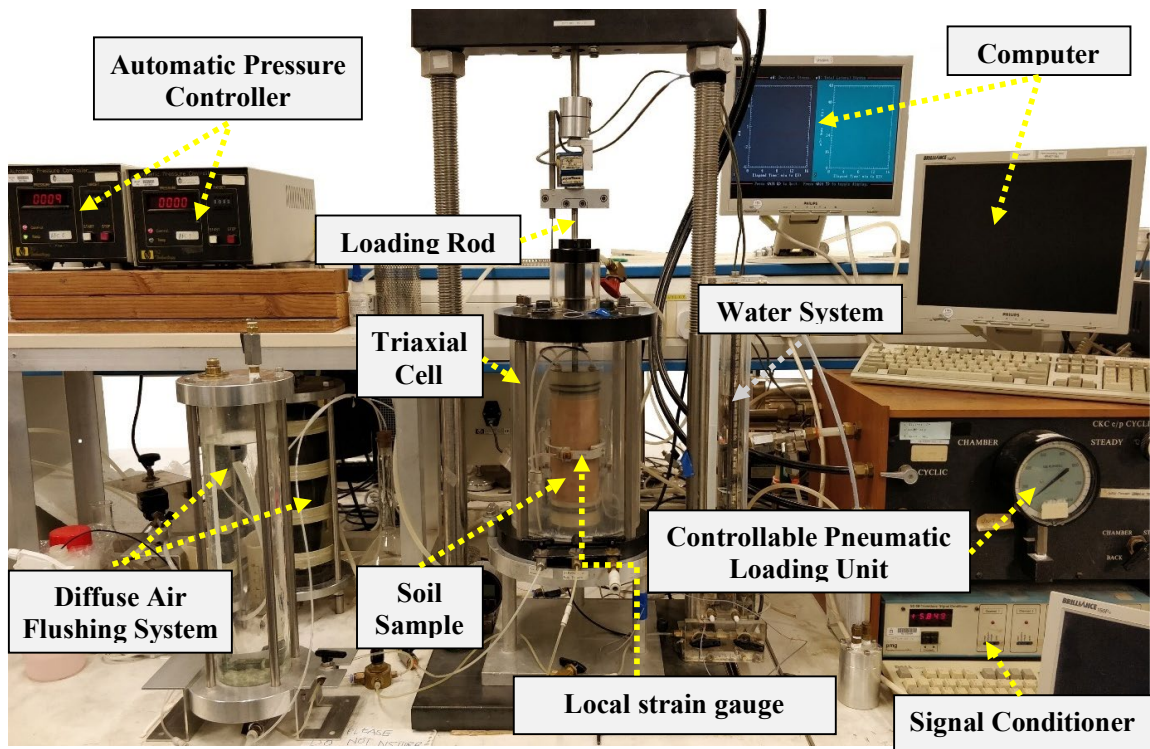


Plate 3.5 Cyclic triaxial apparatus

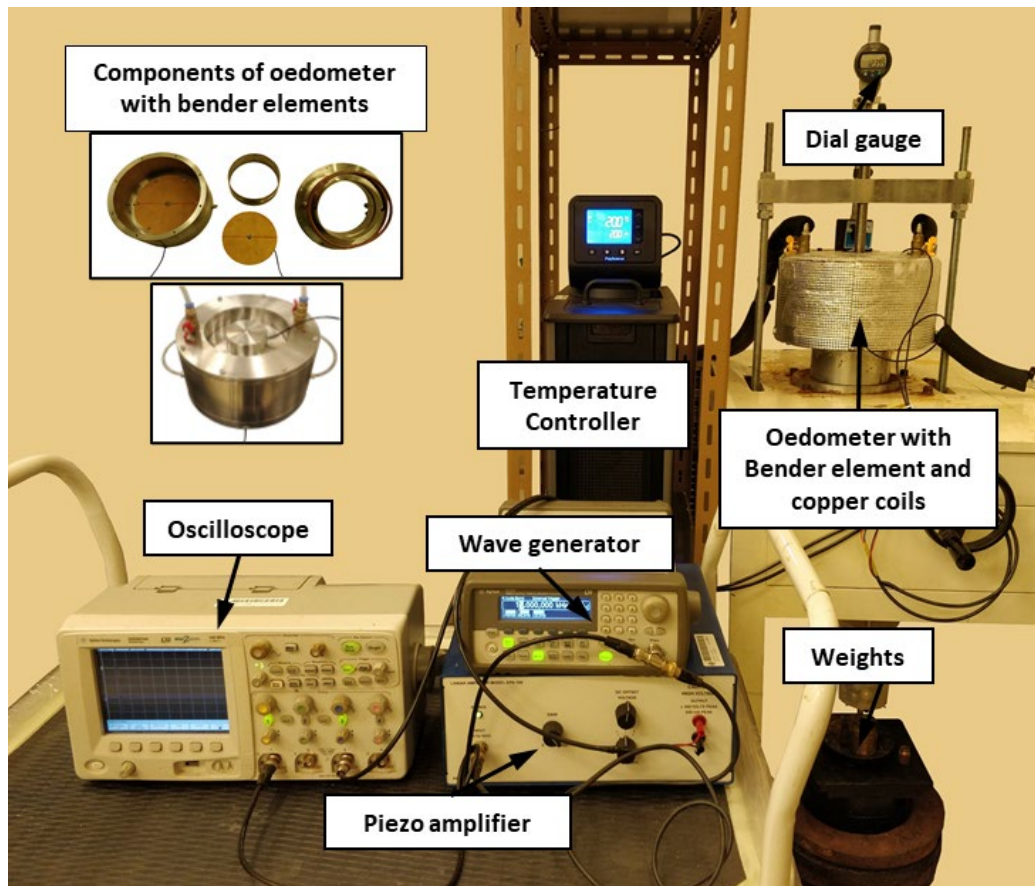


Plate 3.6 Temperature-controlled oedometer with the bender element setup

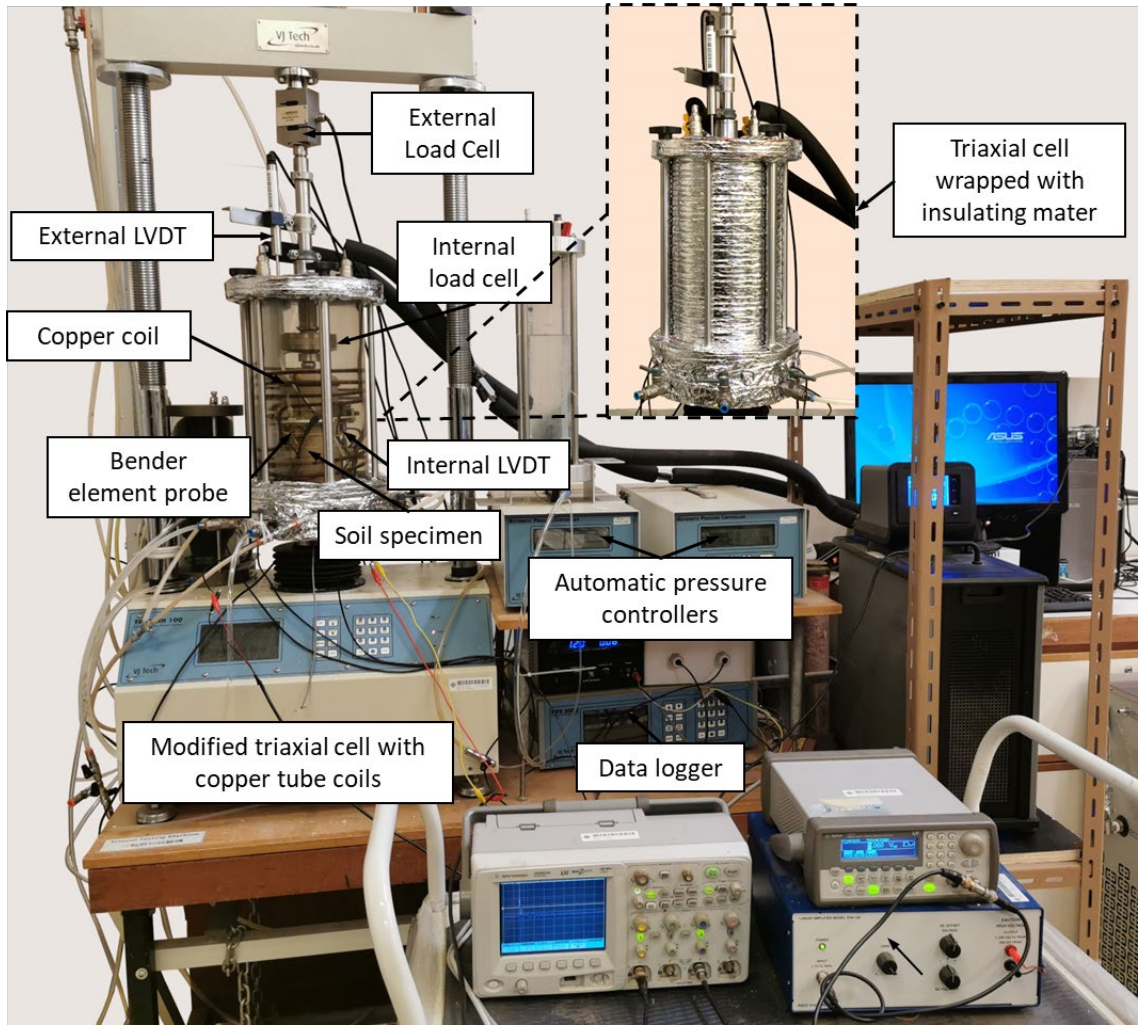


Plate 3.7 Set up of temperature and suction control triaxial apparatus

CHAPTER 4 ANISOTROPIC STIFFNESS AT SATURATED CONDITIONS FROM VERY SMALL TO LARGE STRAINS

This chapter presents the test programme, procedures and data analysis of a series of triaxial compression tests on saturated compacted lateritic soil. The testing systems in [Plates 3.4](#) and [3.7](#) were used. Particular attention was paid to three aspects of saturated lateritic soil's stiffness characteristics, which have not been widely studied in the literature. Firstly, the full set of cross-anisotropic stiffness parameters of the compacted soil from very small to large strains are determined and analysed. Secondly, the anisotropic modulus-strain curves of the compacted saturated lateritic clay at various effective mean stress are also studied. Moreover, the influence of compaction water content and density on anisotropic stiffness is investigated.

4.1 Theoretical consideration, testing programme and testing procedures

4.1.1 Theoretical consideration

The characterisation of anisotropic elastic behaviours requires 21 independent elastic constants ([Graham and Houlsby 1983](#)). When an assumption is made that the soil is cross-anisotropic or transverse isotropic and the plane of isotropy is horizontal, the stress-strain relation is described using the following equation:

$$\begin{bmatrix} \delta\epsilon_v \\ \delta\epsilon_h \\ \delta\epsilon_h \\ \delta\gamma_{vh} \\ \delta\gamma_{hv} \\ \delta\gamma_{hh} \end{bmatrix} = \begin{bmatrix} \frac{1}{E_v} & -\frac{\nu_{hv}}{E_h} & -\frac{\nu_{hv}}{E_h} \\ -\frac{\nu_{vh}}{E_v} & \frac{1}{E_h} & -\frac{\nu_{hh}}{E_h} \\ -\frac{\nu_{vh}}{E_v} & -\frac{\nu_{hh}}{E_h} & \frac{1}{E_h} \\ & & & \frac{1}{G_{vh}} \\ & & & & \frac{1}{G_{hv}} \\ & & & & & \frac{1}{G_{hh}} \end{bmatrix} \begin{bmatrix} \delta\sigma_v \\ \delta\sigma_h \\ \delta\sigma_h \\ \delta\tau_{vh} \\ \delta\tau_{hv} \\ \delta\tau_{hh} \end{bmatrix} \quad (4.1)$$

where E_v and E_h are Young's moduli in the vertical and horizontal directions, respectively, ν_{vh} is Poisson's ratio relating to the horizontal strain caused by an imposed vertical strain, ν_{hv} is Poisson's ratio relating to the vertical strain caused by an imposed horizontal strain, ν_{hh} is Poisson's ratio relating to the horizontal strain caused by an imposed horizontal strain in the normal direction, G_{hv} and G_{vh} are both shear moduli in the vertical plane and G_{hh} is shear

modulus in the horizontal plane. Among these eight stiffness parameters, five are independent since [Love \(1927\)](#) proved that:

$$\frac{\nu_{hv}}{E_h} = \frac{\nu_{vh}}{E_v} \quad (4.2)$$

Secondly, due to isotropy in the horizontal plane, it is obtained that:

$$G_{hh} = \frac{1}{2} \frac{E_h}{(1 + \nu_{hh})} \quad (4.3)$$

In addition, the symmetry of the compliance matrix suggests:

$$G_{vh} = G_{hv} \quad (4.4)$$

4.1.2 Testing programme

The above equations apply to both “effective” and “total” stress analyses. Among the stiffness parameters shown in [Equation \(4.1\)](#), some parameters are more readily measured than others ([Clayton 2011](#)). Laboratory tests are designed to measure some of the parameters, and based on the results, the complete set of stiffness parameters is calculated. In this study, three series of tests were carried out to measure the cross-anisotropic elastic parameters of the studied lateritic soil for both effective and total stress analyses, as summarised in [Table 4.1](#).

Regarding drained condition, the five independent constants may be chosen from different parameter sets ([Lings 2001](#); [Lings et al. 2000b](#); [Pickering 1970](#)) when dealing with a drained condition, typically; E'_v , E'_h , ν'_{vh} , ν'_{hh} and G_v or E'_v , E'_h , ν'_{vh} , G_h and G_v or E'_v , E'_h , ν'_{hv} , ν'_{hh} and G_v or E'_v , ν'_{hv} , ν'_{hh} , G_h and G_v . In the current study, the following five independent parameters are measured: G_{hh} , G_{hv} , E'_v , E'_h , and ν'_{vh} . The other three parameters can be calculated from them by using [Equations \(4.2\) to \(4.4\)](#). Obtaining the values of G_{hh} and G_{hv} is accomplished through elastic shear wave velocity measurements using bender elements. Shear wave velocity measurements were undertaken on compacted specimens in the vertical and horizontal planes to estimate the elastic shear modulus during isotropic compression from 20 to 300 kPa. On the other hand, a series of triaxial compression tests were performed to determine E'_v , E'_h and ν'_{vh} with precise local strain measurements. Two consolidated drained shear tests were carried out each for specimens prepared using compaction preparation with horizontal bedding in the cylindrical mould (referred to as a vertical cut) and for specimens with the bedding rotated 90° to produce vertical alignment (referred to as a horizontal cut). The

preparation alignment surfaces oriented horizontally to the vertical shearing direction are designated with the prefix v CD, whereas the alignment surface oriented parallel to the shearing direction is designated as h CD. The vertically cut specimen results help to obtain the values for E'_v and v'_{vh} . The value of E'_h is measured from the horizontally cut specimen. Moreover, this series of tests also allow for the influence of anisotropy on shear strength and strain-dependent stiffness to be investigated under drained conditions.

Under undrained conditions, the number of independent parameters further reduces to three (Atkinson 1975; Clayton 2011; Lings 2001). Parameters E_v^u , G_{hh}^u , G_{hv}^u are measured, while the other five stiffness parameters in Equation (4.1) are obtained using the equations given in the appendix. The shear modulus value remains unchanged under the drained and undrained conditions (Clayton 2011), thus the results measured under drained conditions are used here. To determine E_v^u , two consolidated undrained shear tests were carried out on the vertically cut specimens, as shown in Table 4.1.

In addition to the testing programme described above, two series of tests were designed to study the influence of compaction water content and void ratio on elastic shear modulus, as shown in Table 4.2. As such, the influence of compaction-induced fabric on stiffness anisotropy could be evaluated. Soil specimens were prepared with an initial compaction water content of 16.5%, 19.5% and 22.5% at dry densities of 90% and 95% MDD. These water contents are the dry side of OMC (i.e., OMC-3%), OMC and wet side (i.e., OMC+3%), respectively. Specimens prepared at each condition were subjected to isotropic compression to investigate the influence of the initial fabric on the stiffness evolution.

4.1.3 Testing procedures

Details of the test procedures adopted for the consolidated drained and undrained triaxial tests under saturated conditions can be found in BS 1377 (BSI 1990) and Head (1998). The saturation of the specimen was carried out following a three-step procedure. First, CO₂ was flushed through the specimen for nearly 1 hour at 10 kPa effective stress with a cell pressure value of 20 kPa. Following CO₂ flushing, de-aired water was percolated through the specimen from the base for nearly 24 hours. Lastly, a minimum back pressure of 200 kPa was applied while maintaining an effective confining stress of 10 kPa. The B-value of the specimen was checked during the back pressure application procedure. The specimen was considered saturated when the Skempton (1954) B-value reached a minimum value of 0.95. The specimen

was then subjected to isotropic compression to the required effective stress by increasing both the inner and outer cell pressures. The volume change of the specimen was measured by the automatic volume indicator attached to the inner cell pressure. The graph of volume change versus the square root of time was utilized to estimate the completion of consolidation. The consolidation was completed after no substantial volumetric changes was observed and at least 95% of excess pore pressure was dissipated. Lastly, the specimen was then sheared using a constant displacement rate depending on whether undrained or drained testing was conducted.

To obtain the elastic anisotropic shear modulus, a bender element electrical system and bender element probe was used to determine the shear wave velocity. A wave generator (Agilent 33220A), a piezo amplifier (Model EPA-104, Piezo System Inc.), and an oscilloscope (Agilent DSO5014A) make up the electrical system for the bender element. Two bender element pieces that are inserted orthogonally into a plastic tube to form a T-shaped assembly make up the bender element probe (Ng et al. 2009). Measurement of v_{hh} is accomplished by producing and receiving horizontally propagating shear waves with horizontal polarization using the lower pair of bender components. The upper pair of bender elements produces and detects vertically polarized, horizontally propagating shear waves, and so measures v_{hv} . The elastic anisotropic shear moduli G_{hh} and G_{vh} can then be calculated from the shear wave velocity and soil density. Therefore, the stiffness anisotropy of the soil specimen at a particular stress state can be evaluated by G_{hh} / G_{hv} . Detailed description of the bender element probe were reported by Ng et al. (2004) and Ng et al. (2009).

In this bender element triaxial cell set-up, cell pressure and back pressure are controlled by water pressure from an automatic pressure/volume controller. The axial deformation is measured using an external LVDT. After the soil specimen is prepared and set up a rubber membrane was wrapped around the soil specimen. O-rings were used to seal the membrane with the cap and the pedestal. The bender elements were installed through the two slots, which were cut on mid-height of rubber membrane diametrically opposite and sealed with an O-ring. Finally, the triaxial cell was assembled. The specimen was saturated using a combination of CO₂ flushing for about 1 hour, water percolation for 24 hours and a minimum back pressure of 200 kPa, respectively, at an effective stress of 10 kPa. Following the saturation state, the desired isotropic effective consolidation stress was applied by increasing the cell pressure. During the consolidation stage, the axial deformation of the soil was monitored from the LVDT, whereas the water volume change of the soil was monitored from the automatic pressure/volume

controller. The soil was consolidated to various effective stress conditions (i.e., 20kPa, 50kPa, 100kPa, 200kPa and 300kPa). At the end of each consolidation stage, the bender element test was carried out to determine the shear wave velocity, hence estimating the elastic shear modulus and stiffness anisotropy of the soil specimen.

4.2 Complete set of cross-anisotropic stiffness parameters for effective and total stress analysis

4.2.1 Anisotropic elastic shear modulus during isotropic compression

Figure 4.1(a) represents the correlation between the measured $G_{0(hv)}$ and $G_{0(hh)}$ and effective mean stress, (p'). The results of CDT, which is also a weathered material and classified as silt, were tested by [Ng et al. \(2004\)](#) along the same stress path in the stress range of 100 to 400 kPa. Their results are also included for comparison. Moreover, the anisotropic elastic modulus $G_{0(ij)}$ of various sedimentary clays, coarse-grained soils and weathered soils under saturated conditions have been reported in the literature ([Gasparre et al. 2007b](#); [Jovičić and Coop 1998](#); [Lings et al. 2000a](#); [Ng et al. 2004](#); [Yimsiri and Soga 2011b](#)). For most soils, including compacted soils ([Heitor et al. 2013](#); [Leong et al. 2006](#)), the following semi-empirical equation proposed by [Hardin and Black \(1968\)](#) suitably describes the results. This equation is therefore used to analyse the results of lateritic soil and CDT:

$$G_{0(ij)} = AF(e)(p')^n \quad (4.5)$$

where $F(e)$ is a function of void ratio, p' represents the current effective mean stress, A and n are material parameters. The values of A and n are primarily used to describe the effects of the soil structure and stress on G_0 , respectively. For most fine-grained soils, these two parameters have been shown to correlate with the plasticity index (PI). With an increase in soil PI, the value of A generally decreases and n increases ([Atkinson 2000](#)), as shown in **Figure 4.1(b)** and **(c)**.

Equation (4.5) is used to fit the results of lateritic soil and CDT showed in **Figure 4.1**. The equation captures the experimental results, and two conclusions can be drawn about the values of A and n . Firstly, it would have been expected that CDT with a low PI of 14 would pose a higher coefficient A , and lower value of n , whereas the compacted lateritic clay has a lower coefficient A and higher value on n (see **Figure 4.1(b)** and **(c)**). Secondly, the A and n values of the lateritic soil cannot be well predicted from its PI value. Such a prediction would

underestimate the value of A by about 70% and overestimate the value of n by about one time. These observations suggest that when the soil is structured or has some degree of aggregation owing to the mineralogy or sesquioxides (cementation agents), the material parameters may not correlate well with PI.

To better understand the results in [Figure 4.1](#), the microstructure of the lateritic soil and CDT are determined and shown in [Figure 4.2](#). The lateritic specimen mainly consists of large aggregates or cladded particles (see [Figure 4.2\(a\)](#)), which could be attributed to the presence of minerals of iron and/or aluminium sesquioxides. Fine particles loosely adhere to the particle surface of the compacted lateritic soil. In contrast, the CDT shows smaller aggregated particles that are platy in shape with no obvious cladding [Figure 4.2\(b\)](#). The mineralogy and sesquioxides that enhance larger particle aggregations of the lateritic clay would influence its structure and stiffness, therefore, producing a larger value of A , compared to CDT. On the other hand, when the stress increases, the increase in the elastic shear modulus is higher for CDT than for the compacted lateritic soil with reference to the power function shown in [Figure 4.1](#). This may be explained by the existence of many smaller aggregated particles that are platy in shape in CDT, causing CDT to respond more like a fine-grained material. This analogy is supported by a previous study ([Cha et al. 2014](#)) since the increased rate of stiffness with effective stress is larger for fine-grained or clayey soils than for granular materials. It should be noted that the considerable aggregation (i.e. cladded particles) may not be the sole reason for the observed behaviour. The sand fraction of the tested lateritic clay is up to 42%. The tested clay may behave in a different way from clays with fewer sand particles due to a large amount of sand particles.

On the other hand, both soils show some degrees of stiffness anisotropy. The results in [Figure 4.1](#) shows that the compacted lateritic specimen is stiffer in the vertical direction than in the horizontal direction. This is likely because the specimens were prepared by heavy dynamic compaction, during which the vertical stress is likely higher than that in the horizontal direction. In addition, CDT shows a relatively higher stiffness in the horizontal direction than in the vertical direction, likely because the platy microstructure and geological formation process may have influenced CDT to be consistently stiffer in the horizontal plane than the vertical plane ([Ng et al. 2004](#)).

4.2.2 Consolidated-drained shear response

Figure 4.3(a) shows the stress-strain curve during the drained shear test at effective consolidation stress of 50 and 200 kPa. The specimens compacted with alignment surfaces oriented horizontally to the vertical shearing direction are designated with the prefix v, whereas the alignment surface oriented parallel to the shearing direction is designated with h. A strain-hardening behaviour is commonly observed for all the specimen orientations. For the shear test conducted with 50 kPa effective mean stress, both specimens v CD p50 and h CD p50 have similar shear strength. For 200 kPa effective mean stress, the specimen h CD p200 had a larger strength than v CD p200. The perceived variations in shear strength between h CD and v CD specimens may be attributed to different factors. Firstly, the initial fabric anisotropy may not be fully destroyed at the end of shearing (i.e., axial strain = 20%), inducing anisotropy of shear strengths. Furthermore, the shearing-induced volumetric response may also affect the strength anisotropy, as explained later.

Figure 4.3(b) shows the corresponding volume change behaviour. The horizontal cut specimens (i.e., h CD p50 and h CD p200) show a larger contractive volumetric strain than the vertical cut specimens (i.e., v CD p50 and v CD p200). This result is probable for the reason that more structure degradation occurs in horizontally cut specimens, as the shearing plane is parallel to the specimen bedding orientation. In addition, the larger contractive response of horizontally cut specimens may lead to higher density at large strains. The higher densification may result in larger strength, particularly at higher confining stress (i.e. 200 kPa in this study), as shown in **Figure 4.3(a)**.

Figure 4.3(b) also indicates that both vertically and horizontally cut specimens are more contractive at 50 kPa than at 200 kPa. This is different from the behaviour of most soils with a higher or similar contraction at a larger stress. This peculiar volumetric response of the lateritic clay could be clarified using the elastoplastic models for structured soils ([Liu and Carter 2002](#); [Zhou and Ng 2018](#)). In elastoplastic modelling, reconstituted specimens are mostly used as a reference and are regarded as non-structured soils. Compacted and intact specimens are regarded as structured soils, and they differ from reconstituted specimens. Some experimental studies have illustrated the different behaviour of intact, compacted and reconstituted specimens at micro and macro levels ([Ng et al. 2019a](#)). Thus, to regard the compacted lateritic clay as structured soil in this study is reasonable. When the structured lateritic clay is consolidated at a larger confining pressure (i.e., 200 kPa), it undergoes a partial structure degradation, so its volumetric contraction during the subsequent shearing is smaller.

Figure 4.4(a) represents the secant Young's modulus against axial strain from the drained shearing response in relation to **Figure 4.3(a)**. For an axial strain less than about 0.2%, the E_{sec} is consistently larger for the v 50 and v 200 specimens than the specimen h 50 and h 200. This trend is consistent with that in **Figure 4.1** and the stiffness anisotropy is mainly controlled by the initial structures of soil specimens. At axial strains beyond 0.2%, the E_{sec} of h CD p200 becomes a little higher than the E_{sec} of v CD p200. This is likely because, during the shearing process, the stiffness anisotropy is strain dependent. The initial soil structures evolve and play a minor role, while some other considerations such as soil density play a more crucial role. The horizontally cut specimens have more obvious densification during shearing (see **Figure 4.3(b)**), which may compensate for and even exceeds the influence of initial soil structures.

Figure 4.4(b) shows the evolution of anisotropy calculated from $E_{sec(h)}/E_{sec(v)}$ for both effective stresses of 50 and 200 kPa. Continuously, the anisotropy evolves but with a similar trend during the drained shearing process. However, the anisotropy is larger at higher effective stress of 200 kPa compared to 50 kPa. The theory developed by **Jardine (1992)**, which describes the pre-failure soil behaviour utilizing yield surfaces relating to elastic and non-linear zones is used to review the anisotropy during shearing. The elastic zone is bounded by the Y1 yield point, where the soil response is interpreted as linear elastic. Soil behaviour in the elastic zone may also be anisotropic. Beyond this point is another yield point Y2, where the response is non-linear but shows some fully recoverable behaviour. In **Figure 4.4(b)**, the linear elastic region may not be reliably estimated. However, **Ng et al. (2021)** reported that the elastic limit of this lateritic soil from a resonant column test is 0.003%. The degree of stiffness anisotropy decreases as the axial strain increases until about 0.03-0.04% axial strain. This point may be considered to be the Y2 yield point of the non-linear small strain region, being the boundary for the recoverable behaviour (**Jardine 1992**). With a further increase in axial strain beyond 0.04% axial strain, the degree of stiffness anisotropy begins to increase closer to the initial value of stiffness anisotropy.

Figure 4.5 shows the E_0 versus effective mean stress, where E_0 is the secant Young's modulus calculated at an axial strain of 0.003%. The data points for each orientation are limited. The fitted curves were obtained by using a similar power formulation utilized for the elastic shear modulus from **Figure 4.1**. The assumption is made to utilize the identical exponent of p' as the relationship from the G and p' based on an elastic theory similar to what was adopted by **Yimsiri and Soga (2011b)**. The lateritic soil is stiffer in the vertical plane than the

horizontal plane, consistent with the results in [Figure 4.1](#) and [Figure 4.4\(a\)](#). On the other hand, the results of CDT were estimated from the measured Poisson's ratio and shear modulus ([Ng et al. 2004](#)). Similar to the results in [Figure 4.1](#), the CDT is stiffer in the horizontal direction than in the vertical direction.

4.2.3 Consolidated-undrained shear behaviour

[Figure 4.6\(a\)](#) shows the stress-strain relations of the vertical cut specimens at effective consolidation stress of 50 and 200 kPa under undrained shearing. From the figure, it can be seen that a peak followed by strain softening behaviour for both effective confining stresses. [Figure 4.6\(b\)](#) represents the changes in the pore water pressure during the undrained shearing for both effective confining stresses. For 50 kPa effective confining stress, the figure shows a build-up of positive pore pressure to a maximum value which becomes steady till the end of the test. At 200 kPa, the positive pore pressure increases to a peak value and then a slight drop from the peak till the end of the test. [Figure 4.6\(c\)](#) shows the stress path during the undrained shearing in the $q - p'$ plane. The figure shows a reduction in p' initially implying a tendency of contraction followed by a phase transformation. This is often observed in dense granular soils but the lateritic clay shows this behaviour, likely because its behaviour is governed by larger particle aggregates ([Ng et al. 2019c](#)). Continuous shearing results in the p' increasing indicating a tendency of dilation, accompanied by an increase in q until the soil reaches the critical state condition.

From the stress-strain relations in [Figure 4.6\(a\)](#), the stiffness degradation curve is calculated and shown in [Figure 4.7](#) as secant Young's modulus against axial strain. The secant Young's modulus (E_{sec}) is calculated from the gradient of the deviatoric stress-shear strain curve as:

$$E_{\text{sec}} = \frac{\delta q}{\delta \varepsilon_a} \quad (4.6)$$

Over the strain range 0.003–1%, the E_{sec} of the saturated compacted lateritic soil investigated generally increases with an increase in effective confining stress.

4.2.4 Complete stiffness and strength parameters for effective and total stress analysis

Although some relevant studies have been reported for stiffness and strength parameters of lateritic soils, most of them do not provide a complete set of cross-anisotropic elastic stiffness and strength parameters. Moreover, results from other soils may not be applicable to

lateritic soils because of the influence of sesquioxides and aggregated structure in lateritic soils, for example, in relation to PI to the stiffness parameters of the soil.

Table 4.3 summarizes the complete set of stiffness parameters for both “effective” stress and “total” stress analysis. The lateritic clay has a different degree of anisotropy under drained “effective” and undrained “total” stress conditions. However, it should be noted that most of the effective stress parameters are measured values, whereas the total stress parameters are calculated or estimated based on theoretical relations. [Lings \(2001\)](#) demonstrated that the drained and undrained elastic stiffness parameters, and the ratios between them, may be different and must not be used interchangeably.

Regarding the critical state shear strength, a unified line in the $q - p'$ space for both drained and undrained shear tests is shown in **Figure 4.8**. The average stress ratio (M) of the critical state line is 1.30, corresponding to a critical state friction angle estimated to be 30° for the soil. Typical values of critical state friction angle reported in the literature in other tropically weathered soils are between 31° to 42° for some lateritic soils ([Ng et al. 2019c](#); [Toll 1990](#)) and about 35° for a CDT ([Zhou et al. 2015b](#)).

4.2.5 Discussion on the relationship between PI and stiffness degradation

With reference to estimating the stiffness of soils at small strains from 0.001% to 1%, different design charts have been proposed to illustrate the stiffness degradation with strain ([Hsu and Vucetic 2006](#); [Vardanega and Bolton 2013](#); [Vucetic 1994](#)). The graphs generally suggest that as soil PI increases, the shear modulus degradation rate becomes smaller (i.e., shifting to a higher strain value). The chart proposed by [Vardanega & Bolton \(2013\)](#) is shown in **Figure 4.9**. The results of the lateritic clay with a PI of 21 are also included for comparison. The threshold strain of the lateritic clay is approximately 0.004%. This value falls within the design chart curves of PI equals 15 and 30, indicating that its threshold strain is common. However, the stiffness degradation of the lateritic clay beyond the threshold strain is more significant and well below the expected range. The high degradation rate may be attributed to the aggregated microstructure of the lateritic clay, so the lateritic clay behaves like coarse-grained soil. The results imply that the PI alone may not be enough to characterise the stiffness of the lateritic clay, as shown in **Figure 4.1**.

[Ng et al. \(2017c\)](#) also observed the influence of soil aggregation on stiffness degradation. They performed experiment on an unsaturated loess at various suctions. With an increase of suction, the aggregate became more stable due to capillary effects. The evolving aggregated

microstructure due to suction-induced desiccation caused the fine-grained soil to behave like coarse-grained soil. As a consequence, the stiffness degradation curve became steeper.

4.3 Influence of compaction-induced fabric on the evolution of anisotropic moduli

4.3.1 Influence of compaction density on the stiffness evolution during compression

Figure 4.10 compares the relationship between shear modulus ($G_{0(hh)}$) and effective mean stress (p') for the saturated specimens prepared at 90% and 95% MDD with $w = 16.5\%$, 19.5% and 22.5% compaction water content.

For the compaction water content of 16.5% , **Figure 4.10(a)** shows that the $G_{0(hh)}$ of the specimen prepared at 90% MDD is lower compared to the specimen at 95% of MDD at p' of 20 kPa. With an increase in p' , the value of $G_{0(hh)}$ increases simultaneously for both specimens until 300 kPa, where the $G_{0(hh)}$ of the two specimens is nearly the same.

Figure 4.10(b) represents the evolution of the $G_{0(hh)}$ for the specimen with a compaction water content of 19.5% . The initial values of the $G_{0(hh)}$ for the two densities were similar. However, with an increase in p' , there was a relatively significant increase of the $G_{0(hh)}$ of the specimen at 95% MDD during compression from 20 kPa to 300 kPa. Compared to the specimen at 90% MDD, the $G_{0(hh)}$ of the specimen at 95% MDD is much greater than that of the up to the p' value of 300 kPa.

Figure 4.10(c) presents the results when the compaction water content is 22.5% . The value of $G_{0(hh)}$ of the specimen prepared at 95% MDD is slightly greater than the specimen at 90% MDD. The trend of the increment of $G_{0(hh)}$ for both specimens is similar during isotropic compression from 20 kPa to 100 kPa. Afterwards, there is a greater increase of $G_{0(hh)}$ value for the sample prepared at 95% MDD, than $G_{0(hh)}$ value of the specimen at 90% MDD up to p' of 300 kPa.

Comparison between **Figure 4.10(a)**, **(b)** and **(c)** shows that, overall, the value $G_{0(hh)}$ of the specimen at 95% MDD is greater than the specimen at 90% of MDD. However, the variation is significantly affected by the compaction water content.

4.3.2 Influence of compaction water content on the stiffness evolution during compression

Figure 4.11 shows the variation of $G_{0(hv)}$ and effective mean stress (p') for the specimens prepared at 90% MDD and 95% MDD with initial or compaction water content (w) of 16.5%, 19.5% and 22.5%, respectively.

With respect to w of 16.5%, **Figure 4.11(a)** shows that $G_{0(hv)}$ of the sample specimen at 95% MDD was greater than the specimen prepared at 90% MDD during compression from 20 to 200 kPa. However, the value of $G_{0(hv)}$ of the sample prepared at 90% MDD increased and became larger than the specimen at 95% of MDD during the compression from 200 to 300 kPa.

From **Figure 4.11(b)**, for w of 19.5%, the values of $G_{0(hv)}$ for the two specimens were identical in the initial compression at p' of 20 kPa. However, the tendency of the $G_{0(hv)}$ increment during compression from p' of 20 kPa to 300 kPa was different. It was observed that $G_{0(hv)}$ of the specimen at 90% MDD gradually increased, while the value of $G_{0(hv)}$ for the specimen at 95% MDD increased relatively larger during the compression from 20 to 300 kPa.

Figure 4.11(c) presents the evolution of $G_{0(hv)}$ for the specimen with compaction w of 22.5%. It can be seen that the value of $G_{0(hv)}$ for the specimen prepared at 95% MDD is greater than the specimen at 90% of MDD during the compression from p' of 20 to 300 kPa. The trend of the increment of $G_{0(hv)}$ for both specimens was similar. It reflected that overall, vertical stiffness for specimens prepared at 95% MDD is larger than that with 90% MDD in different initial fabrics.

4.3.3 Stiffness anisotropy of different compacted soil fabric

Figure 4.12(a) shows the evolving stiffness anisotropy of the specimen prepared at 90% MDD at different initial compaction water content. Regarding the trendline, the stiffness anisotropy of the specimen compacted at w 16% showed no obvious change in anisotropy during isotropic compression. On the other hand, the specimen compacted at w 19% showed a slightly decreasing anisotropy and 22% showed an increasing anisotropy with an increase in isotropic compression. For the specimen prepared at 95% MDD shown in **Figure 4.12(b)**, the specimens compacted at w 16% and w 19% showed no apparent evolution of stiffness anisotropy similar to the trend at 90% MDD. With an increase in w to 22%, there was an increase in stiffness anisotropy with increasing isotropic compression.

Comparison between **Figure 4.12(a)** and **Figure 4.12(b)** reveals that the stiffness anisotropy of samples with 90% MDD reflected a similar trend compared to that of samples with 95% MDD. In particular both specimens with w of 16% and 19% show relatively similar trends when compacted at either 90% or 95 % MDD. On the other hand, the specimen with w of 22% show an increasing trend of stiffness anisotropy for both 90% and 95% MDD. This implies that with compaction water content of 22%, the sample is more prone to particle or aggregate (i.e., cladded particles) rearrangement during increasing isotropic compression. This is because of larger aggregations or cladded particles that have the tendency to deform quickly during isotropic compression.

A summary of the fitting parameters using the semi-empirical proposed by **Hardin and Black (1968)** is shown in **Table 4.4**. The specimens compacted with 16% water content (i.e. dry side of optimum) has a lower degree of aggregation or cladding, resulting in a relatively smaller pore sizes (see **Figure 4.13(a)**). Under the same void density or initial void ratio, the specimens with compaction water content of 22% is expected have a higher degree of aggregation (cladding) or some massive matrix of aggregates that may also result in a relatively larger pore size at the macro level, as shown in **Figure 4.13(c)**. The specimen with compaction water content of 19% (i.e. optimum moisture content) comprises of aggregation that generally lie between what is possessed by the 16% and 22% water content (**Figure 4.13(b)**).

Smaller aggregation caused by cladding of particles is expected to have a lower influence of the parameter that is contributed by the structural effects, hence parameter A . On the other hand, it may produce larger value of n . Hence in general, The value of A is smaller for the specimens with 16% water content. On the hand, when the aggregate size increases due to higher compaction water content, the value of A may increase depending on the relative competing effects caused by the aggregate size, aggregate stiffness, as well as the interlocking of individual particles as shown in **Figure 4.13**. Therefore the value of A for specimens prepared at 19% and 22% becomes larger.

The different trends of stiffness anisotropy of the three samples for both densities may be attributed to different compaction-induced fabric and particle rearrangements in the vertical and horizontal direction that may have occurred during isotropic compression. Further analysis will require the study of the final microstructure through SEM or XCT to identify the evolved microstructure of the specimen at the final compression stage.

4.4 Summary

This chapter presents and interprets experimental results on the small strain stiffness characteristics of saturated and compacted lateritic clay specimens. Isotropic compression tests, drained and undrained shear tests were conducted to (i) determine the full set of stiffness parameters of cross-anisotropic specimens for both total and effective stress analyses; (ii) investigate the stiffness degradation and isotropy evolution during shearing. The evolution of stiffness anisotropy with strain during shearing is similar under drained and undrained conditions. The vertical cut specimens are consistently stiffer than the horizontal cut specimens at effective stresses of 50 and 200 kPa.

Moreover, the influence of different compacted soil structures due to water content and density on stiffness anisotropy was studied. With an increase in the compaction water content, the elastic stiffness anisotropy becomes larger.

Table 4.1 Testing programme for cross-anisotropic elastic parameters of a saturated lateritic clay

Test series	Specimen ID	Compaction method	Initial water content: %	Initial void ratio	Effective consolidation pressure: kPa	Remark
I	V-CU p50	Dynamic	19.5	0.65	50	Undrained test for small strain shear behaviour
	V-CU p200				200	
II	V-CD p50	Dynamic	19.5	0.65	50	Drained test for elastic and plastic anisotropy
	V-CD p200				200	
	H-CD p50	Dynamic horizontally cut	19.5	0.67	50	
	H-CD p200				200	
w19e0.65	Dynamic	19.5	0.65	20 to 300		

Table 4.2 Testing programme for compaction structure on anisotropic elastic stiffness of a saturated lateritic clay

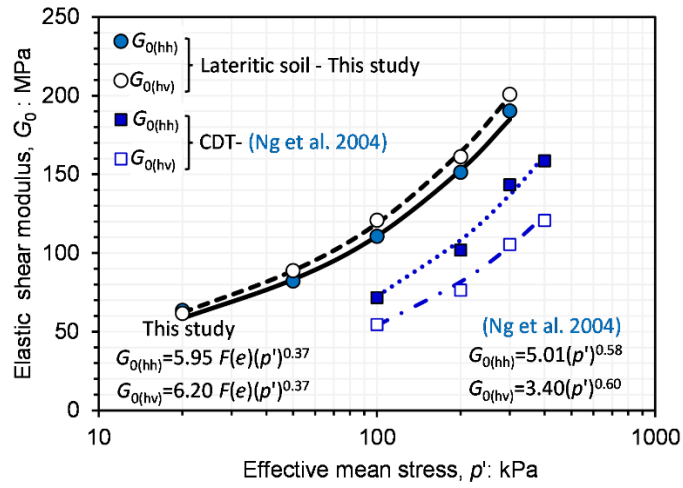
Test series	Specimen ID	Compaction method	Initial water content: %	Initial void ratio	Effective consolidation pressure: kPa	Remark
I	w16e0.65	Static	16.5	0.65	20 to 300	Influence of compaction water content and initial void ratio on elastic shear modulus
	w19e0.65		19.5			
	w22e0.65		22.5			
II	w16e0.74	Static	16.5	0.74	20 to 300	
	w19e0.74		19.5			
	w22e0.74		22.5			

Table 4.3 Cross-anisotropic elastic parameters

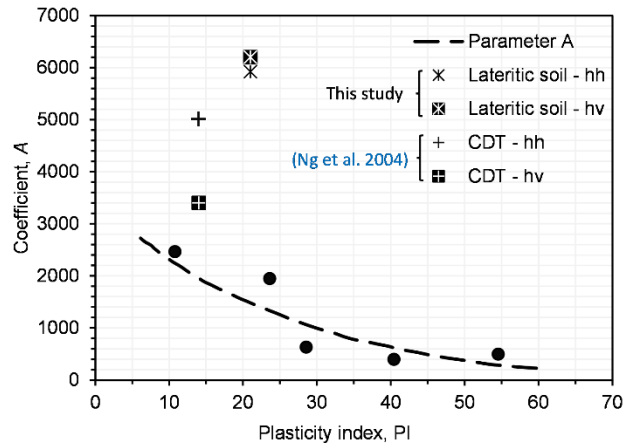
Elastic Parameters	This Study	CDT (Ng et al. 2004)
	Dynamic compacted	Natural
E'_v (MPa)	14.80 $F(e)(p')^{0.37}$	7.52 $(p')^{0.58}$
E'_h (MPa)	13.20 $F(e)(p')^{0.37}$	10.02 $(p')^{0.58}$
ν'_{vh}	0.16	0.3
ν'_{hv}	0.14	0.4
ν'_{hh} *	0.11	0.0
G_{hv} (MPa)	6.20 $F(e)(p')^{0.37}$	3.40 $(p')^{0.60}$
G_{hh} (MPa)	5.95 $F(e)(p')^{0.37}$	5.01 $(p')^{0.58}$
E_v^u (MPa)	16.99 $F(e)(p')^{0.37}$	-
E_h^u (MPa)	17.60 $F(e)(p')^{0.37}$	-
ν_{vh}^u	0.5	-
ν_{hv}^u	0.63	-
ν_{hh}^u	0.4	-

Table 4.4 Summary of fitting parameters on effects of compaction state on the anisotropic elastic stiffness

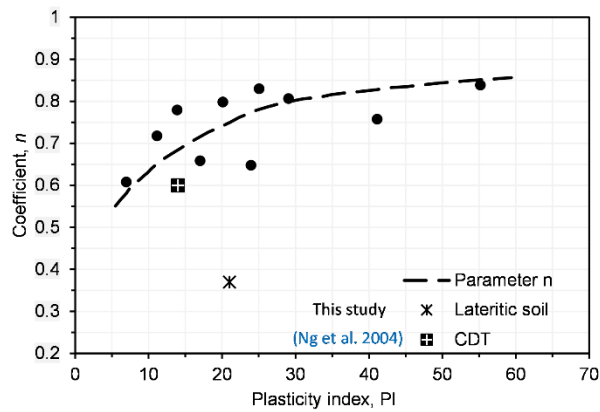
Elastic Shear Modulus, $G_{0(ij)}$	Dry density	Compaction water content		
		16	19	22
$G_{0(hh)}$ (MPa)	95 % MDD	5.38 F(e) $(p')^{0.496}$	5.97 F(e) $(p')^{0.481}$	4.06 F(e) $(p')^{0.615}$
$G_{0(hv)}$ (MPa)	95 % MDD	5.54 F(e) $(p')^{0.499}$	6.37 F(e) $(p')^{0.476}$	6.90 F(e) $(p')^{0.482}$
$G_{0(hh)}$ (MPa)	90 % MDD	2.83 F(e) $(p')^{0.61}$	8.82 F(e) $(p')^{0.381}$	6.86 F(e) $(p')^{0.485}$
$G_{0(hv)}$ (MPa)	90 % MDD	1.82 F(e) $(p')^{0.71}$	8.55 F(e) $(p')^{0.411}$	7.52 F(e) $(p')^{0.440}$



(a)

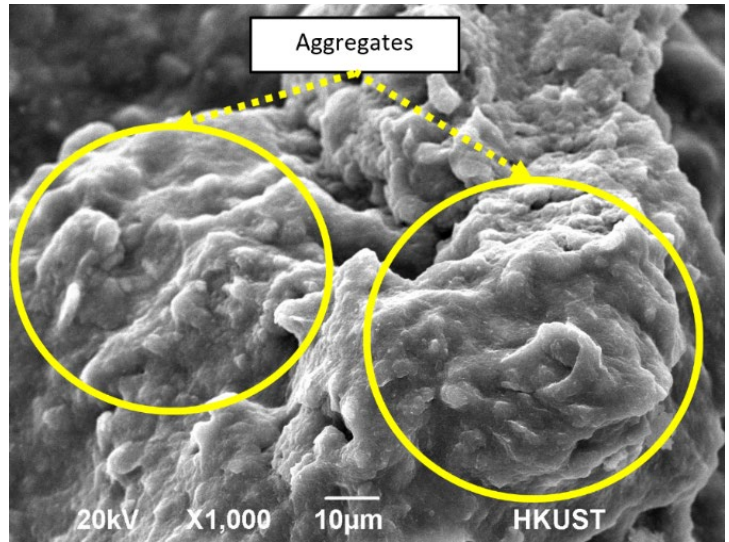


(b)

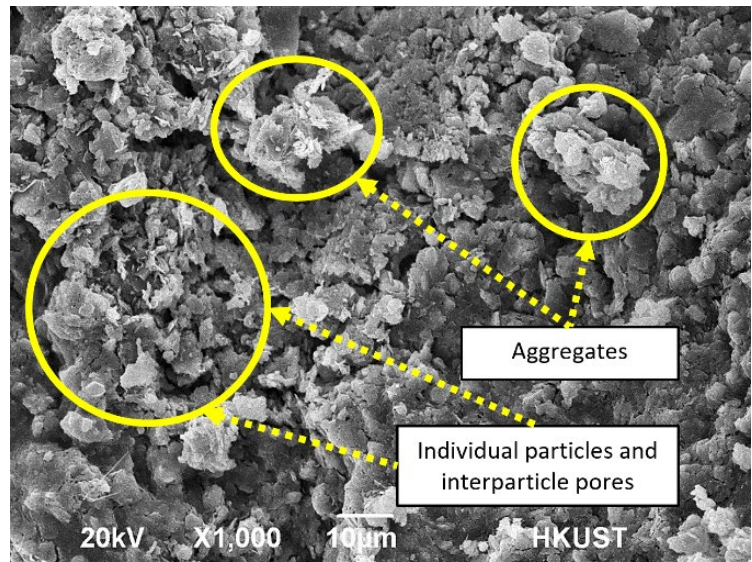


(c)

Figure 4.1 Relationship between (a) elastic shear modulus (G_0) and mean effective stress (b) Parameter A and (c) Parameter n for G_0 (Atkinson 2000)

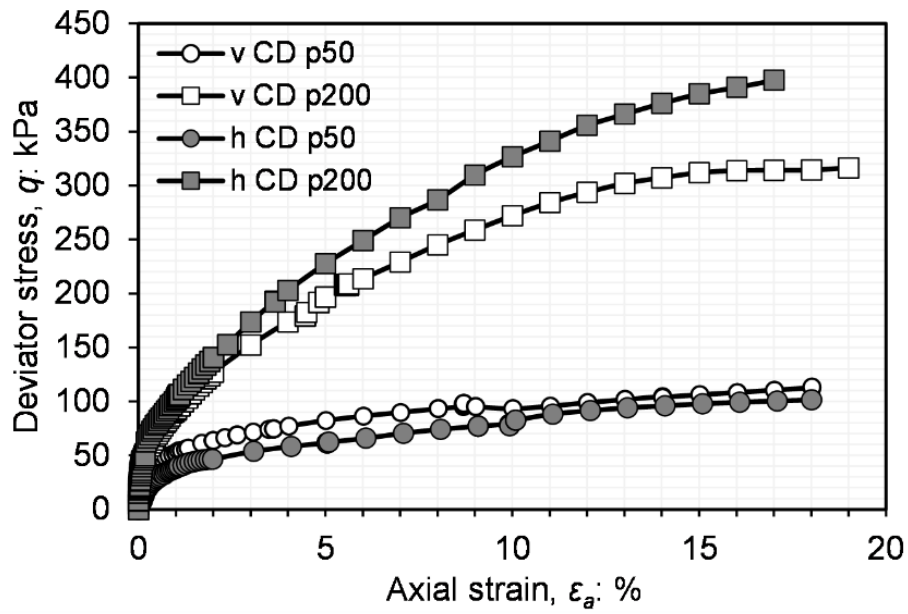


(a)

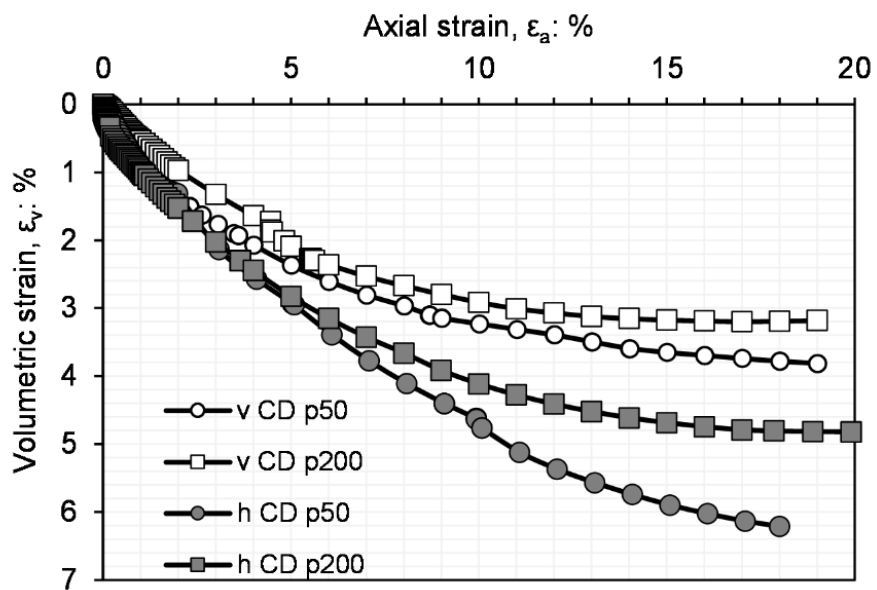


(b)

Figure 4.2 SEM image of (a) Lateritic soil (b) CDT

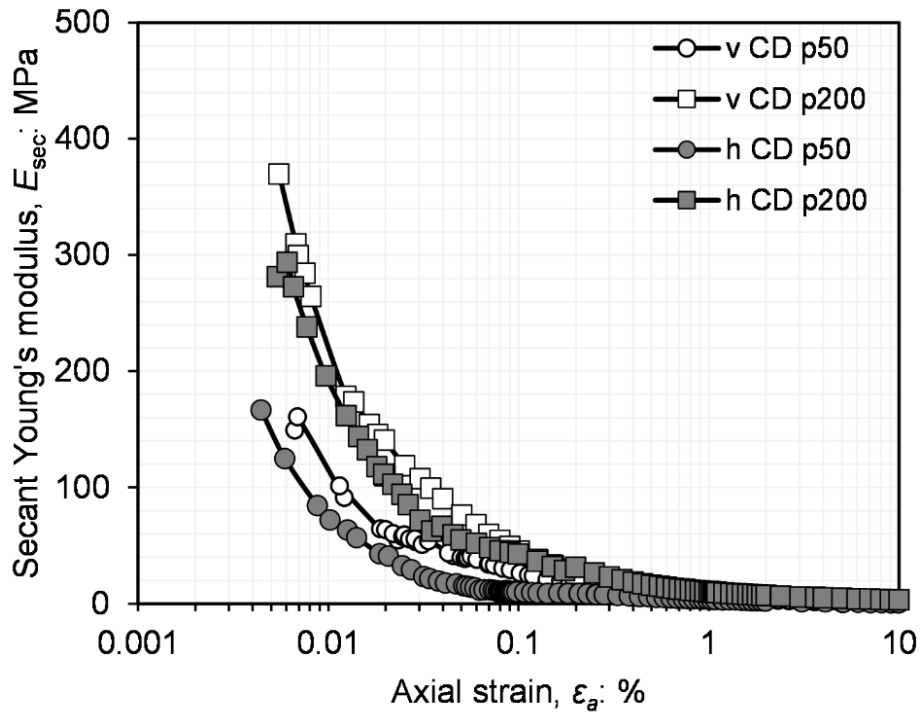


(a)

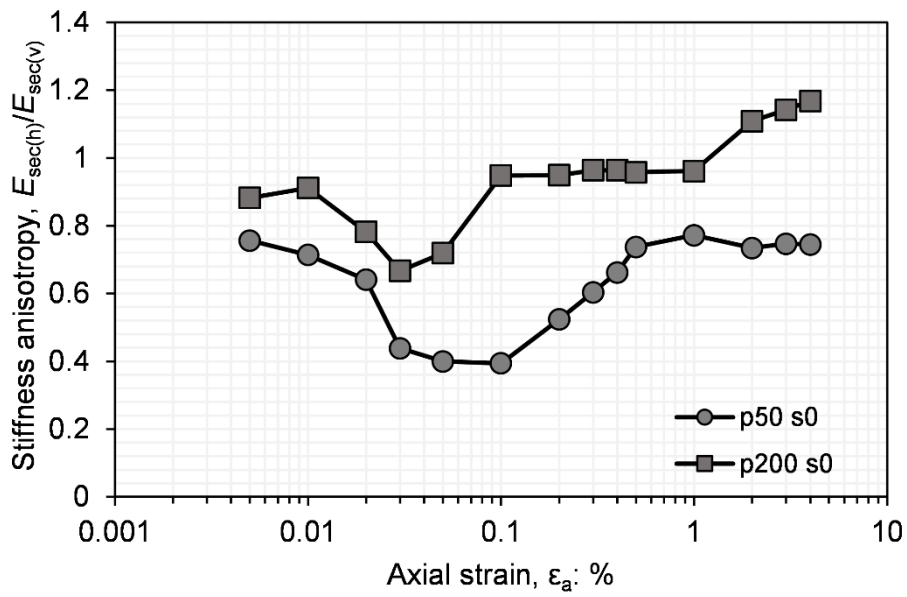


(b)

Figure 4.3 Shear behaviour from drained tests at effective confining stress of 50 and 200 kPa
(a) stress-strain and (b) volumetric response



(a)



(b)

Figure 4.4 Drained small strain stiffness behaviour (a) Stiffness degradation (b) Evolution of stiffness anisotropy

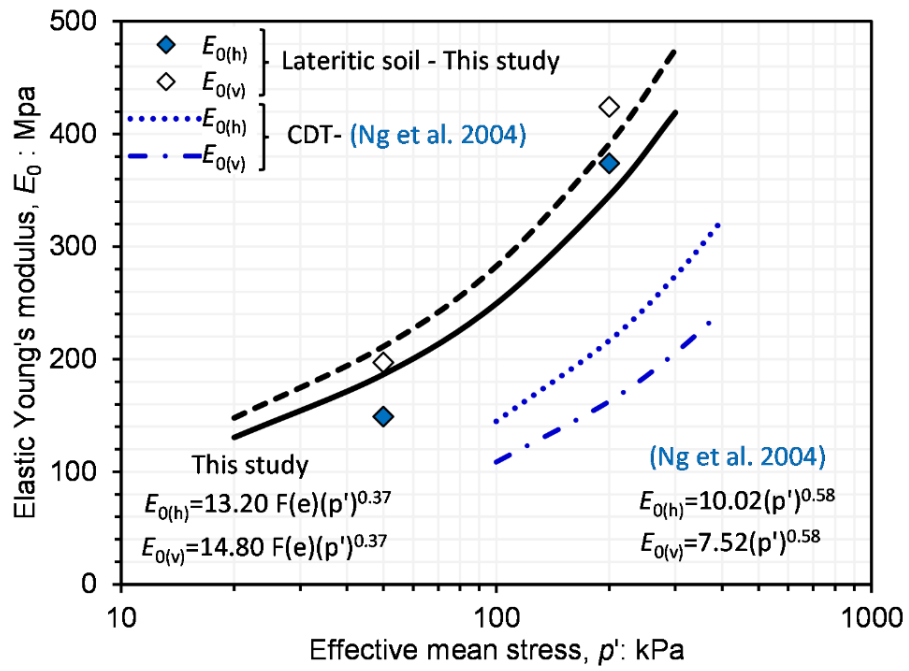
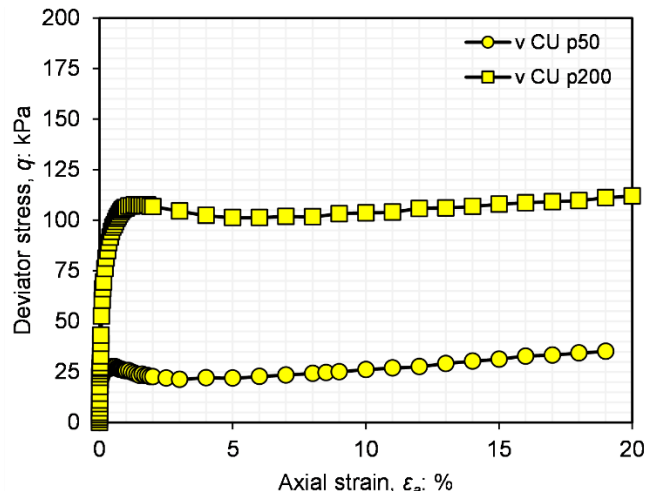
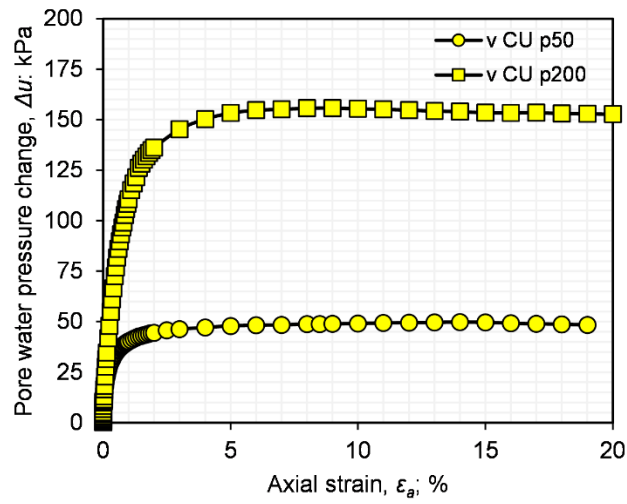


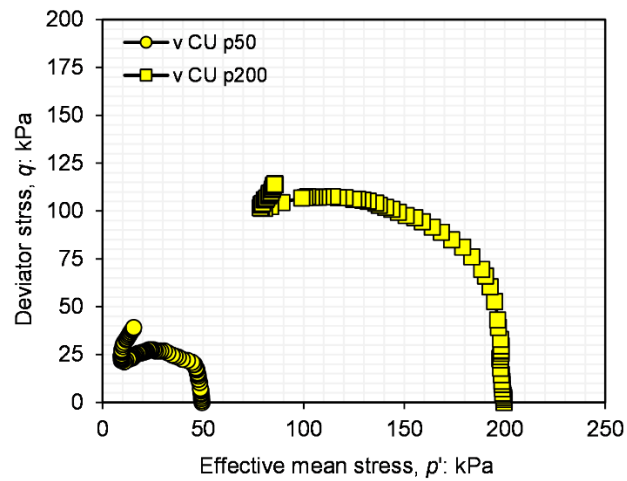
Figure 4.5 Relationship between small strain Young's modulus and mean effective stress



(a)



(b)



(c)

Figure 4.6 Shear behaviour from undrained tests at effective confining stress of 50 and 200 kPa (a) stress-strain and (b) pore pressure change (c) stress path

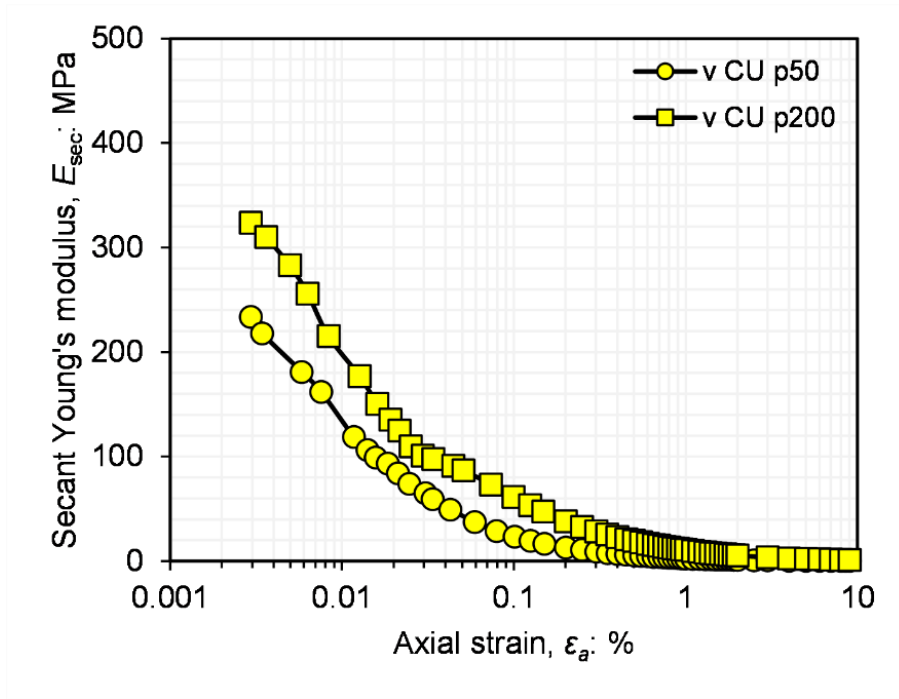


Figure 4.7 Small strain stiffness behaviour

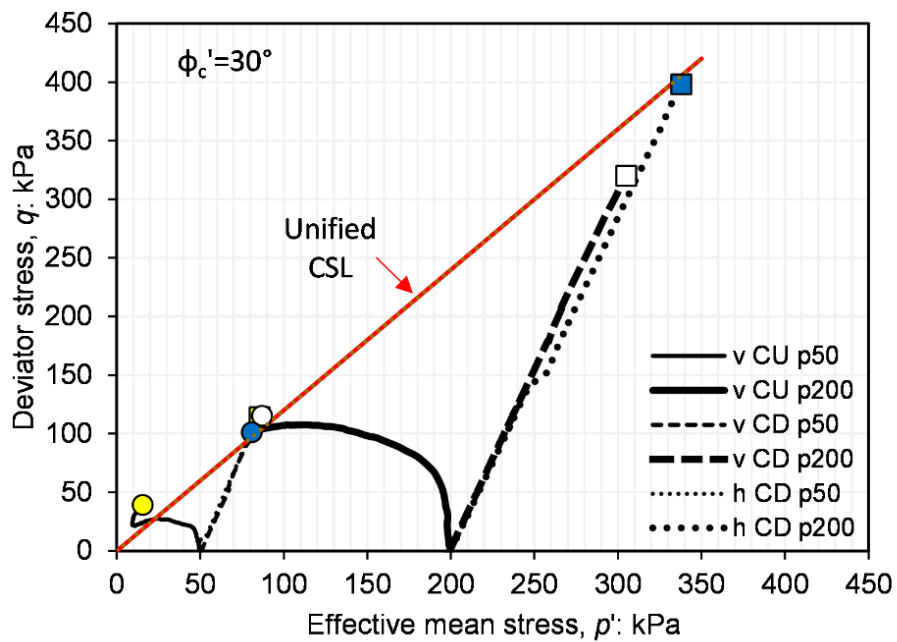


Figure 4.8 Unified critical state in $q - p'$ space

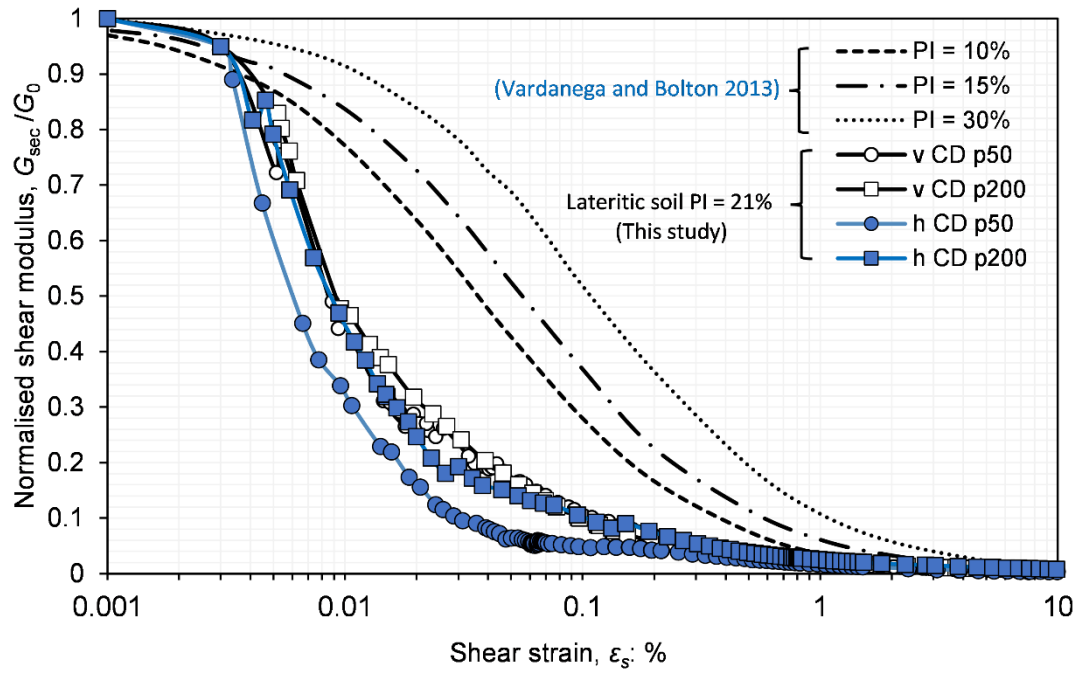
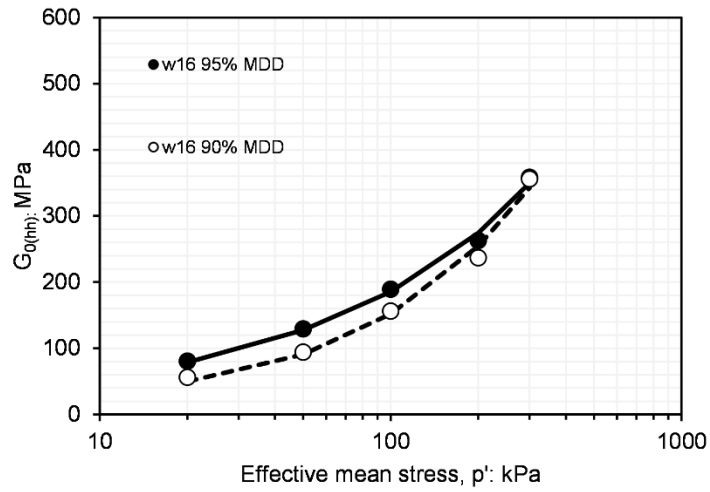
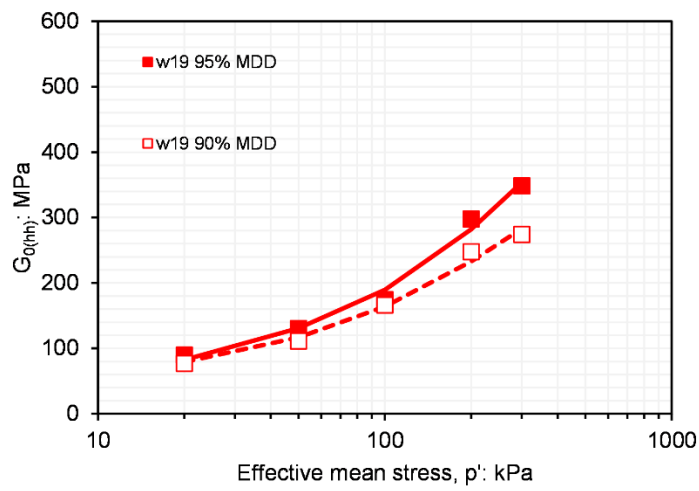


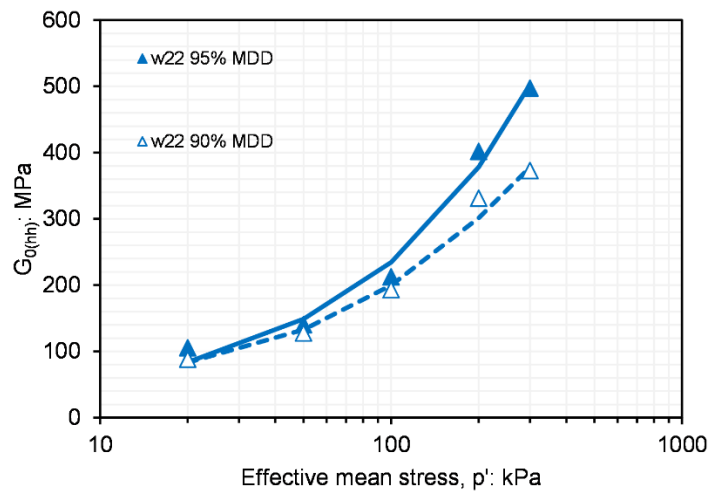
Figure 4.9 Summary of the relationship between PI and degradation with design curves by Vardanega and Bolton (2013)



(a)

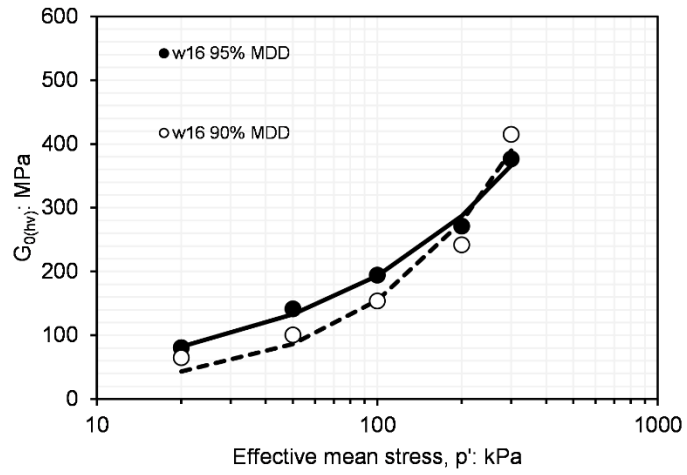


(b)

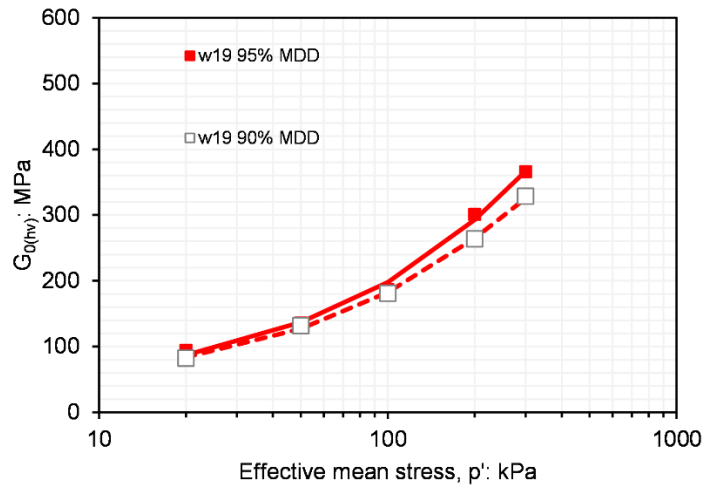


(c)

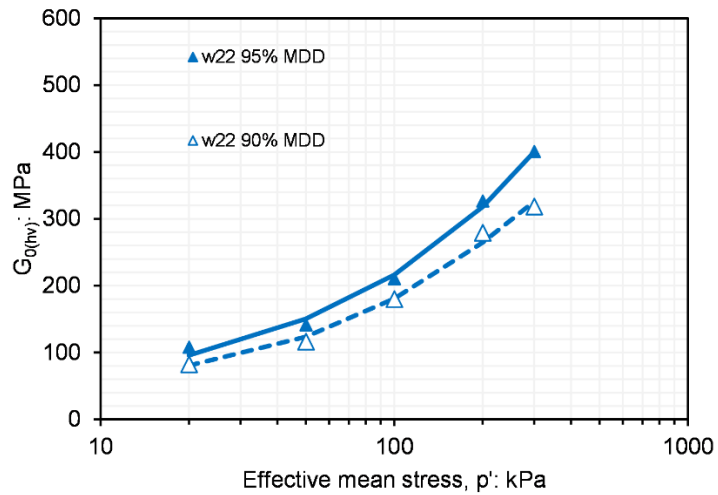
Figure 4.10 Variations of $G_{0(hh)}$ during isotropic compression for specimen with initial compaction water content of (a) 16.5%, (b) 19.5% and (c) 22.5%



(a)

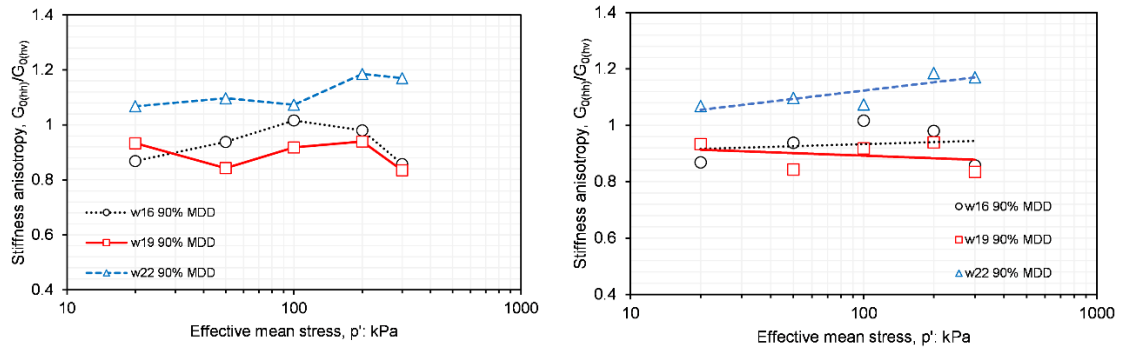


(b)

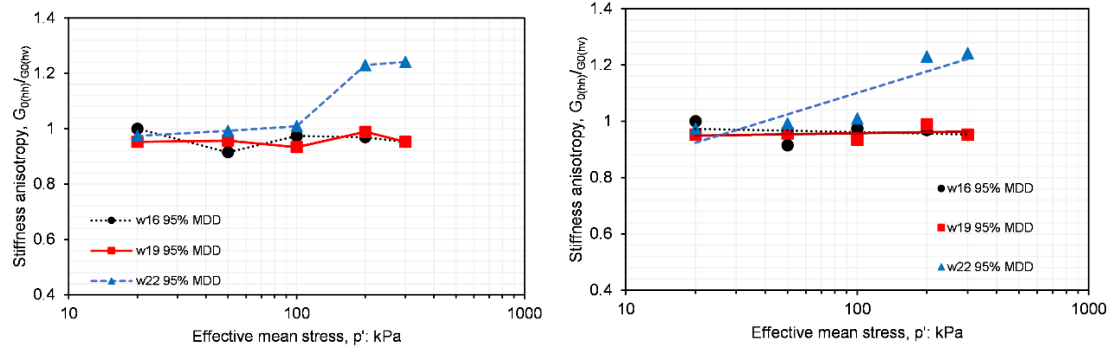


(c)

Figure 4.11 Variations of $G_{0(hv)}$ during isotropic compression for specimen with initial compaction water content of (a) 16.5%, (b) 19.5% and (c) 22.5%

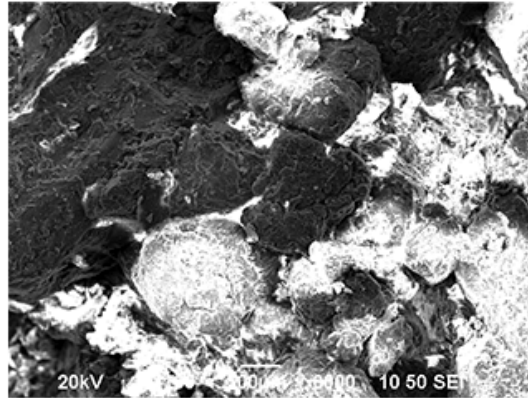


(a)

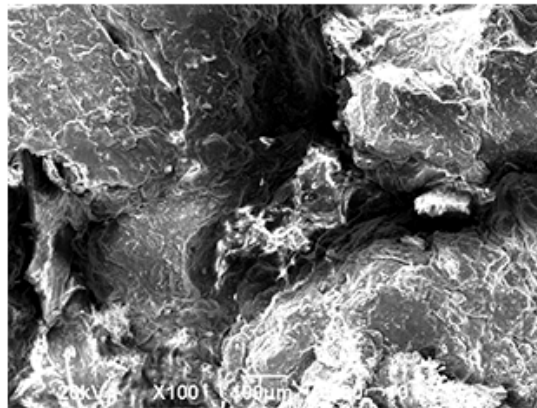


(b)

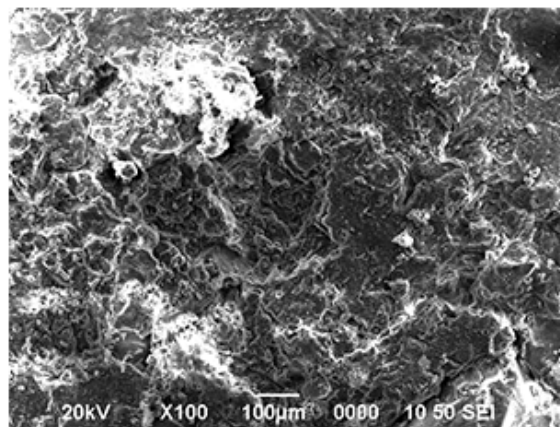
Figure 4.12 Anisotropic shear stiffness at different compaction water content (a) 90% and (b) 95% MDD



(a)



(b)



(c)

Figure 4.13 SEM of specimens at compaction water content of (a) 16% (b) 19 and 22%

CHAPTER 5 LOW SUCTION EFFECTS ON SOIL STIFFNESS UNDER MONOTONIC LOADING

This chapter presents an experimental study on the stiffness characteristics of unsaturated and compacted lateritic soil specimens. Monotonic triaxial tests were performed to study the coupled effects of suction, compaction-induced fabric and mean net stress on the small strain stiffness behaviour. The tests were conducted using a suction-controlled double-cell triaxial system (see [Plate 3.4](#)) in the low suction range (0-400 kPa in this study). All the specimens were prepared at an initial compaction water content of about 19.5% with a void ratio of about 0.65, corresponding to 95% maximum dry density of the standard proctor compaction.

5.1 Theoretical considerations of unsaturated soil stiffness

5.1.1 Soil stiffness at very small strains

It is well-recognised that the stiffness of unsaturated soils is influenced by many factors, including stress, suction and degree of saturation. Several semi-empirical equations have been proposed for the stiffness of unsaturated soils in the literature. Some researchers adopted net stress and suction as constitutive variables ([Alonso et al. 1990](#); [Ng and Yung 2008b](#)), while another group of researchers used the Bishop's effective stress ([Gallipoli et al. 2003](#); [Wheeler et al. 2003](#); [Zhou et al. 2015b](#)) that includes the degree of saturation or a parameter that is related to the degree of saturation as shown in the following equation. Such a formulation allows a smooth transition from unsaturated to saturated states when the degree of saturation is 100%.

$$p^* = (p^t - u_a) + S_r(u_a - u_w) \quad (5.1)$$

where p^* is mean Bishop's stress; p^t is mean total stress; u_a is pore air pressure; u_w is pore water pressure; S_r is the degree of saturation.

Apart from the use of Bishop's stress, which is usually used to describe the average skeleton stress acting on the particle contacts caused by changes in suction, there is an additional stabilisation effect due to the meniscus water ([Gallipoli et al. 2003](#); [Wheeler et al. 2003](#)). This second mechanism can be described by an additional parameter ([Gallipoli et al. 2003](#); [Zhou and Ng 2015b](#)):

$$\xi = f(s)(1 - S_r) \quad (5.2)$$

where ξ is a bonding variable; $f(s)$ is associated with the stabilisation between soil particles caused by the interparticle normal force due to meniscus water (Zhou et al. 2015b).

By using the above two variables and referring to **equation (4.5)**, the following equation is proposed to model the maximum Young's modulus (or elastic Young's modulus, Young's modulus at very small strains) of unsaturated soil:

$$E_0^i = A_0^i \frac{(2.973 - e)^2}{(1 + e)} \left(\frac{p^*}{p_r} \right)^{n_\sigma} (1 + \xi)^{n_s} \quad (5.3)$$

where E_0^i is Young's modulus in the direction i (vertical or horizontal); A_0^i , n_σ and n_s are soil parameters. This equation utilises the void ratio function proposed by Hardin and Black (1968). When the soil is fully saturated, the mean Bishop's stress becomes the mean effective stress and ξ also becomes zero. Such a formulation allows a smooth transition between unsaturated and saturated states. **Equation (5.3)** is similar to the shear modulus formulation proposed by Ng and Yung (2008a) but utilizes Bishop's stress and the bonding variable, as explained above. According to test data in the literature, the influence of Bishop's stress and suction on the shear and Young's moduli are similar (Heitor et al. 2015; Lee and Santamarina 2005; Lu 2018; Lu and Kaya 2014).

This study uses **equation (5.3)** to calculate the elastic Young's modulus of unsaturated lateritic soils and interpret the experimental results. The parameters A_0^i and n_σ can be calibrated at saturated states. The parameter n_s is associated with the pore characteristics and the water retention behaviour of unsaturated soil. For instance, suction effects are significant for clays with smaller pores, so the n_s value is expected to be higher. Suction effects of granular soils are minimal due to their larger pores, and the value of n_s is lower.

5.1.2 Stiffness degradation with strain

In the literature, various semi-empirical equations have been proposed to model the degradation of stiffness with strain (Oztoprak and Bolton 2013; Vardanega and Bolton 2013; Zhang et al. 2005). This study considers and employs the hyperbolic equation introduced by Vardanega and Bolton (2013) to calculate Young's modulus degradation curve at unsaturated conditions as follows:

$$\frac{E_{\text{sec}}^i}{E_0^i} = \begin{cases} 1 & \text{for } \varepsilon_a < \varepsilon_{a_e} \\ \frac{1}{1 + \left(\frac{\varepsilon_a - \varepsilon_{a_e}}{\varepsilon_{a_{\text{ref}}} - \varepsilon_{a_e}} \right)^a} & \text{for } \varepsilon_a > \varepsilon_{a_e} \end{cases} \quad (5.4)$$

where E_{sec}^i is the secant Young's modulus in the direction i ; E_0 is the elastic modulus, ε_a is the axial strain, $\varepsilon_{a_{\text{ref}}}$ is the reference strain; ε_{a_e} is the elastic threshold shear strain; a is a curvature parameter which controls the degradation rate of modulus with strain. The elastic threshold of a soil specimen might represent the state of the contacts between soil particles or aggregates which are still intact and have not begun to slide. Within the threshold strain, the shear modulus remains nearly constant and the soil behaves elastically (Simpson 1992). $\varepsilon_{s_{\text{ref}}}$ is a characteristic reference strain, defined as the shear strain at which the secant shear modulus is reduced $0.5E_0$.

Note that **Equation (5.4)** was originally proposed for shear modulus of saturated soils. It is reasonable to extend it to Young's modulus of unsaturated soils. According to previous studies, the a value is mainly affected by soil type, while the parameters ε_{a_e} and $\varepsilon_{a_{\text{ref}}}$ may depend on not only soil type but also soil states, such as the stress (Vardanega and Bolton 2013) and suction. Experimental evidence is needed for lateritic clay to study its stiffness degradation from small to large strains

Based on **equations (5.3)** and **(5.4)**, the secant Young's modulus E_{sec} of unsaturated soils at any strain can be calculated. A total of five parameters are required (A_0^i , n_σ , $\varepsilon_{a_{\text{se}}}$, $\varepsilon_{a_{\text{ref}}}$ and a). The validity of these two equations is verified experimentally in later sections. If these two equations work, how suction, anisotropy and stress affect the value of each parameter should be investigated based on test results.

5.2 Testing programmes and procedures for suction-controlled triaxial shear tests

5.2.3 Testing programme

Two series of triaxial tests were conducted on the compacted lateritic soil. The summaries of the testing programme and soil states are presented in [Table 5.1](#) and [Table 5.2](#). The first series of tests focused on constant suction-controlled triaxial shear tests on the vertically cut specimens. This test series considered two confining pressures (50 and 200 kPa) and three suction values (0, 10 and 150 kPa). Between 0.1 to 10 kPa suction, there is about a 6% reduction in the degree of saturation. The further reduction in the degree of saturation from 10 to 150 kPa suction is about 18%. Hence, the influence of these changes is investigated for stiffness and strength responses, respectively.

The second test series investigated the small strain stiffness and strength behaviour of horizontally cut specimens. Similar to the test programme in the first series, two mean net stresses of 50 and 200 kPa and two suction values of 0 and 150 kPa were considered. The coupled effects of suction and specimen orientation can be revealed by comparing the first and second series results.

5.2.4 Testing procedures

All the tests conducted at suction at 0 kPa are saturated tests which used a coarse porous stone at the top and bottom pedestal of the triaxial apparatus. The test involved three stages: saturation under effective mean stress of 10 kPa, isotropic compression to effective mean stress of 50 or 200 kPa and shearing under drained conditions. After setting up of specimen and assembly of the triaxial apparatus, saturation of the specimen was performed in three steps. CO₂ was flushed through the specimen for the first hour with an effective mean stress of 10 kPa in the first step. De-aired water was then percolated through the specimen from the bottom for roughly 24 hours after the CO₂ flushing. The final step involved applying a back pressure of 200 kPa while keeping an effective mean stress of 10 kPa. The [Skempton \(1954\)](#) B-value was examined during the back pressure saturation state. The specimen was deemed saturated when the B-value achieved a minimum value of 0.95. After reaching saturation, the specimen was compressed isotropically to the desired effective mean stress by raising the cell pressure. The automatic volume change indicator of the inner cell measured the specimen's volume change during the isotropic compression stage. The degree of consolidation was assessed using the plot of volume change vs square root of time. When there was no substantial volume change and at least 95% of the extra pore pressure dissipated, consolidation was deemed complete.

With a constant displacement rate of 0.005 mm/min, the specimen was sheared after consolidation.

The unsaturated testing also included three steps to adopt a similar stress path at suction values of 10 and 150 kPa: suction control under mean net stress of 20 kPa, constant-suction compression to mean net stress of 50 or 200 kPa, and finally drained and constant-suction shearing. **Figure 5.1** shows the stress path adopted for this study. After setting up the specimen and fixing all the instruments in the triaxial system for a complete assembly of the triaxial apparatus, a mean net stress of 20 kPa was applied while keeping the water drainage valve closed to keep the gravimetric water content constant. The second stage was suction equalization, with equalization criteria of daily gravimetric water content change of less than 0.05%. The suction equalization generally took between 7 to 14 days. Suction equalization was performed by applying cell pressure, pore air pressure and pore water pressure to attain desired values so that suction was 10 or 150 kPa while maintaining mean net stress at 20 kPa. After suction equalisation, the mean net stress was raised to a target value of 50 or 200 kPa. A 48-hour interval was allowed for the dissipation of excess pore water pressure. The last stage involved drained shearing at a rate of 0.005mm/min at constant suction and constant mean net stress, similar to the saturated test.

5.3 Interpretations of strength and dilatancy behaviour of unsaturated specimens

Figure 5.2(a) shows the stress-strain relation of the soil at suctions of 0, 10 and 150 kPa with mean net stress of 50 kPa. The soil shows a strain-hardening response at all suction values. As expected, an increase in suction results in larger deviator stress. With an increase in suction from 0 to 10 kPa, the critical state shear strength (determined at a strain around 20%) increases by approximately 35%. When the suction increases from 10 to 150 kPa, the critical state shear strength increases by only 58%. The incremental rate of shear strength, defined as the incremental strength divided by the incremental suction, is much smaller in the second suction range. Suction effects on the strength of unsaturated lateritic soil are highly non-linear. This non-linearity may be attributed to the SWRC, as shown in **Figure 3.4** or the measured degree of saturation shown in **Table 5.3**.

Based on the changes in the degree of saturation, when suction increase from 0 to 10 kPa, the rate at which the degree of saturation reduces is significant compared to when suction increase from 10 to 150 kPa, although the magnitude of suction increment is higher from 10 to

150 kPa. This finding implies that suction changes between 10 to 150 kPa may have a minor effect on the ultimate limit response of the unsaturated compacted lateritic soil within this suction range than the initial changes from 0 to 10 kPa. Moreover, the test soil clearly shows a dual-porosity structure. When suction increases in the second range, pore water within inter-aggregate pores and thus the effective degree of saturation reduce significantly, so the overall incremental rate of shear strength decreases.

Figure 5.2(b) shows the stress-strain response at mean net stress of 200 kPa for suctions of 0, 10 and 150 kPa. Similar to the results at 50 kPa mean net stress, the soil shows a strain-hardening response for the different suctions. Moreover, the critical state shear strength shows a non-linear increment with the increase of suction from 0, 10 to 150 kPa and the interpretation for 50 kPa mean net stress could be used to explain the results.

Figure 5.3(a), (b) and (c) shows the effects of mean net stress on the stress-strain relationship at various suction. As expected, an increase in mean net stress increases the strength of the soil. At an axial strain of about 19%, an increase of mean net stress from 50 to 200 kPa can increase the deviator stress by 175%, 185% and 93% at the suction of 0, 10 and 150 kPa, respectively.

The shear-induced volumetric response at mean net stress of 50 kPa is shown in **Figure 5.4(a)**. The specimen shows a contractive response for the three suctions of 0, 10 and 150 kPa, and the suction of 10 kPa showed the lowest contractive strain. **Figure 5.4(b)** shows the shear-induced volumetric response at various suctions for mean net stress of 200 kPa. The specimen shows a contractive response for all suctions considered. However, different from the results in **Figure 5.4(a)** for mean net stress of 50 kPa, the contractive strain is larger as the suction increases.

Note that the shearing-induced volume change of unsaturated soil is affected by various factors, including the suction-dependent preconsolidation pressure, Bishop's stress and density before shearing. Previous researchers reported that as suction increases, unsaturated soil becomes either more dilative (Ng and Menzies 2007a; Ng et al. 2020a) or more contractive (Uchaipichat and Khalili 2009a). In the current study, when the net mean stress is 50 kPa, the specimens at various suctions have similar void ratios (difference < 0.02). The volume change behaviour is therefore mainly related to the competing effects of suction-dependent preconsolidation pressure and Bishop's stress. At a suction of 10 kPa, unsaturation effects on the Bishop's stress are likely minor due to the low suction value, but the influence of the water

meniscus on preconsolidation could be significant, as supported by the S_r value in [Table 5.1](#). Hence, the ratio of preconsolidation pressure and Bishop's stress seems largest at 10 kPa suction.

The difference between the volumetric strain response for 50 and 200 kPa mean net stress, as shown in [Figure 5.4\(c\) and \(d\)](#), may also be explained by competing effects of suction hardening and densification. At the final state before shearing, suction effects may play a dominant role in the strength behaviour, whereas density effects may dominate the changes in volume change. The denser the soil, the less contractive its volumetric response will be. Hence, a monotonic trend regarding suction effects on the volumetric response may not be observed. As shown in [Table 5.1](#), the soil at 50 kPa mean net stress and 10 kPa suction has the lowest void ratio and is denser compared to 150 kPa and zero suctions, likely because of the stress path. Similarly, at 200 kPa mean net stress, the soil at zero suction has the lowest void ratio. Hence, the lower the void ratio, the lower the contractive strain during shearing. Moreover, when the lateritic clay is subjected to a higher compression of 200 kPa at 150 kPa suction, the forces at aggregated contacts become larger. During shearing under triaxial compression, crushing at sliding contacts or particle aggregation breakage may increase the volumetric contraction rate.

[Figure 5.5 \(a\), \(b\) and \(c\)](#) shows the effects of mean net stress on the shearing-induced volume change behaviour at various suctions. It can be seen from [Figure 5.5](#) that at zero suction, the soil is more contractive at lower mean net stress. On the other hand, as suction increases to 10 and 150 kPa, the soil becomes more contractive at higher suction. The larger contraction may be attributed to structural degradation and the collapse of inter-aggregation pores in the unsaturated state.

5.4 Small strain stiffness of unsaturated specimens

[Figure 5.6\(a\)](#) shows the secant Young's modulus (E_{sec}) against axial strain at mean net stress of 50 kPa, obtained from the stress-strain relations in [Figure 5.2\(a\)](#). As expected, the E_{sec} is consistently larger as suction increases. For a mean net stress of 50 kPa, when suction increases from 0 to 10 kPa, the E_{sec} at an axial strain of about 0.005% increases by about 100%. With an increase of suction from 10 kPa to 150 kPa, the E_{sec} increases by about 80%. Although the measured E_{sec} increases with increasing suction, the increment occurs at a reducing rate. In other words, the gradients of the relationship between E_{sec} and suction decrease with increasing

suction. Hence, the rate of change of E_{sec} from 0 to 10 kPa suction is significant, whereas the change rate of E_{sec} from 10 to 150 kPa suction is relatively smaller. It can be inferred that suction effects on the E_{sec} at a mean net stress of 50 kPa are highly non-linear.

Figure 5.6(b) shows the relationship between E_{sec} and axial strain at mean net stress of 200 kPa, obtained from the stress-strain relations in **Figure 5.2(b)**. At a given strain, the value of E_{sec} is consistently larger as suction increases. The rate of change at mean net stress of 200 kPa is similar to results at mean net stress of 50 kPa. Hence, the incremental rate of stiffness with suction decreases with increasing suction. Similar to the results at mean net stress of 50 kPa, the suction effect on E_{sec} at a mean net stress of 200 kPa is also non-linear. At mean net stress of 200 kPa, the overall increase of E_{sec} is about 140%, as the suction increases from 0 to 150 kPa. This incremental rate is smaller than that obtained in **Figure 5.6(a)**. The magnitude of the increase in stiffness depends on the mean net stress, and the influence of suction reduces as the mean net stress becomes larger. This result is because a change in matric suction does not have the same impact on stiffness at different stress conditions. The trend could be captured by **equation (5.3)**, which sums the stress and suction variables. Moreover, due to the non-linear influence of suction on soil behaviour, the interparticle contact stresses are dominated by the mean stress at high stress, and suction influence becomes minor.

Comparing the changes in strength and stiffness, as the suction increases from 10 to 150 kPa, E_{sec} increases more significantly than the strength. The influence of water meniscus in the unsaturated soil may explain the differences in terms of stiffness and strength increment as suction increases. The unsaturated soil's water meniscus is more stable at small strains. However, during shearing at large strains, the particles tend to roll and slide past each other there is breakage of the water meniscus ([Cho and Santamarina 2001](#); [Hamid and Miller 2009](#); [Romero et al. 2014](#)). Hence, the stabilization effects provided by the water meniscus become insignificant.

Figure 5.7(a), (b) and (c) shows the effects of mean net stress on the stress-strain relationship at various suction. As expected, the increase of mean net stress increases the E_{sec} . At an axial strain of about 0.005% in **Figure 5.7 (a)**, for the suction of 0 kPa, E_{sec} increases by about 110%. On the other hand, at a suction of 10 kPa, E_{sec} increases by about 50%, whereas at a suction of 150 kPa, E_{sec} increases by only 22%. As the suction value increases, the contribution of mean net stress to the measured E_{sec} reduces, particularly within the small strain

range. This trend is likely because the influence of net mean stress becomes less significant as suction increases, as reflected by the summation form of suction and stress in [equation \(5.3\)](#).

5.5 Anisotropic strength and dilatancy of unsaturated lateritic soil

[Figure 5.8\(a\)](#) depicts the stress-strain curves comparing the different specimen orientations and suction effects at mean net stress of 50 kPa. Prefix v is used to denote specimens that were cut vertically, whereas the prefix h is used to designate specimens that were cut horizontally, as shown in [Figure 3.3](#). A strain hardening behaviour is observed irrespective of the specimen orientation and suction. For the suction of 0 kPa, the specimen v p50 s0 has a similar strength to h p50 s0. At a suction of 150 kPa, the specimen h p50 s150 had a slightly larger strength than v p50 s150, partially attributed to the void ratio of the soil before shearing, as shown in [Table 5.3](#). The h p50 s150 specimen had a slightly lower void ratio and hence denser than the v p50 s150 specimen.

Compared to the vertical cut specimen, whose strength increases by about 115%, the critical state shear strength for the horizontal cut specimen increases by approximately 185% when the suction is increased from 0 to 150 kPa, with a mean net stress of 50 kPa. This implies that suction effects are more significant on the strength of the horizontal cut specimen than the vertical cut specimen. The observed differences in shear strength between horizontally and vertically cut specimens may be attributed to slightly larger changes in the void ratio or density of the horizontal cut specimen when subjected to suction and compression before shearing. Moreover, the variable anisotropic fabric of the vertical and horizontal cut specimen may affect the water distribution in the soil specimen.

[Figure 5.8\(b\)](#) shows the stress-strain curves comparing the different specimen orientations and suction effects at mean net stress of 200 kPa. Similar to 50 kPa, a strain hardening behaviour is observed irrespective of the specimen orientation and suction. For the suction of 0 kPa, the specimen v p200 s0 has a lower strength than h p200 s0. At a suction of 150 kPa, the specimen h p200 s150 had a lower strength than v p200 s150, partially attributed to a higher degree of saturation of h p200 s150. The v p200 s150 specimen had a slightly lower degree of saturation, hence more meniscus water than the h p200 s150 specimen. Compared to the vertical cut specimen, whose critical state strength increases by about 46%, the critical state shear strength for the horizontal cut specimen increases by approximately 10% when the suction is increased from 0 to 150 kPa for 200 kPa mean net stress. This implies that suction

effects are more significant on the vertical cut sample than the horizontal cut specimen. The observed differences in shear strength between horizontally and vertically cut specimens may be attributed to slightly larger differences in the degree of saturation of the vertical cut specimen when subjected to suction and compression before shearing. The larger the change in the degree of saturation of the vertical cut specimen resulted in more meniscus water bridges between aggregate contacts. Hence, as expected, there is a larger strength increment.

The corresponding shear-induced volumetric behaviour at a mean net stress of 50 kPa is shown in [Figure 5.8\(c\)](#). A contractive behaviour is observed during the shearing process. Both horizontally and vertically cut specimens are more contractive at a suction of 0 kPa than 150 kPa. The difference between the volumetric response induced by specimen orientation is significant at saturated condition 0 kPa compared to 150 kPa. Considering the specimen orientation effects at a particular suction, the soil is significantly more contractive for the horizontal cut specimen at 0 kPa suction with a mean net stress of 50 kPa. [Figure 5.8\(d\)](#) shows the shear-induced volumetric behaviour at a mean net stress of 200 kPa. Contractive behaviour is also generally observed during the shearing process. Both horizontally and vertically cut specimens at 200 kPa mean net stress are more contractive at a suction of 0 kPa than 150 kPa. The difference between the volumetric response is more significantly induced by specimen orientations at saturated condition 0 kPa, compared to 150 kPa. Considering the specimen orientation effects at a particular suction, the soil is more contractive for the horizontal cut specimen at both suctions at mean net stress of 200 kPa.

5.6 Anisotropic small strain stiffness during drained shearing

[Figure 5.9\(a\)](#) represents the coupled influence of specimen orientation and suction effects on the small strain stiffness at mean net stress of 50 kPa. The soil is generally stiffer for vertical cut specimens than the horizontal cut specimen. This result may be explained using the soil's microstructural characteristics, its force chain in soil structure and degree of saturation. Because of the large size aggregated microstructure of the lateritic soil ([Ng et al. 2021](#)), the force chain of particle arrangement and orientation may be much stronger in the vertical than the horizontal directions. Further work is required to characterise and quantify the particle orientation to discuss and verify the above postulation. [Figure 5.9\(b\)](#) represents the coupled influence of specimen orientation and suction effects on the small strain stiffness at mean net stress of 200 kPa. Similar to the mean net stress of 50 kPa, the soil is generally stiffer for the vertical cut specimen than the horizontal cut specimen. A similar explanation may be applied

here. Owing to the larger size aggregated structure, the force chain of particle arrangement and orientation may be much stronger in the vertical direction than in the horizontal direction. However, as mentioned previously, future research is needed to characterise and quantify the particle orientation to discuss and verify the above postulation.

There is a consistent trend of stiffness being higher for the vertical cut specimen than the horizontal cut specimen for both mean net stress and suction values in **Figure 5.9(a)** and **(b)**. However, at 50 kPa mean net stress, for the vertical cut sample, an increase in suction from 0 to 150 kPa results in a percentage increment of about 260% stiffness at 0.004 - 0.007% strain. For the horizontal cut specimen, with the same suction increase, the resultant percentage increment of stiffness is about 196%. On the other hand, for the 200 kPa mean net stress, the vertical cut specimen increases in stiffness by about 140% when suction increases from 0 to 150 kPa. With respect to the horizontal cut specimen at mean net stress of 200 kPa, an increase of suction from 0 to 150 kPa results in about a 75% increase of stiffness at 0.005% axial strain. These results imply that the mean net stress reduces the effects of suction for both the horizontal and vertical cut specimens, and this reduction effect is more significant in the horizontal cut specimen.

To further analyse the evolution of stiffness anisotropy during shearing, **Figure 5.10** shows the relationship between axial strain and $E_{\text{sec}(h)}/E_{\text{sec}(v)}$ for both suctions of 0 and 150 kPa, at mean net stress of 50 and 200 kPa. It can be seen that suction influences the anisotropy evolution during shearing. In other words, different suction values show different evolution patterns. For the initial anisotropy at a small strain up to about 0.2%, the stiffness for the vertical cut specimen is consistently larger than the horizontal cut specimen. Hence, the measured anisotropy is generally lower than 1. When suction increases from 0 to 150 kPa, within this strain range (up to about 0.2%), the stiffness anisotropy tends to decrease with increasing suction. This implies that the stiffening effects of suction are more significant for vertical cut specimens than the horizontal cut specimen.

When suction is zero kPa, the stiffness anisotropy first decreases until the axial strain is between 0.03 and 0.04%. Beyond an axial strain of 0.1%, the stiffness anisotropy increases until it approaches a constant value at an axial strain of about 0.5%. On the other hand, at 150 kPa suction, there is no initial decline of stiffness anisotropy. However, starting at an axial strain of 0.01%, the degree of stiffness anisotropy increases until it achieves a nearly constant value at 0.2% axial strain and above. In general, as the strain increases beyond 0.2%, the

measured stiffness anisotropy tends to increase irrespective of the suction value, implying that the magnitude of stiffness increase for the horizontal cut is higher than the vertical cut with increasing strain. These trends are similar for both mean net stress of 50 and 200 kPa

5.7 Verification of small strain stiffness and stiffness degradation with strain

To evaluate the capability of [Equation \(5.3\)](#), the measured and calculated E_0 results of the lateritic clay are shown in [Figure 5.11](#). The E_0 values in the vertical and horizontal directions increase with increasing suction at a given mean net stress. The measured and estimated E_0 are generally consistent, despite some variations. The parameters are summarised in [Table 5.3](#), and a constant n_s value of 0.35 is used in all cases. It should be highlighted that the vertical and horizontal specimens have different n_s values because suction and anisotropy effects are coupled, as discussed above.

[Figure 5.12](#) plots the stiffness degradation curves of saturated and unsaturated lateritic clay specimens. The calculated degradation curve using [Equation \(5.4\)](#) is also included for comparison. It should be noted that ε_{a_e} is assumed to be 0.003%, and the reference strain is calibrated to be about 0.01%. The assumptions are based on the fact that for the lateritic clay, the degradation E_{sec}/E_0 with strain does not change significantly with suction, stress and anisotropy. The predictions and experimental findings are generally consistent.

The results are also compared to the design chart of [Vardanega and Bolton \(2013\)](#). The chart was originally proposed for the relationship between normalised shear modulus and shear strain for saturated soils. It is slightly modified here to show the normalised Young's modulus against axial strain, based on the assumption that the influence of PI on the shear and Young's moduli degradation is similar. Furthermore, although the chart was originally for saturated soils, it has been used in the literature to study suction effects on the stiffness degradation of unsaturated soils ([Ng et al. 2021](#); [Ng et al. 2017c](#)). [Figure 5.12](#) reveals that the stiffness degradation rate of saturated lateritic clay is significant and notably below the expected range of PI. The aggregated microstructure of lateritic clay could explain this behaviour. The test soil with significant aggregation behaves like coarse-grained materials, even though it is classified as clay with a low PI. It should be pointed out that the significant aggregate might not be the sole contributing factor. A considerable fraction of sand particles are also present in the tested clay, and it may respond differently from other clays with fewer sand particles.

5.8 Summary

This chapter reports the small to large strain response of an unsaturated compacted lateritic clay, considering compaction-induced anisotropic stiffness and strength. The results of the isotropic compression and constant-suction shearing test reveal that the lateritic clay exhibits anisotropy in unsaturated compacted specimens. At very small strains below 0.001%, the shear modulus in the vertical direction is greater than that in the horizontal direction for both saturated and unsaturated states. Anisotropy evolves with increasing strain during the subsequent shearing.

As expected, between a strain range of 0.001% to 1%, the secant Young's modulus (E_{sec}) is larger at higher suction. Considering a mean net stress of 50 kPa, as the suction increases from 0 to 10 kPa, the rate of increment E_{sec} of compacted lateritic soil increase significantly. However, the incremental rate of E_{sec} reduces when suction further increases from 10 kPa to 150 kPa. Similarly, at a mean net stress of 200 kPa, the incremental rate of stiffness with suction decreases with increasing suction. The non-linear response of the increment in stiffness and suction at different mean net stress occurs because of the combined effects of particle aggregation and water retention behaviour. In general, this lateritic soil can form large particle aggregates that may be difficult to desaturate since the intra-aggregate pores hold some significant amount of water.

A semi-empirical equation is proposed for E_0 based on the experimental results, which incorporated the coupled effects of suction and anisotropy. The measured and calculated results are generally consistent.

Table 5.1 Test programme for investigating suction effects on stiffness characteristics

Specimen ID	Mean net stress, p : kPa	Suction, s : kPa	As-compacted void ratio, e	Void ratio before shearing, e	Degree of saturation after suction equalisation, S_r	Bishop's stress, p^* : kPa	Bonding variable, ξ
v p50 s0	50	0	0.65	0.64	1	50	0
v p200 s0	200		0.65	0.55	1	200	0
v p50 s10	50	10	0.65	0.62	0.82	58	0.19
v p200 s10	200		0.65	0.57	0.79	208	0.22
v p50 s150	50	150	0.65	0.63	0.70	155	0.35
v p200 s150	200		0.65	0.62	0.68	302	0.37

Table 5.2 Test programme for investigating the coupled influence of anisotropy and suction.

Specimen ID	Mean net stress, p: kPa	Suction, s: kPa	As-compacted void ratio, e	Void ratio before shearing, e	Degree of saturation after suction equalisation, S_r	Bishop's stress, p^* : kPa	Bonding variable, ξ
v p50 s0	50	0	0.65	0.64	1	50	0
h p50 s0	50		0.67	0.64	1	50	0
v p50 s150	50	150	0.65	0.63	0.70	155	0.34
h p50 s150	50		0.66	0.62	0.75	163	0.29
v p200 s0	200	0	0.65	0.55	1	200	0
h p200 s0	200		0.67	0.57	1	200	0
v p200 s150	200	150	0.65	0.62	0.68	302	0.37
h p200 s150	200		0.68	0.58	0.70	305	0.35

Table 5.3 Summary of measured and calculated parameters

Specimen ID	Mean net stress, p: kPa	Suction, s: kPa	Void ratio, e	Degree of saturation, S_r	Calculated elastic Young's modulus, E_0 : MPa	A_0^i	n_σ	n_s	ξ	a
v p50 s0	50	0	0.64	1	287	22	0.35	2.8	0	0.95
v p200 s0	200		0.55	1	532	22	0.35	2.8	0	0.95
v p50 s150	50	150	0.63	0.69	994	22	0.35	2.8	0.35	0.95
v p200 s150	200		0.62	0.64	1335	22	0.35	2.8	0.37	0.95
h p50 s0	50	0	0.64	1	235	18	0.35	2.4	0	0.95
h p200 s0	200		0.62	1	671	18	0.35	2.4	0	0.95
h p50 s150	50	150	0.62	0.75	423	18	0.35	2.4	0.29	0.95
h p200 s150	200		0.58	0.70	929	18	0.35	2.4	0.35	0.95

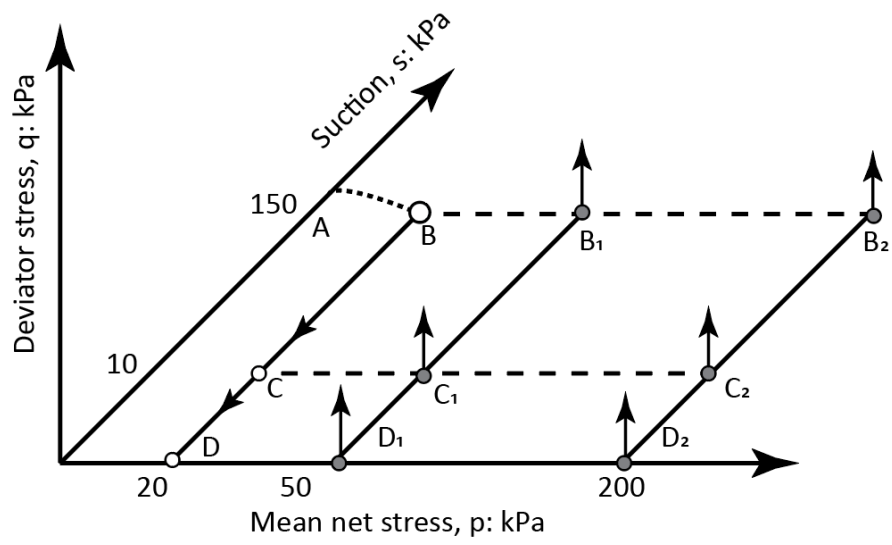
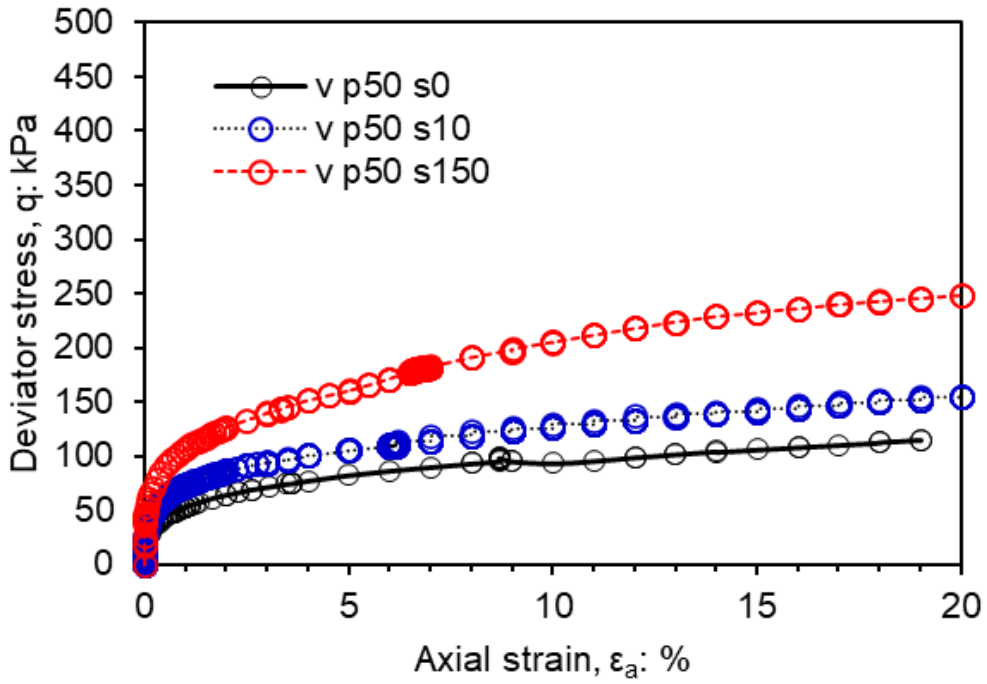
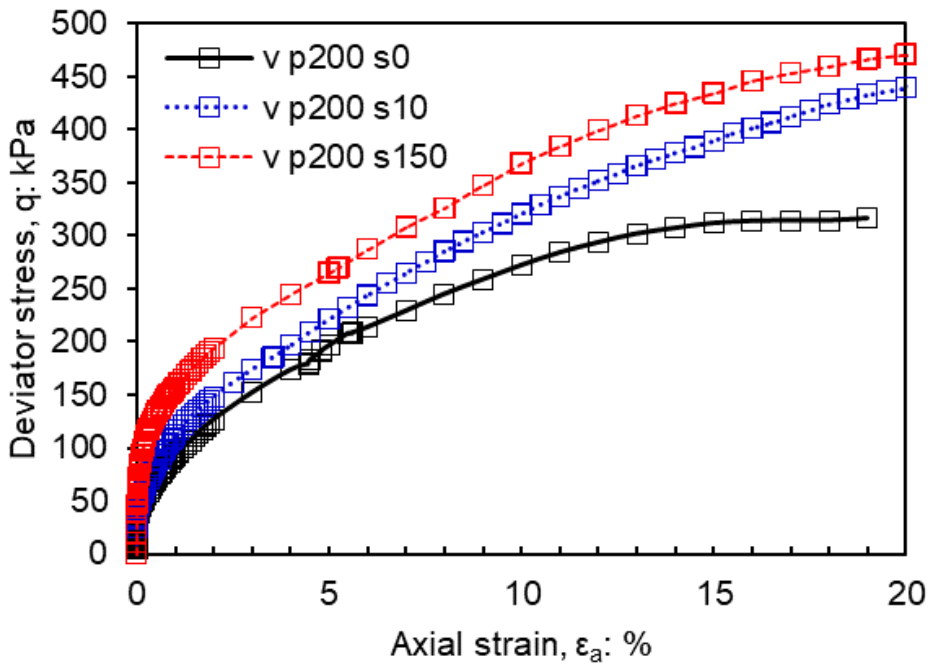


Figure 5.1 Stress path for suction effects on small to large strain behaviour of soil under monotonic loading

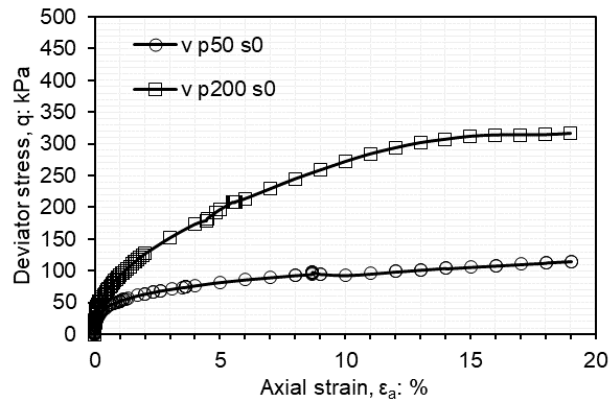


(a)

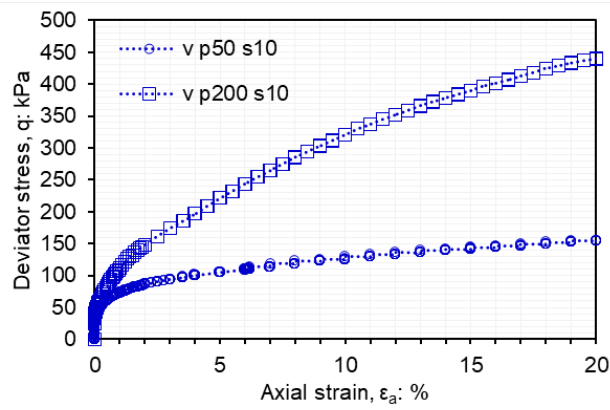


(b)

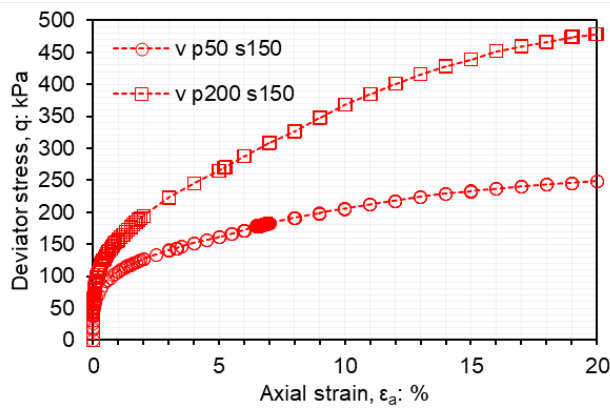
Figure 5.2 Stress-strain behaviour of unsaturated compacted lateritic soil at (a) 50 and (b) 200 kPa mean net stress



(a)

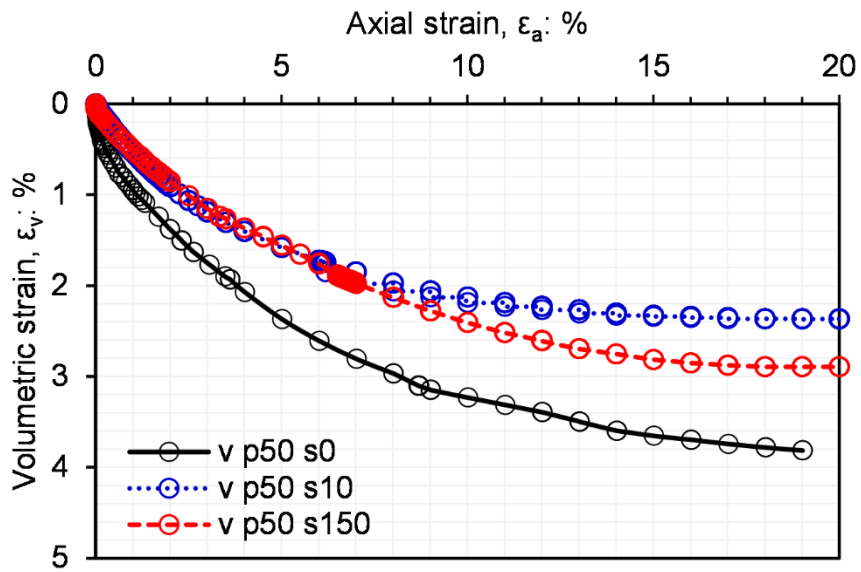


(b)

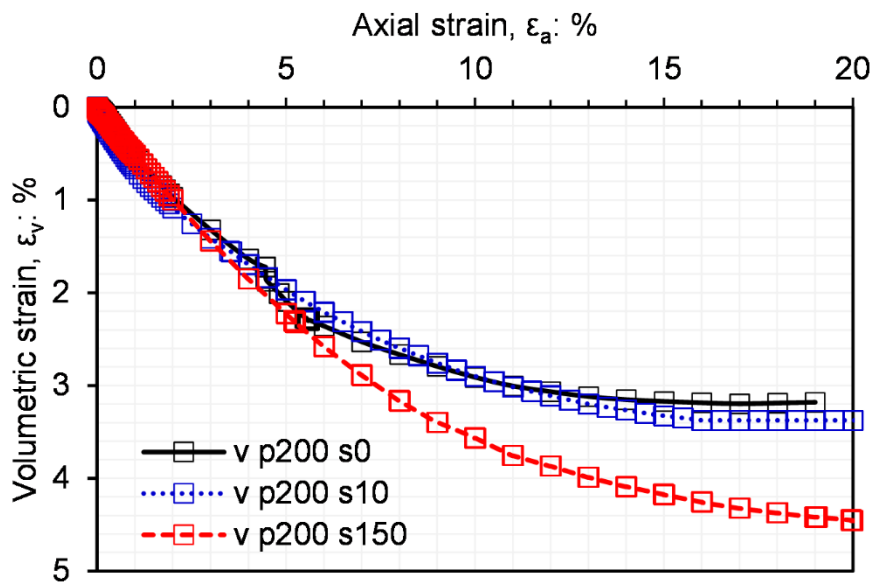


(c)

Figure 5.3 Effects of mean net stress on stress strain behaviour at a particular suction of (a) 0 kPa (b) 10 kPa and (c) 150 kPa

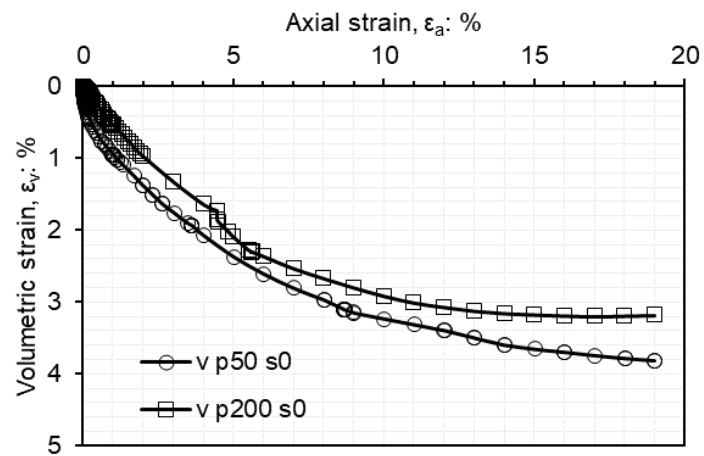


(a)

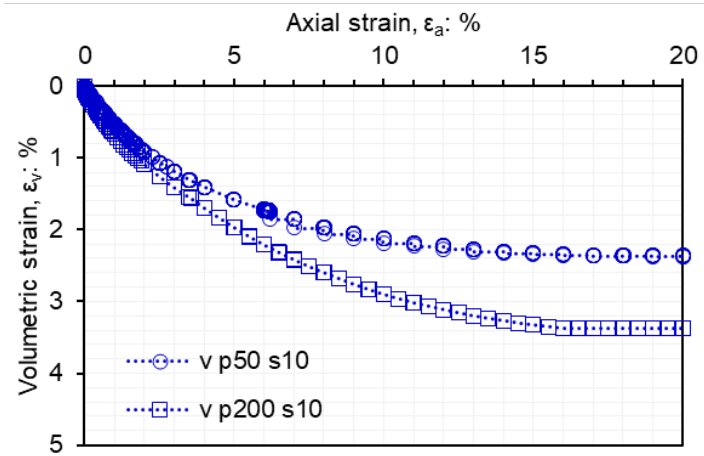


(b)

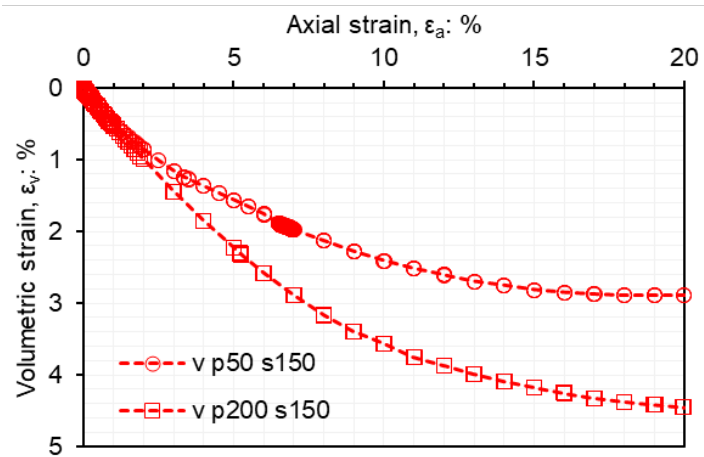
Figure 5.4 Volume change response of unsaturated compacted lateritic soil at (a) 50 and (b) 200 kPa mean net stress



(a)

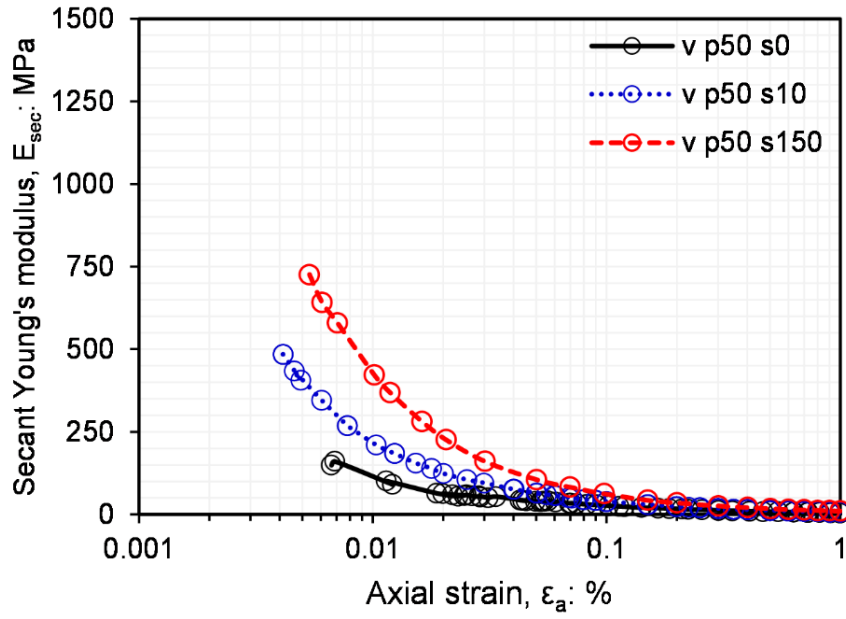


(b)

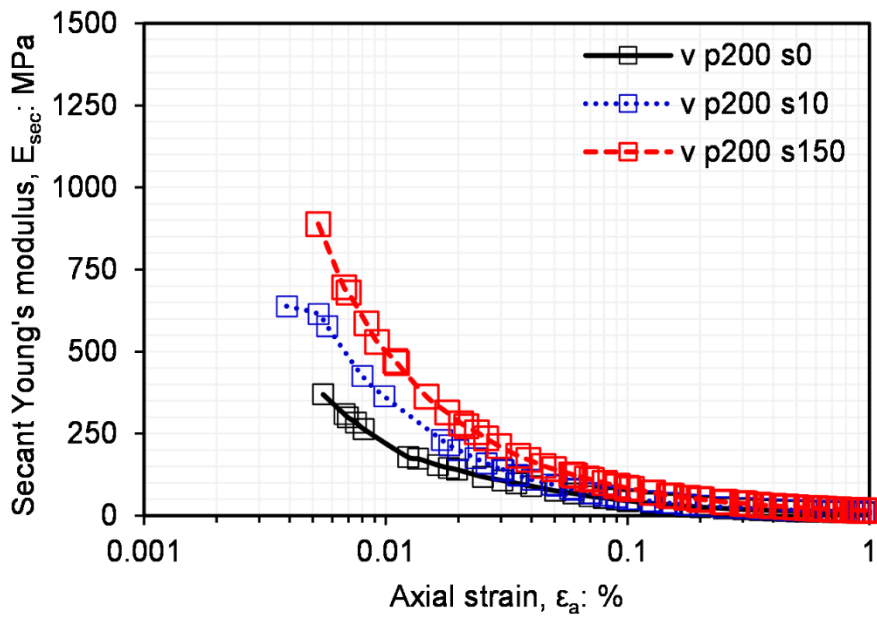


(c)

Figure 5.5 Influence of mean net stress on volumetric response at a particular suction of (a) 0 kPa (b) 10 kPa and (c) 150 kPa

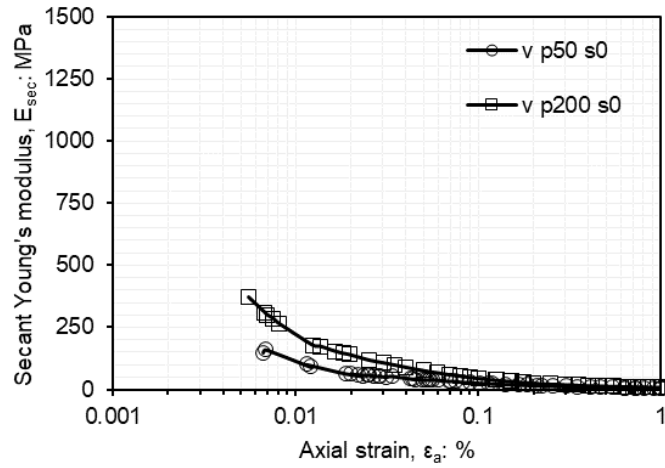


(a)

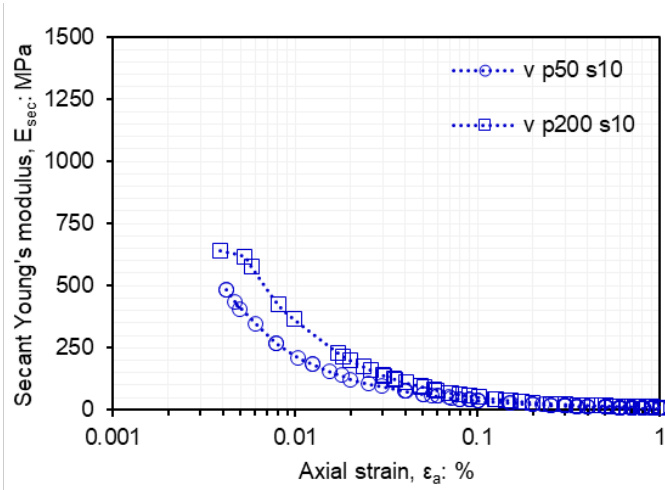


(b)

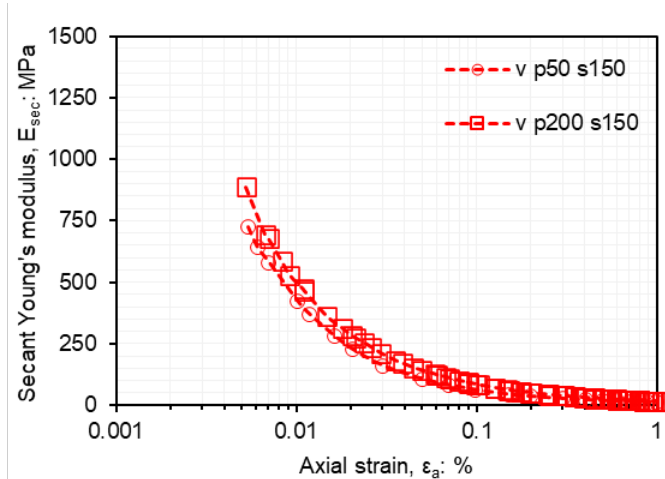
Figure 5.6 Small-strain stiffness of unsaturated compacted lateritic soil at (a) 50 kPa (b) 200 kPa mean net stress



(a)

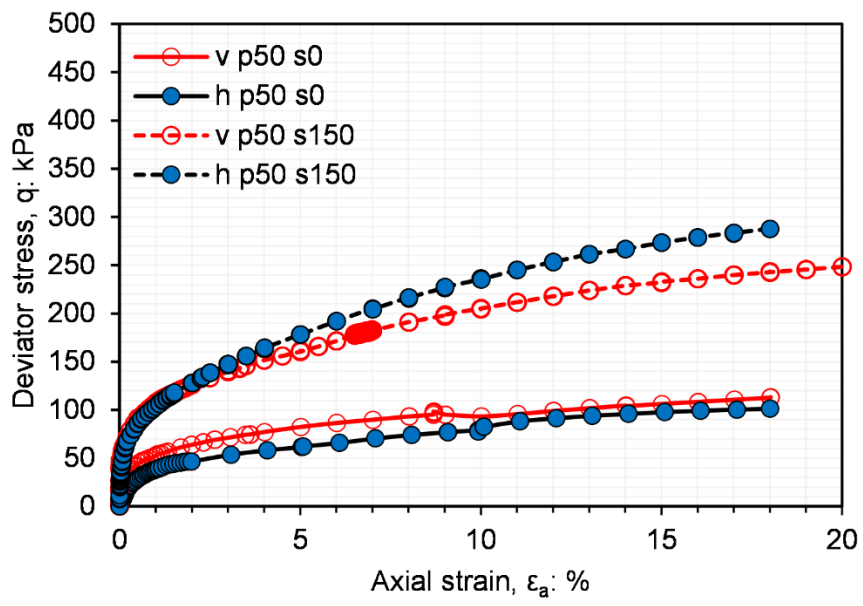


(b)

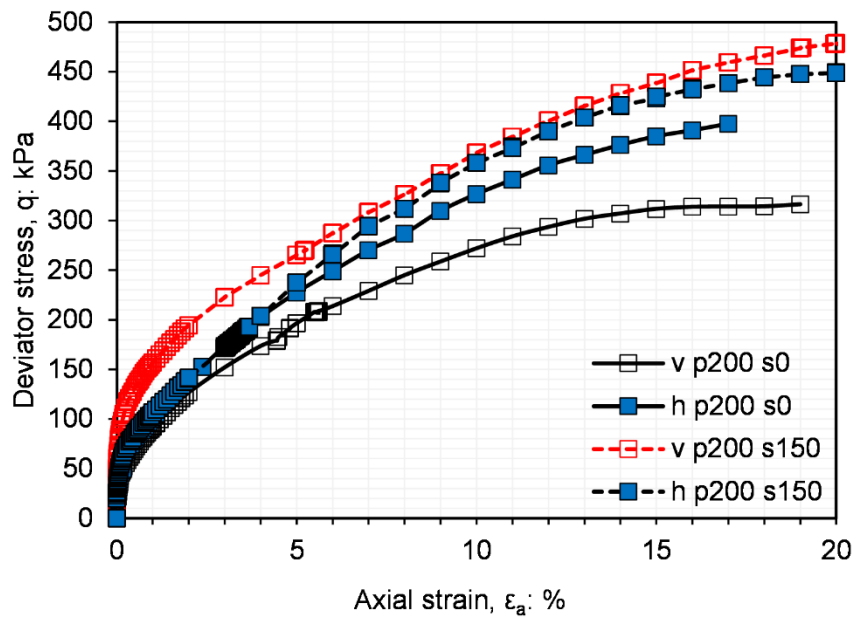


(c)

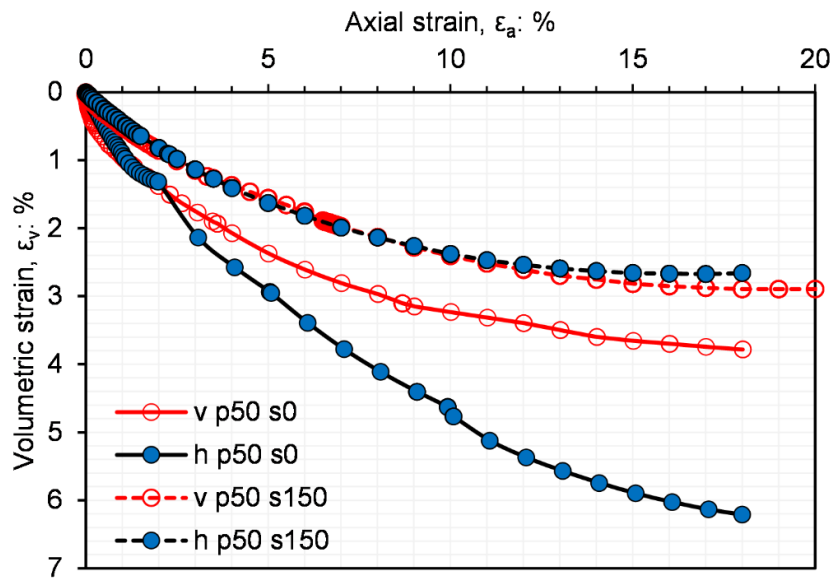
Figure 5.7 Effects of mean net stress small strain stiffness at a particular suction



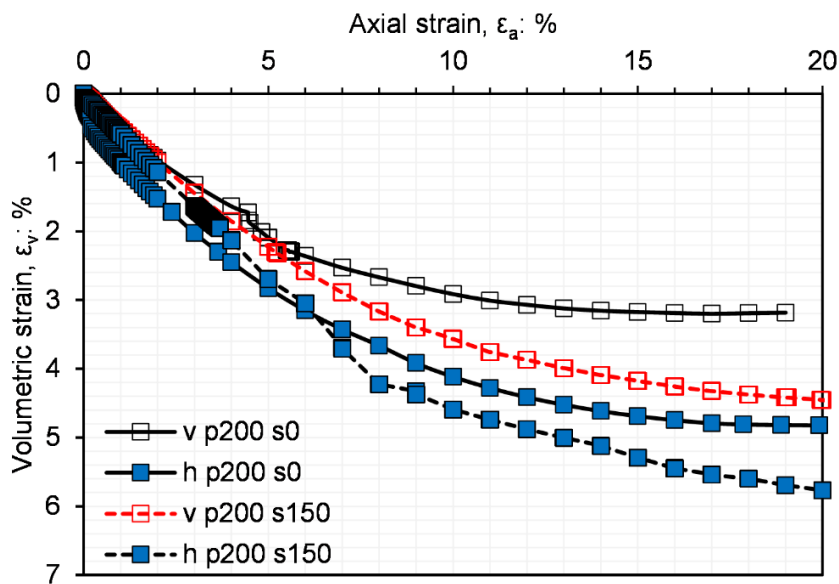
(a)



(b)

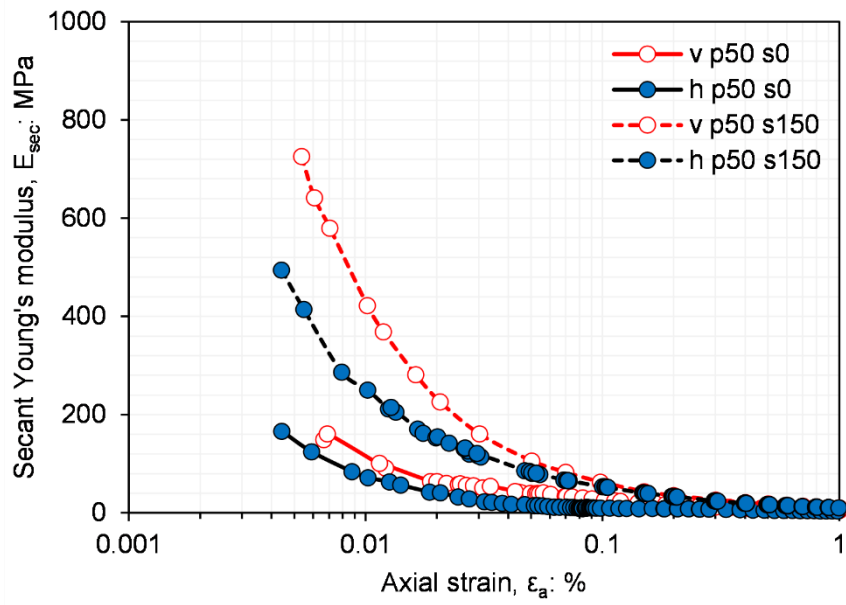


(c)

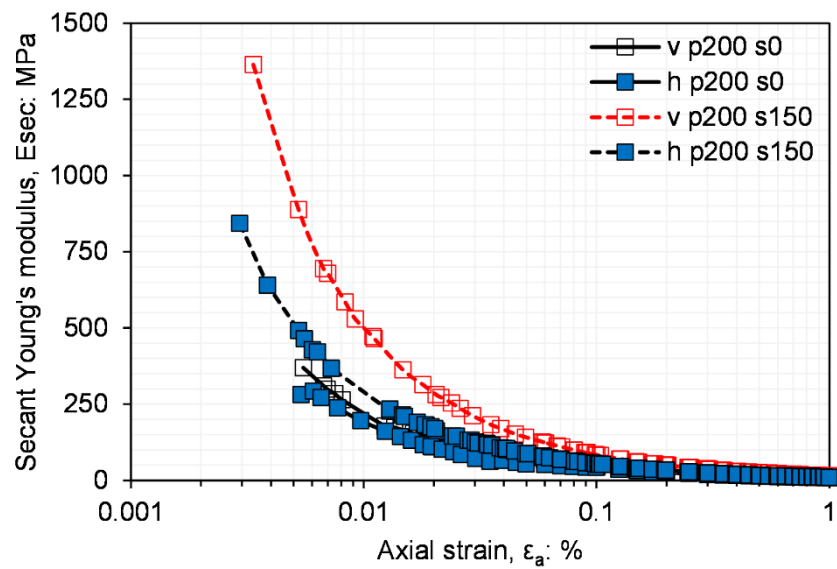


(d)

Figure 5.8 Specimen orientation and suction effects at 50 and 200 kPa mean net stress: (a), (b) stress-strain behaviour; (c), (d) volume change response



(a)



(b)

Figure 5.9 Specimen orientation and suction effects on small-strain stiffness at (a) 50 kPa (b) 200 kPa mean net stress

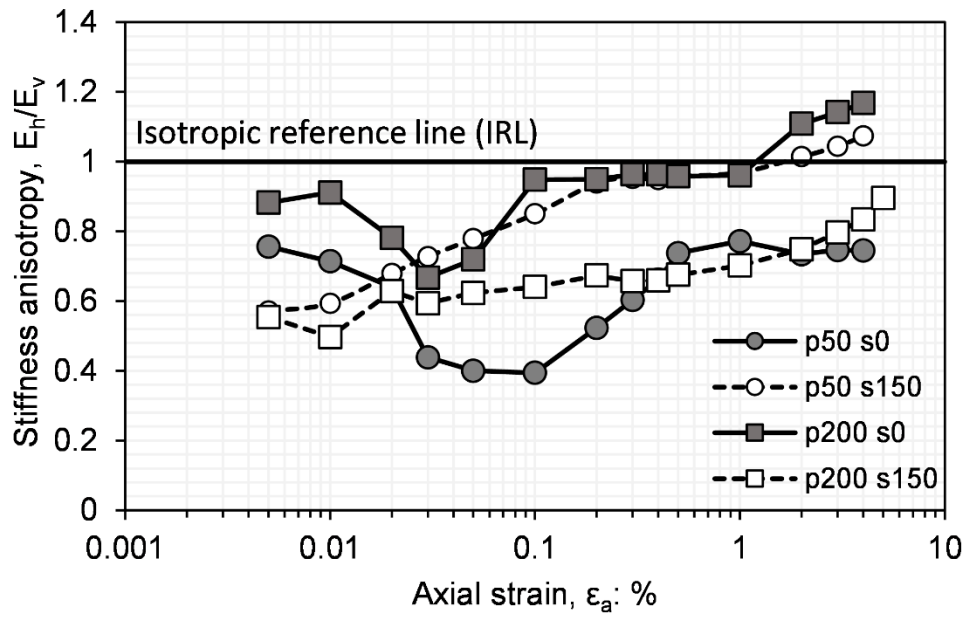
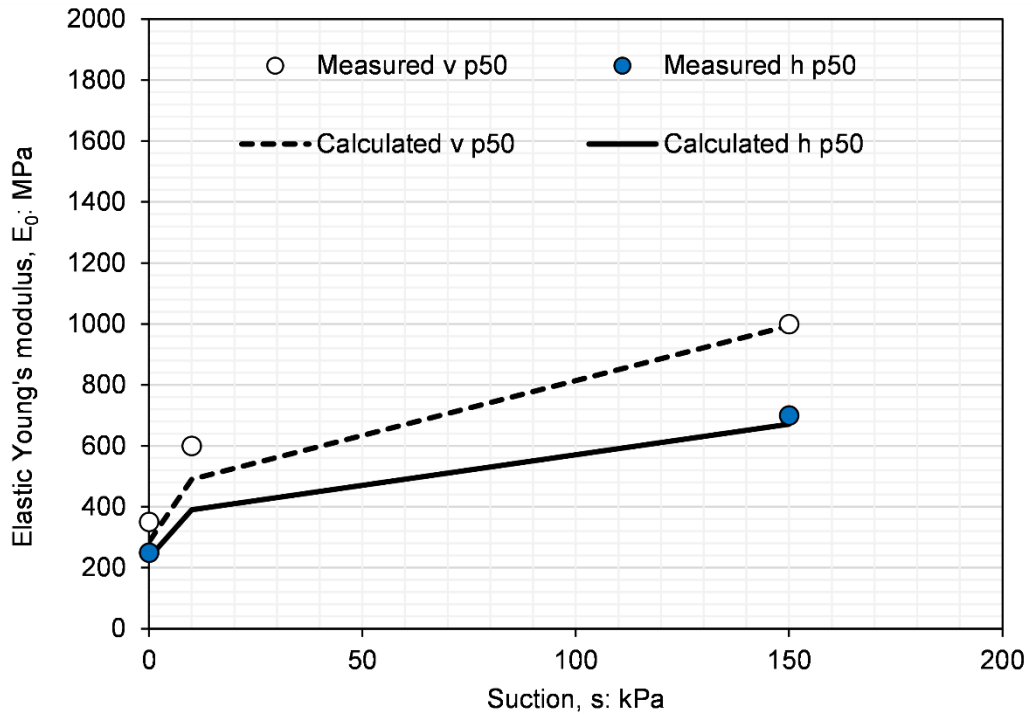
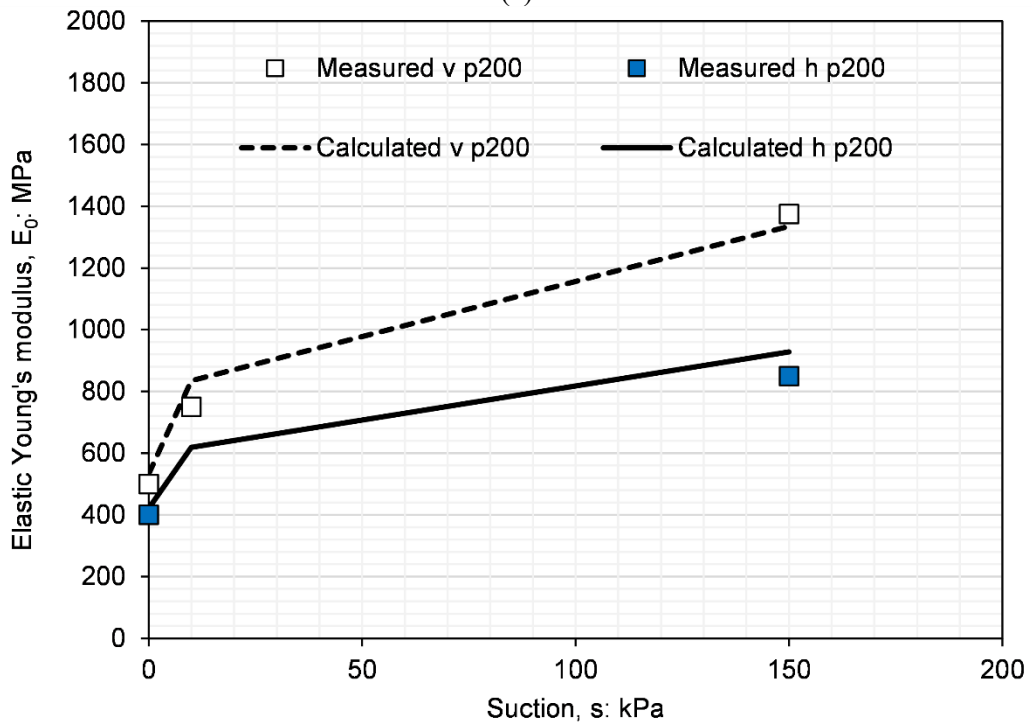


Figure 5.10 Suction effects on the evolution of stiffness anisotropy of compacted specimen



(a)



(b)

Figure 5.11 Comparison between measured and calculated E_0 at mean net stress of (a) 50 kPa; (b) 200 kPa.

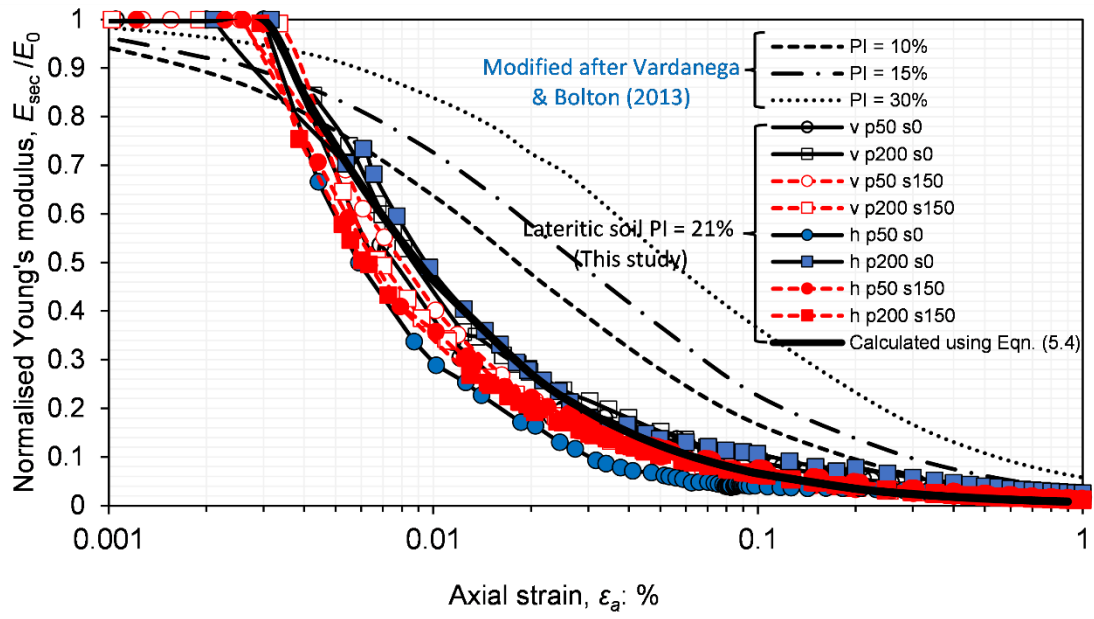


Figure 5.12 Summary of all measured degradation curves in comparison with design charts

CHAPTER 6 HIGH SUCTION EFFECTS ON STIFFNESS UNDER MONOTONIC AND CYCLIC LOADING

This chapter presents an experimental study of compacted lateritic soil's monotonic and cyclic stiffness. High suction values over 3 MPa were investigated to capture the small strain stiffness and large strain strength response of the compacted lateritic soil under extreme drying conditions. For the cyclic triaxial tests, two parameters, including the accumulated axial plastic strain and resilient modulus, are presented and discussed, considering the effect of initial compaction water content. These two factors are frequently employed to calculate soil deformations brought on by cyclic traffic loads in pavement engineering. For the monotonic loading tests, the observed small strain stiffness response (i.e., secant Young's modulus) of the unsaturated compacted lateritic soil is first presented, and the large strain behaviour is then discussed. The analysis of the results in this chapter focuses on the coupled effects of high suction and the initial compaction water contents that induce different particle aggregations.

6.1 Testing programme for high on both monotonic and cyclic shear behaviour

6.1.1 Monotonic shear behaviour

For the monotonic shear test, a series of tests were performed to study the effects of initial (i.e., during sample preparation and compaction) water content on the small strain stiffness (i.e., secant Young's modulus) and large strain response (shear strength), during monotonic loading. Three initial water content conditions (i.e., 16.5, 19.5% and 22.5%) with similar void ratio (i.e., 0.65, corresponding to 95% maximum dry density of the standard proctor compaction) were considered at as-compacted state, similar to the initial state for the cyclic loading tests mentioned below.

High suction was also imposed using the vapour equilibrium technique (Blatz et al. 2008). The total suction of different specimens was approximately 4, 40, and 300 MPa, respectively. The compacted specimens were equilibrated in a closed desiccator (see [Plate 6.1](#)) under total suctions of approximately 4, 40 and 300 MPa using saturated salt solutions of Potassium Sulphate, Sodium Chloride and Lithium Chloride, respectively. The suction equalization took at least 3 months for 300 MPa suction and 6-12 months for suction 4 and 40 MPa. The samples were taken out at least once weekly to measure their weight and calculate the gravimetric water content. [Figure 6.1](#) shows a typical plot of the changes in gravimetric water content, which was measured once a week. The total suction was considered complete or equilibrated within

the soil after the rate of change in total soil specimen mass was less than 0.2 g/day, corresponding to daily water content changing rate of less than 0.02%. Similar criteria were utilized by [Banerjee et al. \(2020\)](#), even though a different methodology was used to control high suction in their study.

At the end of the suction equalisation, the specimens were wrapped in a cling wrap and stored for at least 24 hours before monotonic triaxial testing. [Table 6.1](#) represents the soil state and test program for the effects of high suction on monotonic shear response. These tests were conducted under constant water content conditions after reaching suction equalisation in the desiccators. After setting up the specimen and instrumentations in the triaxial apparatus, a mean net stress of 50 kPa was directly applied to the specimen. At the end of compression at constant water content, the specimen was sheared at a constant displacement rate of 0.005 mm/min, similar to the shearing rate used for the saturated drained triaxial testing program.

6.1.2 Cyclic shear behaviour

A series of tests were performed for the cyclic loading test to study the effects of initial (i.e., sample preparation or compaction) water content on the resilient modulus and plastic strain accumulation during cyclic loading. Four initial water content conditions (i.e., 10% and 16.5, 19.5% and 22.5%) with similar void ratios (0.65, i.e., corresponding to 95% maximum dry density of the standard proctor compaction) were considered at as-compacted state. These water contents corresponded to the field moisture content of the soil when the soil was acquired, the dry side of OMC, the OMC and the wet side of OMC obtained from standard proctor compaction, respectively.

High suction was imposed using the vapour equilibrium technique ([Blatz et al. 2008](#)), as explained above. At the end of the suction equalisation, the specimens were wrapped in a cling wrap and stored for a minimum of 24 hours before cyclic triaxial testing. [Table 6.2](#) shows the soil state and test program for the effects of initial compaction water content on cyclic behaviour. [Table 6.3](#) represents the soil state and test program for the effects of high suction on cyclic response.

The AASHTO T307-99 ([AASHTO 2017](#)) procedure was modified and used to determine the cyclic response and resilient behaviour of each specimen, with 12 load sequences, and then four deviator stresses of 35, 50, 70, and 90 were applied in sequence at a constant confining pressure of 42, 30 and 15 kPa. In the standard T 307 test, a minimum of 100 repetitions are applied for each loading sequence using the cyclic triaxial apparatus (see [Plate 3.5](#)).

6.2 High suction effects on the pore size distribution

Figure 6.2 represents the differential pore volume of the lateritic clay after suction-induced desiccation to high suctions of about 40 and 300 MPa. The two primary peaks, which correspond to the inter- and intra-aggregate pores, indicate a dual-porosity structure, which is present in all of the specimens. A diameter of roughly 0.2 μm marks the separation between intra-aggregate and inter-aggregate pores. Furthermore, there are more small-size intra-aggregate pores than large-size inter-aggregate pores.

With an initial compaction water content of 16% (**Figure 6.2(a)**) and suction-induced desiccation of 40 and 300 MPa, the peak value of the inter-aggregate pores is observed at about 70 μm , whereas the peak value of the intra-aggregate pores is observed at about 0.02 and 0.03 μm , respectively. For the specimen with an initial compaction water content of 19% and suction-induced desiccation of 40 and 300 MPa (**Figure 6.2(b)**), the peak value of the inter-aggregate pores is observed at about 123 μm and 74 μm , respectively. The peak value of the intra-aggregate pores is observed at about 0.02 and 0.03 μm for the 40 and 300 MPa suctions, respectively. Regarding the specimen with an initial compaction water content of 22% (**Figure 6.2(c)**), the peak value of the inter-aggregate pores is found at about 70 μm and 20 μm for the 40 and 300 MPa suctions, respectively. On the other hand, the peak value of the intra-aggregate pores is also observed at about 0.02 and 0.03 μm for the 40 and 300 MPa suctions, respectively. Irrespective of the initial compaction water content, the lateritic clay has a significant disparity between its intra-aggregate and inter-aggregate pores, indicating the presence of large-size pores caused by the size of its aggregates.

Figure 6.2 reveals that there is no significant change in the inter-aggregation region when the suction increases from 40 to 300 MPa for specimens with an initial compaction water content of 16%. However, for specimens with an initial compaction water content of 19%, the inter-aggregate pores region shifts from 123 μm at 40 MPa to about 74 μm at 300 MPa. Similarly, the inter-aggregate pores region shifts from 123 μm at 40 MPa to about 74 μm at 300 MPa, for specimens compacted at 22% water content. The decrease in peak pore diameter shows that desiccation caused certain large inter-aggregate pores to decrease due to specimen shrinking.

It can be seen from **Figure 6.3** that the aggregates shrink, leading to decreasing intra-aggregate pore volume. On the other hand, the inter-aggregate pores tend to collapse or reduce as the soil shrinks and aggregates move closer.

6.3 Interpretations of monotonic shear behaviour

6.3.1 Stress-strain response

Figure 6.4(a) and **(b)** show the stress-strain response of the compacted lateritic soils sheared at various high-suction (i.e., approximately 40 and 300 MPa) induced desiccation. These series of tests are for one initial mean net stress of 50 kPa. The deviator stress reaches a peak value for all the specimens sheared at all suction states before it starts to decline with increasing axial strain (i.e., strain softening response) and finally reaches a critical state deviator stress. All the specimens tested at high suction failed by the formation of shear bands at the critical state, which is represented by the strain softening response. The strain at which the deviator stress reaches the peak is affected by the suction value and the initial compaction water content. This finding is because the high suction-induced desiccation for different compaction water contents results in different shrinkage and final void ratios before shearing. However, the peak deviator stress is achieved at axial strains ranging from 1 to 4%. In general, all the high suction desiccated samples reached a critical state at approximately 5% axial strains. Details of the influence of high suction and compaction water content are presented later.

Figure 6.5(a), (b) and **(c)** compare the influence of high suction on the stress-strain response for specimens compacted at 16%, 19% and 22%, respectively. It can be seen from **Figure 6.5** that for the same compaction water content, the higher peak deviator stress occurs for 40 MPa suction. With a suction increase from 40 to 300 MPa, peak shear strength is reduced. This trend differs from the experimental results in the low suction range, where an increase in suction generally enhances the strength. The observed behaviour at a high suction range is likely related to water distribution in unsaturated soil. When the suction is larger (i.e., 300 MPa), the number of water meniscus reduces significantly between aggregates, reducing their stabilisation effects on the inter-aggregate soil skeleton. Irrespective of the initial compaction water content or the high suction-induced desiccation, the critical state deviator stress is reached at about 4% axial strain.

6.3.2 Shearing-induced dilatancy

Figure 6.6(a) and **(b)** represent the volume change response of the compacted lateritic soils sheared after various high suction (i.e., approximately 40 and 300 MPa) induced desiccation. An initial contractive behaviour was observed, followed by a dilative response until a critical state was reached. The maximum contractive volumetric strain is about 2%,

whereas the maximum dilative strain at which the critical state occurs is about 4%. Because of the formation of a shear band (i.e. strain localization), there is a continuous increase in the dilative strain. A constant value of volumetric strain is not observed at the end of shearing, although the critical state deviator stress has been reached.

Figure 6.7(a), (b) and (c) compare the influence of high suction on the volume change response for specimens compacted at 16%, 19% and 22%, respectively. For the 16% compaction water content, the difference between the initial contractive response seems insignificant. Moreover, the maximum contractive strain is less than 1%, as shown in **Figure 6.7(a)**. Significant differences are observed for specimens compacted at 19% water content under high suction, as shown in **Figure 6.7(b)**. There is also a significant variable dilative strain in **Figure 6.7(b)**. The specimen at 300 MPa experiences the lowest contractive strains and the highest dilative strains for the compaction water content of 19%. With respect to **Figure 6.7(c)**, which shows the volumetric response of specimens compacted at 22% compaction water content, the difference between the contractive strain is smaller compared to **Figure 6.7(b)**. In **Figure 6.7(c)**, the specimen at 300 MPa experiences the lowest contractive strains and the highest dilative strains for the compaction water content of 22%. This response is similar to the observations at 19% compaction water content in **Figure 6.7(b)**.

6.3.3 Influence of compaction water contents on peak and critical state strengths

Figure 6.8 shows the influence of compaction water content on shear strength (i.e. both peak and critical state) at various high suctions. It can be concluded from **Figure 6.8** that with an increase in compaction water content, the peak shear strength increases for the high suction-induced specimen. On the other hand, the influence of the initial compaction water content on the critical shear strength is not very clear. Considering all the high suction desiccated samples, it may conclude that the critical state shear strength is nearly constant (i.e. unaffected by the initial compaction water content).

In addition, the high suction-induced desiccation can modify the soil fabric. The highest suction value (i.e. 300 MPa) and lowest degree of saturation increased the susceptibility of the samples to experience strain localisation ([Fern et al. 2016](#); [Higo et al. 2011](#)).

6.3.4 Effects of high suction on small strain stiffness for same compaction water content

Figure 6.9(a) and (b) show the secant Young's modulus (E_{sec}) against axial strain from small to large strains (i.e., 0.001 to 1% axial strain) of the compacted lateritic soils sheared after various high suction (i.e., approximately 40 and 300 MPa) induced desiccation. For the

suction value of 40 MPa, the E_{sec} is consistently larger for the specimens prepared with an initial water content of 16% than those prepared with 19% and 22%, as shown in **Figure 6.9(a)**. This is partially attributed to the pore size distribution and degree of saturation at 40 MPa. The presence of relatively more small-size aggregates, more interaggregate pore volume and a higher degree of saturation will result in higher meniscus water for 16% than for 19% and 22% at 40 MPa suctions. On the other hand, for a high suction value of 300 MPa, the largest E_{sec} is possessed by the specimen prepared at 19% compaction water content, as shown in **Figure 6.9(b)**.

Figure 6.10(a), (b) and (c) are plotted to explore the influence of high suction on the small strain stiffness for specimens compacted at 16%, 19% and 22%, respectively. In **Figure 6.10(a)**, by considering the desiccated specimens prepared initially at 16% water content, the specimen with 40 MPa suction has the larger E_{sec} , than the specimen with 300 MPa suction. Referring to **Figure 6.10(b)**, which represents the specimens prepared with 19% compaction water content, the suction of 300 MPa resulted in the larger E_{sec} , than 40 MPa suction. For the specimens prepared at 22% water contents **Figure 6.10(c)**, the E_{sec} is larger for suction values of 40 MPa compared to 300 MPa. In **Figure 6.10(a), (b) and (c)**, a preliminary trend can be observed. At 16% compaction water content, E_{sec} for 40 MPa suction is the largest, whereas at 19%, E_{sec} for 300 MPa suction is the largest and at 22% compaction water content, E_{sec} for 40 MPa suction is the largest. However, the difference between the maximum and minimum values at 19% and 22% is relatively small, whereas that of 16% is significantly large. This implies that an increase in compaction water content, which results in larger particle aggregation, leads to higher E_{sec} at higher suction. This trend is also likely to be possible due to larger shrinkage and hence lower void ratio experienced by higher compaction water contents.

6.3.5 Discussion about the stiffness behaviour based on microstructures.

As shown in **Figure 6.10(a)**, the specimen at w16 s40 has a higher small strain stiffness than that at w16 s300. Based on the microstructural evidence shown in **Figure 6.2** and **Table 6.4**, with a degree of saturation of 21% in w16 s40 and the presence of small aggregates, the meniscus water present may play a more dominant role than the void ratio, by comparing w16 s40 and w16 s300.

On the other hand, regarding w19 s40 and w19 s300, they both have very similar void ratios and similar intra-aggregate pores (see [Figure 6.2](#) and [Table 6.4](#)). It is reasonable to assume that the higher degree of saturation in w19 s40 has a significant portion in the intra-aggregate pores. Then, the higher inter-aggregate pores of w19 s40 can result in lower stiffness than w19 s300.

For the specimens w22 s40 and w22 s300, by comparing just the void ratios, it is likely that w22 s300 should have a higher small strain stiffness. However, due to significantly larger aggregations, and if a greater fraction of the water is held in the intra-aggregate pores, then there is little meniscus water effect in the inter-aggregate pores for w22 s300. The excess amount of water for w22 s40 implies that there might be some contribution of meniscus water effect leading to a high small strain stiffness for w22 s40 than w22 s300.

It should be mentioned that the differences between the highest E_{sec} and the lowest E_{sec} caused by high suction reduce as the compaction water content increases. In other words, there is a small difference between the magnitude of E_{sec} for w19 and w22 at high suctions, possibly due to competing effects of meniscus water and particle aggregations. These results, therefore, need to be interpreted with caution as the findings might not apply to other soils state.

6.4 Interpretations of cyclic shear behaviour

6.4.1 Influence of deviator stress on resilient modulus

[Figure 6.11](#) to [Figure 6.13 \(a\)](#) and [\(b\)](#) shows the relationship between resilient modulus (M_R) and cyclic deviator stress (q_{cyc}) at different suctions for the three compaction water contents and when the specimen is subjected to drying at three suctions (approximately 4, 40, and 300 MPa). M_R was estimated using the cyclic response of the last five cycles at each stress state. It can be seen from the figure that, at low suction (less than or equal to 4 MPa), M_R reduces with increasing q_{cyc} . On the other hand, at high suction (greater than or equal to 40 MPa), M_R increases with increasing q_{cyc} . The decrease of M_R with q_{cyc} can be attributed to the nonlinearity of the elasto-plastic response of soils. Previous studies have revealed that soil stiffness is high at small strains, but it decays with an increase in strain level as a result of increasing deviator stresses ([Atkinson 2000](#)). However, this non-linearity may not be able to fully explain the increase of M_R with increasing q_{cyc} .

Many prediction models have been proposed to describe the resilient modulus of soils as a non-linear function of the stress state (Ng et al. 2013; Zhang et al. 2019). Equation (6.1) was proposed and verified (Ng et al. 2013) based on their experimental results and some available results in the literature. The equation considers the effects of net confining pressure, suction and cyclic deviator stress on M_R .

$$M_R = M_0 \left(\frac{p}{p_r} \right)^{k_1} \left(1 + \frac{q_{cyc}}{p_r} \right)^{k_2} \left(1 + \frac{s}{p} \right)^{k_3} \quad (6.1)$$

where mean net stress, p , is defined as $[(\sigma_1 + \sigma_2 + \sigma_3)/3 - u_a]$; q_{cyc} is cyclic stress; s is matric suction; k_1 , k_2 , and k_3 are regression exponents. The first term on the right-hand side denotes the resilient modulus at the reference stress state where $p = p_r$, $q_{cyc} = p_r$, and $s = 0$.

The second term quantifies the influence of net mean stress on M_R . It is widely recognised that the M_R increases with confinement (Lekarp et al. 2000), hence the value of k_1 is always positive. The third term reflects the variation of M_R with cyclic stress. For a soil specimen characterized by the nonlinearity of stress-strain behaviour, the exponent k_2 is negative because soil stiffness decreases with increasing strain (Atkinson 2000). Experimental results have shown that the stiffness of unsaturated soil increases significantly with matric suction (Dong et al. 2016b; Ng and Yung 2008b). Similarly, M_R of unsaturated soil is expected to increase with matric suction. Therefore, parameter k_3 should be positive.

Based on the experimental results in this study, the value of k_2 may not be always negative but should have a limiting positive value at high suction depending on the soil type. This is because M_R increases with increasing q_{cyc} at high suction. The increase in M_R with cyclic deviator stress at high suction has also been reported by Yang et al. (2008a). The authors (Yang et al. 2008a) speculated that it is attributed to the hardening of the soil at the suction of 450 kPa such that an increase in recoverable strain is insignificant with high cyclic deviator stress. Another possible explanation might be that the mean bishop's stress is significantly larger at high suction and tends to reduce the deformation at high suction.

6.4.2 Influence of suction and stress on resilient modulus

Figure 6.14 to Figure 6.16(a) and (b) shows the effects of suction-induced desiccation on M_R at different q_{cyc} for each compaction water contents. For compaction water content of 16.5%,

the initial suction is about 1 MPa (see [Figure 6.14](#)). When suction is higher than 4 MPa, the value of M_R decreases then the remains unchanged from 40 MPa to 300 MPa at mean net stress of 42 kPa. At 15 kPa mean net stress, an increase in suction beyond 4 MPa consistently results in a slight decrease in M_R .

[Figure 6.15](#) shows the influence of suction on M_R when the compaction water content is 19.5%. Similar to the soil with compaction water content at 16.5%, M_R increases with an increase in suction to 4 MPa for both mean net stress of 42 and 15 kPa. However, when suction exceeds 4 MPa, M_R response is highly dependent on the value of q_{cyc} . At 42 kPa mean net stress and low q_{cyc} of 35 and 50 kPa, M_R decreases with an increase in suction above 4 MPa. At a high q_{cyc} of 70 and 90 kPa, M_R first increases with an increase in suction to 40 MPa before a small decrease at 300 MPa. With respect to a mean net stress of 15 kPa, at low a q_{cyc} of 35 and 50 kPa, M_R decreases with an increase in suction above 4 MPa. On the other hand, at a high q_{cyc} of 70 and 90 kPa, M_R increases with an increase in suction.

The effects of suction on M_R when the compaction water content is 22.5% are shown in [Figure 6.16](#). M_R increases with an increase in suction to 4 MPa for both mean net stress of 42 and 15 kPa, which is identical to the compaction water content of 16.5% and 19.5%. M_R response significantly decreases between 4 to 40 MPa suction. When suction increases from 40 MPa to 300 MPa, M_R then becomes larger for all the values of q_{cyc} .

The trend shown in [Figure 6.14](#) to [Figure 6.16\(a\)](#) and [\(b\)](#) may be dependent on both the initial aggregated microstructure and the corresponding drying effects on the soil structure. An increase in compaction water content is capable of inducing larger particle aggregation ([Tarantino 2011](#)) in the compacted lateritic soil. Particles may be weakly aggregated and their contacts could break down under mechanical loading ([Airey et al. 2012](#)). Hence, the degree of particle aggregation is more significant in 22.5% followed by 19.5% and 16.5% compaction water contents, respectively. Suction-induced desiccation results in the hardening of soil and aggregates. However, during repeated loading crushing of aggregate contacts causes stiffening of the soil skeleton may occur. Initial crushing of larger aggregate contacts may yield a reduction in stiffness. The larger the particle aggregation, the easier its tendency for the breakage at contacts at higher suction. This results in a consistent decrease in stiffness, hence a reduction in M_R . After the contacts fill in voids the overall soil stiffness may tend to increase.

Figure 6.17 shows the resilient modulus versus the deviator stress for samples with an initial compaction water content of 16.5% after suction-induced desiccation to 4, 40 and 300 MPa. As expected, an increase in mean net stress increases the M_R . A similar trend was observed for other compaction water and they are not presented here.

6.4.3 Accumulated plastic strain.

Figure 6.18 shows the relationship between the accumulated plastic strain and cyclic deviator stress of the compacted lateritic soil specimen at different compaction water contents. The accumulated plastic strain increases with an increase in cyclic deviator stress for all water contents, but at different rates. For specimens compacted at a water content of 16% (see **Figure 6.18(a)**), the accumulated plastic strain is only up to about 0.4% at suction of 1 MPa. At a compaction water content of 19% (see **Figure 6.18(b)**), the measured accumulated plastic strain increases significantly and non-linearly to about 5.6% at a suction of about 200 kPa. On the other hand, when the suction is more than 4 MPa, there is only a small linear increase of accumulated plastic strain, which is less than 0.2%. Similarly, for specimens compacted at water contents of 22% (see **Figure 6.18(c)**), there is a significant non-linear increase of accumulated plastic strain up to about 5.6% at low suction of zero kPa, and at cyclic deviator stress of 90 kPa. The accumulated plastic strain at high suctions of more than 4 MPa is significantly small and increases almost linearly. This implies that the accumulated plastic is more noticeable at high water content with low suction values. The measured accumulated axial strain at high suction is generally lower compared to the test at the initial compacted state.

The influence of high suction-induced desiccation on accumulated plastic strain at various compaction water contents is shown in **Figure 6.19**. It appears that at different compaction water contents, the accumulated plastic strain decreases with increasing of suction to 40 MPa and there is an increase of accumulated plastic strain at the suction of 300 MPa. At cyclic stress of 90 kPa and compaction water content of 16%, the accumulated plastic strain decreases from 0.11% to 0.09% when suction decreases from about 4 MPa to 40 MPa. When suction increases from 40 to about 300 MPa, the accumulated plastic strain increases from 0.09% to 0.11% in **Figure 6.19(a)**. With regards to specimens compacted at 19% water content, the accumulated plastic strain decreases from 0.17% to 0.11% when suction decreases from about 4 MPa to 40 MPa. When suction increases from 40 to about 300 MPa, the accumulated plastic strain increases from 0.11% to 0.16% in **Figure 6.19(b)**. For specimens prepared with a compaction water content of 22%, the accumulated plastic strain changes from 0.18% to 0.16% when suction decreases from about 4 MPa to 40 MPa. The accumulated plastic strain in the range of

suction changes from 40 to about 300 MPa, increases from 0.16% to 0.18%. With the three water contents considered, the variations in accumulated plastic strain with cyclic deviator stress are more significant at high compaction water contents of 19% and 22%, which may be because of significantly larger and/or more variable particle aggregations at higher compaction water contents.

6.5 Summary

The small strain stiffness and large strain strength characteristics of compacted lateritic clay were studied by performing a series of constant water content monotonic triaxial tests on the soil specimens after high suction desiccation was imposed on them through VET. The soil specimens were prepared at different initial compaction water content to investigate the influence of compaction water content-induced particle aggregation on the small strain stiffness and strength of the soil.

The experimental results revealed that all the specimens tested under high suction have their deviator stress reaching a peak value before it starts to decline with increasing axial strain (i.e., strain softening response) and finally reaching a critical state deviator stress. As a result of this response all the specimens failed by the formation of shear bands at the critical state. In general, with an increase in compaction water content, the peak deviator stress increases. This may be partially attributed to the compaction-induced particle aggregation of the specimen. Although the peak strain was influenced by the compaction-induced structure and suction, it appears that the critical state shear strength is nearly constant and unaffected by the compaction-induced structure. In addition, the strength of the soil decreases with an increase in high suction (i.e. the strength at 40 MPa is larger than the strength at 300 MPa).

With respect to the small strain stiffness results, the difference between the highest E_{sec} and the lowest E_{sec} caused by high suction reduces, as the compaction water content increases. Moreover, on the dry side ($w=16\%$) and wet side ($w=22\%$), the E_{sec} is larger at a suction of 40 MPa than at 300 MPa. On the other hand, at optimum conditions ($w=19\%$), the E_{sec} is larger at a suction of 300 MPa than at 40 MPa. At relatively high suctions of 300 MPa, the soil water may be in the form of adsorption. A possible explanation of the above trends may be related to both the dual porosity nature of the soil structure and more fines migration to fill some of the inter-aggregate voids at high suction. Hence, there is a stiffening effect at higher suction of 300 MPa for specimen compacted at water contents of 19%

The measured resilient modulus is found dependent on the compaction water content due to its initial suction or suction imposed. At low suction below 4MPa, M_R decreases with deviator stress. This might be due to the effect of the nonlinear elasto-plastic behaviour of compacted fine-grained soil specimens and the significant increase of resilient strain. When the suction imposed is larger than 4 MPa, the M_R increases with cyclic deviator stress. A possible explanation for this might be that the increase in recoverable strain is insignificant with an increase of cyclic deviator stress. Moreover, the mean bishop's stress is significantly larger at high suction and tends to reduce the deformation at high suction.

The accumulated plastic strain increases with an increase in cyclic deviator stress all water contents, but at different rates. This is also due to the initial suction of the soil (or suction imposed) at various initial water content. The measured accumulated plastic strain with cyclic deviator stress is only up 0.4% for suctions above 4 MPa (i.e., water content below 16%), compared to the accumulated plastic strain of about 5.6% for suctions below 4 MPa (for example suction of 150 kPa at a compaction water content of 19%).

Table 6.1 High suction effect on monotonic behaviour at small strains

Specimen ID	Initial Water Content, w: %	Saturated Salt solution	Approximate Suction, s: MPa
w16 s40	16.5	Sodium Chloride, NaCl	40
w16 s300		Lithium Chloride, LiCl	300
w19 s40	19.5	Sodium Chloride, NaCl	40
w19 s300		Lithium Chloride, LiCl	300
w22 s40	22.5	Sodium Chloride, NaCl	40
w22 s300		Lithium Chloride, LiCl	300

Table 6.2 Effects of initial compaction water content on cyclic behaviour

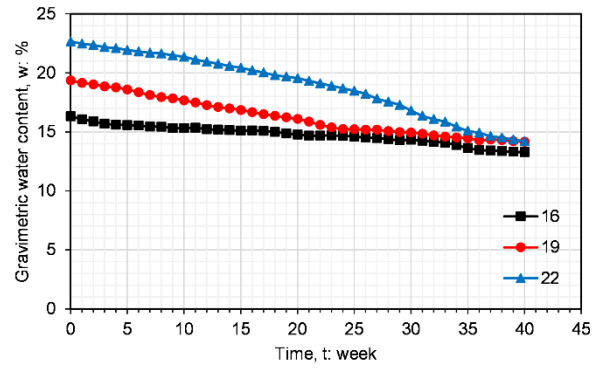
Specimen ID	Initial Water Content, w: %	Initial Suction, s: kPa
w10	10.0	6800
w16	16.5	1000
w19	19.5	150
w22	22.5	0

Table 6.3 High suction effect on cyclic behaviour at small strains

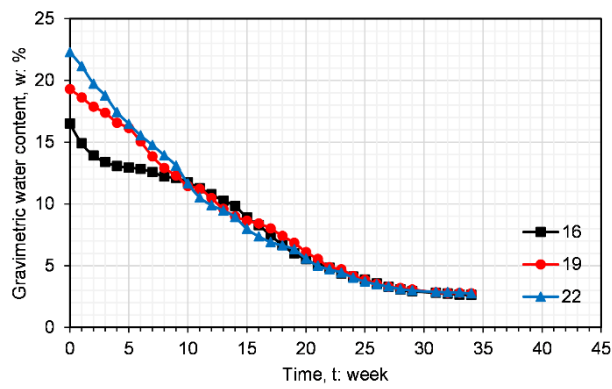
Specimen ID	Initial Water Content, w: %	Saturated Salt solution	Approximate Suction, s: MPa
w16 s4	16.5	Potassium Sulphate, K ₂ SO ₄	4
w16 s40		Sodium Chloride, NaCl	40
w16 s300		Lithium Chloride, LiCl	300
w19 s4	19.5	Potassium Sulphate, K ₂ SO ₄	4
w19 s40		Sodium Chloride, NaCl	40
w19 s300		Lithium Chloride, LiCl	300
w22 s4	22.5	Potassium Sulphate, K ₂ SO ₄	4
w22 s40		Sodium Chloride, NaCl	40
w22 s300		Lithium Chloride, LiCl	300

Table 6.4 Soil state after suction-induced desiccation via VET

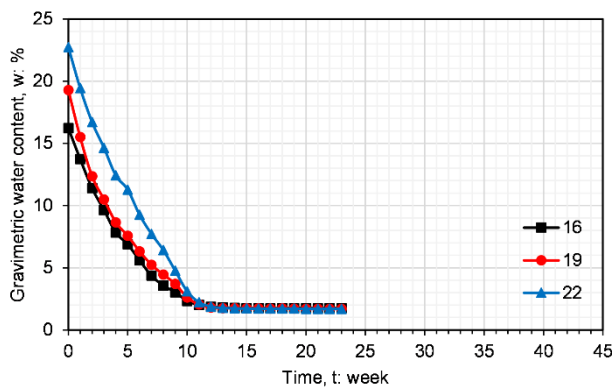
Specimen ID	Initial state			After VET suction equalisation		
	Suction, s: MPa	Void ratio, e	Degree of saturation, S _r	Suction, s: MPa	Void ratio, e	Degree of saturation, S _r
w16 s40	1	0.65	0.68	40	0.62	0.21
w16 s300	1	0.65	0.68	300	0.57	0.04
w19 s40	0.2	0.65	0.8	40	0.56	0.21
w19 s300	0.2	0.65	0.8	300	0.56	0.05
w22 s40	0	0.65	0.92	40	0.52	0.24
w22 s300	0	0.65	0.92	300	0.50	0.07



(a)

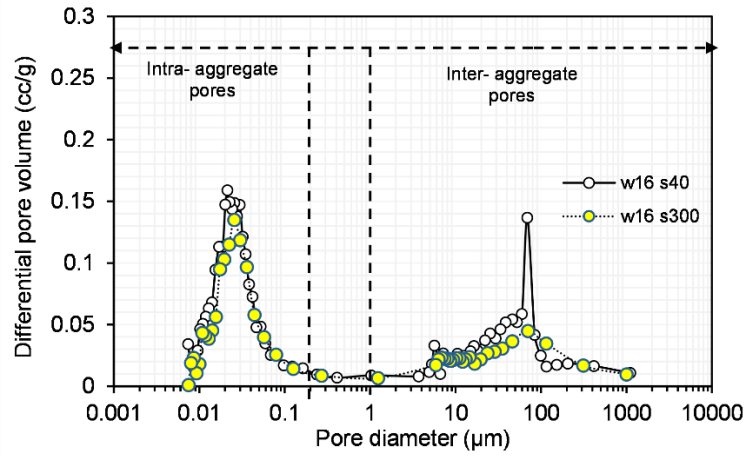


(b)

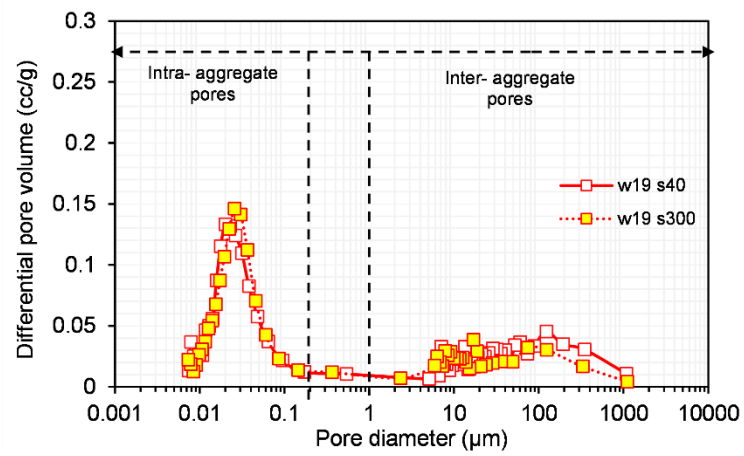


(c)

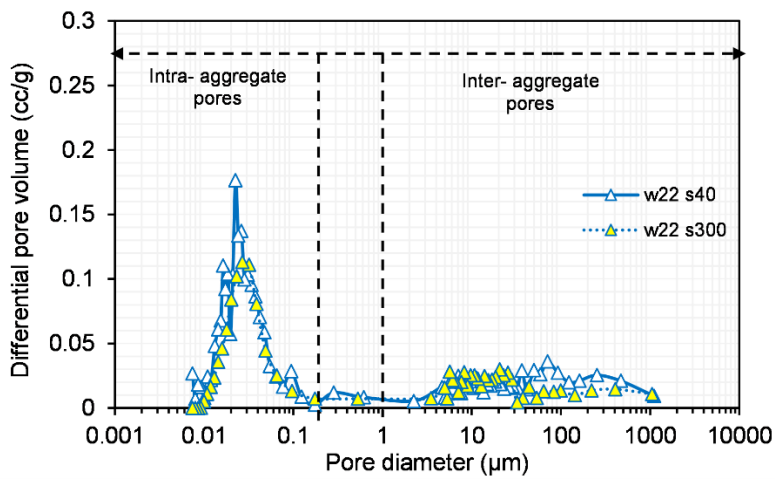
Figure 6.1 Changes in gravimetric water content in desiccators for (a) K₂SO₄ (b) NaCl (c) LiCl



(a)

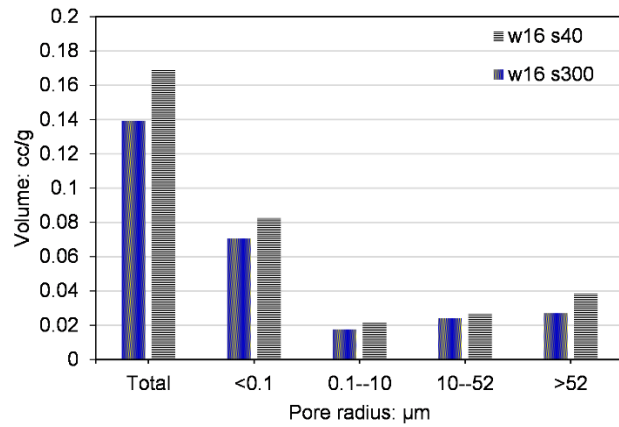


(b)

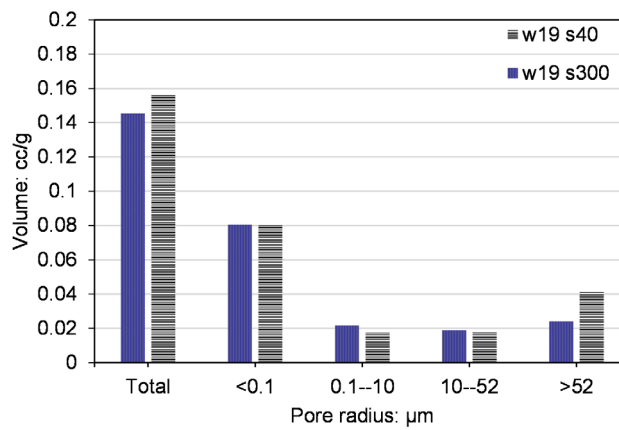


(c)

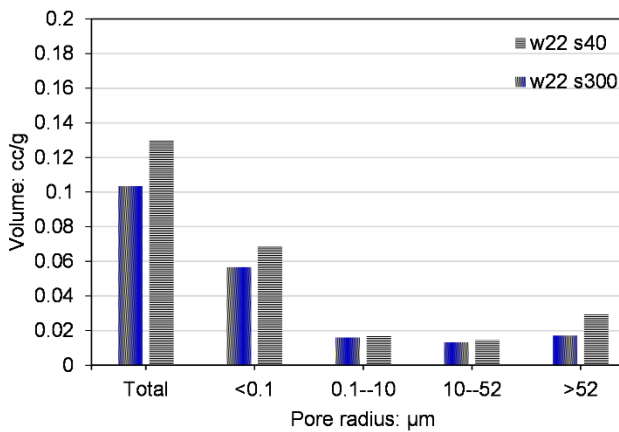
Figure 6.2 Pore size distribution of the lateritic specimen after various suction induced desiccation for different compaction water contents (a) w16, (b) w19 and (c) w22.



(a)

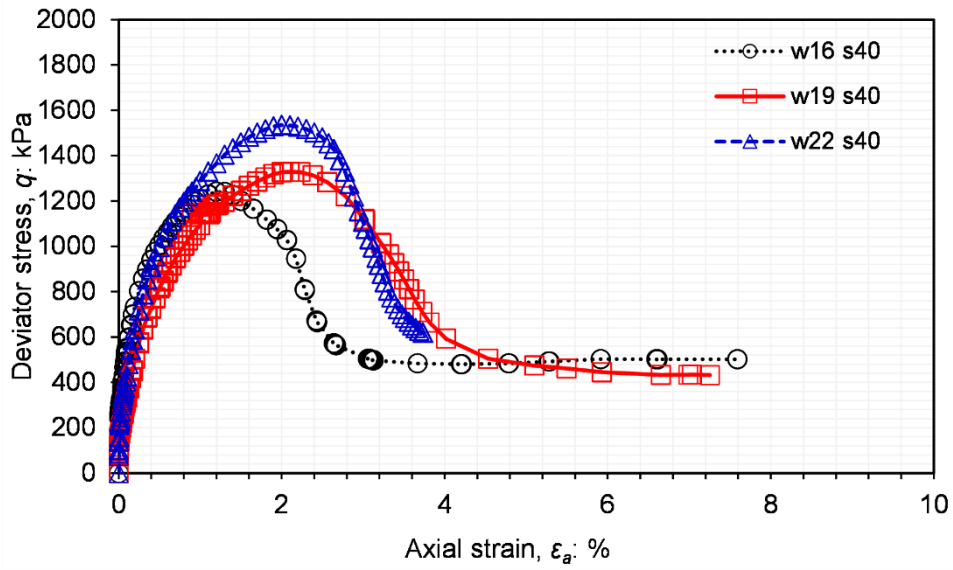


(b)

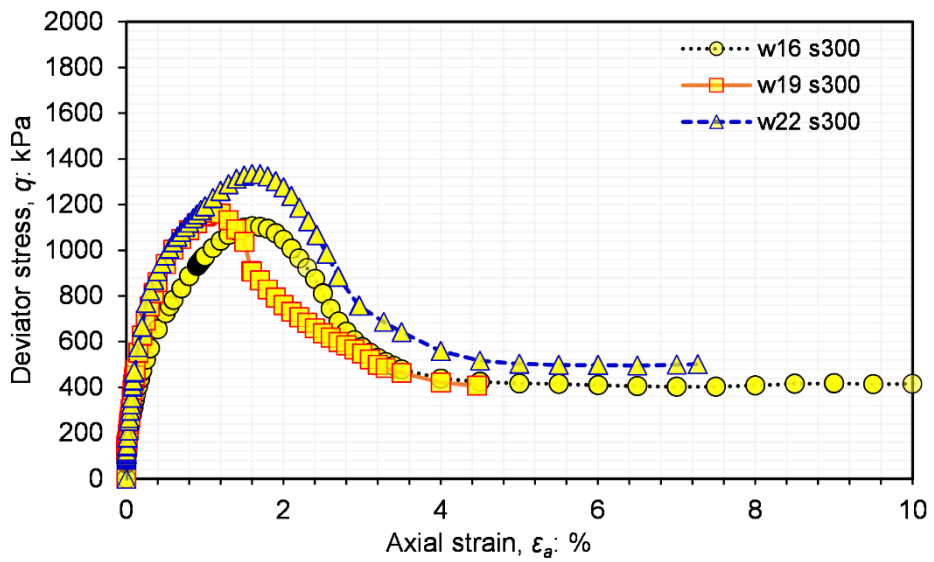


(c)

Figure 6.3 Comparison of suction of effects on inter-aggregate and intra-aggregate pore volume for different compaction water contents (a) w16, (b) w19 and (c) w22

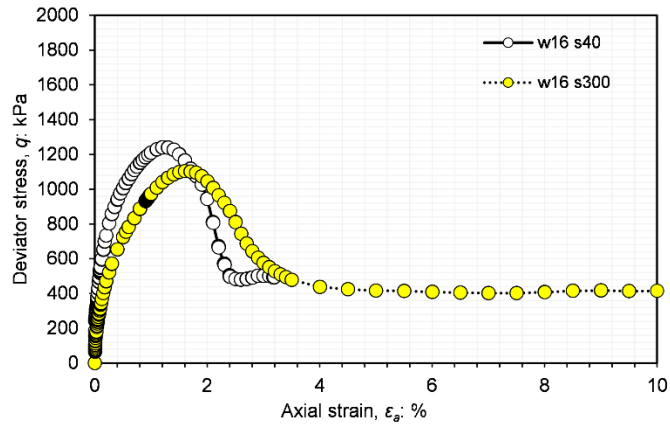


(a)

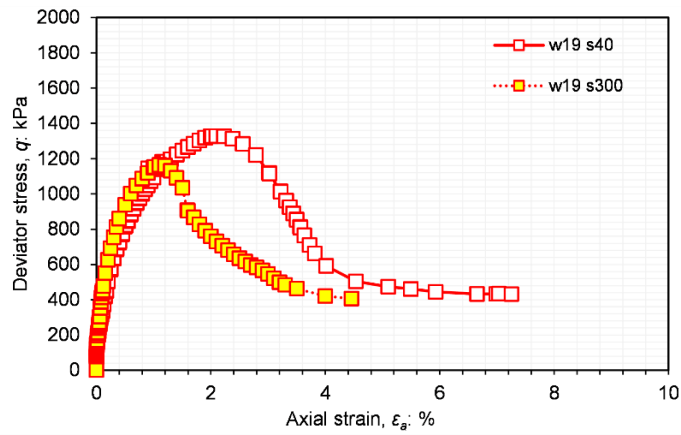


(b)

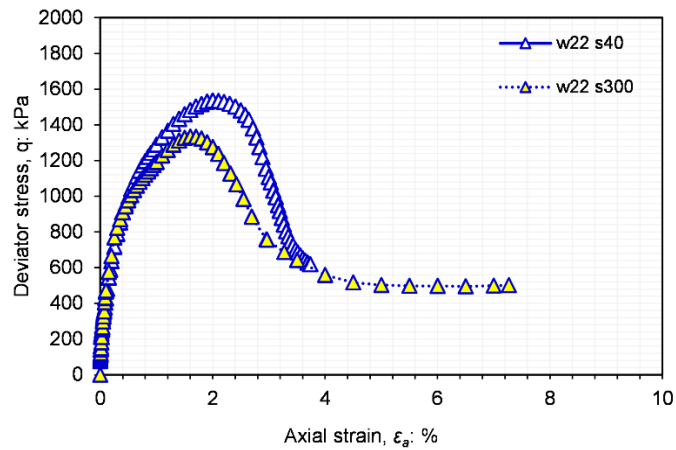
Figure 6.4 Influence of compaction water content on stress-strain at (a) 40 MPa and (c)300 MPa



(a)

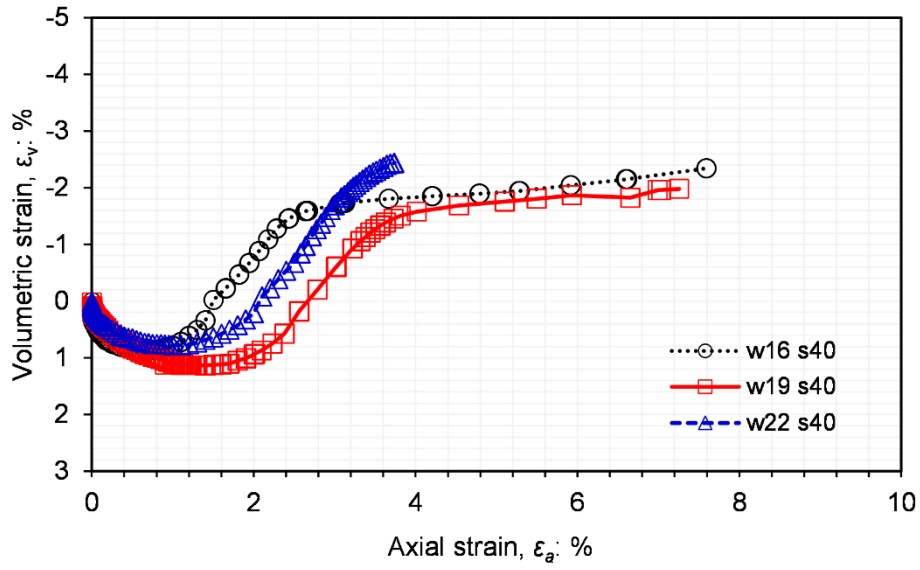


(b)

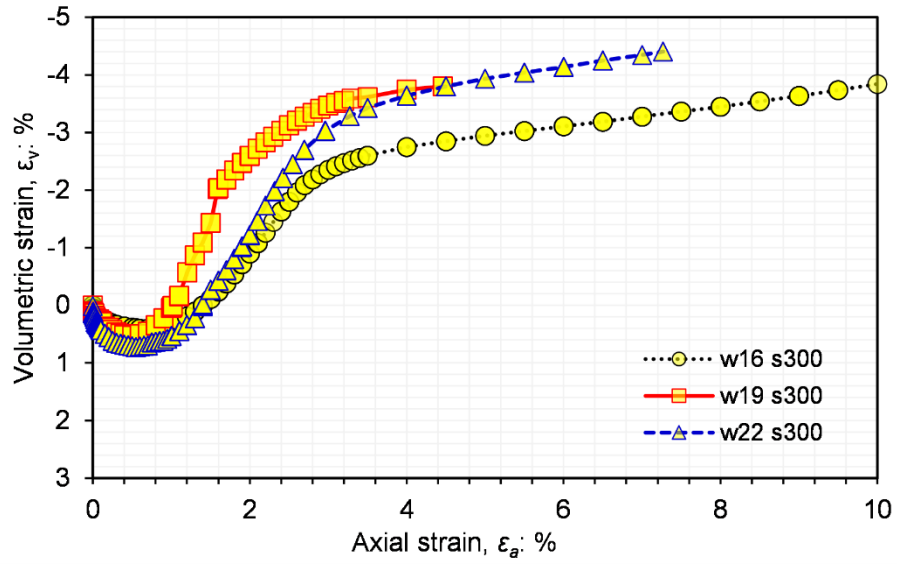


(c)

Figure 6.5 Effects of high suction on stress-strain for the compaction water content of (a) 16%, (b) 19% and (c) 22%

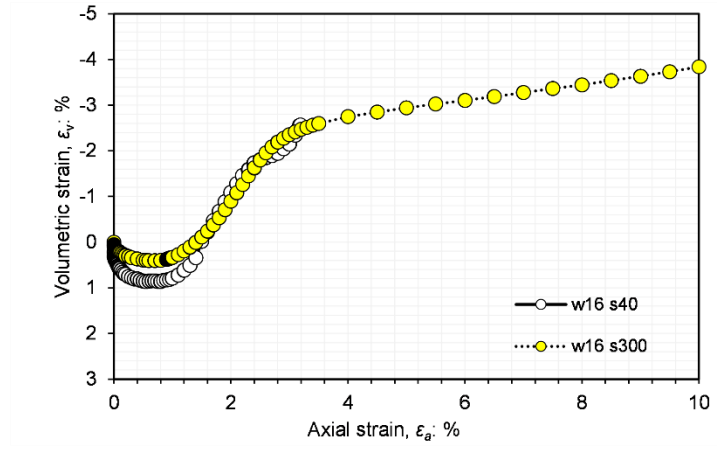


(a)

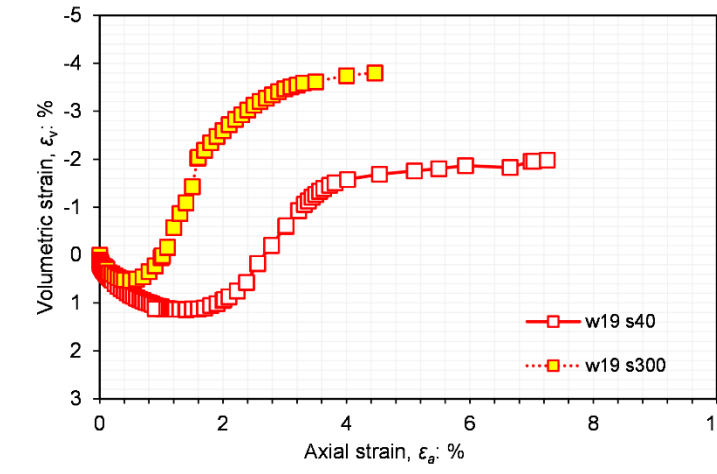


(b)

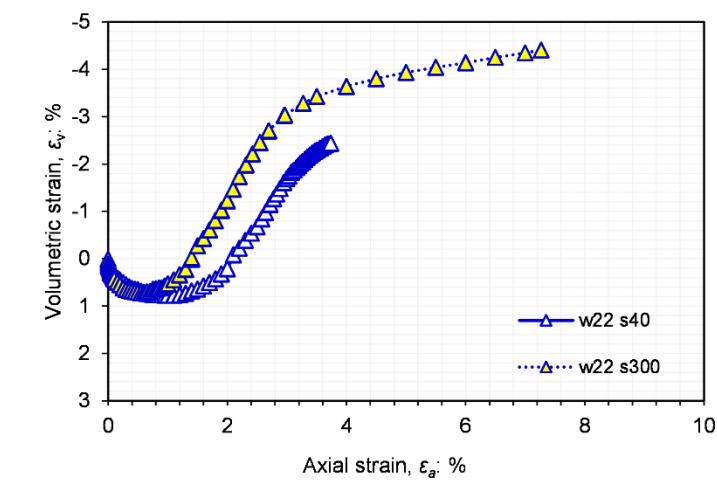
Figure 6.6 Influence of compaction water content on dilatancy at (a) 40 MPa and (b) 300 MPa



(a)



(b)



(c)

Figure 6.7 Effects of high suction on dilatancy for the compaction water content of (a) 16%, (b) 19% and (c) 22%

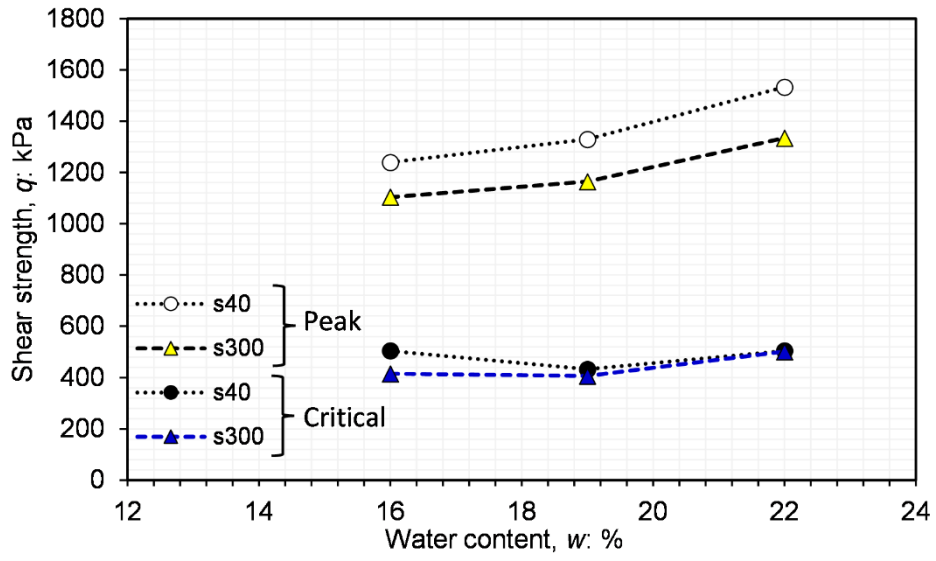
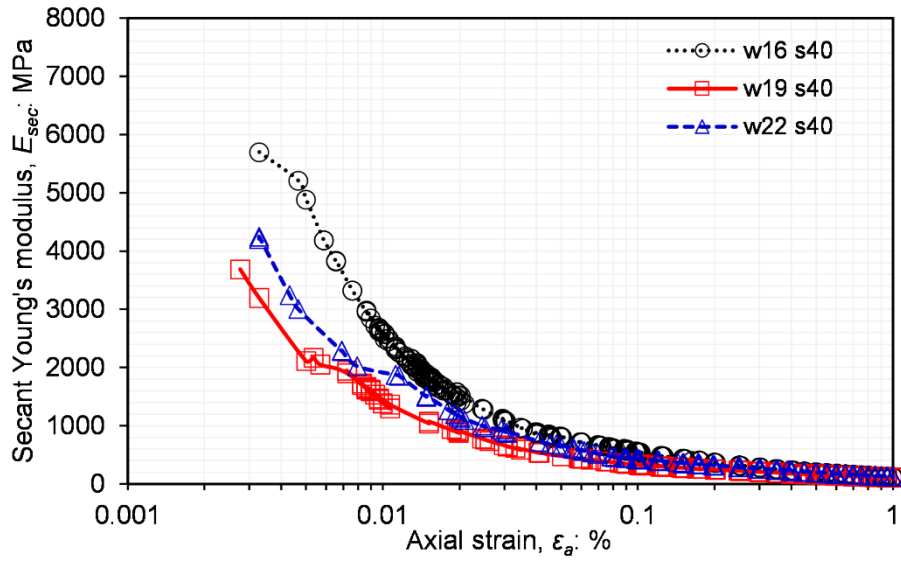
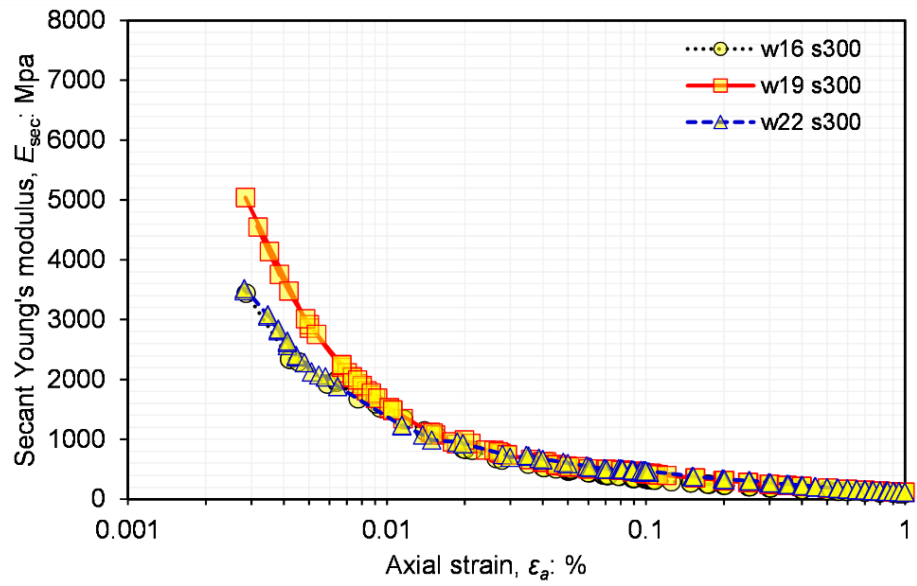


Figure 6.8 Effects of compaction water content on peak and critical state strength after high suction-induced desiccation

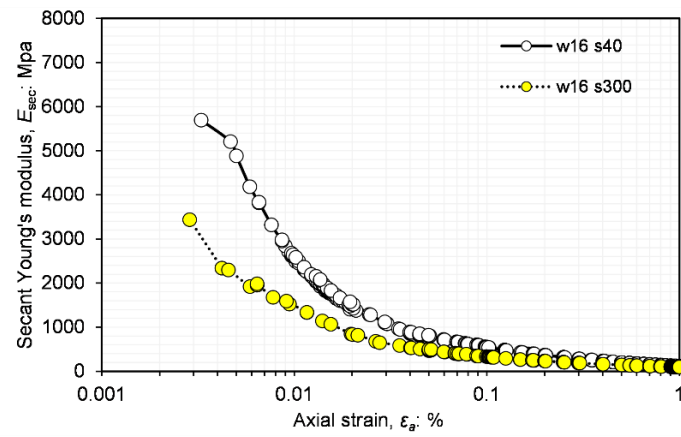


(a)

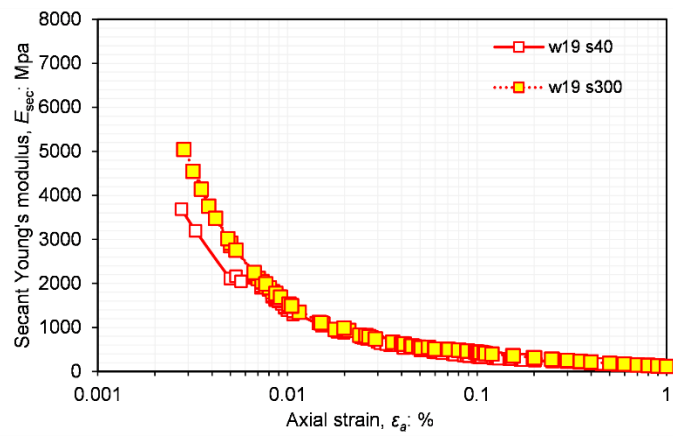


(b)

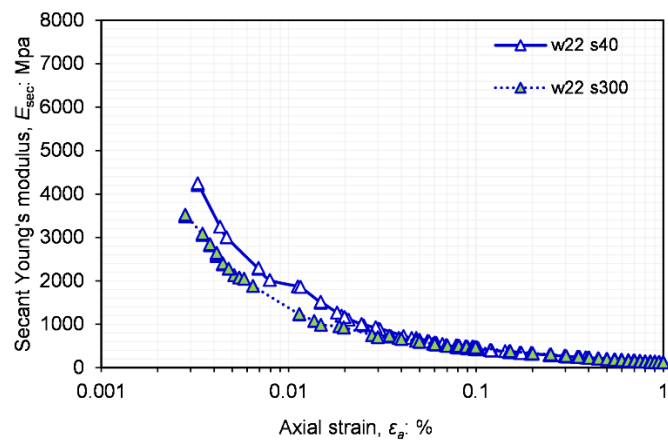
Figure 6.9 Influence of compaction water content on small strain at (a) 40 MPa and (c)300 MPa



(a)

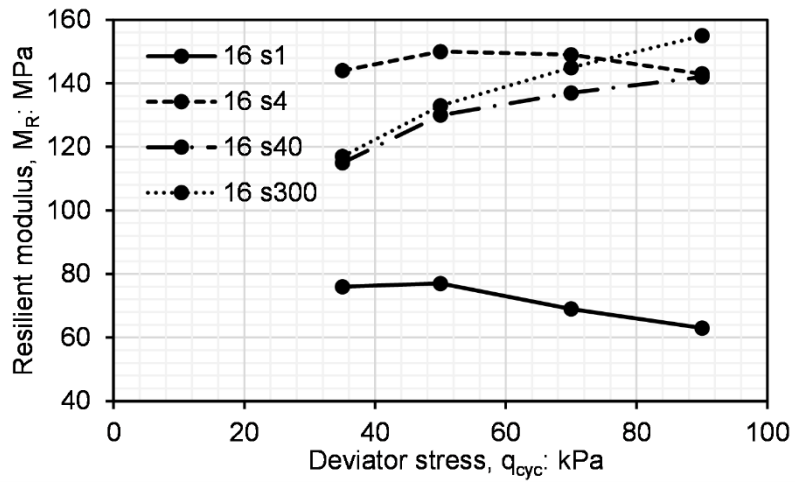


(b)

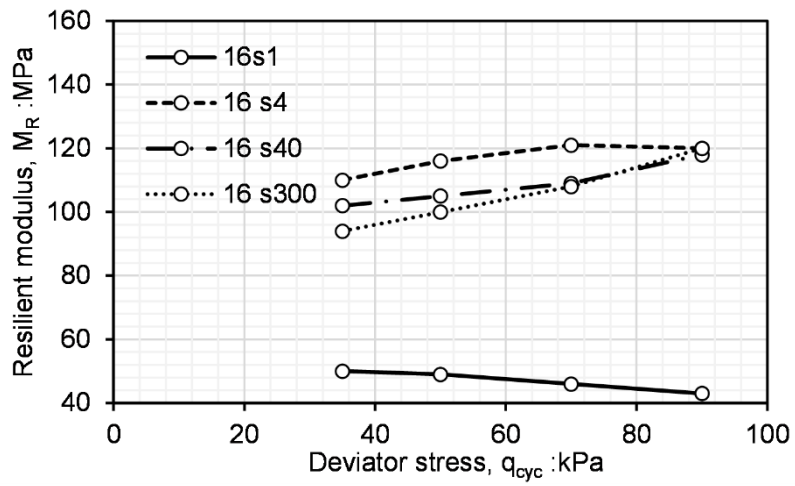


(c)

Figure 6.10 Effects of high suction on small strain stiffness for the compaction water content of (a) 16%, (b) 19% and (c) 22%

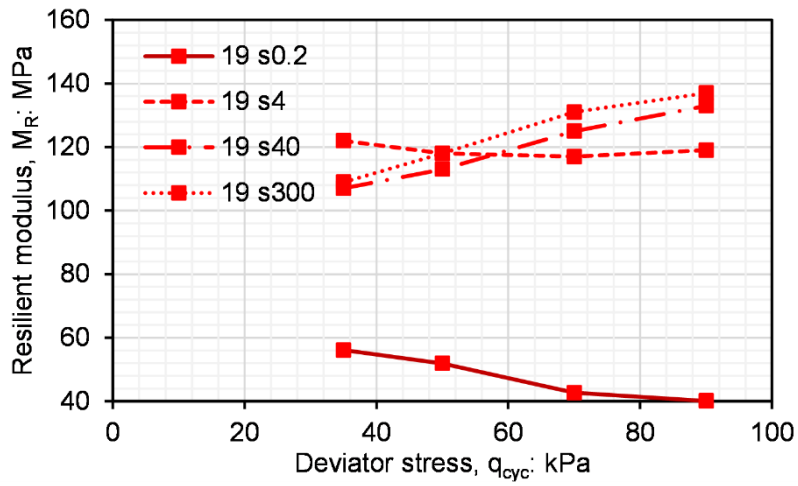


(a)

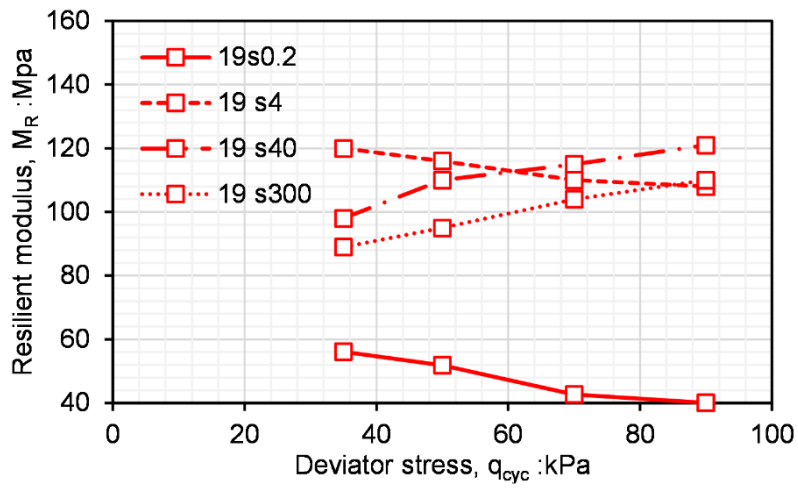


(b)

Figure 6.11 Influence of deviator stress on M_R when the compaction water content in 16.5% (a) 42 kPa and (b) 15 kPa

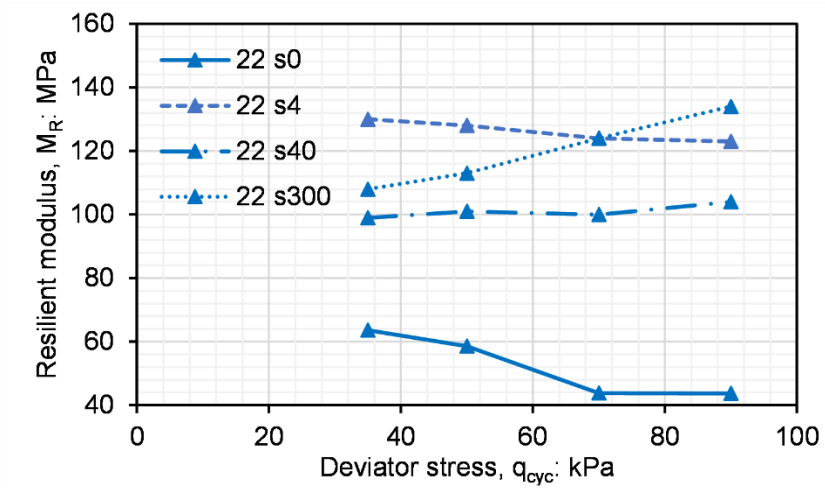


(a)

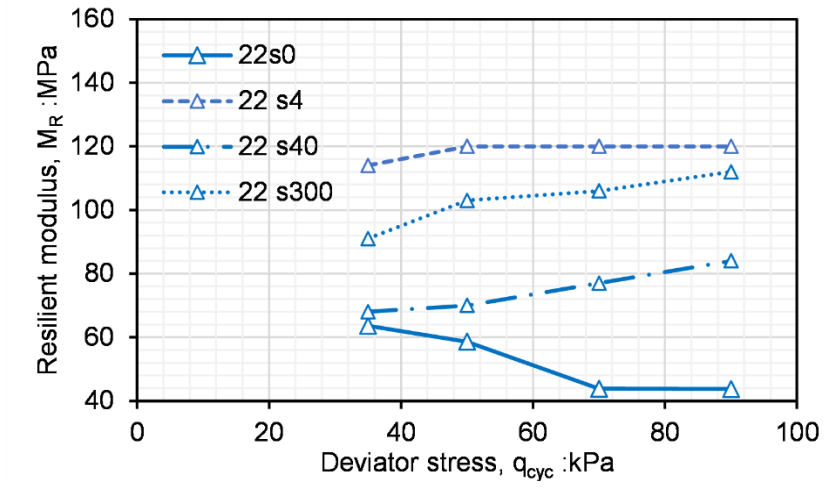


(b)

Figure 6.12 Influence of deviator stress on M_R when the compaction water content in 19.5% (a) 42 kPa and (b) 15 kPa

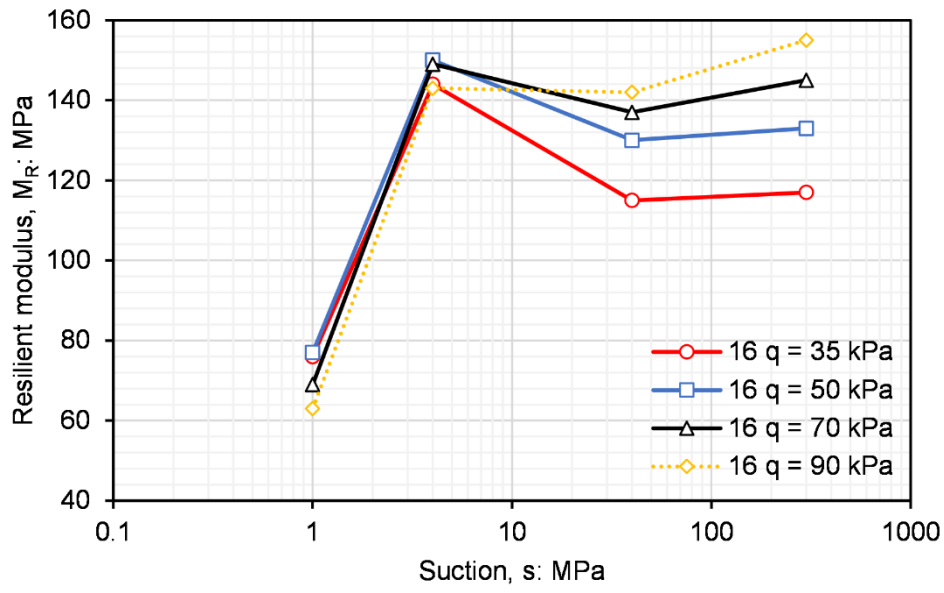


(a)

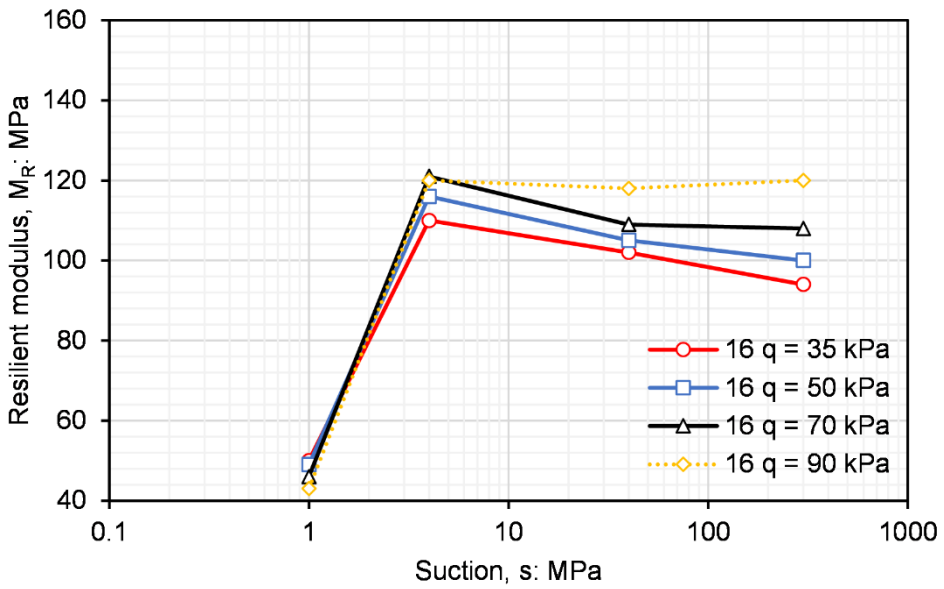


(b)

Figure 6.13 Influence of deviator stress on M_R when the compaction water content in 22.5% (a) 42 kPa and (b) 15 kPa

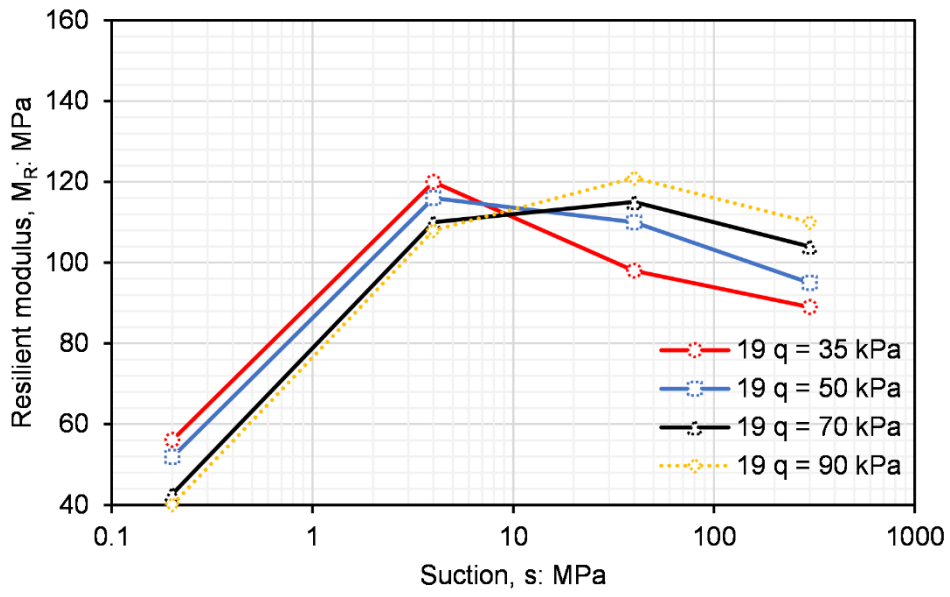


(a)

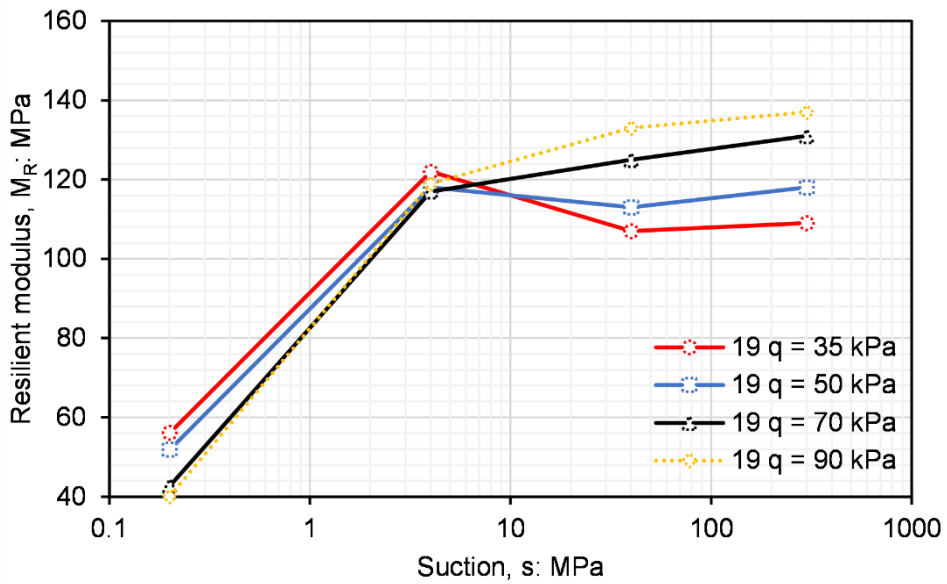


(b)

Figure 6.14 Effects of suction on M_R when the compaction water content in 16.5% (a) 42 kPa and (b) 15 kPa

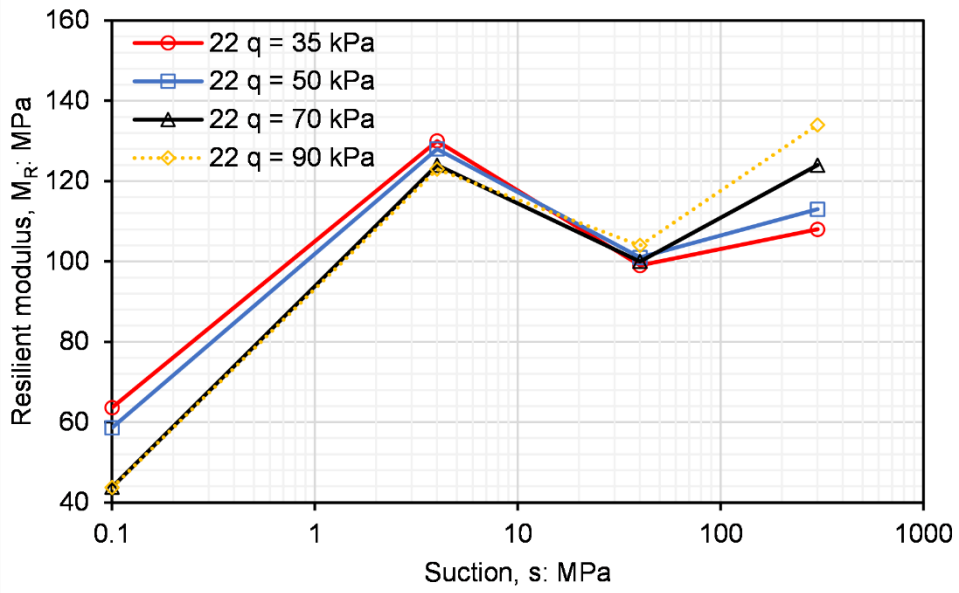


(a)

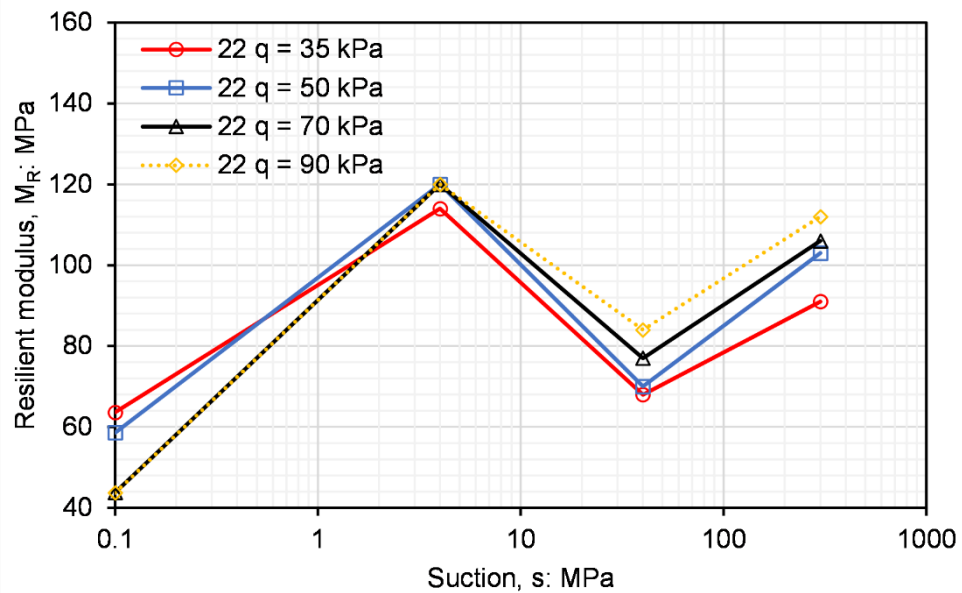


(b)

Figure 6.15 Effects of suction on M_R when the compaction water content in 19.5% (a) 42 kPa and (b) 15 kPa

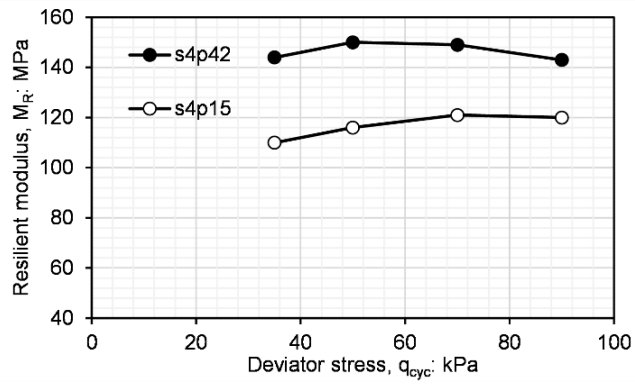


(a)

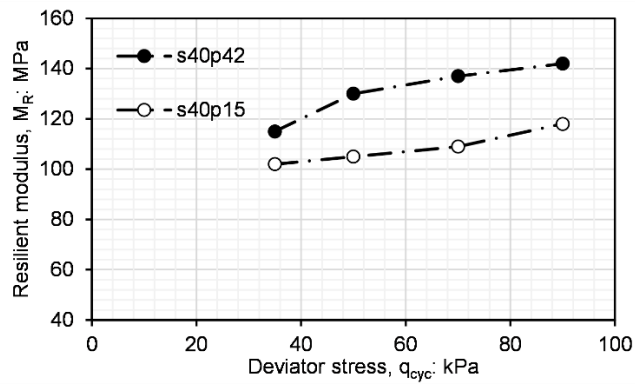


(b)

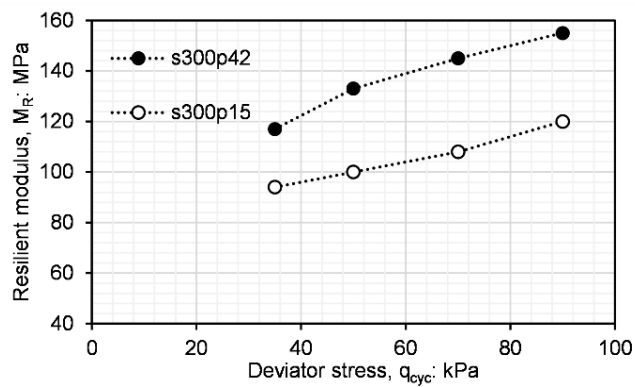
Figure 6.16 Effects of suction on M_R when the compaction water content in 22.5% (a) 42 kPa and (b) 15 kPa



(a)

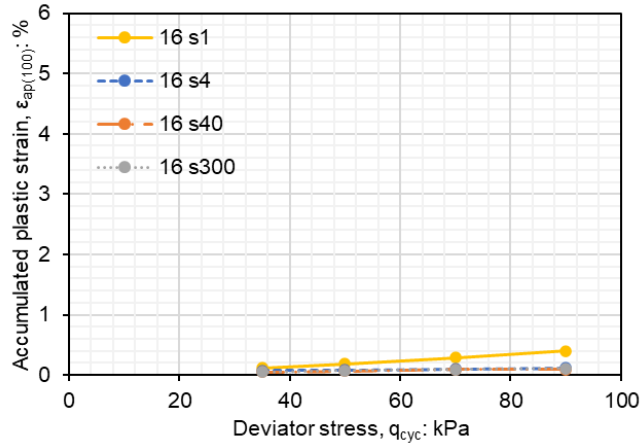


(b)

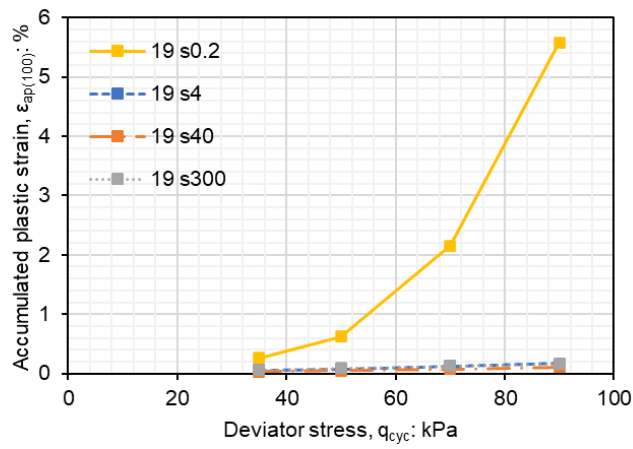


(c)

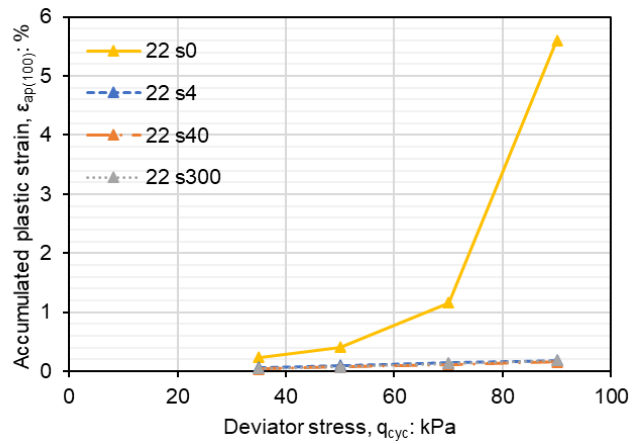
Figure 6.17 Influence of mean net stress on M_R when $w = 16\%$ at suctions of approximately (a) 4 (b) 40 (c) 300 MPa



(a)

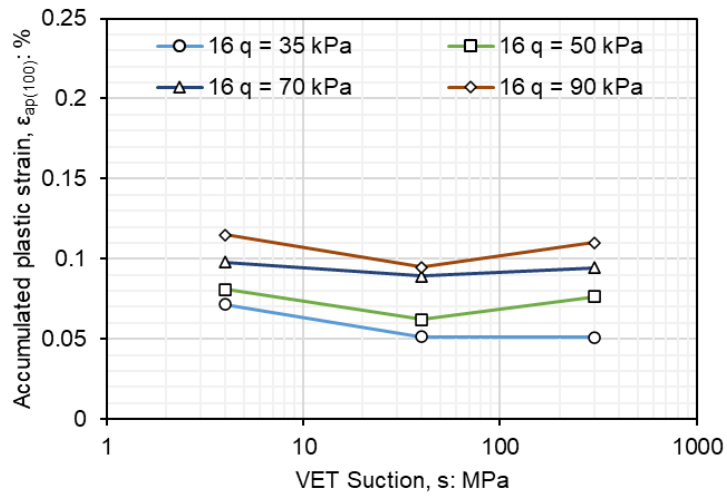


(b)

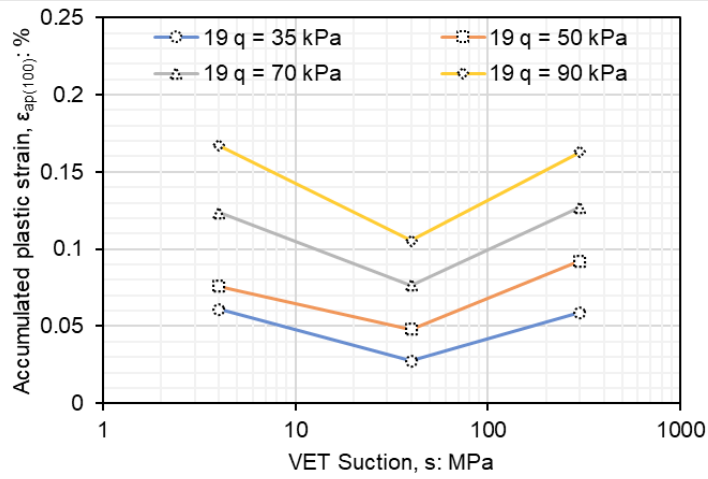


(c)

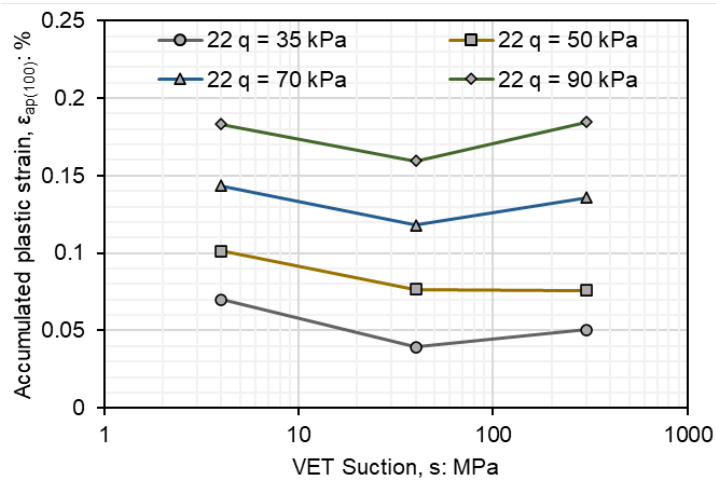
Figure 6.18 Influence of cyclic stress on plastic stain accumulation at different compaction water contents (a) w16, (b) w19 and (c) w22



(a)



(b)



(c)

Figure 6.19 Influence of high suction on plastic strain accumulation at different compaction water contents (a) w16, (b) w19 and (c) w22



Plate 6.1 Suction imposed via Vapour equilibrium technique in desiccators.

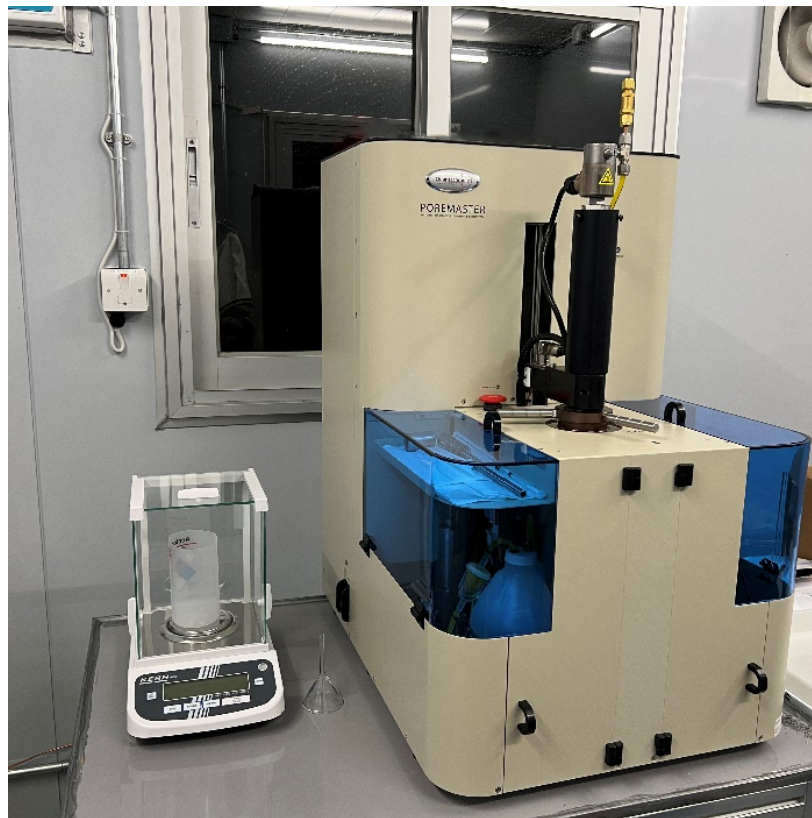


Plate 6.2 PoreMaster[®] mercury intrusion pore size analyser at HKUST

CHAPTER 7 CYCLIC THERMAL EFFECTS ON SOIL STIFFNESS AT SATURATED AND UNSATURATED CONDITIONS

This chapter presents an experimental investigation on the influence of temperature and thermal cycles on the elastic shear modulus at saturated and unsaturated conditions. The testing systems in [Figure 3.7](#) and [Figure 3.8](#) were used. A temperature range of 5 to 60°C and soil suctions below 300 kPa were considered. Temperature-controlled oedometer and isotropic compression tests were carried out. These types of tests allow for examining temperature-dependent elastic shear modulus at different boundary conditions and carrying out parallel tests. Two stress paths were utilised for the oedometer tests: constant-temperature loading-unloading and constant-stress cyclic heating-cooling at saturated conditions. On the other hand, constant stress and suction heating and cooling tests were performed for the triaxial tests at saturated and unsaturated conditions. This test results analysis focuses on the thermal effects. In addition, a semi-empirical equation was proposed to capture thermal and suction effects on elastic shear modulus.

7.1 Testing programme and procedures

7.1.1 Temperature-controlled oedometer apparatus at saturated conditions

Two types of stress- and temperature-controlled tests were carried out to investigate the effects of temperature and thermal cycles on the elastic shear modulus at saturated conditions. [Figure 7.1](#) shows their stress paths. First of all, two 1D compression tests were performed at temperatures of 5 and 40°C, as shown in [Figure 7.1\(a\)](#). In each test, the compacted specimen in the oedometer ring was submerged in water for 48 hours to achieve saturation at a low vertical effective stress of about 12 kPa and room temperature. After saturation, the required testing temperature was applied (i.e., O-A and O-B). After thermal equalisation, the vertical effective stress was increased from 30 to 400 kPa stepwise and then decreased to 30 kPa (as indicated by the short dashes and solid symbol between A-A2 and B-B2, respectively). The consolidation under a given vertical effective stress was considered to be completed when the dial gauge reading reached a value that stayed constant after 24 hours.

Secondly, two cyclic heating/cooling tests in the temperature range of 5 to 60°C were carried out at vertical effective stresses of 50 and 400 kPa [Figure 7.1\(b\)](#). After saturating the specimens using the method explained above, the specimens were loaded to the desired stress

(i.e., O-C and O-D, respectively) at room temperature and then subjected to three heating-cooling cycles stepwise (i.e., C-C1-C2 and D-D1-D2 for each cycle, respectively). Six temperature stages were considered, including 5, 20, 30, 40, 50 and 60°C. Each temperature stage was maintained for 12 hours to ensure that the specimen reached an equilibrium state. In addition, the vertical deformation of the soil specimen was monitored in all tests by a dial gauge. At the desired thermo-mechanical states indicated by markers in **Figure 7.1**, bender element tests were performed to measure the shear wave velocity to estimate $G_{0(vh)}$.

In addition to the tests on the lateritic clay, a test was carried out on Speswhite kaolin to investigate the influence of thermal cycles on $G_{0(vh)}$. The clay compacted at the OMC (i.e., 29.5%) and to 95% MDD and then saturated. After that, the specimen was subjected to three heating-cooling cycles in the temperature range of 5 to 60°C at a vertical effective stress of 400 kPa. Only two temperature stages (5 and 60°C) were considered in the process of cyclic heating-cooling to reduce the test duration. Details of the test programme are summarised in **Tables 7.1** and **7.2**.

7.1.2 Temperature- and suction-controlled tests at saturated and unsaturated conditions

Two series of tests were designed to study the coupled effects of suction and temperature on the elastic shear modulus and stiffness anisotropy of saturated and unsaturated soils. Three suctions (i.e., 0, 150 and 300 kPa) and two mean net stresses (i.e., 50 and 200 kPa) were considered. At each suction and stress condition, one thermal cycle was applied to the specimen, during which temperatures were changed stepwise (20→5→20→40°C) and anisotropic shear moduli were monitored. **Table 7.3** shows the summary of the testing programme.

Figure 7.2 shows the thermo-hydro-mechanical stress path of all specimens. Each test consists of three stages: isotropic compression, suction equalisation and thermal equalisation. After specimen preparation and setting it up in the triaxial apparatus, each specimen was compressed isotropically to mean net stress of 50 or 200 kPa at constant water content and room temperature of 20°C. Zero suction was applied to the soil specimen by controlling the air and water pressures to the same value while maintaining a constant mean net stress. After suction equalisation, which generally took about 7 to 12 days, one thermal cycle was conducted by first changing the value of temperature from 20°C to 5°C, increasing from 5°C back to 20°C, from 20°C to 40°C and finally from 40°C back to 20°C. Each applied temperature value was maintained for 24 hours, which was enough for thermal equilibrium. The bender element test

was conducted after suction and thermal equalisation. After the thermal cycle at zero suction, the specimen was dried to a suction of 150 kPa. After suction equalisation, one thermal cycle described above was applied to the specimen. Similar procedures were used for a suction value of 300 kPa.

Note that each sample was used for the testing at three different suctions. The procedures adopted here are similar to the multi-stage triaxial testing. The advantages include fewer soil specimens being tested, less laboratory time consumption and reduced effects of heterogeneity among the specimens tested. However, it should be noted that the results may be affected by the strain history of earlier stages of suction and temperature changes. These effects should be taken into account in the data analysis.

7.2 Thermal effect under one-dimensional stress conditions

7.2.1 Influence of temperature on the elastic shear modulus during one-dimensional compression

Figure 7.3 shows the one-dimensional compression curves at temperatures of 5 and 40°C. The two compression curves are almost identical in the stress range below 200 kPa. On the contrary, the specimen at 40°C is more compressible than that at 5°C above 200 kPa. During unloading, the specimens at 5 and 40°C show a similar swelling index. **Figure 7.4** shows the G_0 measured during the compression process. It can be seen that $G_{0(vh)}$ at 40°C are consistently lower than those at 5°C during both loading and unloading, even though the specific volume is lower at 40°C. The maximum difference is about 10% during loading (at 100 kPa vertical effective stress). During unloading, the maximum difference is up to 30% (at 30 kPa vertical effective stress). As discussed in the literature review, previous studies of thermal effects on soil stiffness in the literature ([Vahedifard et al. 2020](#); [Zhou et al. 2015a](#)) only considered a single stress condition. The new results of this study suggest that the significance of thermal effects was highly stress path dependent.

The observed thermal effects are likely attributed to the fact that as soil temperature increases, the repulsive electrical force between soil particles becomes larger ([Israelachvili 2011](#)). The reduction in the inter-particle forces would lead to a decrease in the shear wave velocity and $G_{0(vh)}$.

7.2.2 Effects of thermal cycles on the elastic shear modulus at different stress states

Figure 7.5 shows the volumetric strain response of the specimens subjected to cyclic heating and cooling at constant vertical effective stress of 50 kPa and 400 kPa. At 50 kPa, during the first cooling from room temperature (20°C) to 5°C, no noticeable volumetric strain was observed. When the soil was heated from 5°C back to 20°C, an expansion of about 0.03% strain was observed. A contraction was observed with further heating from 20°C to 60°C. As the thermal loading cycles increase, an accumulation of contractive axial strain of 0.11% was observed. With regards to a vertical effective stress of 400 kPa, the first cooling stage from 20°C to 5°C showed a small contractive strain of about 0.01%. With heating from 5°C to 20°C, an additional contractive strain of up to about 0.09% occurred. The contractive strain increased up to about 0.44% when the temperature was increased to 60°C. After four thermal loading cycles, there was an accumulation of contractive volumetric strain of about 0.66%. The results at 50 kPa are similar to those at 400 kPa, but the thermal strains are much smaller. The difference is mainly because the specimens at 400 and 50 kPa are normally consolidated and overconsolidated, respectively. Similar findings were reported in the literature (Abuel-Naga et al. 2007; Di Donna and Laloui 2015).

Figure 7.6(a) shows the measured $G_{0(vh)}$ during the thermal loading cycles at a vertical effective stress of 50 kPa. During the first cooling phase from 20°C to 5°C, a reduction in the value of $G_{0(vh)}$ was observed. Further heating from 5°C to 60°C, a continuous decrease in G_0 until 40°C, followed by an increase in $G_{0(vh)}$ at 50°C and then lastly a decrease at 60°C. During the subsequent cooling stage from 60°C to 5°C, the value of $G_{0(vh)}$ continuously increases with a decrease in temperature. **Figure 7.6(b)** shows the measured $G_{0(vh)}$ during the thermal loading cycles for a vertical effective stress of 400 kPa. Similar to the vertical effective stress state at 50 kPa, the value of $G_{0(vh)}$ generally decreased during heating and increased during cooling, but with different magnitudes. The decrease in $G_{0(vh)}$ at a higher temperature during thermal cycles is consistent with the results from one-dimensional compression at two different temperatures.

Figure 7.7 presents the evolution of $G_{0(vh)}$ measured at room temperature of 5°C but after thermal cycles. At both vertical effective stresses of 50 and 400 kPa, the $G_{0(vh)}$ consistently increased during heating and cooling, very likely due to heating/cooling cycles-induced soil

densification and particle rearrangement. When the vertical effective stresses are 50 and 400 kPa, the $G_{0(vh)}$ increased by about 12% and 16% over four thermal cycles, respectively. The difference is most probably because the contractive thermal strain is much larger at 400 kPa, as shown in **Figure 7.6**. The results of the kaolin clay are also included in **Figure 7.7**. It can be seen that the thermal cycles result in an increase in $G_{0(vh)}$ by about 30%, similar to that of the lateritic clay.

7.3 Thermal and suction effects under isotropic stress conditions

7.3.1 Influence of temperature on G_0 at different suctions under isotropic stress condition

Figure 7.8 shows the changes in G_0 with temperature at various suctions for a mean net stress of 50 kPa. As shown in **Figure 7.8(a)**, an increase in temperature generally results in a decrease in $G_{0(hh)}$ for all the suction values considered. The reduction rate appears to be dependent on the suction value. When suction is 0 kPa, as the temperature increases from 5°C to 20°C, the value of $G_{0(hh)}$ reduces by about 5% and further reduces by 21% when the temperature increases from 20°C to 40°C. At a suction of 150 kPa, the value of $G_{0(hh)}$ reduces by about 2% when the temperature increases from 5°C to 20°C. $G_{0(hh)}$ further decrease by about 6% from 20°C to 40°C. Lastly, when the value of suction increases to 300 kPa, the value of $G_{0(hh)}$ reduces by about 6% when temperature increases from 5°C to 20°C. $G_{0(hh)}$ further decrease by about 5% from 20°C to 40°C. Similar in **Figure 7.8(b)**, $G_{0(hv)}$ reduces with an increase in temperature for all suction values investigated. The maximum reduction is about 22% at 0 kPa suction for $G_{0(hh)}$ and $G_{0(hv)}$.

Figure 7.9 represents the variation of G_0 with temperature at various suctions for mean net stress of 200 kPa. With respect to $G_{0(hh)}$ shown in **Figure 7.9(a)**, when the temperature increases from 5°C to 20°C, the value of $G_{0(hh)}$ reduces by about 8%, and further reduces by 13% when temperature increases from 20°C to 40°C when suction is 0 kPa. At a suction of 150 kPa, the value of $G_{0(hh)}$ reduces by about 6% when the temperature increases from 5°C to 20°C. $G_{0(hh)}$ further decrease by about 18% from 20°C to 40°C. Lastly, when the value of suction

increases to 300 kPa, the value of $G_{0(hh)}$ reduces by about 11% when the temperature increases from 5°C to 20°C. $G_{0(hh)}$ further decrease by about 45% from 20°C to 40°C. The magnitude of reduction in stiffness with temperature for mean net stress of 200 kPa appears to be dependent on the suction value.

To interpret the experiment results, an idealised parking of soil particles and distribution of air water interfaces is used, as previously shown in [Figure 2.4](#) ([Gallipoli et al. 2003](#); [Wheeler and Karube 1996](#)). When the soil is fully saturated, there is no air-water interface or meniscus water present. There is a possible reduction of G_0 with an increase in temperature and that reduction cannot be attributed to a decrease in surface tension. The observed thermal effects are likely attributed to the fact that as soil temperature increases, the electrical repulse force between soil particles becomes larger ([Israelachvili 2011](#)). On the other hand, as the soil becomes unsaturated with the presence of meniscus water ([Fisher 1926](#); [Gallipoli et al. 2003](#); [Lourenço et al. 2012](#); [Wheeler and Karube 1996](#)), there is an increase of inter-particle contact force to stabilize the soil. However, at that unsaturated condition, owing to an increase of temperature there is an additional reduction of G_0 because of the reduction in surface tension from the air-water interface. Moreover, it can be seen from [Table 7.3](#) that at the same suction, the Bishop's effective stress also reduces with an increase of temperature. The decreasing Bishop's effective stress is because of a decrease of degree of saturation, and the reduced the water retention ability of the soil at higher temperature.

7.3.2 Effects of suction on the G_0 at different temperatures

[Figure 7.10](#) shows the changes of G_0 with suction for the temperatures considered in this study. At mean net stress of 50 kPa, as expected, an increase in suction results in an increase in both $G_{0(hh)}$ and $G_{0(hv)}$, irrespective of the temperature. Similar to 50 kPa, as the suction increases, the value of $G_{0(hh)}$ and $G_{0(hv)}$ increase for mean net stress of 200 kPa ([Figure 7.11](#)), irrespective of the temperature. The difference in G_0 becomes larger, particularly for $G_{0(hh)}$, as the suction increases for 200 kPa mean net stress, unlike at 50 kPa mean net stress.

Considering the influence of suction G_0 at various temperatures, similar results were obtained by [Vahedifard et al. \(2020\)](#), who reported that difference of G_0 at 20°C to 43°C

becomes larger as suction increases. However, they only measured the G_0 value at one plane (i.e., $G_{0(vh)}$).

The results of this study reveal a possible thermal-induced anisotropy that may be significant for other soils as shown in [Figure 7.12](#). This should be considered depending on the microstructural characteristics of the soil and mineralogy in further studies. This thermal-induced anisotropy may be due to thermal strains observed in the axial and radial directions of the specimen. Although heating may result in the contraction of the specimen and a possible additional drying effect (i.e., reduced water retention), reduction in the interparticle forces between the particle contacts may play a dominant role. Moreover, the particle orientation and distribution of the air-water interface may be different at different planes.

7.4 Discussion about cyclic thermal effects on soil stiffness

7.4.1 Discussion on the existing formulations for temperature-dependent G_0

Several important findings can be obtained based on the results shown in the previous section. Firstly, the shear modulus would decrease with an increase in temperature ([Figure 7.4](#) and [Figure 7.6](#)), at least for the tested lateritic clay. At saturated conditions, the reduction can be attributed to the influence of temperature on the interparticle force of saturated clay ([Laloui 2001](#)). As suggested by the double layer theories ([Israelachvili 2011](#)), an increase in soil temperature would increase the repulsive electrical force between soil particles, thereby causing a reduction of shear modulus. At unsaturated conditions, some other mechanisms, like reducing surface tension coefficient with heating, also reduce the shear modulus. In an unsaturated soil, the temperature dependence of T_s , which is equivalent to 72.8 mN/m and 68.8 mN/m at 20°C and 40°C, respectively, could be the cause of the observed decrease in G_0 ([Ng and Menzies 2007b](#)). According to [Romero et al. \(2003\)](#), the drop in T_s with rising temperature would impact both the soil's capacity for retention, which would result in a fall in S_r and the inter-granular additional stress brought on by the meniscus water.

Secondly, the shear modulus increases with an increasing number of thermal cycles ([Figure 7.7](#)), particularly for normally consolidated soil. This is partially due to the irreversible contractive strain accumulated during the heating-cooling cycles.

Thirdly, as expected, the shear modulus increases with an increase in effective stress (**Figure 7.4**). This is well expected, because an increase in effective stress can enhance the inter-particle contact.

The preliminary data implies that a switch of the mechanical and thermal loading paths is likely to affect shear modulus. For example, the specimens at point A1 in **Figure 7.1(a)** and point C1 in **Figure 7.1(b)** have the same effective stress and temperature, but their shear moduli differ by 8%. The specimen subjected to a compression-cooling path shows a larger shear modulus than that with a cooling-compression path. This is at least partially because the former specimen was compressed at a higher temperature, resulting in a larger reduction of void ratio.

7.4.2 Discussion on the existing formulations for temperature-dependent G_0

The findings from this study can be readily applied in the theoretical modelling of soil behaviour. So far, many thermo-mechanical models have been reported in the literature within the elastoplastic framework. The thermo-plasticity has been well understood and incorporated in the models ([Abuel-Naga et al. 2009b](#); [Graham et al. 2001](#); [Hamidi et al. 2014](#); [Hueckel and Baldi 1990](#); [Zhou and Ng 2015a](#)). However, the existing models do not consider thermal effects on the elastic behaviour due to the lack of experimental data, except the models reported by [Graham et al. \(2001\)](#) and [Hamidi et al. \(2014\)](#). Even though these two models have incorporated thermal effects on the G_0 , the relevant formulations were not verified using experimental results. The results from this study may give some insights into their formulations for G_0 . Since their G_0 formulations are similar, only the one by [Hamidi et al. \(2014\)](#) is discussed here:

$$G_{T(OC)} = G_{T_0(NC)} \left(\frac{p'}{p'_c} \right)^b \left[1 + D \ln \left(\frac{T}{T_0} \right) \right] \quad (7.1)$$

where $G_{T(OC)}$ is the shear modulus of overconsolidated soil at a temperature of T ; $G_{T_0(NC)}$ is the shear modulus of normally consolidated soil at a reference temperature T_0 ; p'_c is the preconsolidation stress; p' is the current effective mean stresses; and D and b are model parameters. Based on the experimental results shown in **Figure 7.6**, G_0 can be either larger or small when the temperature is higher, depending on soil type, temperature range, etc. In addition, the equation suggests that the effects of temperature and OCR are independent, whereas the observed thermal effects are more significant when the OCR is lower (see **Figure 7.6**). The above analysis illustrates that D is a function of several factors, such as soil type,

temperature range and OCR, rather than a constant value. More experimental results are required to fully understand the evolution of D .

7.4.3 A semi-empirical equation for temperature-dependent modulus of saturated and unsaturated soils

To analyse, discuss and later propose a semi-empirical equation for elastic shear modulus that considers temperature and suction, the following shear modulus equation is considered:

$$G_0 = C_0 \frac{(2.973 - e)^2}{(1 + e)} \left(\frac{p^*}{p_r} \right)^{n_\sigma} (1 + \xi)^{n_s} \quad (7.2)$$

where C_0 , n_σ , n_s are soil parameters; all the other parameters retain the same definitions as mentioned in previous chapters (see [equation \(5.3\)](#)). As mentioned previously, the influence of Bishop's stress and suction can be considered to be similar to the changes that occur in the shear modulus and Young's modulus at an unsaturated state, respectively ([Heitor et al. 2015](#); [Lee and Santamarina 2005](#); [Lu 2018](#); [Lu and Kaya 2014](#)).

As can be seen from [Figure 7.8](#) and [Figure 7.9](#), the measured G_0 values were consistently smaller at a higher temperature of 40°C than that at 20°C and 5°C for the same suction. There are several possible explanations for this result, as discussed above. Thus, the temperature-dependent elastic shear modulus of unsaturated soil is calculated by the following new equation:

$$G_{0(T)} = C_0 \frac{(2.973 - e)^2}{(1 + e)} \left(\frac{p^*}{p_r} \right)^{n_\sigma} (1 + \xi)^{n_s} \left[\frac{T}{T_r} \right]^{-\omega} \quad (7.3)$$

where $G_{0(T)}$ is the elastic shear modulus at a particular temperature; T is temperature; T_r is reference temperature which can be taken as room temperature (i.e. 20°C); ω is a parameter controlling the reduction of elastic shear modulus with temperature. All other parameters retain the same meaning as previously mentioned. These parameters may be calibrated by using elastic shear modulus results of suction-controlled tests at room temperature.

Few experimental studies directly describing the elastic shear modulus of unsaturated soils at various temperatures are available in the literature. Hence, the proposed semi-empirical equation was verified by comparing measured results from the experiments on a lateritic clay in this study and predicted values, in addition to results on silty soil reported in the literature by [Vahedifard et al. \(2020\)](#).

Figure 7.13 represents the measured and estimated elastic shear moduli at various suctions and temperatures for the lateritic clay in this study. G_0 increases with suction at the same mean net stress and measured plane but decreases with temperature. The temperature had a greater effect on shear modulus at higher matric suctions. **Figure 7.14** shows the measured and calculated elastic shear moduli for a silty soil in a study by [Vahedifard et al. \(2020\)](#). The measured and calculated elastic shear moduli are fairly matched, showing similar trends. The parameters in [equation \(7.3\)](#) are summarised in **Table 7.5**. Based on the fitting parameters, the measured and estimated elastic shear moduli are generally consistent, despite some variations.

The influence of suction on the measured stiffness in this Chapter is qualitatively similar to the results obtained in Chapter 5. The proposed semi-empirical relations build on the one utilized in Chapter because the power soil parameters for stress and suction are calibrated with reference to Chapter 5. Stress and suction effects are accounted for utilising the values of n_σ and n_s are soil parameters. These two parameters are kept consistent in both Chapters. The results in Chapter 5 serve as a reference in the description of the suction effects at room temperature. With changes in temperature at a particular suction, the soil stiffness changes, as revealed in this chapter.

7.4.4 Potential applications of temperature-dependent G_0 in the geotechnical analysis

There are very limited studies of G_0 at non-isothermal conditions in the literature, but it is an important parameter in many methods of analyzing thermally active structures like energy piles. For the soils surrounding energy piles, they are subjected to heating-cooling cycles.

[\(Ng et al. 2015\)](#) derived an analytical solution to predict the influence of temperature on the shaft resistance of energy piles based on the cavity expansion theory. In their solution, the shear modulus of soil is dependent on two factors, including G_0 and the stiffness degradation rate with strain. The value of G_0 (typically in the range below 0.001%) would affect the predicted shear modulus at various strains, so G_0 is a crucial input parameter. This study provides useful experimental data to reveal the influence of temperature and thermal cycles on G_0 . When the operational temperature of energy piles increases from 5 to 40°C in a typical range, the reduction of G_0 can be up to 30% (**Figure 7.4**). It would be more conservative to adopt the value of G_0 measured at the highest operating temperature in the design of energy piles. Moreover, G_0 increases as the number of thermal cycles increases (**Figure 7.7**). This would be beneficial to the long-term performance of energy piles. In addition, the progressive

thermal contraction of soils (**Figure 7.5**) could reduce the normal force at pile-soil interfaces and therefore induce additional pile settlement.

Note that the above observations and discussion should be treated with caution, since they may be specific and only applicable to some soil types. Experimental data in the literature suggest that the thermo-mechanical behaviour of fine-grained soils is qualitatively similar. At a quantitative level, some researchers ([Abuel-Naga et al. 2007](#); [Di Donna and Laloui 2015](#); [Ng et al. 2020b](#); [Sultan et al. 2002](#)) correlated the plastic index (PI) and thermal effects on soil behaviour. When the PI of soil is higher, its behaviour is more sensitive to the change in temperature. Further studies are recommended to examine G_0 for a variety of soils.

7.5 Summary

The elastic shear modulus G_0 is lower at a higher temperature. When the temperature increases from 20 to 40°C, the increase is up to 30% for the tested lateritic clay. This may be because an increase in temperature causes an increase in the repulsive electric forces between particle contacts of fine-grained soils. Consequently, the shear wave velocity and hence G_0 decreases during heating. After four thermal cycles in the temperature of 5 and 60°C, the value G_0 increased, mainly attributed to soil densification and particle rearrangement induced by heating/cooling cycles. Moreover, the increase is about 12% and 16% for specimens loaded at 50 and 400 kPa, respectively. The stress-dependency of G_0 increase is since the accumulated contractive volumetric strain at 400 kPa (normally consolidated) is much larger than that at 50 kPa (overly consolidated).

The elastic shear modulus G_0 is lower at a higher temperature for the same suction. This result may be explained by the fact that an increase in temperature causes an increase in the repulsive electric forces between particle contacts of fine-grained soils. Thus, the shear wave velocity and hence G_0 decreases during heating. Another possible explanation for this is that with increasing temperature at constant suction, there is a reduction in the air-water surface tension between particles and aggregates.

It has been found that the reduction in elastic shear modulus with temperature increase varies in magnitude and depends on the measuring plane. This dependency may be explained by the varied rates at which minerals expand in different measured planes or, more likely, by variations in the amount by which surface tension is reduced in different measured planes,

reducing the interaction between particles and aggregates. The data thus suggest a potential thermally induced anisotropy, which calls for additional research.

A semi-empirical equation is proposed based on the experimental results and limited data from the literature. The prediction of elastic shear modulus is reasonable, showing that an increase in temperature reduces the elastic shear modulus at various suctions. To analyse and improve the semi-empirical equation for various soil types and wider ranges of suction and temperature, more experiments are advised for the different measurement planes of shear modulus.

Table 7.1 Testing programme for constant temperature loading and unloading one-dimensional stress

Specimen ID	Compaction method	Initial Water Content, w: %	Initial Void Ratio, e	Temperature, T: °C	Stress: kPa
e0.65-T5	Static	19.5	0.65	5	30, 50, 100, 200 & 400
e0.65-T40			0.65	40	30, 50, 100, 200 & 400

Table 7.2 Testing programme for thermal cycles on G_0 at constant one-dimensional stress

Specimen ID	Compaction method	Initial Water Content, w: %	Initial Void Ratio, e	Stress: kPa	Temperature Cycles, T: °C
e0.65p50	Static	19.5	0.65	50	20-5-20-30-40-50-60
e0.65p400			0.65	400	20-5-20-30-40-50-60

Table 7.3 Testing programme for coupled suction and thermal effects on G_0 at constant stress

Test series	Specimen ID	Mean net stress: kPa	Suction, s: kPa	Stress path
1	p50-s0	50	0	A-B1-C1* D1*-E1*
	p50-s150		150	
	p50-s300		300	
2	p200-s0	200	0	A-B2-C2* D2*-E2*
	p200-s150		150	
	p200-s300		300	

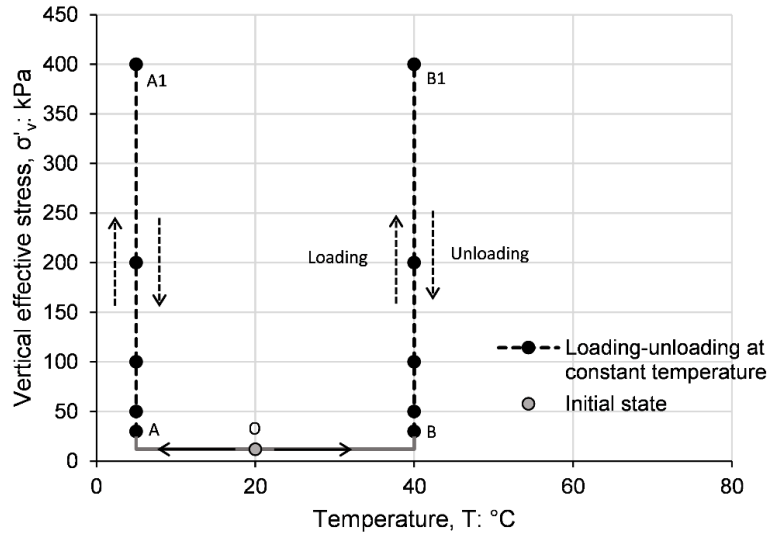
*At each suction condition, one thermal cycle was applied to the specimen with the following stages: 20 ↔ 5 ↔ 20 ↔ 40°C.

Table 7.4 Soil states at suction and thermal equilibrium

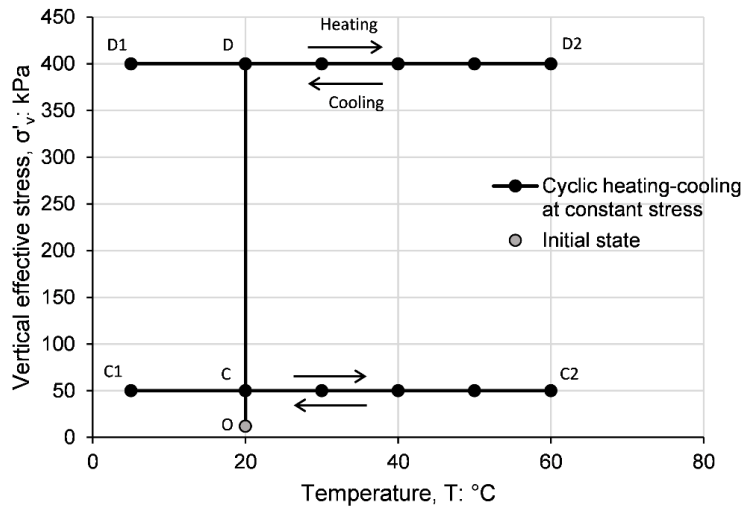
Test series	Specimen ID	Mean net stress, p: kPa	Suction, s: kPa	Temperature, T: °C	Degree of saturation, S_r	Bishop's stress, p^* : kPa	Void ratio, e
1	p50 s0 T5	50	0	5	0.422	50	0.675
	p50 s150 T5		150		0.532	130	0.678
	p50 s300 T5		300		0.400	170	0.673
	p50 s0 T20	50	0	20	0.417	50	0.675
	p50 s150 T20		150		0.521	128	0.677
	p50 s300 T20		300		0.392	167	0.674
	p50 s0 T40	50	0	40	0.405	50	0.663
	p50 s150 T40		150		0.493	124	0.666
	p50 s300 T40		300		0.352	156	0.661
2	p200 s0 T5	200	0	5	0.949	200	0.582
	p200 s150 T5		150		0.716	307	0.581
	p200 s300 T5		300		0.596	379	0.577
	p200 s0 T20	200	0	20	0.937	200	0.583
	p200 s150 T20		150		0.710	306	0.582
	p200 s300 T20		300		0.578	373	0.578
	p200 s0 T40	200	0	40	0.923	200	0.575
	p200 s150 T40		150		0.697	304	0.573
	p200 s300 T40		300		0.539	362	0.579

Table 7.5 Calibrated fitting parameters for the proposed semi-empirical equation

Soil Type (Reference)	C_0	n_σ	n_s	ω
Lateritic clay (this study)	6	0.35	2.8	0.20
Silty soil (Vahedifard et al. 2020)	3.8	0.35	1.5	0.35



(a)



(b)

Figure 7.1 Thermo-mechanical paths (a) 1D compression at constant temperature (b) cyclic heating-cooling at constant stress

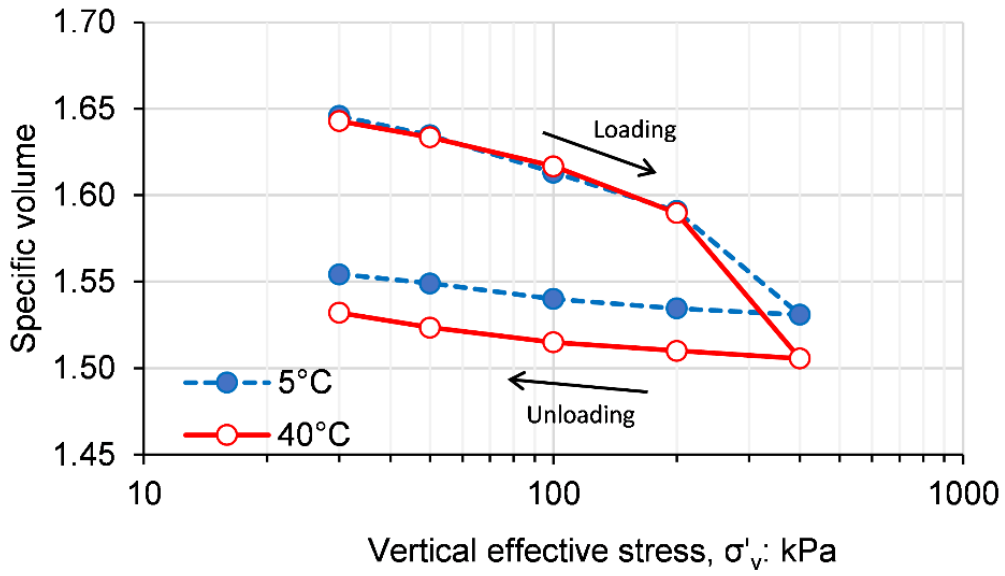


Figure 7.3 Influence of temperature on one-dimensional compression.

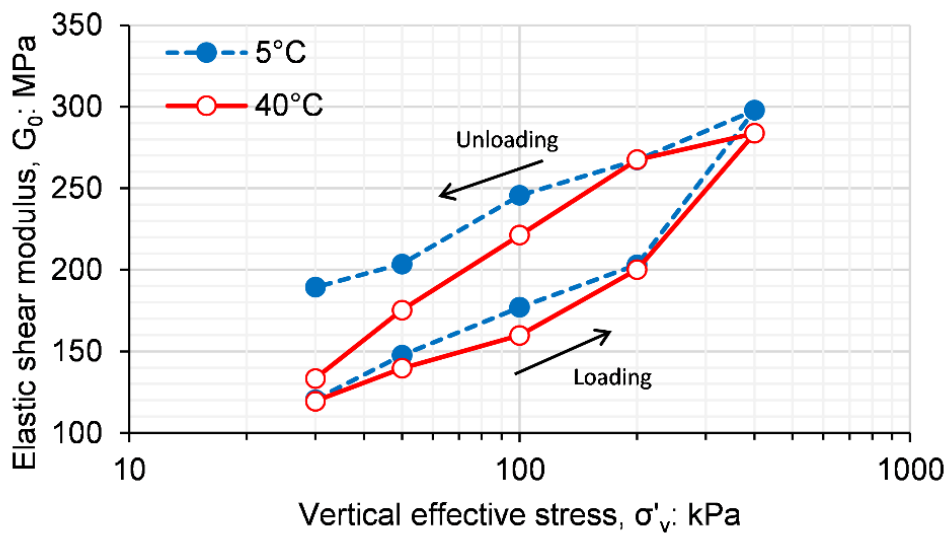


Figure 7.4 Influence of temperature on elastic shear modulus.

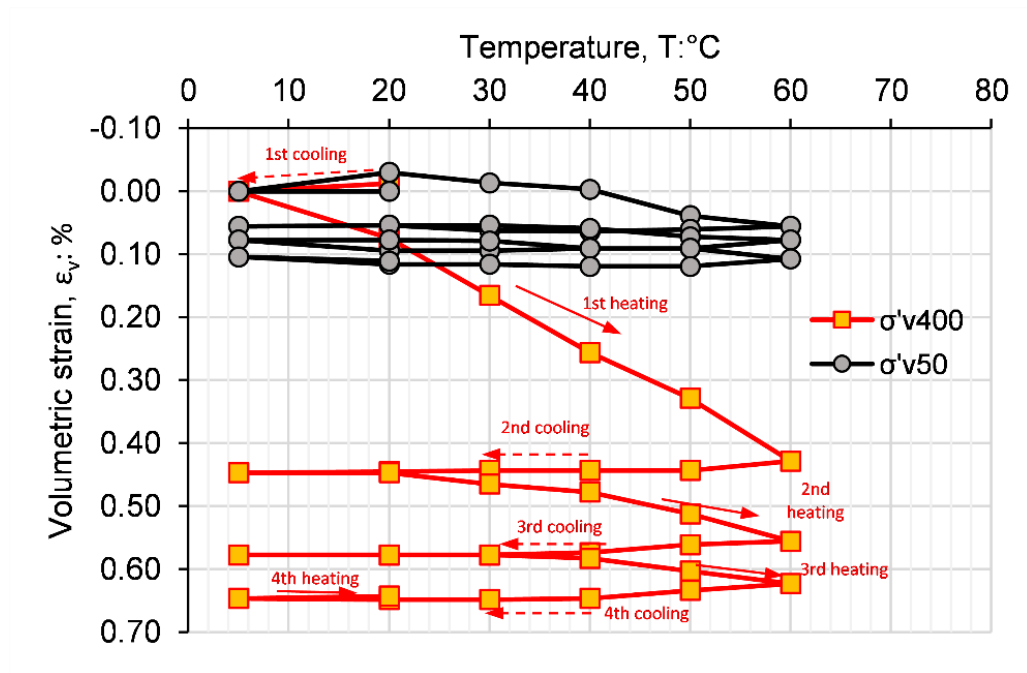
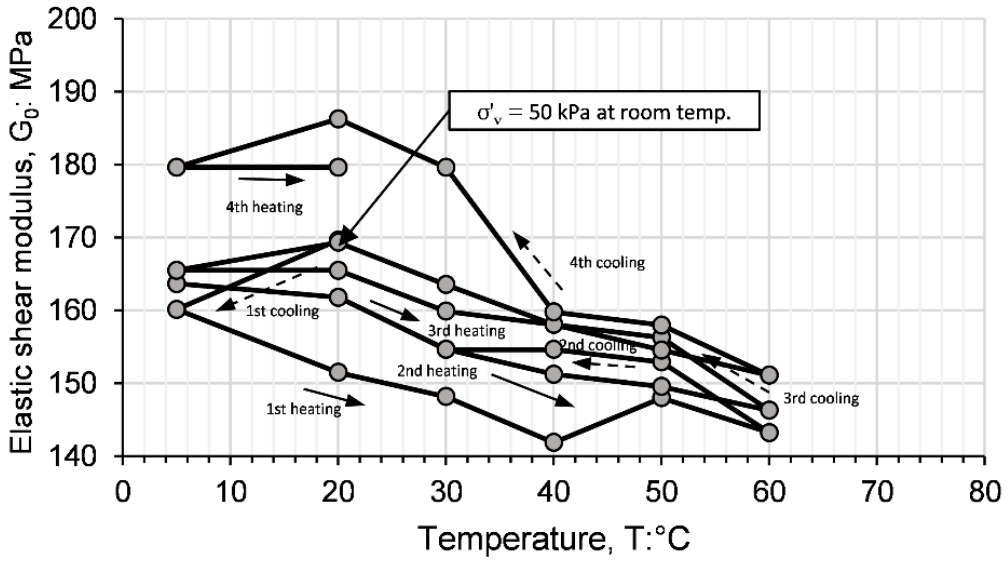
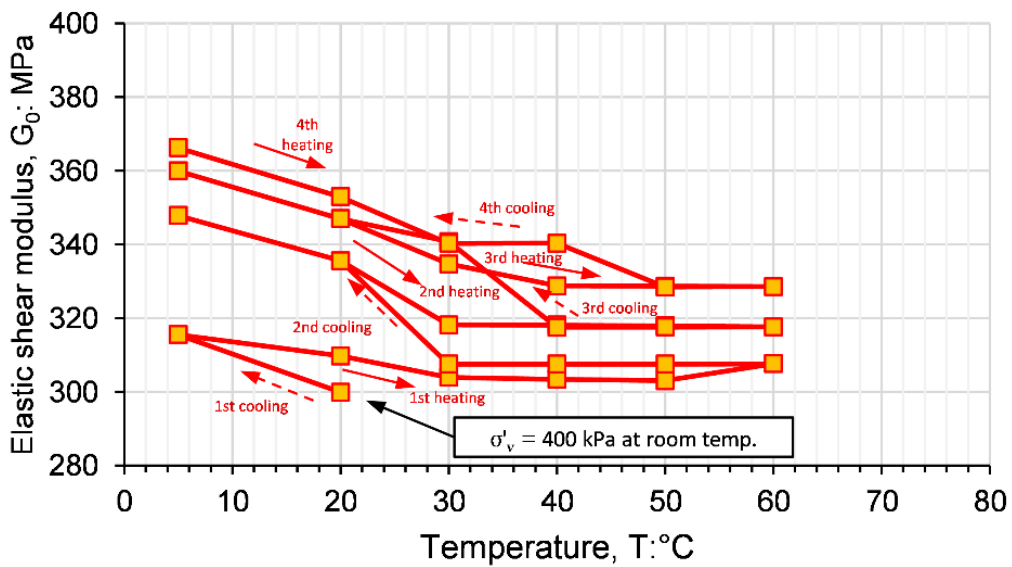


Figure 7.5 Accumulation of cyclic thermal strains at vertical effective stresses of 50 kPa (overly consolidated) and 400 kPa (normally consolidated)



(a)



(b)

Figure 7.6 Elastic shear modulus during cyclic heating and cooling at vertical effective stresses of (a) 50 kPa (overly consolidated) and (b) 400 kPa (normally consolidated)

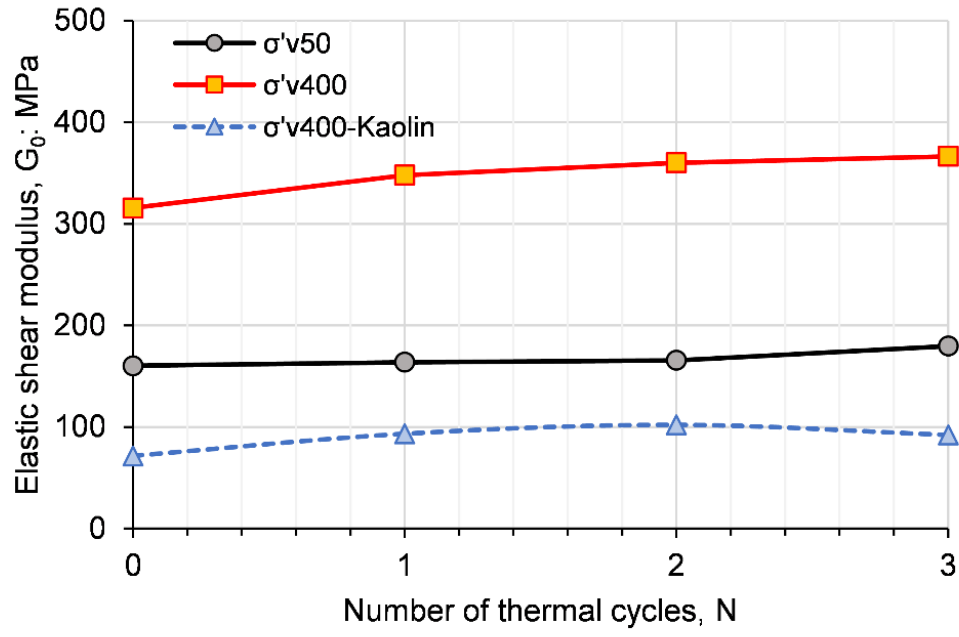
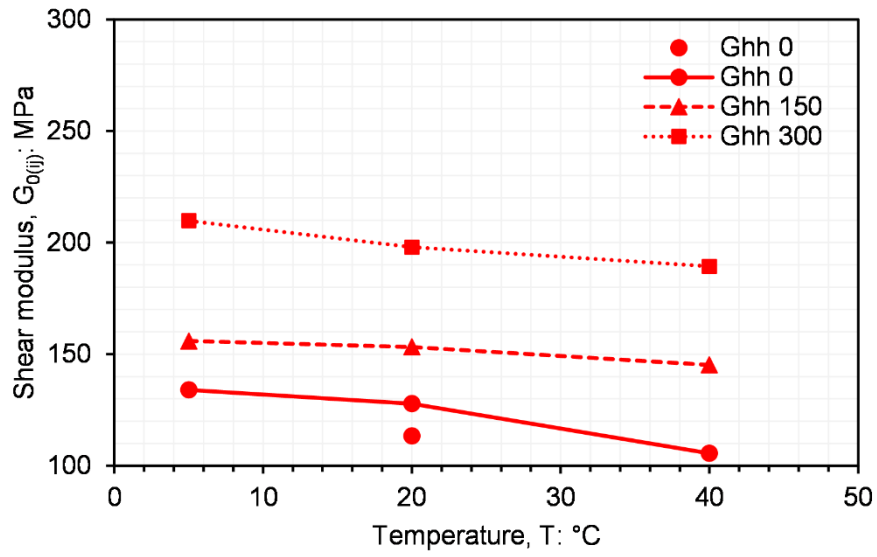
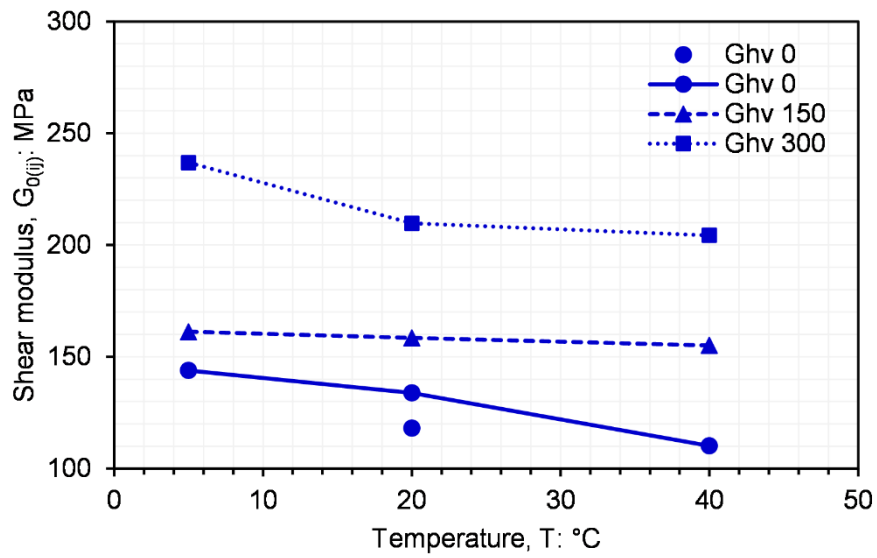


Figure 7.7 Effects of thermal cycles on the elastic shear modulus at vertical effective stresses of 50 kPa (overly consolidated) and 400 kPa (normally consolidated)

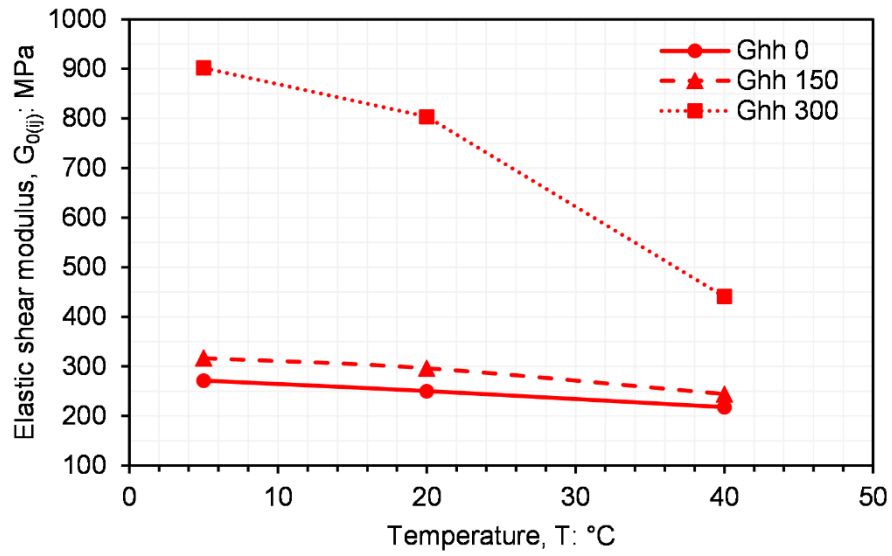


(a)

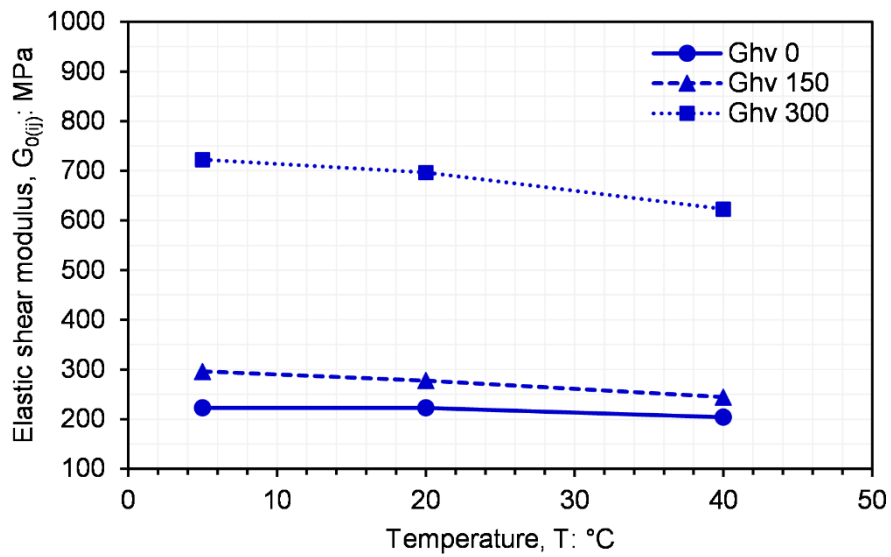


(b)

Figure 7.8 Effects of temperature on (a) $G_{0(hh)}$ and (b) $G_{0(hv)}$ at various suctions (mean net stress = 50 kPa)

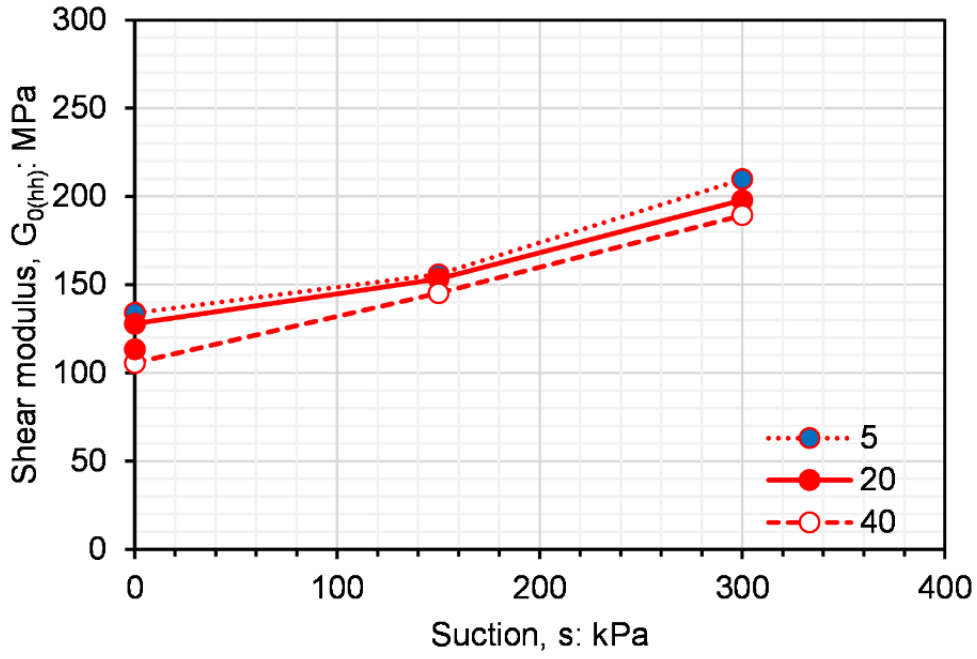


(a)

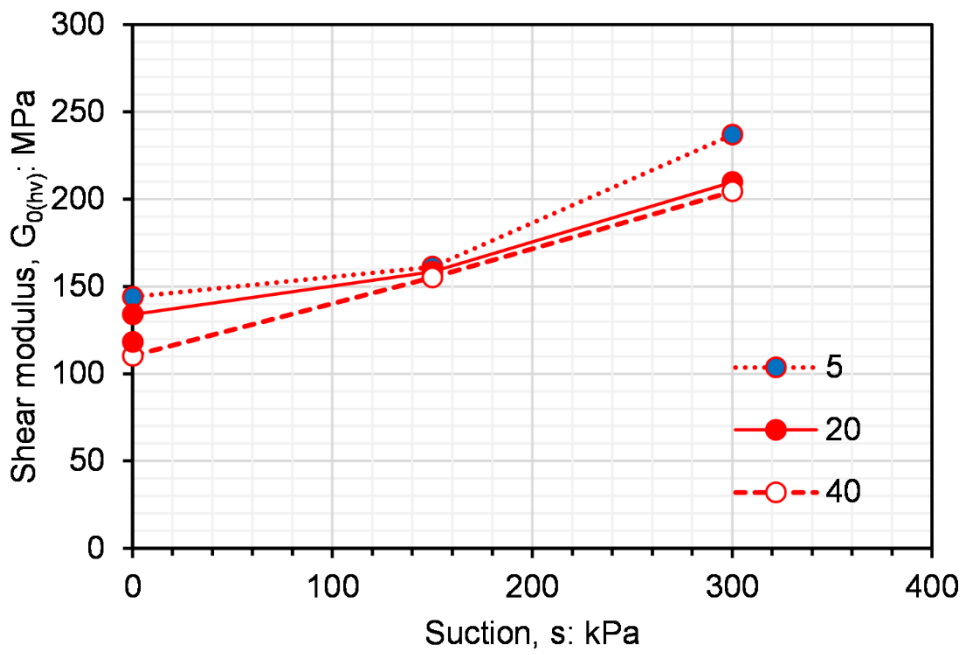


(b)

Figure 7.9 Effects of temperature on (a) $G_{0(hh)}$ and (b) $G_{0(hv)}$ at various suctions (mean net stress = 200 kPa)

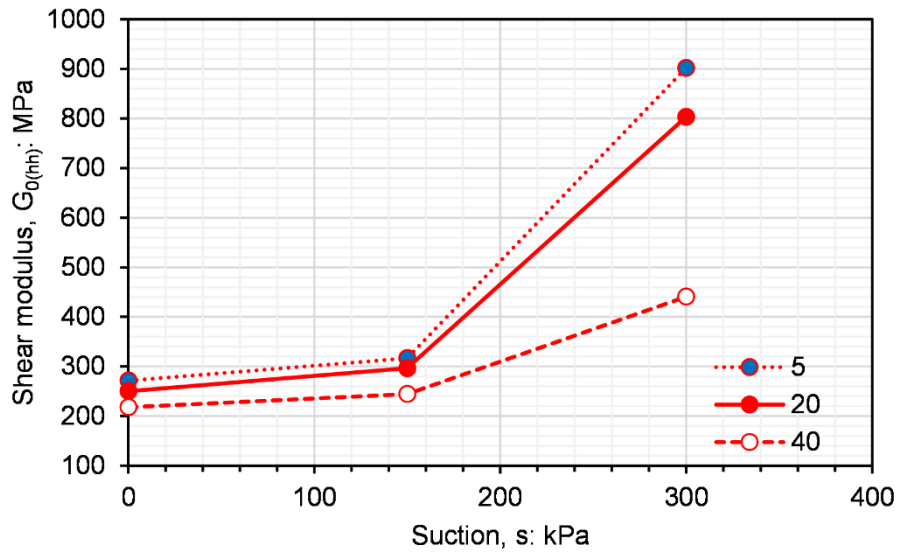


(a)

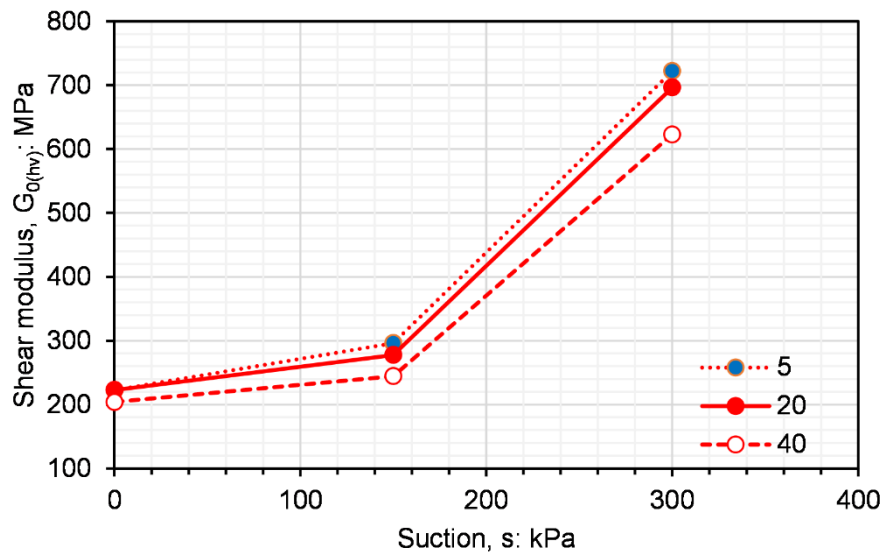


(b)

Figure 7.10 Suction effects on the (a) $G_{0(hh)}$ and (b) $G_{0(hv)}$ at different temperatures (mean net stress = 50 kPa)

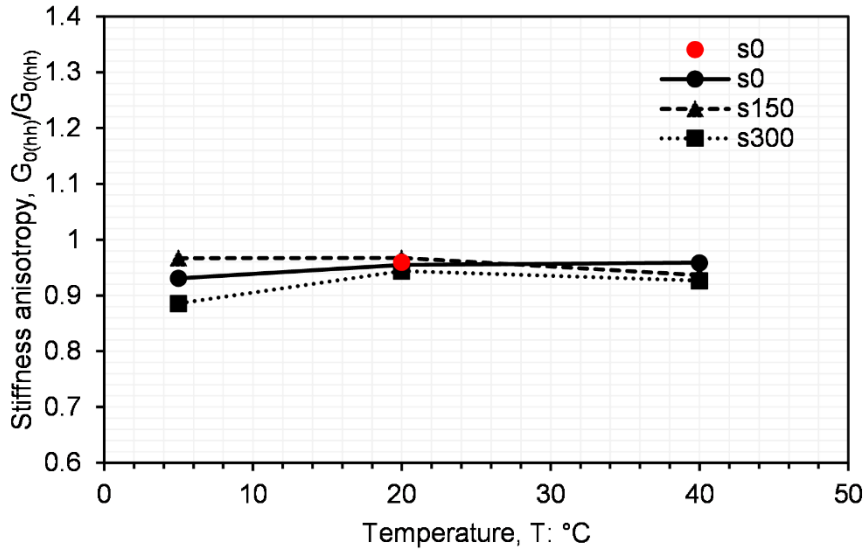


(a)

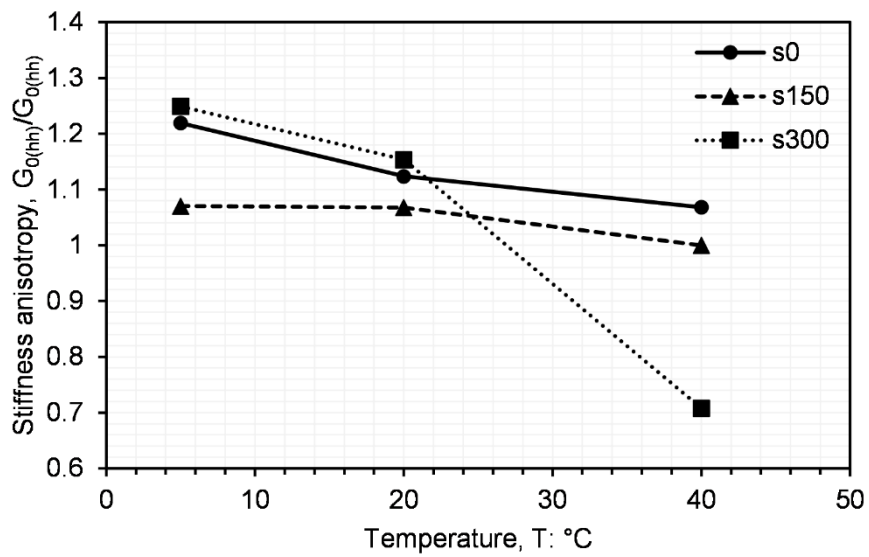


(b)

Figure 7.11 Suction effects on the (a) $G_{0(hh)}$ and (b) $G_{0(hv)}$ at different temperatures (mean net stress = 200 kPa)

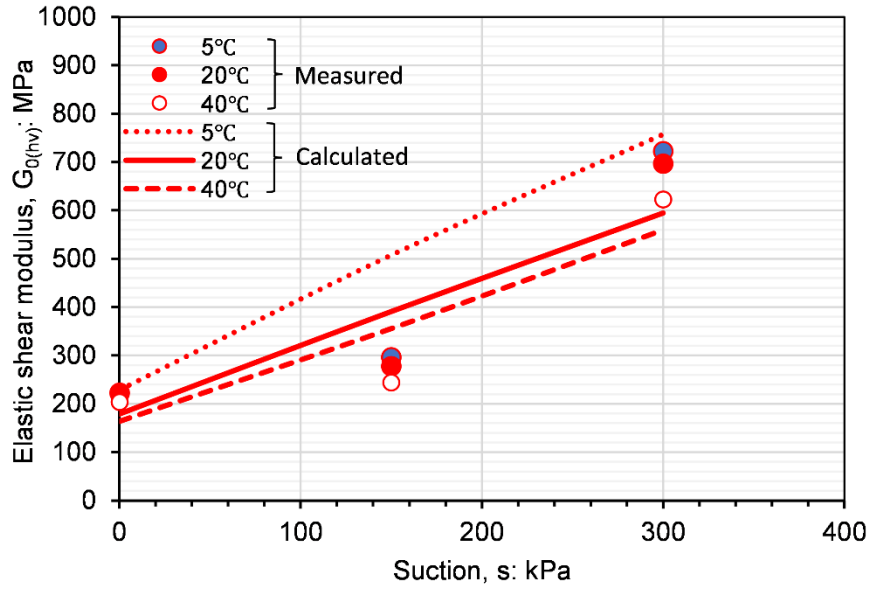


(a)

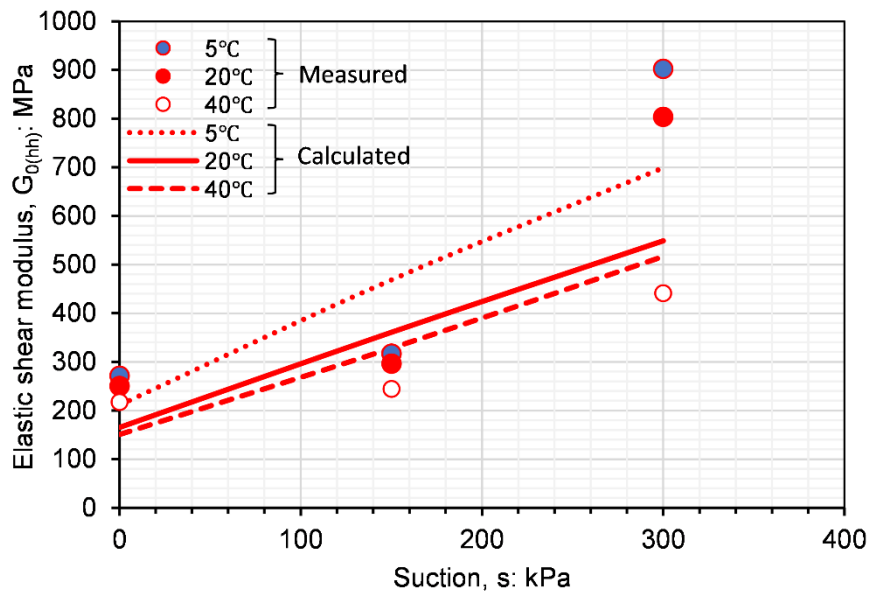


(b)

Figure 7.12 Thermal induced anisotropy at various suctions



(a)



(b)

Figure 7.13 Comparison between measured and calculated temperature and suction-dependent G_0 of unsaturated lateritic clay (a) $G_{0(hv)}$ and (b) $G_{0(hh)}$

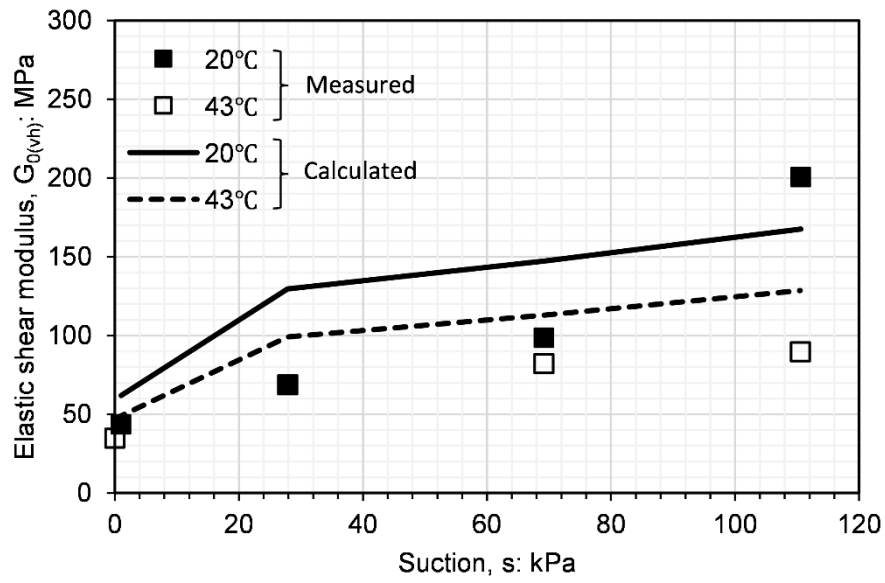


Figure 7.14 Comparison between measured and calculated temperature and suction-dependent G_0 of unsaturated silt (measured data from Vahedifard et al. (2020))

CHAPTER 8 PAVEMENT PERFORMANCE ANALYSIS

This chapter applies the experimental results from the previous chapters in pavement analysis to investigate the influence of climatic factors (suction and temperature) on pavement performance. The change in the subgrade soil stiffness is an important part of pavement performance. The effects of temperature and suction on the subgrade soil are considered in the analysis of a simple pavement that consists of asphalt, base and subgrade. Details of the analysis and computer program utilised are presented in this chapter.

8.1 Pavement performance analysis

8.1.1 Pavement performance analysis using KENPAVE.

The KENPAVE computer program by [Huang \(2004\)](#) was used in the numerical simulations to predict the vertical and horizontal strains at various locations to calculate rutting and fatigue cracking in the flexible pavement structure shown in [Figure 8.1](#). In the recent literature, KENPAVE has been used to predict the performance of different pavements, such as the pavements constructed using construction and demolition wastes ([Arisha et al. 2018](#)). Some researchers also used it to develop a methodological framework to model post-flooding road damage by identifying the importance of several parameters, including pavement material and analysis location ([Matini et al. 2022](#)). These two recent works served as a reference to deciding on a pavement cross-section and corresponding pavement performance analysis using the experimental results in this study.

8.1.2 Numerical model and input parameters

Based on the experimental results from the previous sections, a simple flexible pavement section consisting of three layers was adopted, as shown in [Figure 8.1](#). It was then used for a flexible pavement damage prediction using the different subgrade materials as the compacted lateritic soil. The asphalt layer properties were selected from the literature published by ([Brown 1996](#)). A granular base was employed as the base material in the mid-section of the pavement structure. The material properties of the granular base were taken from ([Mousa et al. 2015](#)). The subgrade stiffness was taken from the triaxial testing conducted on the compacted lateritic clay used in this study. The subgrade stiffness was taken from the secant Young's modulus values obtained from low suction controlled triaxial tests on the compacted lateritic clay used in this study at a strain of about 0.05%, with reference to [Figure 1.1](#) (i.e., stiffness degradation

curve). This secant Young's modulus values were used as input Resilient modulus values for the analysis in the KENPAVE software. It should be noted that according to the literature, the resilient modulus, also known as resilient Young's modulus, is identical to the secant Young's modulus during the unloading process (Ng et al. 2013). Suction effects are considered using part of the results presented in Chapter 5. The secant Young's modulus at an axial strain of about 0.05% for the unsaturated conditions is used in the representative stiffness characteristics of the subgrade. To account for the effects of temperature on pavement performance, the experimental results in the previous section are considered. An increase in temperature may cause a reduction in the elastic modulus by as much as 30% (for example, see Figure 7.4). Hence, the values of the resilient modulus are further reduced by 30% to consider thermal effects and used for the damage analysis in the following sections.

8.2 Equations for calculating rutting and fatigue cracking.

Several parameters are used to quantify the performance of the pavement. The compressive vertical strains for the total rutting prediction were calculated vertically at the mid-depth of each asphalt and base layer, the top of the subgrade, and several positions below the surface of the subgrade. Vertical compressive strains were determined at three horizontal positions for each vertical location: the wheel's centre, edge, and mid-distance between the two wheels. Additionally, the tensile strains at the base of the asphalt layer (at the same horizontal locations) were evaluated to determine fatigue cracking. These locations were selected to capture the critical responses for performance predictions. The standard axle (18 kips, 8.2 t, single axle with dual tires) was used for all simulation runs. The spacing between the dual tires was 34.3 cm (13.5 in.). The contact radius was 8.78 cm (3.46 in.) for a contact pressure of 120 psi (827.4 kPa).

8.2.3 Rutting Prediction

The permanent or plastic deformation, which occurred in the asphalt layer, the base layer and the subgrade, was added to determine the amount of rutting. For the asphalt layer, rutting estimation is determined by the laboratory-derived equation obtained from the MEPDG:

$$\Delta_{p(HMA)} = \varepsilon_{p(HMA)} h_{HMA} = \beta_{1r} k_z \varepsilon_{r(HMA)} 10^{k_{1r}} n^{k_{2r}} \beta_{2r} T^{k_{3r}} \beta_{3r} \quad (8.1)$$

where $\Delta_{p(HMA)}$ = Accumulated permanent or plastic vertical deformation in the asphalt layer/sublayer, in., $\varepsilon_{p(HMA)}$ = Accumulated permanent or plastic axial strain in the asphalt

layer/sublayer, in/in., $\varepsilon_{r(HMA)}$ = Resilient or elastic strain calculated by the structural response model at the mid-depth of each asphalt sublayer, in/in., h_{HMA} = The thickness of the asphalt layer/sublayer, in., n = Number of axle-load repetitions., T = Number of axle-load repetitions., k_z = Depth confinement factor, k_{1r}, k_{2r}, k_{3r} = Global field calibration parameters (from the NCHRP 1-40D recalibration; $k_{1r} = -3.35412$, $k_{2r} = 0.4791$, $k_{3r} = 1.5606$), and $\beta_{1r}, \beta_{2r}, \beta_{3r}$ = Local or mixture field calibration constants; for the global calibration, these constants were all set to 1.0.

$$k_z = (C_1 + C_2 D) 0.328196^D \quad (8.2)$$

$$C_1 = -0.1039(H_{HMA})^2 + 2.4868H_{HMA} - 17.342 \quad (8.3)$$

$$C_2 = 0.0172(H_{HMA})^2 - 1.7331H_{HMA} + 27.428 \quad (8.4)$$

where D = Depth below the surface, in. and H_{HMA} = Total HMA thickness, (in.)

$$\Delta_{p(HMA)} = 4.425 \times 10^{-4} (C_1 + C_2 D) 0.328196^D \varepsilon_{r(HMA)} n^{0.4791} T^{1.5606} \quad (8.5)$$

The equation used to calculate the plastic deformation in the base layer, and the subgrade is shown below:

$$\Delta_{p(soil)} = \beta_{s1} k_{s1} \varepsilon_v h_{soil} \left(\frac{\varepsilon_0}{\varepsilon_r} \right) e^{-\left(\frac{\rho}{n} \right)^\beta} \quad (8.6)$$

where $\Delta_{p(soil)}$ = Permanent or plastic deformation for the layer/sublayer, in., n = Number of axle-load applications, ε_0 = Intercept determined from laboratory repeated load permanent deformation tests, in/in., ε_r = The resilient strain imposed in laboratory tests to obtain material properties ε_0 , ε , and ρ , in/in., ε_v = Average vertical resilient or elastic strain in the layer/sublayer and calculated by the structural response model (KENLAYER), in/in., h_{soil} = The thickness of the base or soil layer/sublayer, in., k_{s1} = Global calibration coefficients; $k_{s1} = 1.673$ for granular materials and 1.35 for fine-grained materials, and β_{s1} = Local calibration constant for the rutting in the unbound layers; the local calibration constant was set to 1.0 for the global calibration effort.

$$\text{Log } \beta = -0.61119 - 0.017638(W_c) \quad (8.7)$$

$$\rho = 10^9 \left(\frac{C_0}{(1 - (10^9)^\beta)} \right)^{\frac{1}{\beta}} \quad (8.8)$$

$$C_0 = Ln \left(\frac{a_1 M_r^{b_1}}{a_9 M_r^{b_9}} \right) = 0.0075 \quad (8.9)$$

where W_c = water content, %, M_r = resilient modulus of the base or soil layer or sublayer, psi, a_1 , a_9 , b_1 and b_9 are regression constants; a_1 and a_9 are 0.15 and 2.00, respectively, b_1 and b_9 are both 0.0.

In the final calculation of rutting for each base and subgrade layer, the equation in (Arisha et al. 2018) is used. The equation is as follows:

$$\Delta_{p(soil)} = k_s \varepsilon_v h_{soil} \left(\frac{(e^{(\rho)^\beta} \times 0.15) + (e^{\left(\frac{\rho}{109}\right)^\beta} \times 20)}{2} \right) e^{-\left(\frac{\rho}{n}\right)^\beta} \quad (8.10)$$

8.2.4 Fatigue Cracking

The allowable number of axle-load repetitions (N_f) for bottom-up alligator fatigue cracking (FC) was first estimated. This value is related to the tensile strain at the bottom of the asphalt layer with the expression:

$$N_f = 0.007566 (C_H) \left(10^{\left(4.84 \left(\frac{V_{be}}{V_a + V_{be}} - 0.69 \right) \right)} \right) (\varepsilon_t^{-3.9492}) (E_{(HMA)})^{-1.281} \quad (8.11)$$

where N_f = the allowable number of axle-load applications for a flexible pavement; ε_t = tensile strain at the bottom of the asphalt layer, in./in., which is calculated by KENPAVE; $E_{(HMA)}$ = dynamic modulus of the asphalt layer measured, psi; V_{be} = Effective asphalt content by volume, %; V_a = Percent air voids in the HMA mixture; and C_H = Thickness correction term, dependent on the type of cracking. C_H was estimated for a bottom-up or alligator cracking as:

$$C_H = \frac{1}{0.000398 + \frac{0.003602}{1 + e^{(11.02 - 3.49H_{HMA})}}} \quad (8.12)$$

The amount of damage is expressed as a damage index (DI), which can be determined by dividing the actual number of axle loads by N_f .

$$DI = \sum (\Delta DI)_{j,m,l,p,T} = \sum \left(\frac{n}{N_f} \right)_{j,m,l,p,T} \quad (8.13)$$

where n = Actual number of axle-load applications within a specific period; j = Axle-load interval, m = Axle-load type (single, tandem, tridem, quad, or special axle configuration), l = Truck type using the truck classification groups included in the MEPDG, P = Month, and T = Median temperature for the five temperature intervals or quintiles used to subdivide each month, °F.

The area of the alligator cracking and length of longitudinal cracking are calculated from the total damage over time.

$$FC_{Bottom} = \left(\frac{1}{60} \right) \left(\frac{6000}{1 + e^{(-2C_2^* + C_2^* \log(DI_{Bottom} * 100))}} \right) \quad (8.14)$$

where FC_{Bottom} = area of alligator cracking that starts at the bottom of the HMA layers (percentage of total lane area); DI_{Bottom} = cumulative damage index at the bottom of the HMA layers; and $C_2^* = -2.40874 - 39.748(1 + H_{HMA})^{-2.856}$.

8.3 Numerical programme

Six subgrade modulus values were considered to simulate the influence of suction and temperature on pavement performance. The first three sets of values consider the changes in the modulus values with increasing suction, whereas the second set of values considers the influence of temperature on the modulus values. In general, the influence of temperature is considered by a 30% reduction of modulus, according to the conclusion from the experimental results in the previous section, as explained above. A constant Poisson's ratio was used for all the subgrade layer with a value of 0.16. Although temperature changes may likely affect the values of Poisson's ratio, this was not the focus of this analysis. A summary of the parameters is presented in [Table 8.1](#). It should be noted that other parameters for the KENPAVE analysis were assumed to be constant.

8.4 Analysis of numerical results

8.4.1 Stress and strain distribution under the pavement at constant suction

Figure 8.2 shows the vertical stress distribution under the pavement at a suction of 0 kPa. As expected, the most critical stress at the top of the pavement layer occurs at the centre of the wheels, followed by the edge and finally the mid-point between two wheels. At a depth of about 10 inches, the vertical stress experienced by points under the wheel remains almost the same. The difference in stress at the centre and the edge of the wheel is about a 46% decrease.

Figure 8.3 shows the radial stress distribution under the pavement 0 kPa. At the mid-depth of the asphalt layer, the radial stress is highest at the centre of the wheel. The radial stress at the edge of the wheel, when compared to the centre is about 100% smaller. At the depth of about 10 inch and lower, the radial stress approaches zero and remain constant in the subgrade layer.

Figure 8.4 compares the vertical compressive strain distribution under the pavement at the centre, edge and mid-point between two wheels for suction of 0 kPa. In general, the compressive strain experienced at the centre of the wheel is the largest throughout the pavement layer. However, in the mid-depth of the asphalt layer (i.e. 1-inch depth), the compressive strain at the centre of the wheel is lower by about 60% when compared to the compressive strain at the edge. The compressive strain is 0.000348 and 0.000139 at the edge and centre of the wheel within the 1-inch depth of the asphalt layer. The compressive strain at the bottom of the asphalt layer becomes larger at the centre of the wheel compared to the edge of the wheel. The percentage decrease of compressive strain at the bottom of the asphalt layer is about 53%. The difference in compressive strain becomes less obvious at a depth of 10 inches and lower.

Figure 8.5 shows the horizontal tensile strain distribution under the pavement at zero suction. At 1 inch depth within the asphalt layer, there is a compressive strain response, irrespective of the point under the wheel (i.e., centre, edge or mid-point between two wheels). The pavement begins to experience horizontal tensile stains at the bottom (1 inch) of the asphalt layer and beyond, particularly at the wheel's centre and edge. The horizontal strain is about 25% larger than the wheel's centre compared to the wheel's edge at the bottom of the asphalt layer. Likewise, in **Figure 8.4**, the difference in compressive strain is become less obvious at the depth of 10 inch and lower.

A similar conclusion can be drawn for other suction values. Hence a detailed description of such results is not presented here.

8.4.2 Suction effects on compressive strain and rutting

Figure 8.6 shows the vertical compressive strain profile predicted by the KENPAVE software along the centre of the wheel load. These calculated strains are used in the damage analysis to estimate the permanent deformations in the various pavement layers. It can be seen from **Figure 8.6** that the vertical compressive strain values in the pavement's layers, particularly in the subgrade layer, were lowered when the subgrade modulus values were increased from the value at 0 kPa suction to the value at 150 kPa suction. Because of changes in subgrade modulus, the vertical compressive strain in the mid-height of the asphalt layer increases by about 27%. At the top of the base layer, the vertical compressive strain increases by about 1%.

Meanwhile, the vertical compressive strain decreases by about 42% at the top of the subgrade layer with increased suction. The comparison above is between a suction of zero and 150 kPa. Since the purpose of the pavement's layers is to distribute the load on the surface and lessen it with depth increase so that the pressure on the subgrade is significantly lower than that on the top and can be tolerable without excessive subgrade deformation (Mallick and El-Korchi 2008), when the subgrade stiffness is lower, less deformation is taken by the top layers. On the other hand, with an increased subgrade stiffness, the compressive strain becomes larger in the top layers.

Figure 8.7 shows the calculated rutting depth along the centre of the wheel for the pavement section with different subgrade moduli due to changes in suction. This figure indicates that the total rutting depth increases at the subgrade modulus decrease because of a reduction in suction. It can be seen from **Figure 8.7** that the total rut depths for the different suction values are asymptotic and becomes almost constant after about 5 million load repetitions. Changes in suction from 0 to 150 kPa can cause about a 26% decrease in the rutting deformation of the pavement at about 10 million ESALs.

8.4.1 Suction effects on horizontal strain and fatigue cracking

Figure 8.8 represents the horizontal strain profile with depth along the centreline of wheel loading. Within the asphalt layer, the horizontal strains calculated by KENPAVE indicate that the soil at a suction of 150 kPa causes an increase in the horizontal tensile strains. However, the horizontal tensile strains for suction of 150 kPa become smaller within the base and the subgrade layers. In other words, a stiffer subgrade layer increases the tendency increased horizontal tensile strains in the surface layers.

Figure 8.9 shows the effects of suction on the fatigue cracking presented as a percentage versus the number of equivalent standard axle loads for the pavement section. At 10 million ESALs, with an increase in suction from 0 kPa to 10 kPa, the fatigue cracking increases by about 5%. With further increase of suction from 10 to 150 kPa, the fatigue cracking increases by about 6%. Although there is significant changes in the subgrade modulus it appears that the resultant effects on the fatigue cracking is relatively minimal as compared to the rutting response presented in the previous section.

8.4.2 Thermal effects on compressive strain and rutting

To evaluate the influence of temperature on the pavement performance in terms of rutting, **Figure 8.10** compares the vertical compressive strain profile for the two suction values of 0 and 150 kPa and when temperature causes about a 30% reduction in the soil modulus. From **Figure 8.10**, it can be seen that the thermal-induced reduction of modulus influences the vertical compressive strain profile. The increase in temperature causing a reduction in subgrade modulus increases the vertical compressive strain, which is more evident in the subgrade layer with a suction of 0 kPa. With a 30% reduction of subgrade modulus due to thermal effects, the compressive strain at the mid-height of the asphalt layer decreases by about 12%. On the other hand, the compressive strain at the top of the base layer reduces by about 0.5%.

Meanwhile, the compressive strain increases by about 19% at the top of the subgrade layer. For the subgrade modulus at suction 150 kPa, the compressive strain at the mid-height of the asphalt layer decreases by about 8%. On the other hand, the compressive strain at the top of the base layer reduces by about 0.4%. Right at the top of the subgrade layer, the compressive strain increases by about 15%. It should be noted that temperature may affect the asphalt and base layer stiffness (Mallick and El-Korchi 2008), but such effects are not considered in the analysis above because it is beyond the scope of this work..

Figure 8.11 represents the calculated rut depth considering the thermal-induced reduction of subgrade modulus. The thermal-induced reduction of subgrade modulus of about 30% obviously increases the total rutting deformation of the pavement layers. With respect to the subgrade modulus of suction 0 kPa **Figure 8.11(a)**, at 1 million ESALs, the total and subgrade rutting increases by about 17% and 25%, respectively. With a further increase of ESALs to 10 million, the total rutting and subgrade increases by about 15% and 25%, respectively. On the other hand, for the subgrade modulus at the suction of 150 kPa **Figure 8.11(b)** the total and subgrade rutting at 1 million ESALs increases by about 14% and 29%, respectively. **Figure**

8.11 indicates that thermal effects on subgrade modulus can cause considerable pavement damage regarding rutting, which should not be thoroughly ignored in pavement design and analysis. Moreover, rutting could be enhanced if the thermal effects on other layers are accounted for.

8.4.3 Thermal effects on horizontal strain and fatigue cracking

Figure 8.12 represents the calculated horizontal strain profile with depth considering thermal effects on subgrade modulus. For the specimen with 0 kPa suction, the horizontal tensile strain reduces by about 22% with an increased temperature at the mid-height of the asphalt layer. With a suction of 150 kPa, the horizontal tensile strain at the mid-height reduces by 39% with increased temperature. The horizontal tensile strains in the asphalt layers become smaller as the thermally induced reduction in the subgrade modulus is considered. In other words, larger stiffness results in larger tensile horizontal strains. Moreover, due to the thermal reduction in subgrade modulus, the tensile strains in the subgrade layer become larger.

The fatigue cracking presented as a percentage versus the number of equivalent standard axle loads for the pavement section is shown in **Figure 8.13**. It can be seen from **Figure 8.12** that when the stiffness of the subgrade layer increases, the horizontal strain at the bottom of the asphalt layer becomes larger. Thus, increasing fatigue cracking. Moreover, a stiffness reduction of about 30% due to thermal-induced stiffness decrease resulted in about a 6% decrease in fatigue cracking in **Figure 8.13** at about 10 million ESALs.

8.5 Summary

Reasonable prediction of small strain deformation is essential to various geotechnical infrastructure designs, including pavements. In the literature, it is recognised that the modulus of soil is affected by suction and temperature. Although, design guides may have considered soil moisture on soil behaviour using empirical methods (AASHTO 2008). Variations in subgrade stiffness with suction and thermal effects revealed in this study have rarely been accounted for. The influence of these state variables on the performance of a simple pavement structure is investigated in this chapter. The pavement response is investigated using the KENPAVE software. The secant Young's modulus values obtained from low suction controlled triaxial tests is used as input values for the analysis in the KENPAVE software.

The prediction from the KENPAVE software indicates that the subgrade modulus values due to changes in suction influence the stress and strain distributions in the pavement layers. The higher the subgrade modulus, the lower the induced vertical compressive strain in the pavement layers. However, due to thermal-induced reduction in modulus, the compressive strains increase in the pavement layers and consequently, the rut depth of the pavement increases.

These results and interpretations should be treated with caution as they may be specific and not applicable to the actual performance of pavement in the field. Moreover, the discussions above do not consider the thermal and suction effects of the modulus of various base and subbase layers of pavements. Further sensitivity analysis is recommended to examine the changes in pavement thickness and thermal effects of other pavement layers for various pavements.

Table 8.1 Modulus parameters for subgrade layer

Case ID	Suction, s: kPa	Modulus: psi
s 0	0	6092
s 10	10	9137
s 150	150	15229
s 0 T	0*	4264
s 10 T	10*	6396
s 150 T	150*	10660

*At each suction condition, the values of the modulus were reduced by 30%, based on the general conclusion from previous sections.

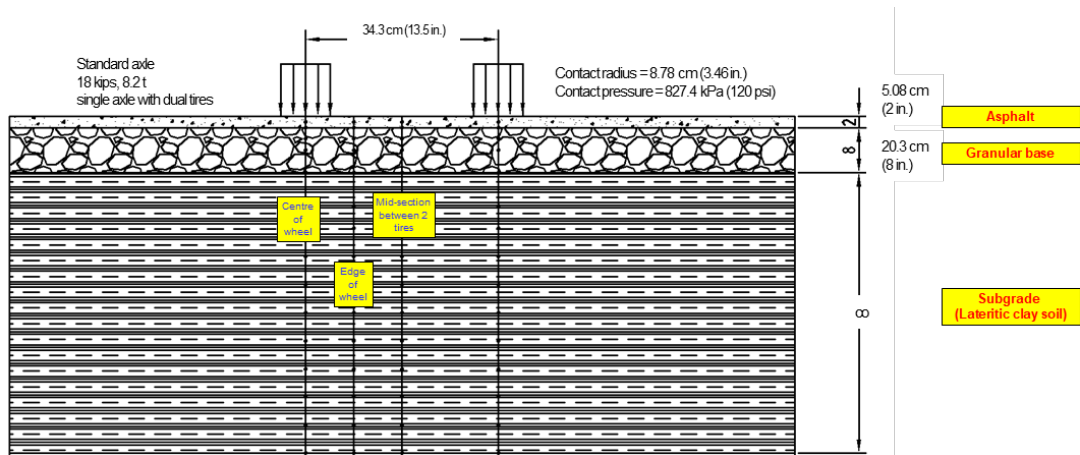


Figure 8.1 Flexible pavement adopted for performance prediction on lateritic soil subgrade

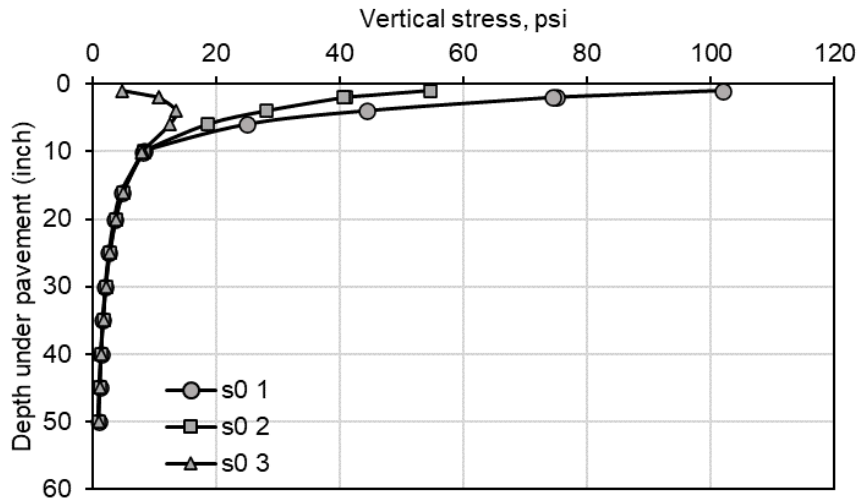


Figure 8.2 Vertical stress distribution under the pavement (1) centre (2) edge (3) mid-point between the two wheels (note: compression is positive)

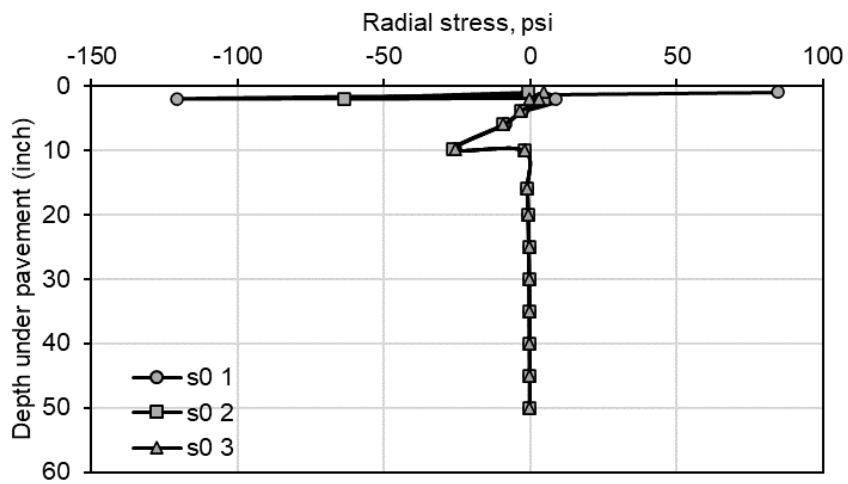


Figure 8.3 Radial stress distribution under the pavement (1) centre (2) edge (3) mid-point between the two wheels (note: compression is positive)

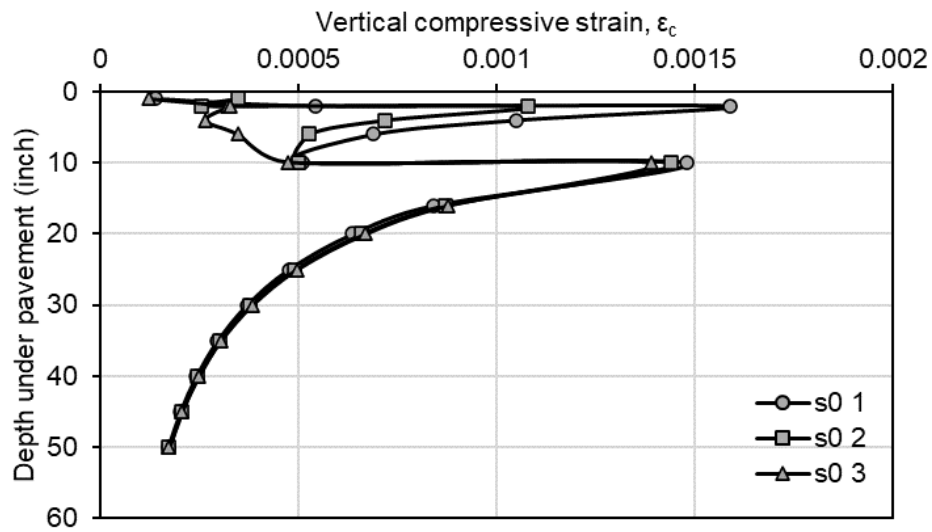


Figure 8.4 Vertical compressive strain distribution under the pavement (1) centre (2) edge (3) mid-point between the two wheels (note: compression is positive)

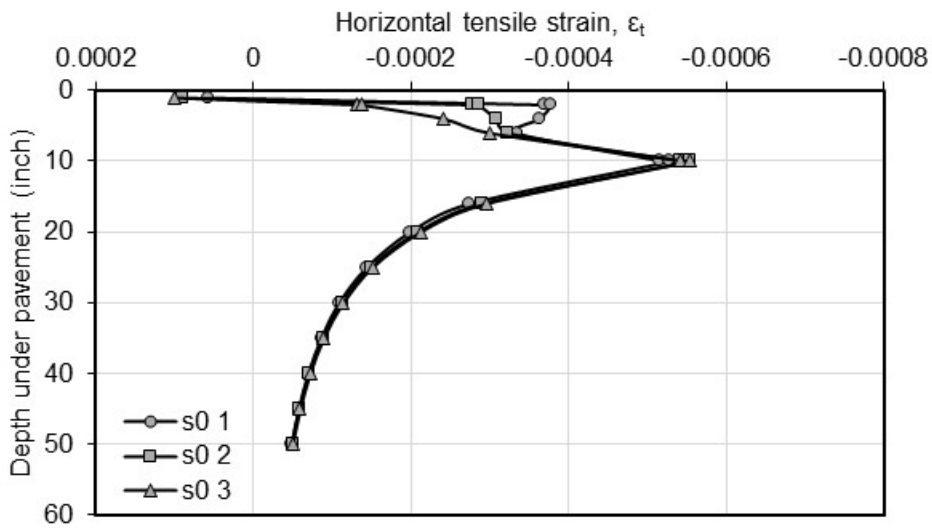


Figure 8.5 Horizontal tensile strain distribution under the pavement (1) centre (2) edge (3) mid-point between the two wheels (note: compression is positive)

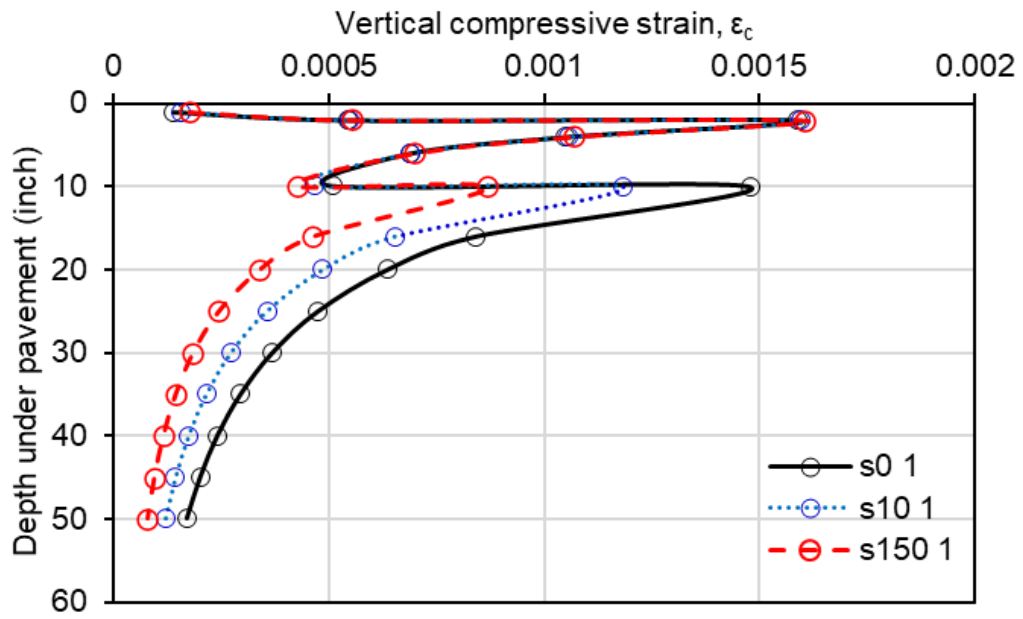


Figure 8.6 Vertical resilient strain profile with depth along the centreline of wheel loading

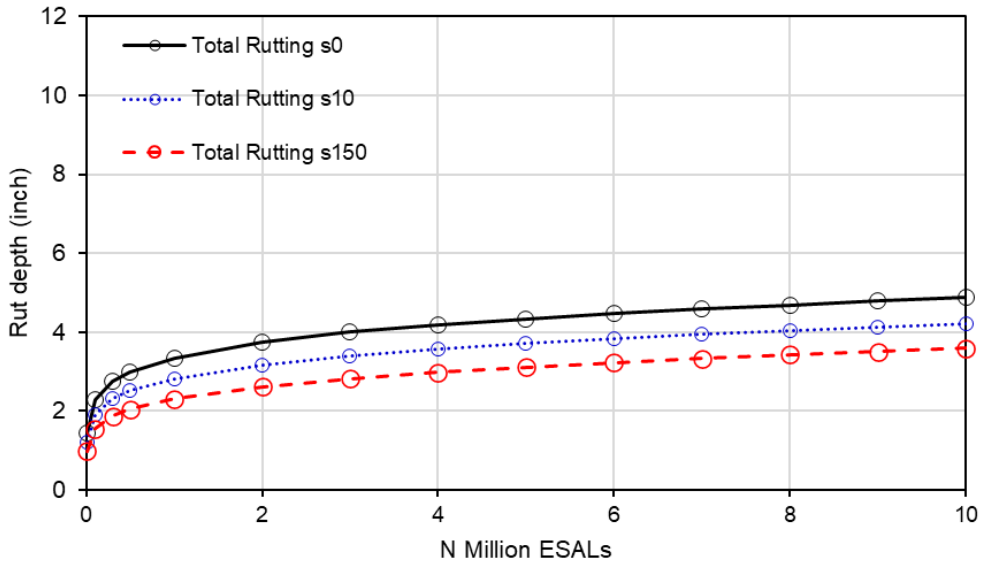


Figure 8.7 Calculated rutting depth versus the number of load applications.

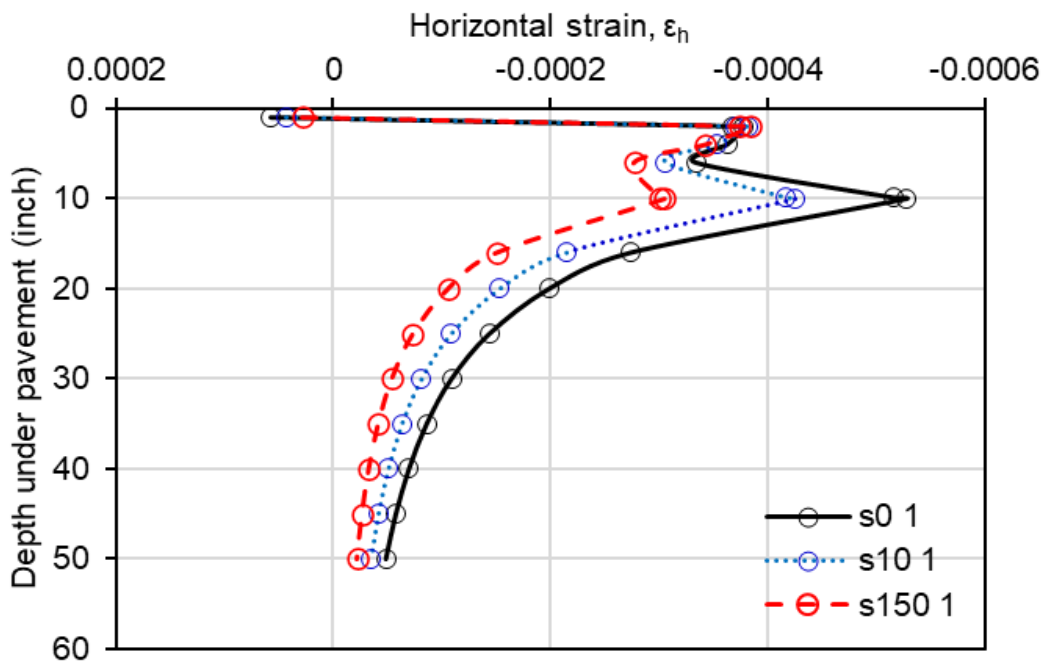


Figure 8.8 Horizontal strain profile with depth along the centreline of wheel loading

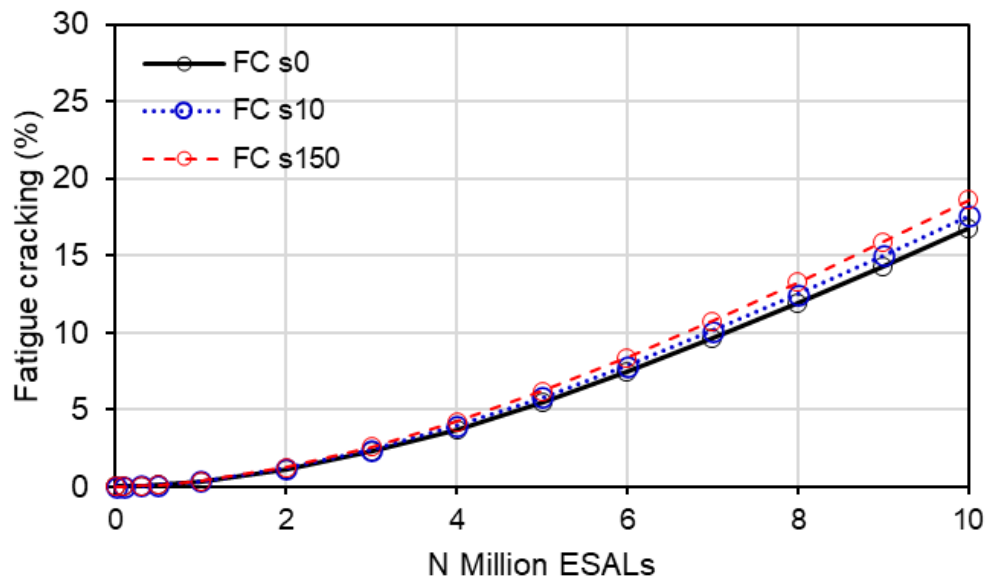


Figure 8.9 Suction effects on fatigue cracking

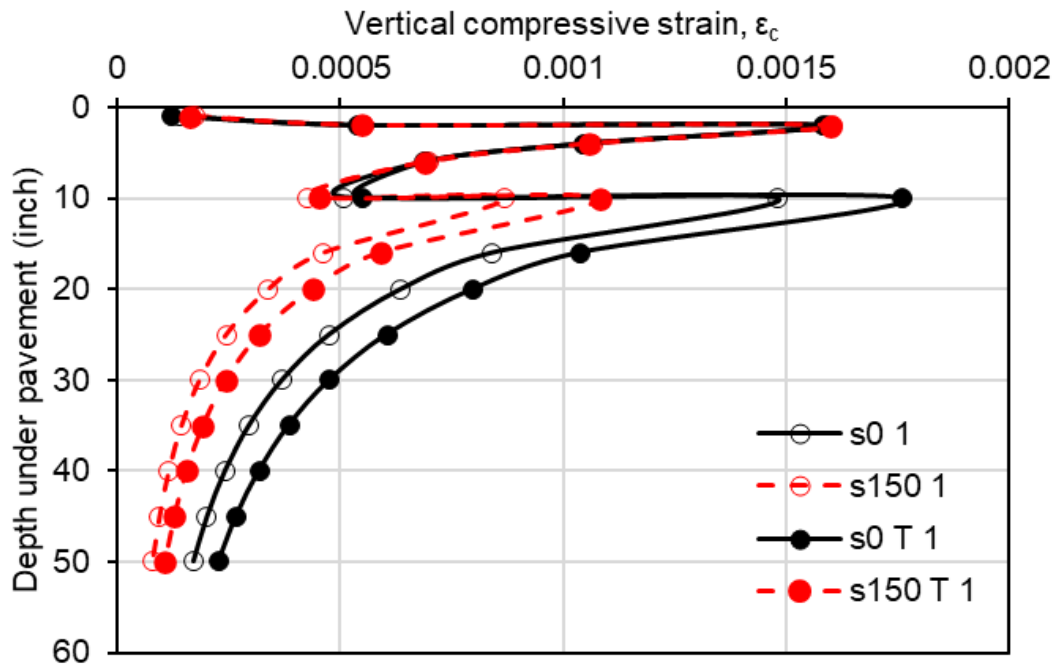
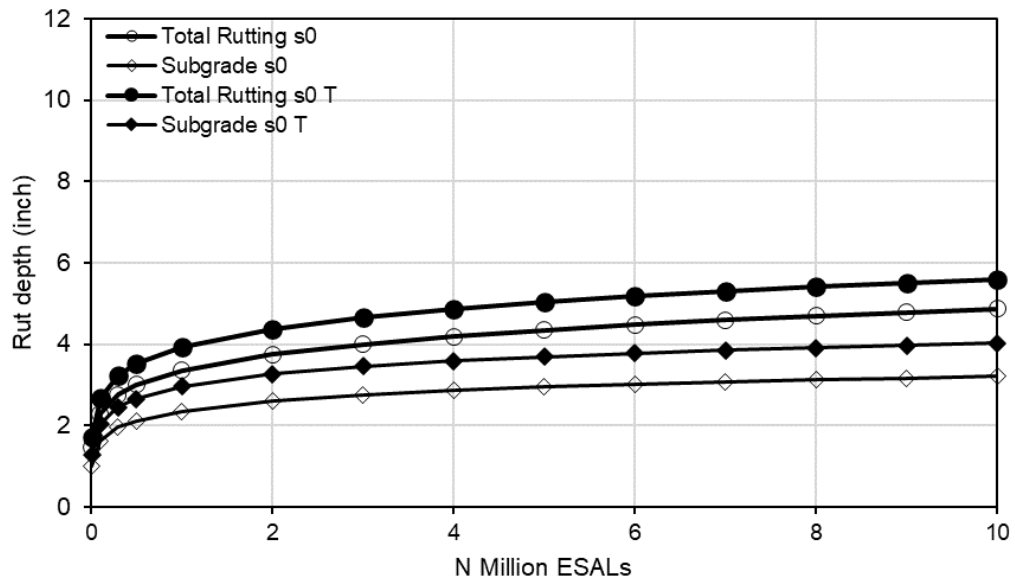
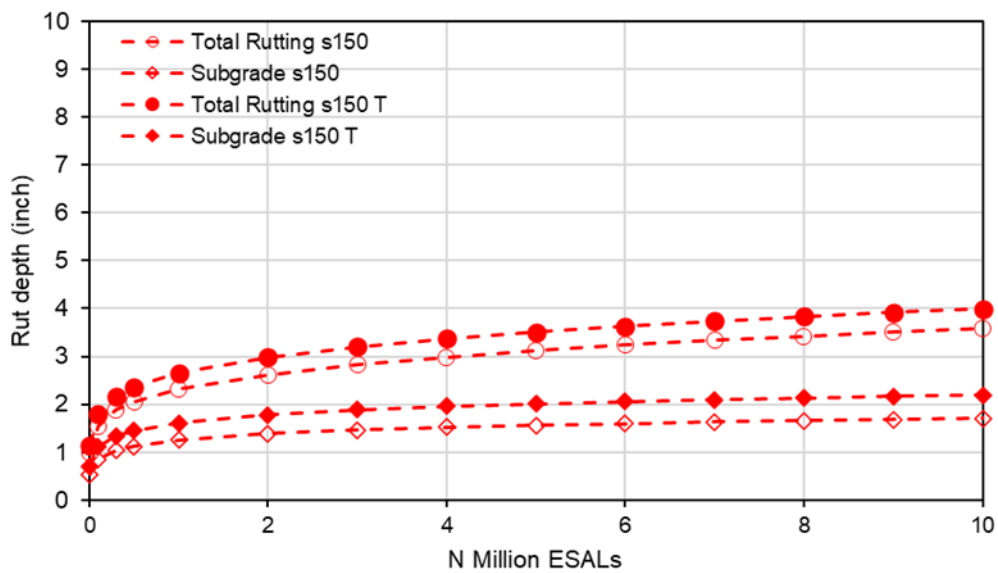


Figure 8.10 Temperature effect on estimated vertical resilient strain profile



(a)



(b)

Figure 8.11 Thermal influence on calculated rutting depth versus the number of load applications (a) $s = 0$ kPa (b) $s = 150$ kPa

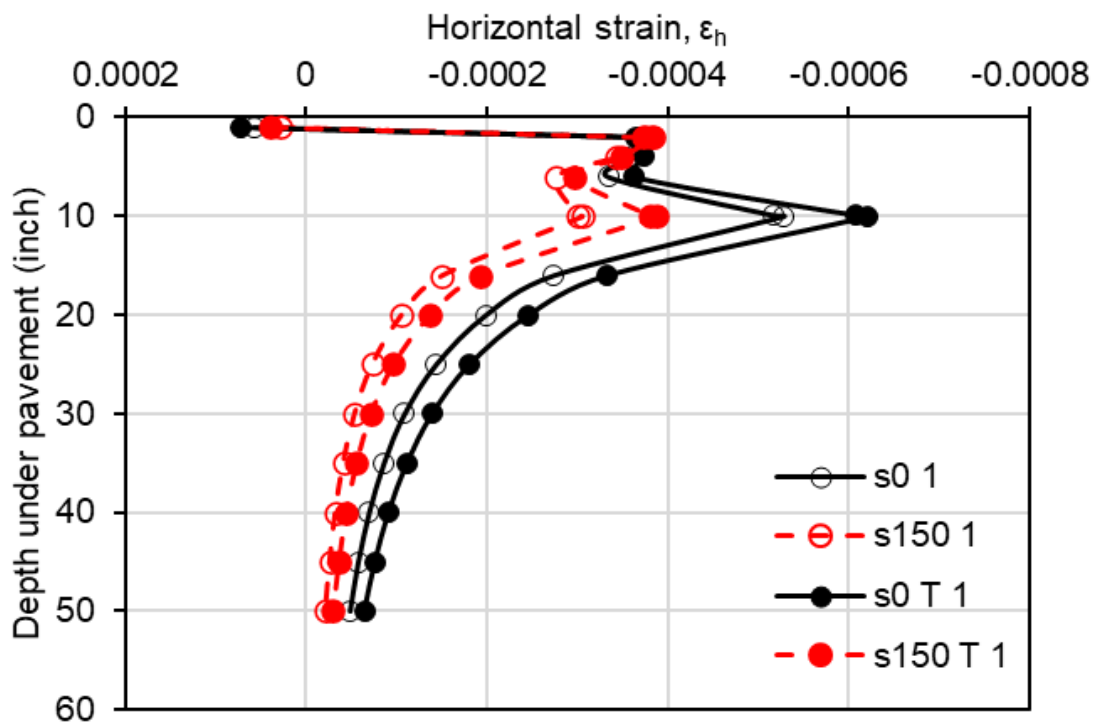


Figure 8.12 Thermal effects on tensile strain profile with depth along the centreline of wheel loading

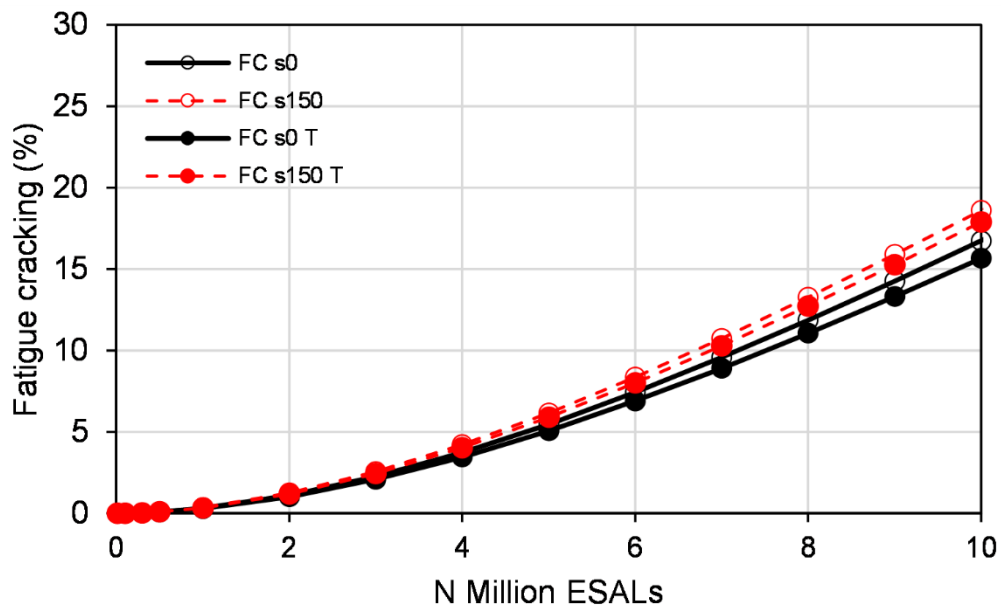


Figure 8.13 Fatigue cracking with the number of load applications.

CHAPTER 9 CONCLUSIONS AND RECOMMENDATIONS FOR FURTHER WORK

The small strain stiffness of saturated and unsaturated soils is important for analysing and predicting ground movement and the serviceability of many geotechnical structures. Furthermore, the soils may be anisotropic inherently from their natural formation process, compaction or induced through stress or strain. Soils in many geostructures (e.g., pavements and railway embankments) experience complex working conditions, like daily and seasonal variations of temperature and suction. Hence, it is crucial to investigate the effects of suction and temperature on the small strain stiffness of saturated and unsaturated soils.

Lateritic clayey soils are widely distributed in tropical and subtropical regions, where they have been extensively used as fill materials for subgrade construction of highways and railways, foundations and retaining walls. An important characteristic of lateritic soils is that they are highly aggregated due to their high iron and aluminium sesquioxides content as cementing agents. The structure of lateritic clayey soils is sensitive to the compaction water content changes. The effects of anisotropy, temperature, and suction on the small strain behaviour of compacted lateritic soils have rarely been explored in literature and thus are not fully understood.

To investigate the small strain deformation characteristics of lateritic clay soils considering anisotropy, temperature and suction effects, comprehensive experimental work is carried out in this study. The major conclusions and recommendations for further studies are summarized in this chapter.

9.1 Conclusions

9.1.1 Anisotropic stiffness of a saturated compacted lateritic clay from very small to large strains

The study in Chapter 4 aimed to determine the cross-anisotropic stiffness response of a saturated compacted lateritic clay. A comprehensive test programme was designed to investigate the anisotropic stiffness from very small to large strains using bender element tests and consolidated drained and undrained compression tests in a triaxial apparatus. This test programme allowed the complete set of cross-anisotropic stiffness parameters for both total and effective stress analysis to be obtained and analysed. The results provide a valuable

addition to the data in the literature about the cross-anisotropy of soils because the knowledge of cross-anisotropy of soils, which has primarily focused on sedimentary clays and other weathered soils may not apply to lateritic soils.

The compacted lateritic clay specimens show some degree of anisotropy from very small to large strains. At very small strains below 0.001%, stiffness in the vertical plane is larger than in the horizontal direction, mainly attributed to the specimen preparation technique. The anisotropy changes continuously during shearing at small strains from 0.001% to 1%. At large strains above 1%, the horizontal cut specimen shows higher strength because of larger contraction during shearing. The above results suggest differences between the stiffness anisotropy at small strains and strength anisotropy at large strains.

It seems unreasonable to solely relate the stiffness characteristics of the lateritic clay to its PI. Compared with other clays with a similar PI, the lateritic clay has a lower elastic shear modulus (i.e. a larger A value in [equation \(4.5\)](#)) at the same confining pressure. The elastic shear moduli of lateritic clay are less sensitive to a change in confining pressure (i.e. a smaller n value in [equation \(4.5\)](#)). Beyond the elastic strain limit, a high stiffness degradation rate is observed for the lateritic clay. These observations imply that the widely used correlations between stiffness parameters and PI may not apply to the lateritic clay. Even though the tested lateritic clay has a high clay content of 28% and a PI of 21%, it behaves more like a granular material in general, owing to its high degree of particle aggregations.

At a given stress condition, the very small strain shear modulus of the lateritic clay is generally larger than that of CDT. This can be attributed to the nature of the soil microstructure, as illustrated in the SEM images. The lateritic clay specimen comprises larger aggregates, whereas CDT comprises many small platy-like particles and smaller aggregates. The lateritic clay is thus stiffer at a given stress condition because of its larger aggregates and accumulation of fines at the inter-aggregate contacts. As a fine-grained material, the lateritic clay behaves more like a granular material because of its high degree of particle aggregations. CDT is used as one example, and similar findings are expected if another fine-grained soil is compared with the lateritic clay. On the other hand, the very small strain shear modulus of the lateritic clay is less sensitive to stress.

9.1.2 Low suction effects soil stiffness under monotonic loading

Chapter 5 reports the stiffness and strength behaviour of an unsaturated compacted lateritic clay considering the coupled effects of compaction-induced anisotropy and suction in the low

suction range (less than 150 kPa). The results of the isotropic compression and constant-suction shearing test are presented and analysed. The findings add to the body of knowledge regarding the anisotropy behaviour of unsaturated soils, which has mostly concentrated on natural sedimentary clays and other weathered soils that may not apply to lateritic soils.

The secant Young's modulus (E_{sec}) increases non-linearly with an increase of suction between a strain range of 0.001% to 1%. Moreover, the incremental rate of stiffness with suction decreases with increasing suction. The non-linear response of the increment in stiffness and suction at different mean net stress occurs because of a combined effect of particle aggregation and water retention behaviour.

Similar to the results at saturated conditions, the lateritic clay exhibits some degree of anisotropy in unsaturated compacted specimens. In various stress and suction conditions, the vertically cut specimens are consistently stiffer than the horizontally cut specimens (i.e., $E_h/E_v < 1$) at strains below 0.2%. The difference is likely because the force chain of particle arrangement and orientation may be much stronger in the vertical direction than in the horizontal direction. Within this strain range, the degree of anisotropy increases as the suction increases from 0 to 150 kPa, because suction effects on soil stiffness are more significant for vertical specimens than horizontal specimens. On the other than, when the strain is above 0.2%, the value of E_h/E_v can exceed 1 in some cases, mainly attributed to the influence of strength anisotropy.

In addition, some semi-empirical equations are proposed based on the experimental results. In particular, the coupled effects of suction and anisotropy are incorporated. The measured and computed results are generally consistent.

9.1.3 High suction effects on the stiffness under monotonic shearing

Most previous studies on suction-controlled effects on soil stiffness are limited to suctions less than 1 MPa. This limits our understanding and predicting soil behaviour over high suction ranges in relatively extreme dry conditions. The effects of suction over 3 MPa on the monotonic and cyclic shear response of compacted lateritic soil were examined in Chapter 6. The resilient modulus, stiffness degradation and shear-induced volume change are measured and discussed.

The experimental results of monotonic shear tests revealed that all the specimens tested under high suction have their deviator stress reaching a peak value before it starts to decline with increasing axial strain (i.e., strain softening response) and finally reaching a critical state

deviator stress. All the specimens at high suctions failed with the formation of shear bands, different from the observations at low suctions.

As stiffness at the suction of 40 MPa is generally larger than the stiffness at 300 MPa, for the compaction water contents at 16% (i.e. dry side) and 22% (i.e., wet side). However, for the compaction water content of 19% (i.e. optimum), the stiffness is larger at 300 MPa than at 40 MPa. The above results are likely attributed to microstructural characteristics, the presence of meniscus water and their evolution due to high suction-induced desiccation.

With increased compaction water content, the peak deviator stress at a given suction increases, likely attributed to the compaction-induced particle aggregation of the specimen. Although the compaction-induced structure and suction influenced the peak strain, the critical state shear strength is nearly constant and unaffected by the compaction-induced structure.

9.1.4 High suction effects on the stiffness under cyclic shearing

The cyclic deviator stress has different effects on M_R depending on whether its suction is relatively low (below 1 MPa) or high (above 4 MPa). At low suction, M_R reduces with cyclic deviator stress. The reduction may be because of the highly non-linear stress-strain behaviour of soils under cyclic loads and the decrease in soil stiffness with increasing stress (or strain). However, at high suction, M_R increases with cyclic deviator stress. Soil may be hardened because crushing of aggregate contacts the fill voids spaces, and stiffening of soil skeleton may occur. Thus, M_R increases with cyclic deviator stress.

In general, it was also shown that at the same compaction water content, within the low suction range, M_R increases with suction. These suction effects are more obvious at high cyclic stress. On the other hand, at relatively high suction, resilient modulus varies with suction depending on the compaction water content. Suction effects are more obvious at low cyclic stress.

The accumulated plastic strain increases with an increase in cyclic deviator stress. This is attributed to the initial suction of the soil (or suction imposed) at various initial water content. The measured accumulated plastic strain with cyclic deviator stress is only up 0.4% for suctions above 1 MPa (i.e., water content below 16%), compared to the accumulated plastic strain of about 5.6% for suctions below 150 kPa (i.e., water content above 19%). The very small plastic strain accumulations at high suction may be attributed to the crushing of aggregate contacts, which fill voids spaces preventing further plastic deformation.

9.1.5 Thermal and suction effects on elastic shear modulus of compacted lateritic clay

The investigation of thermal effects on elastic shear modulus from a temperature control oedometer has shown that when the temperature increases from 20 to 40°C, the decrease in the elastic shear modulus G_0 can be up to 30% for the tested lateritic clay. The shear modulus reduction may be because the heating causes an increase in the repulsive electric force between soil particles. Consequently, the shear wave velocity and hence the G_0 become smaller.

After four thermal cycles in the temperature range of 5 and 60°C, the G_0 increases by 12% and 16% for lateritic specimens loaded at 50 and 400 kPa, respectively. Under the same thermal cycles, G_0 increases by about 30% for the kaolin clay loaded at 400 kPa. The increase is mainly attributed to soil densification and particle rearrangement induced by heating-cooling cycles.

The investigation of elastic shear modulus using temperature and suction-controlled triaxial apparatus has shown that an increase in temperature generally reduces the elastic shear modulus at constant suction. With an increase in the suction, the effects of temperature in reducing the elastic shear modulus become significant. Higher temperatures would increase the likelihood of particle and aggregate slippage because of thermal softening effects.

A different magnitude of reduction of elastic shear modulus with increasing temperature is observed, which is also dependent on the measurement plane. This dependency may be attributed to the different expansion of minerals in measured planes or the difference in the magnitude of surface tension reduction in measured planes, weakening the interaction between particles and aggregates. Hence the results show a possible thermal-induced anisotropy.

9.1.6 Pavement performance analysis

The KENPAVE software's analysis revealed how much stress and strain are distributed throughout the pavement layers. The resultant vertical compressive strain in the pavement layers is inversely proportional to the subgrade modulus. However, the pavement layers' compressive strains rise due to thermally induced modulus reduction, leading to an increase in the pavement's rut depth.

In the analysis presented, an increase in subgrade modulus due to suction changing from 0 to 150 kPa can cause about a 26% decrease in the rutting deformation of the pavement. However, the effect of an increase in subgrade modulus within the same suction range on fatigue cracking is about 11%, which is less than half the rutting response.

As the thermally induced decrease in the subgrade modulus is considered, the horizontal tensile strains in the asphalt layers decrease. On the other hand, due to the thermal reduction in subgrade modulus, the tensile strains in the subgrade layer become larger. The pavement damage due to thermal reduction in subgrade modulus is more detrimental in rutting than fatigue cracking.

9.2 Recommendations for Further work

The previous discussion and conclusions should be treated cautiously since they may be specific and only apply to some soil types. Before any recommendations for further work are mentioned, several limitations to this thesis need to be acknowledged. Although more microstructural evidence was provided in this study, it may be unclear how specific sesquioxides solely contribute to the microstructural aggregation and small strain stiffness. Hence, this study may also be unable to quantify the hydromechanical behaviour of lateritic soils regarding sesquioxide content. Unfortunately, the study did not include intact specimens of natural lateritic soils. Because of differences in uniformity and water distribution, the microstructure evolution and suction effects on the stiffness of naturally lateritic soils will probably differ compared to the compacted specimens investigated in this study. The stiffness anisotropy of the unsaturated lateritic soil was limited to a small suction range in terms of the water retention of the lateritic soil. An issue that was not addressed in this study was the thermal effects and coupled suction and thermal effects of the cyclic mechanical behaviour of unsaturated lateritic soils.

9.2.1 Recommendations for experimental study

Although efforts were made in this study to explain the thermo-hydro-mechanical behaviour of the lateritic clay with some microstructural analysis, the explanation may be subjective. For instance, many pores were not detected in the MIP tests due to equipment limitations. Future research using the X-CT combined with MIP/SEM may be able to better identify aggregate size and dimensions, which could help quantify and improve the understanding of small strain stiffness anisotropy of unsaturated lateritic soils.

Further research on the influence of the whole range of SUCTION on the stiffness anisotropy at an unsaturated state would be worthwhile. Because of the relatively high fine-grained fraction and the soil's dual porosity, the residual degree of saturation is expected to possibly occur at suctions over 1 MPa. Future research, in particular, could therefore

concentrate on investigating high suction magnitudes greater than 1 MPa and how high suction magnitudes alter the anisotropic characteristics.

This experimental study did not apply the different suction control methods in the same testing apparatus. In other words, there was no combination of the suction control techniques in the same apparatus to obtain small strain stiffness characteristics for the same specimen over a wide suction range. Such a method could help eliminate the repetition of many tests and specimen variability. This research approach might encompass all potential saturation levels, from saturated to comparatively dry.

More research is also required to better understand and establish whether temperature changes can induce significant anisotropy of stiffness and how the stiffness anisotropy evolves with increasing or decreasing temperature.

Some possible future studies using the same experimental setups but different stress paths are apparent. Different stress path is well recognised as an influencing factor of the thermo-hydro-mechanical behaviour of soils. More experimental data considering a switch of the mechanical, hydro and thermal loading paths may help validate and improve our current understanding of the small strain stiffness of unsaturated lateritic soils.

9.2.2 Recommendations for modelling and analysis

Although the proposed semi-empirical equation for the temperature dependent elastic shear modulus may be useful for constitutive modelling of unsaturated soil, it can further be improved by considering a model for the strain dependent modulus degradation curve. By adopting a state-dependent bounding surface plasticity model, an enhanced temperature and suction dependent stiffness degradation curve may be incorporated into numerical models for unsaturated soils under non-isothermal conditions.

With regard to the pavement performance analysis, the effects of stiffness anisotropy were not considered. A more efficient approach could be simulating changes in stress-state variables such as temperature and suction of the pavement using finite element code based on advanced constitutive model. Advanced numerical simulations may also be used to predict the pavement performance with a consideration of more complex soil behaviour, which could then be compared with results from KENPAVE in the future.

APPENDIX

Derivation of cross-anisotropic elastic constants

Based on the constant volume restrictions on the values of the undrained anisotropic Poisson's ratios, it has been shown that (Atkinson 1975, 2000; Chowdhury and King 1971)

$$v_{vh}^u = 0.5 \quad (A1)$$

$$v_{hv}^u + v_{hh}^u = 1 \quad (A2)$$

On the other hand, a parameter N is defined as the degree of stiffness anisotropy under undrained loading (Atkinson 1975),

$$\frac{E_v^u}{E_h^u} = N \quad (A3)$$

It can be derived based on equations (4.2) and (A3) that,

$$\frac{v_{vh}^u}{v_{hv}^u} = N \quad (A4)$$

Equations (A1) and (A4) suggest that,

$$v_{hv}^u = \frac{0.5}{N} \quad (A5)$$

$$v_{hh}^u = 1 - \frac{0.5}{N} \quad (A6)$$

Equation (4.2) is applicable for both drained and undrained conditions, hence,

$$E_h^u = 2G_{hh}^u (1 + v_{hh}^u) \quad (A7)$$

Substituting equation (A5) into equation (A7) gives:

$$2G_{hh}^u \left(2 - \frac{0.5}{N} \right) = \frac{E_v^u}{N} \quad (A8)$$

The above equations obtained the complete stiffness parameters for total stress analysis. After the measurement of E_v^u and G_{hh}^u , the value of N was estimated from equation (A8)

and used to calculate E_h^u using equation (A3). The undrained Poisson's ratios ν_{hv}^u and ν_{hh}^u were determined using equations (A5) and (A6).

REFERENCES

- AASHTO. 2008. Mechanistic-Empirical Pavement Design Guide. Washington, D.C.
- AASHTO. 2017. AASHTO: T 307-99 Standard Method of Test for Determining the Resilient Modulus of Soils and Aggregate Materials. *In* American Association of State Highway and Transportation Officials, Washington D.C., USA.
- Abuel-Naga, H.M., Bergado, D.T., Bouazza, A., and Ramana, G.V. 2007. Volume change behaviour of saturated clays under drained heating conditions: experimental results and constitutive modeling. *Canadian Geotechnical Journal*, **44**: 942-956. doi:10.1139/t07-031.
- Abuel-Naga, H.M., Bergado, D.T., Bouazza, A., and Pender, M. 2009a. Thermomechanical model for saturated clays. *In* *Géotechnique*. pp. 273-278.
- Abuel-Naga, H.M., Bergad O, D.T., Ouazza, A.B., and Pend Er, M. 2009b. Thermomechanical model for saturated clays. *Géotechnique*, **59**: 273-278. doi:10.1680/geot.2009.59.3.273.
- Airey, D., Suchowerska, A., and Williams, D. 2012. Limonite – a weathered residual soil heterogeneous at all scales. *Géotechnique Letters*, **2**: 119-122. doi:10.1680/geolett.12.00026.
- Aitchison, G.D. 1965a. Moisture equilibria and moisture changes in soils beneath covered areas; a symposium in print. *In* A Symposium in Print, Australia: Butterworths. p. 278.
- Aitchison, G.D. Soil properties, shear strength and consolidation. *In* Proceedings of the 6th International Conferences on Soil Mechanics and Foundation Engineering. Montreal, Canada 1965b. pp. 318-321.
- Aitchison, G.D., and Donald, I. 1955. Some preliminary studies of unsaturated soils. CSIRO, Division of Soils, Soil Mechanics Laboratory.
- Akinniyi, D.B. 2019. Compressibility and shear behaviour of saturated and unsaturated lateritic clay rich in sesquioxide. The Hong Kong University of Science and Technloly, Clear Water Bay, Kowloon, Hong Kong.
- Alonso, E.E., Gens, A., and Josa, A. 1990. A constitutive model for partially saturated soils. *Géotechnique*, **40**: 405-430. doi:10.1680/geot.1990.40.3.405.
- Alonso, E.E., Pinyol, N.M., and Gens, A. 2013. Compacted soil behaviour: initial state, structure and constitutive modelling. *Géotechnique*, **63**: 463-478. doi:10.1680/geot.11.P.134.
- Alonso, E.E., Pereira, J.-M., Vaunat, J., and Olivella, S. 2010. A microstructurally based effective stress for unsaturated soils. *Géotechnique*, **60**: 913-925. doi:10.1680/geot.8.P.002.
- Arisha, A.M., Gabr, A.R., El-Badawy, S.M., and Shwally, S.A. 2018. Performance Evaluation of Construction and Demolition Waste Materials for Pavement Construction in Egypt. *Journal of Materials in Civil Engineering*, **30**(2): 04017270. doi:doi:10.1061/(ASCE)MT.1943-5533.0002127.
- ASTM. 2007. D4015-07: Standard test methods for modulus and damping of soils by resonant-column method. ASTM International, West Conshohocken, Pa. USA.
- ASTM. 2017a. D2487 – 17e1: Standard Practice for Classification of Soils for Engineering Purposes (Unified Soil Classification System). ASTM International, West Conshohocken, Pa. USA.

- ASTM. 2017b. D6913/D6913M - 17: Standard Test Methods for Particle-Size Distribution (Gradation) of Soils Using Sieve Analysis. ASTM International, West Conshohocken, Pa. USA.
- ASTM. 2017c. D7928 - 17: Standard Test Method for Particle-Size Distribution (Gradation) of Fine-Grained Soils Using the Sedimentation (Hydrometer) Analysis. ASTM International, West Conshohocken, Pa. USA.
- Atkinson, J.H. 1975. Anisotropic elastic deformations in laboratory tests on undisturbed London Clay. *Géotechnique*, **25**: 357-374. doi:10.1680/geot.1975.25.2.357.
- Atkinson, J.H. 2000. Non-linear soil stiffness in routine design. *Géotechnique*, **50**: 487-508. doi:10.1680/geot.2000.50.5.487.
- Atkinson, J.H., and Salfors, G. Experimental determination of stress-strain- time characteristics in laboratory and in-situ tests. *In* Proceeding of the 10th European Conference on Soil Mechanics and Foundation Engineering. 1991. pp. 915-956.
- Baker, R., and Frydman, S. 2009. Unsaturated soil mechanics: Critical review of physical foundations. *Engineering Geology*, **106**(1-2): 26-39. doi:10.1016/j.enggeo.2009.02.010.
- Banerjee, A., Puppala, A.J., Congress, S.S.C., Chakraborty, S., Likos, W.J., and Hoyos, L.R. 2020. Variation of Resilient Modulus of Subgrade Soils over a Wide Range of Suction States. *Journal of Geotechnical and Geoenvironmental Engineering*, **146**: 04020096. doi:10.1061/(ASCE)GT.1943-5606.0002332.
- Behbehani, F., and McCartney, J.S. 2022. Compression Response of Sedimented Unsaturated Soils. *Journal of Geotechnical and Geoenvironmental Engineering*, **148**(12). doi:10.1061/(asce)gt.1943-5606.0002931.
- Biglari, M., D'Onofrio, A., Mancuso, C., Jafari, M.K., Shafiee, A., and Ashayeri, I. 2012. Small-strain stiffness of Zeno kaolin in unsaturated conditions. *Canadian Geotechnical Journal*, **49**: 311-322. doi:10.1139/t11-105.
- Bilodeau, J.-P., and Doré, G. 2012. Relating resilient behaviour of compacted unbound base granular materials to matrix and interlock characteristics. *Construction and Building Materials*, **37**: 220-228.
- Bishop, A.W. 1959. The principle of effective stress. *Teknisk ukeblad*, **39**: 859-863.
- Bishop, A.W., and Blight, G. 1963. Some aspects of effective stress in saturated and partly saturated soils. *Géotechnique*, **13**(3): 177-197.
- Blackmore, L., Clayton, C.R.I., Powrie, W., Priest, J.A., and Otter, L. 2020. Saturation and its effect on the resilient modulus of a pavement formation material. *Géotechnique*, **70**: 292-302. doi:10.1680/jgeot.18.P.053.
- Blatz, J.A., Cui, Y.J., and Oldecop, L. 2008. Vapour Equilibrium and Osmotic Technique for Suction Control. *In* Laboratory and Field Testing of Unsaturated Soils. Springer, Dordrecht. pp. 49-61.
- Blight, G.E. 1991a. Theme lecture: Tropical processes causing rapid geological change. *In* Geological Society, London, Engineering Geology Special Publications. pp. 459-471.
- Blight, G.E. 1991b. Theme lecture: Tropical processes causing rapid geological change. Geological Society, London, Engineering Geology Special Publications, **7**: 459-471. doi:10.1144/GSL.ENG.1991.007.01.43.
- Brown, S.F. 1996. Soil mechanics in pavement engineering. *Géotechnique*, **46**: 383-426. doi:10.1680/geot.1996.46.3.383.
- Brown, S.F. Achievements and challenges in asphalt pavement engineering. *In* Proc. of 8th Int. Conf. on Asphalt Pavements, Seattle. 1997.
- BSI. 1990. Methods of test for soils for civil engineering purposes. British Standards Institution, London.

- Burghignoli, A., Desideri, A., and Miliziano, S. 1992. Deformability of clays under non isothermal conditions. *Rivista italiana di Geotecnica*, **4**(92): 227-236.
- Burmister, D.M. 1945. The general theory of stresses and displacements in layered soil systems. III. *Journal of applied Physics*, **16**(5): 296-302.
- Cai, G., Zhou, A., Liu, Y., Xu, R., and Zhao, C. 2020. Soil water retention behavior and microstructure evolution of lateritic soil in the suction range of 0–286.7 MPa. *Acta Geotechnica*, **15**: 3327-3341. doi:10.1007/s11440-020-01011-w.
- Cai, Y., Sangghaleh, A., and Pan, E. 2015. Effect of anisotropic base/interlayer on the mechanistic responses of layered pavements. *Computers and Geotechnics*, **65**: 250-257. doi:10.1016/j.compgeo.2014.12.014.
- Caicedo, B., Coronado, O., Fleureau, J.M., and Correia, A.G. 2009. Resilient behaviour of non standard unbound granular materials. *Road Materials and Pavement Design*, **10**: 287-312.
- Callisto, L., and Rampello, S. 2002. Shear strength and small-strain stiffness of a natural clay under general stress conditions. *Géotechnique*, **52**: 547-560. doi:10.1680/geot.2002.52.8.547.
- Campanella, R.G., and Mitchell, J.K. 1968. Influence of Temperature Variations on Soil Behavior. *Journal of the Soil Mechanics and Foundations Division*, **94**: 709-734. doi:10.1061/jsfeaq.0001136.
- Carvalho, J.C., and Leroueil, S. 2000. Normalizing models for soil retention curves. *In Proceedings of 32nd Pavements Meeting, Brasilia*. pp. 96-106.
- Cekerevac, C., and Laloui, L. 2004. Experimental study of thermal effects on the mechanical behaviour of a clay. *International Journal for Numerical and Analytical Methods in Geomechanics*, **28**: 209-228. doi:10.1002/nag.332.
- Cha, M., Santamarina, J.C., Kim, H.-S., and Cho, G.-C. 2014. Small-Strain Stiffness, Shear-Wave Velocity, and Soil Compressibility. *Journal of Geotechnical and Geoenvironmental Engineering*, **140**: 06014011-06014011-06014014. doi:10.1061/(asce)gt.1943-5606.0001157.
- Chen, W.-B., Yin, J.-H., and Feng, W.-Q. 2018. A new double-cell system for measuring volume change of a soil specimen under monotonic or cyclic loading. *Acta Geotechnica*, **14**: 71-81. doi:10.1007/s11440-018-0629-6.
- Chen, W.-B., Feng, W.-Q., Yin, J.-H., and Borana, L. 2020. LVDTs-based radial strain measurement system for static and cyclic behavior of geomaterials. *Measurement*, **155**: 107526. doi:<https://doi.org/10.1016/j.measurement.2020.107526>.
- Cheng, Q., Ng, C.W.W., Zhou, C., and Tang, C.S. 2019. A new water retention model that considers pore non-uniformity and evolution of pore size distribution. *Bulletin of Engineering Geology and the Environment*, **78**(7): 5055-5065. doi:10.1007/s10064-019-01476-4.
- Cho, G.C., and Santamarina, J.C. 2001. Unsaturated Particulate Materials&-Particle-Level Studies. *Journal of Geotechnical and Geoenvironmental Engineering*, **127**(1): 84-96. doi:doi:10.1061/(ASCE)1090-0241(2001)127:1(84).
- Chowdhury, R.N., and King, G.J.W. 1971. Discussion: Anisotropic Elastic Parameters For Soil. *Géotechnique*, **21**: 181-183. doi:10.1680/geot.1971.21.2.181.
- Clayton, C.R.I. 2011. Stiffness at small strain: research and practice. *Géotechnique*, **61**: 5-37. doi:10.1680/geot.2011.61.1.5.
- Clayton, C.R.I., and Khatrush, S.A. 1986. A new device for measuring local axial strains on triaxial specimens. *Géotechnique*, **36**: 593-597. doi:10.1680/geot.1986.36.4.593.
- Clayton, C.R.I., and Heymann, G. 2001. Stiffness of geomaterials at very small strains. *Géotechnique*, **51**: 245-255. doi:10.1680/geot.2001.51.3.245.

- Coccia, C.R., and McCartney, J. 2012. A thermo-hydro-mechanical true triaxial cell for evaluation of the impact of anisotropy on thermally induced volume changes in soils. *Geotechnical Testing Journal*, **35**(2): 227-237.
- Cokca, E., Erol, O., and Armangil, F. 2004. Effects of compaction moisture content on the shear strength of an unsaturated clay. *Geotechnical and Geological Engineering*, **22**: 285-297. doi:10.1023/B:GEGE.0000018349.40866.3e.
- Çokça, E., and Tilgen, H.P. 2009. Shear strength-suction relationship of compacted Ankara clay. *Applied Clay Science*. doi:10.1016/j.clay.2009.08.028.
- Coleman, J.D. 1962. Stress strain relations for partly saturated soil. *Correspondence to Géotechnique*, **12**(4): 348-350. doi:10.1680/geot.1962.12.4.348.
- Cuccovillo, T., and Coop, M.R. 1997. The measurement of local axial strains in triaxial tests using LVDTs. *Géotechnique*, **47**: 167-171. doi:10.1680/geot.1997.47.1.167.
- Cui, Y.-J., Terpereau, J.-M., Marcial, D., Delage, P., Antoine, P., Marchadier, G., and Ye, W.-M. A geological and geotechnical characterisation of the loess of Northern France. *In Advances in geotechnical engineering: The Skempton conference: Proceedings of a three day conference on advances in geotechnical engineering, organised by the Institution of Civil Engineers and held at the Royal Geographical Society, London, UK, on 29–31 March 2004*. 2004. Thomas Telford Publishing. pp. 417-428.
- Cui, Y.J., and Delage, P. 1996. Yielding and plastic behaviour of an unsaturated compacted silt. *Géotechnique*, **46**: 291-311. doi:10.1680/geot.1996.46.2.291.
- De Jong, D. 1979. Computer program BISAR, Layered systems under normal and tangential loads. External Report, Koninklijke/Shell-Laboratorium.
- Delage, P., and Cui, Y.J. 2008. An evaluation of the osmotic method of controlling suction*. *Geomechanics and Geoengineering*, **3**(1): 1-11. doi:10.1080/17486020701868379.
- Delage, P., Howat, M.D., and Cui, Y.J. 1998. The relationship between suction and swelling properties in a heavily compacted unsaturated clay. *Engineering Geology*, **50**(1-2): 31-48. doi:10.1016/s0013-7952(97)00083-5.
- Delage, P., Audiguier, M., Cui, Y.-J., and Howat, M.D. 1996. Microstructure of a compacted silt. *Canadian Geotechnical Journal*, **33**: 150-158. doi:10.1139/t96-030.
- Di Donna, A., and Laloui, L. 2015. Response of soil subjected to thermal cyclic loading: Experimental and constitutive study. *Engineering Geology*, **190**: 65-76. doi:10.1016/j.enggeo.2015.03.003.
- Dong, Y., McCartney, J.S., and Lu, N. Small-Strain Shear Modulus Model for Saturated and Unsaturated Soils. *In Geo-Chicago 2016*. 2016-08-08 2016a. American Society of Civil Engineers.
- Dong, Y., Lu, N., and McCartney, J.S. 2016b. Unified Model for Small-Strain Shear Modulus of Variably Saturated Soil. *Journal of Geotechnical and Geoenvironmental Engineering*, **142**: 04016039- 04016031-04016010. doi:10.1061/(ASCE)GT.1943-5606.0001506.
- Edlefsen, N.E., and Anderson, A.B.C. 1943. Thermodynamics of soil moisture. *In Hilgardia*. University of California Agriculture and Natural Resources (UC ANR). pp. 31-298.
- Eriksson, L.G. 1989. Temperature effects on consolidation properties of sulphide clays. *In 12th International Conference on Soil Mechanics and Foundation Engineering, Rio de Janeiro*. pp. 2087-2090.
- Fagundes, L.S., and Rodrigues, R.A. 2015. Shear strength of a natural and compacted tropical soil. *Electronic Journal of Geotechnical Engineering*, **20**: 47-58.
- Fam, M., and Santamarina, C. 1995. Study of Geoprocesses with Complementary Mechanical and Electromagnetic Wave Measurements in an Oedometer. *Geotechnical Testing Journal*, **18**: 307. doi:10.1520/GTJ10999J.

- Fam, M.A., Cascante, G., and Dusseault, M.B. 2002. Large and Small Strain Properties of Sands Subjected to Local Void Increase. *Journal of Geotechnical and Geoenvironmental Engineering*, **128**: 1018-1025. doi:10.1061/(ASCE)1090-0241(2002)128:12(1018).
- Fern, E.J., Robert, D.J., and Soga, K. 2016. Modeling the Stress-Dilatancy Relationship of Unsaturated Silica Sand in Triaxial Compression Tests. *Journal of Geotechnical and Geoenvironmental Engineering*, **142**(11): 04016055. doi:10.1061/(asce)gt.1943-5606.0001546.
- Fisher, R.A. 1926. On the capillary forces in an ideal soil; correction of formulae given by W. B. Haines. *The Journal of Agricultural Science*, **16**: 492-505. doi:10.1017/S0021859600007838.
- Fredlund, D.G. 2006. Unsaturated Soil Mechanics in Engineering Practice. *Journal of Geotechnical and Geoenvironmental Engineering*, **132**(3): 286-321. doi:doi:10.1061/(ASCE)1090-0241(2006)132:3(286).
- Fredlund, D.G., and Morgenstern, N.R. 1977. Stress state variable for unsaturated soils. *Journal of Geotechnical Engineering*, **105**(5): 447-466.
- Fredlund, D.G., and Rahardjo, H. 1993. *Soil mechanics for unsaturated soils*. John Wiley & Sons.
- Futai, M.M., and Almelda, M.S.S. 2005. An experimental investigation of the mechanical behaviour of an unsaturated gneiss residual soil. *Géotechnique*, **55**: 201-214.
- Gallipoli, D., Gens, A., Sharma, R., and Vaunat, J. 2003. An elasto-plastic model for unsaturated soil incorporating the effects of suction and degree of saturation on mechanical behaviour. *Géotechnique*, **53**: 123-136. doi:10.1680/geot.53.1.123.37251.
- Gasparre, A., Nishimura, S., Coop, M.R., and Jardine, R.J. 2007a. The influence of structure on the behaviour of London Clay. *In Géotechnique*. pp. 19-31.
- Gasparre, A., Nishimura, S., Minh, N.A., Coop, M.R., and Jardine, R.J. 2007b. The stiffness of natural London Clay. *Géotechnique*, **57**: 33-47. doi:10.1680/geot.2007.57.1.33.
- Gens, A., Sánchez, M., and Sheng, D. 2006. On constitutive modelling of unsaturated soils. *Acta Geotechnica*, **1**(3): 137-147. doi:10.1007/s11440-006-0013-9.
- Ghahremannejad, B. 2003a. Thermo-mechanical behaviour of two reconstituted clays.
- Ghahremannejad, B. 2003b. Thermo-Mechanical Behaviour of Two Reconstituted Clays.
- Gidigas, M.D. 1976. *Laterite Soil Engineering - Pedogenesis and Engineering Principles*. In Elsevier Scientific Pub. Co., Amsterdam.
- Graham, J., and Houlsby, G.T. 1983. Anisotropic elasticity of a natural clay. *Géotechnique*, **33**: 165-180. doi:10.1680/geot.1983.33.2.165.
- Graham, J., Tanaka, N., Crilly, T., and Alfaro, M. 2001. Modified Cam-Clay modelling of temperature effects in clays. *Canadian Geotechnical Journal*, **38**: 608-621. doi:10.1139/cgj-38-3-608.
- Hamid, T.B., and Miller, G.A. 2009. Shear strength of unsaturated soil interfaces. *Canadian Geotechnical Journal*, **46**(5): 595-606. doi:10.1139/t09-002.
- Hamidi, A., Asce, A.M., Turchi, S., Asce, S.M., and Khazaei, C. 2014. Thermomechanical Constitutive Model for Saturated Clays Based on Critical State Theory.
- Han, Z., and Vanapalli, S.K. 2016. Relationship between resilient modulus and suction for compacted subgrade soils. *Engineering Geology*, **211**: 85-97.
- Hardin, B.O., and Richart, F.E. 1963. Elastic wave velocities in granular soils. *Journal of Soil Mechanics & Foundations Div*, **89**: 33-65.
- Hardin, B.O., and Black, W.L. 1966. Sand stiffness under various triaxial stresses. *Journal of Soil Mechanics & Foundations Div*, **92**: 27-42.

- Hardin, B.O., and Black, W.L. 1968. Vibration Modulus of Normally Consolidated Clay. *Journal of the Soil Mechanics and Foundations Division*, **94**: 353-369. doi:10.1061/JSFEAQ.0001100.
- Hasan, A.M. 2016. Small strain elastic behaviour of unsaturated soil investigated by bender/extender element testing. University of Glasgow, Glasgow.
- Hasan, A.M., and Wheeler, S.J. Influence of compaction procedure on elastic anisotropy. *In Unsaturated Soils: Research and Applications - Proceedings of the 6th International Conference on Unsaturated Soils, UNSAT 2014*. 2014. pp. 285-289.
- Head, K.H. 1998. Manual of soil laboratory testing: Effective stress tests. *Manual of Soil Laboratory Testing*. John Wiley & Sons, USA.
- Heitor, A., Indraratna, B., and Rujikiatkamjorn, C. 2013. Laboratory study of small-strain behavior of a compacted silty sand. *Canadian Geotechnical Journal*, **50**: 179-188. doi:10.1139/cgj-2012-0037.
- Heitor, A., Indraratna, B., and Rujikiatkamjorn, C. 2015. The role of compaction energy on the small strain properties of a compacted silty sand subjected to drying–wetting cycles. *Géotechnique*, **65**: 717-727.
- Higo, Y., Oka, F., Kimoto, S., Sanagawa, T., and Matsushima, Y. 2011. Study of Strain Localization and Microstructural Changes in Partially Saturated Sand During Triaxial Tests Using Microfocus X-Ray CT. *Soils and Foundations*, **51**(1): 95-111. doi:10.3208/sandf.51.95.
- Hilf, J.W. 1956. An investigation of pore-water pressure in compacted cohesive soils. University of Colorado at Boulder.
- Hoyos, L.R., Suescún-Florez, E.A., and Puppala, A.J. 2015. Stiffness of intermediate unsaturated soil from simultaneous suction-controlled resonant column and bender element testing. *Engineering Geology*, **188**: 10-28. doi:10.1016/j.enggeo.2015.01.014.
- Hsu, C.-C., and Vucetic, M. 2006. Threshold shear strain for cyclic pore-water pressure in cohesive soils. *Journal of Geotechnical and Geoenvironmental Engineering*, **132**(10): 1325-1335.
- Huang, Y.H. 2004. Pavement analysis and design. Pearson Prentice Hall Upper Saddle River, NJ.
- Hueckel, T., and Baldi, G. 1990. Thermoplasticity of Saturated Clays: Experimental Constitutive Study. *Journal of Geotechnical Engineering*, **116**: 1778-1796. doi:10.1061/(ASCE)0733-9410(1990)116:12(1778).
- Hveem, F.N. 1955. Pavement deflections and fatigue failures.
- Hwang, D., and Witzak, M. 1979. Program DAMA (Chevron), User's Manual. Department of Civil Engineering, University of Maryland, **338**.
- Ingale, R., Patel, A., and Mandal, A. 2017. Performance analysis of piezoceramic elements in soil: A review. *In Sensors and Actuators, A: Physical*. Elsevier B.V. pp. 46-63.
- Israelachvili, J. 2011. Intermolecular and surface forces. 3rd Edition. Academic Press, New York.
- Jardine, R.J. 1992. Some Observations on the Kinematic Nature of Soil Stiffness. *Soils and Foundations*, **32**: 111-124. doi:10.3208/sandf1972.32.2_111.
- Jardine, R.J., Symes, M.J., and Burland, J.B. 1984. The Measurement of soil stiffness in the triaxial apparatus. *Géotechnique*, **34**: 323-340. doi:10.1680/geot.1984.34.3.323.
- Jennings, J.E.B., and Burland, J.B. 1962. Limitations to the Use of Effective Stresses in Partly Saturated Soils. *Géotechnique*, **12**(2): 125-144. doi:10.1680/geot.1962.12.2.125.
- Jin, M.S., Lee, K.W., and Kovacs, W.D. 1994. Seasonal variation of resilient modulus of subgrade soils. *Journal of Transportation Engineering*, **120**(4): 603-616.
- Jommi, C. 2000. Remarks on the constitutive modelling of unsaturated soils.

- Jotisankasa, A., Coop, M., and Ridley, A. 2009. The mechanical behaviour of an unsaturated compacted silty clay. pp. 415-428.
- Jovičić, V., and Coop, M.R. 1998. The Measurement of Stiffness Anisotropy in Clays with Bender Element Tests in the Triaxial Apparatus. *Geotechnical Testing Journal*, **21**: 3-10. doi:10.1520/GTJ10419J.
- Kaewsong, R. 2017. Anisotropic small-strain stiffness of unsaturated compacted and intact collapsible loess. Clear Water Bay, Kowloon, Hong Kong.
- Khosravi, A., and McCartney, J.S. 2011. Resonant column test for unsaturated soils with suction–saturation control. *Geotechnical Testing Journal*, **34**(6): 730-739.
- Khosravi, A., and McCartney, J.S. 2012. Impact of Hydraulic Hysteresis on the Small-Strain Shear Modulus of Low Plasticity Soils. *Journal of Geotechnical and Geoenvironmental Engineering*, **138**: 1326-1333. doi:10.1061/(ASCE)GT.1943-5606.0000713.
- Khosravi, A., Shahbazan, P., and Pak, A. 2018. Impact of hydraulic hysteresis on the small strain shear modulus of unsaturated sand. *Soils and Foundations*, **58**: 344-354. doi:10.1016/j.sandf.2018.02.018.
- Khosravi, A., Ghayoomi, M., McCartney, J., and Ko, H.-Y. 2010. Impact of Effective Stress on the Dynamic Shear Modulus of Unsaturated Sand. *In GeoFlorida 2010*. pp. 410-419.
- Khoury, a., Khoury, C.N., Khoury, N.N., and Miller, G.A. 2011. Effect of Cyclic Suction History (Hydraulic Hysteresis) on Resilient Modulus of Unsaturated Fine-Grained Soil. *Transportation Research Record: Journal of the Transportation Research*, **2232**: 68-75. doi:10.3141/2232-07.
- Kopperman, S., Tiller, G., and Tseng, M. 1986. ELSYM5: Interactive microcomputer version: User's manual. Rep. No. FHWA-TS-87, **206**.
- Krahn, J., and Fredlund, D.G. 1972. ON TOTAL, MATRIC AND OSMOTIC SUCTION. *In Soil Science*.
- Kung, J.H.S., Lin, H.D., Yang, S.-J., and Huang, W.-H. 2006. Resilient Modulus and Plastic Strain of Unsaturated Cohesive Subgrade Soils. *In Unsaturated Soils 2006*. American Society of Civil Engineers, Reston, VA. pp. 541-552.
- Ladd, R.S. 1978. Preparing Test Specimens Using Undercompaction. *In Geotechnical Testing Journal*. pp. 16-23.
- Laloui, L. 2001. Thermo-mechanical behaviour of soils. *Revue Française de Génie Civil*, **5**(6): 809-843. doi:10.1080/12795119.2001.9692328.
- Laloui, L., and Di Donna, A. 2013. Energy Geostructures. *In Energy Geostructures: Innovation in Underground Engineering*. Edited by L. Laloui and A. Di Donna. John Wiley & Sons, Inc., Hoboken, NJ USA. pp. 1-304.
- Lambe, T.W. 1958. The structure of compacted clay. *In J. Soil Mech. and Foundation, Div., ASCE*. p. paper 1654.
- Lambe, T.W. 1962. Soil Stabilization. *In Chap. 4 of Foundation Engineering*.
- Lee, J.-S., and Santamarina, J.C. 2005. Bender Elements: Performance and Signal Interpretation. *In Journal of Geotechnical and Geoenvironmental Engineering*. pp. 1063-1070.
- Lekarp, F., Isacsson, U., and Dawson, A. 2000. State of the art. I: Resilient response of unbound aggregates. *In Journal of Transportation Engineering*. American Society of Civil Engineers. pp. 66-75.
- Leong, E.C., Cahyadi, J., and Rahardjo, H. Stiffness of a Compacted Residual Soil. *In Unsaturated Soils 2006*. 2006-03-17 2006. American Society of Civil Engineers.
- Leong, E.C., Cahyadi, J., and Rahardjo, H. 2009. Measuring shear and compression wave velocities of soil using bender–extender elements. *In Canadian Geotechnical Journal*. pp. 792-812.

- Li, X., and Zhang, L.M. 2009. Characterization of dual-structure pore-size distribution of soil. *In Canadian Geotechnical Journal*. pp. 129-141.
- Lingnau, B.E., Graham, J., and Tanaka, N. 1995. Isothermal modeling of sand-bentonite mixtures at elevated temperatures. *In Canadian Geotechnical Journal*. pp. 78-88.
- Lings, M.L. 2001. Drained and undrained anisotropic elastic stiffness parameters. *In Géotechnique*. pp. 555-565.
- Lings, M.L., Pennington, A.D.S., and Nash, D.F.T. 2000a. Anisotropic stiffness parameters and their measurement in a stiff natural clay.
- Lings, M.L., Pennington, D.S., and Nash, D.F.T. 2000b. Anisotropic stiffness parameters and their measurement in a stiff natural clay. *In Stiff Sedimentary Clays: Genesis and Engineering Behaviour - Geotechnique Symposium in Print 2007*. pp. 301-317.
- Liu, K., Yin, J.-H., Chen, W.-B., Feng, W.-Q., and Zhou, C. 2020. The stress-strain behaviour and critical state parameters of an unsaturated granular fill material under different suctions. *Acta Geotechnica*, **15**(12): 3383-3398. doi:10.1007/s11440-020-00973-1.
- Liu, M., and Carter, J. 2002. A structured Cam Clay model. *Canadian Geotechnical Journal*, **39**(6): 1313-1332.
- Lourenço, S.D.N., Gallipoli, D., Augarde, C.E., Toll, D.G., Fisher, P.C., and Congreve, A. 2012. Formation and evolution of water menisci in unsaturated granular media. *Géotechnique*, **62**(3): 193-199. doi:10.1680/geot.11.p.034.
- Love, A. A treatise on the mathematical theory of elasticity. *In Cambridge 1927*. Cambridge University Press.
- Lu, N. 2008. Is Matric Suction a Stress Variable? *Journal of Geotechnical and Geoenvironmental Engineering*, **134**(7): 899-905. doi:doi:10.1061/(ASCE)1090-0241(2008)134:7(899).
- Lu, N. 2016. Generalized Soil Water Retention Equation for Adsorption and Capillarity. *Journal of Geotechnical and Geoenvironmental Engineering*, **142**(10): 04016051. doi:doi:10.1061/(ASCE)GT.1943-5606.0001524.
- Lu, N. 2018. Generalized Elastic Modulus Equation for Unsaturated Soil. *In PanAm Unsaturated Soils 2017*. pp. 32-48.
- Lu, N., and Kaya, M. 2014. Power Law for Elastic Moduli of Unsaturated Soil. *Journal of Geotechnical and Geoenvironmental Engineering*, **140**(1): 46-56. doi:10.1061/(asce)gt.1943-5606.0000990.
- Lu, N., Godt, J.W., and Wu, D.T. 2010. A closed-form equation for effective stress in unsaturated soil. *Water Resources Research*, **46**(5). doi:<https://doi.org/10.1029/2009WR008646>.
- Lyon-Associates, and BRRI. 1971. Laterite and lateritic soils and other problem soils of Africa. Baltimore, Md.
- Macari, E.J., and Hoyos, L. 2003. Effect of Degree of Weathering on Dynamic Properties of Residual Soils. *In Journal of Geotechnical Engineering*.
- Mair, R.J. 1993. Unwin memorial lecture 1992. Developments in geotechnical engineering research: application to tunnels and deep excavations. *In Proceedings of the Institution of Civil Engineers-Civil Engineering*. Thomas Telford-ICE Virtual Library. pp. 27-41.
- Malaya, C., and Sreedeeep, S. 2012. Critical Review on the Parameters Influencing Soil-Water Characteristic Curve.
- Mallick, R.B., and El-Korchi, T. 2008. *Pavement engineering: principles and practice*. CRC Press.
- Mancuso, C., Vassallo, R., and D'Onofrio, A. 2002. Small strain behavior of a silty sand in controlled-suction resonant column - torsional shear tests. *In Canadian Geotechnical Journal*. pp. 22-31.

- Matini, N., Qiao, Y., and Sias, J.E. 2022. Development of Time–Depth–Damage Functions for Flooded Flexible Pavements. *Journal of Transportation Engineering, Part B: Pavements*, **148**(2). doi:10.1061/jpeodx.0000352.
- McCartney, J.S., and Khosravi, A. 2013. Field-Monitoring System for Suction and Temperature Profiles under Pavements. *In Journal of Performance of Constructed Facilities*. pp. 818-825.
- McCartney, J.S., Sánchez, M., and Tomac, I. 2016. Energy geotechnics: Advances in subsurface energy recovery, storage, exchange, and waste management. *In Computers and Geotechnics*. Elsevier Ltd. pp. 244-256.
- Mendoza, C.E., and Colmenares, J.E. 2006. Influence of the suction on the stiffness at very small strains. *In Unsaturated Soils 2006*. pp. 529-540.
- Miguel, M.G., and Bonder, B.H. 2012. Soil-Water Characteristic Curves Obtained for a Colluvial and Lateritic Soil Profile Considering the Macro and Micro Porosity. *In Geotechnical and Geological Engineering*. pp. 1405-1420.
- Mitchell, J.K., and Soga, K. 2005. *Fundamentals of Soil Behavior*. John Wiley & Sons, New York.
- Mitchell, J.K., Hooper, D.R., and Campenella, R.G. 1965. Permeability of Compacted Clay. *Journal of the Soil Mechanics and Foundations Division*, **91**(4): 41-65. doi:10.1061/jsfeaq.0000775.
- Mitchell, J.K., McMillan, J.C., Green, S.L., and Sisson, R.C. 1982. Field testing of cable backfill systems. *In Underground Cable Thermal Backfill*. Elsevier. pp. 19-33.
- Mohammad, L.N., Puppala, A.J., and Alavilli, P. 1994. Influence of testing procedure and LVDT location on resilient modulus of soils. *Transportation Research Record*,(1462).
- Mousa, R., El-Badawy, S., Azam, A., Gabr, A., and Arab, M. Resilient modulus characterization for granular base material in Egypt. *In 8th Int. Engineering Conf., Sharm Al-Shiekh, Egypt*. 2015.
- Mun, W., and McCartney, J.S. 2017. Constitutive Model for Drained Compression of Unsaturated Clay to High Stresses. *Journal of Geotechnical and Geoenvironmental Engineering*, **143**(6): 04017014. doi:10.1061/(asce)gt.1943-5606.0001662.
- Muñoz-Castelblanco, J., Delage, P., Pereira, J.M., and Cui, Y.J. 2011. Some aspects of the compression and collapse behaviour of an unsaturated natural loess. *Géotechnique Letters*, **1**(2): 17-22. doi:10.1680/geolett.11.00003.
- Muñoz-Castelblanco, J., Delage, P., Pereira, J.M., and Cui, Y.J. 2012. On-sample water content measurement for a complete local monitoring in triaxial testing of unsaturated soils. pp. 595-604.
- Netterberg, F. 2014. Review of specification for the use of laterite in road pavements. Contract AFCAP/GEN/124: Association of Southern Africa National Road Agency, UK Department of International Development. pp. 1-60.
- Ng, C.W., Leung, E.H., and Lau, C.K. 2004. Inherent anisotropic stiffness of weathered geomaterial and its influence on ground deformations around deep excavations. *In Canadian Geotechnical Journal*. pp. 12-24.
- Ng, C.W.W., and Menzies, B.K. 2007a. *Advanced unsaturated soil mechanics and engineering*. Taylor & Francis, London and New York.
- Ng, C.W.W., and Menzies, B. 2007b. *Advanced unsaturated soil mechanics and engineering*. Taylor & Francis. p. 690.
- Ng, C.W.W., and Yung, S.Y. 2008a. Determination of the anisotropic shear stiffness of an unsaturated decomposed soil. *Géotechnique*, **58**(1): 23-35. Available from <Go to ISI>://000253013100003 [accessed].
- Ng, C.W.W., and Yung, S.Y. 2008b. Determination of the anisotropic shear stiffness of an unsaturated decomposed soil. *In Géotechnique*. pp. 23-35.

- Ng, C.W.W., and Zhou, C. 2014. Cyclic behaviour of an unsaturated silt at various suctions and temperatures. *In Géotechnique*. pp. 709-720.
- Ng, C.W.W., Xu, J., and Yung, S.Y. 2009. Effects of wetting–drying and stress ratio on anisotropic stiffness of an unsaturated soil at very small strains. *In Canadian Geotechnical Journal*. pp. 1062-1076.
- Ng, C.W.W., Mu, Q.Y., and Zhou, C. 2017a. Effects of boundary conditions on cyclic thermal strains of clay and sand. *In Géotechnique Letters*. pp. 73-78.
- Ng, C.W.W., Mu, Q.Y., and Zhou, C. 2019a. Effects of specimen preparation method on the volume change of clay under cyclic thermal loads. *Geotechnique*, **69**(2): 146-150. Available from <https://doi.org/10.1680/jgeot.16.P.293> [accessed].
- Ng, C.W.W., Mu, Q.Y., and Zhou, C. 2019b. Effects of specimen preparation method on the volume change of clay under cyclic thermal loads. *In Géotechnique*. pp. 146-150.
- Ng, C.W.W., Zhou, C., and Chiu, C.F. 2020a. Constitutive modelling of state-dependent behaviour of unsaturated soils: an overview. *Acta Geotechnica*, **15**: 2705–2725.
- Ng, C.W.W., Akinniyi, D.B., and Zhou, C. 2020b. Volume change behaviour of a saturated lateritic clay under thermal cycles. *In Bulletin of Engineering Geology and the Environment*. pp. 653-661.
- Ng, C.W.W., Bentil, O.T., and Zhou, C. 2021. Small strain shear modulus and damping ratio of two unsaturated lateritic sandy clays. *In Canadian Geotechnical Journal*. pp. 1426-1435.
- Ng, C.W.W., Zhou, C., Yuan, Q., and Xu, J. 2013. Resilient modulus of unsaturated subgrade soil: experimental and theoretical investigations. *In Canadian Geotechnical Journal*. pp. 223-232.
- Ng, C.W.W., Kaewsong, R., Zhou, C., and Alonso, E.E. 2016. Small strain shear moduli of unsaturated natural and compacted loess. *In Géotechnique*. pp. 646-651.
- Ng, C.W.W., Akinniyi, D.B., Zhou, C., and Chiu, C.F. 2019c. Comparisons of weathered lateritic, granitic and volcanic soils: Compressibility and shear strength. *Engineering Geology*, **249**: 235-240. doi:10.1016/j.enggeo.2018.12.029.
- Ng, C.W.W., Owusu, S.T., Zhou, C., and Chiu, A.C.F. 2020c. Effects of sesquioxide content on stress-dependent water retention behaviour of weathered soils. *In Engineering Geology*. Elsevier B.V.
- Ng, C.W.W., Shi, C., Gunawan, A., Laloui, L., and Liu, H.L. 2015. Centrifuge modelling of heating effects on energy pile performance in saturated sand. *In Canadian Geotechnical Journal*. pp. 1045-1057.
- Ng, C.W.W., Baghbanrezvan, S., Sadeghi, H., Zhou, C., and Jafarzadeh, F. 2017b. Effect of specimen preparation techniques on dynamic properties of unsaturated fine-grained soil at high suctions. *In Canadian Geotechnical Journal*. pp. 1310-1319.
- Ng, C.W.W., Baghbanrezvan, S., Sadeghi, H., Zhou, C., and Jafarzadeh, F. 2017c. Effect of specimen preparation techniques on dynamic properties of unsaturated fine-grained soil at high suctions. *Canadian Geotechnical Journal*, **54**: 1310-1319. doi:10.1139/cgj-2016-0531.
- Nuth, M., and Laloui, L. 2008. Effective stress concept in unsaturated soils: Clarification and validation of a unified framework. *International Journal for Numerical and Analytical Methods in Geomechanics*, **32**(7): 771-801.
- O'reilly, M.P., and Brown, S.F. Observations on the resilient shear stiffness of granular materials. *In 1992*. pp. 631-633.
- Otálvaro, I.F., Neto, M.P.C., Delage, P., and Caicedo, B. 2016. Relationship between soil structure and water retention properties in a residual compacted soil. *In Engineering Geology*. Elsevier B.V. pp. 73-80.

- Oztoprak, S., and Bolton, M.D. 2013. Stiffness of sands through a laboratory test database. *Géotechnique*, **63**(1): 54-70. doi:10.1680/geot.10.p.078.
- Paddy, J.F. 1969. Theory of surface tension. *In* Surface and colloid science. Wiley Interscience, Toronto, Canada.
- Pan, Y., Coulibaly, J.B., and Rotta Loria, A.F. 2020. Thermally induced deformation of coarse-grained soils under nearly zero vertical stress. *In* *Géotechnique Letters*. pp. 486-491.
- Pennington, D.S., Nash, D.F.T.T., and Lings, M.L. 1997. Anisotropy of G₀ shear stiffness in Gault Clay. *Géotechnique*, **47**: 391-398. doi:10.1680/geot.1997.47.3.391.
- Philip, J.R. 1977. Unitary approach to capillary condensation and adsorption. *The Journal of Chemical Physics*, **66**(11): 5069-5075. doi:10.1063/1.433814.
- Pickering, D.J. 1970. Anisotropic Elastic Parameters for Soil. *In* *Géotechnique*. Thomas Telford Ltd. pp. 271-276.
- Pineda, J.A., Colmenares, J.E., and Hoyos, L.R. 2014. Effect of Fabric and Weathering Intensity on Dynamic Properties of Residual and Saprolitic Soils via Resonant Column Testing. *In* *Geotechnical Testing Journal*. pp. 800-816.
- Puppala, A.J., Manosuthkij, T., Nazarian, S., and Hoyos, L.R. 2011. Threshold moisture content and matric suction potentials in expansive clays prior to initiation of cracking in pavements. *In* *Canadian Geotechnical Journal*. pp. 519-531.
- Qian, X., Gray, D.H., and Woods, R.D. 1993. Voids and granulometry: effects on shear modulus of unsaturated sands. *In* *Journal of Geotechnical Engineering*. pp. 295-314.
- Romero, E. 2013. A microstructural insight into compacted clayey soils and their hydraulic properties. *In* *Engineering Geology*. Elsevier. pp. 3-19.
- Romero, E., and Simms, P.H. 2008. Microstructure investigation in unsaturated soils: A review with special attention to contribution of mercury intrusion porosimetry and environmental scanning electron microscopy. *In* *Geotechnical and Geological Engineering*. pp. 705-727.
- Romero, E., Gens, A.A., and Lloret, A. Suction effects on a compacted clay under non-isothermal conditions. *In* 2003. pp. 65-81.
- Romero, E., Vaunat, J., and Merchán, V. 2014. Suction effects on the residual shear strength of clays. *Journal of Geo-Engineering Sciences*, **2**(1-2): 17-37.
- Sawangsurriya, A. 2012. Wave Propagation Methods for Determining Stiffness of Geomaterials. *In* *Wave Processes in Classical and New Solids*. pp. 157-200.
- Sawangsurriya, A., Edil, T.B., and Bosscher, P.J. 2008. Modulus-suction-moisture relationship for compacted soils. *In* *Canadian Geotechnical Journal*. pp. 973-983.
- Sawangsurriya, A., Edil, T.B., and Benson, C.H. 2009a. Effect of Suction on Resilient Modulus of Compacted Fine-Grained Subgrade Soils. *In* *Transportation Research Record: Journal of the Transportation Research Board*. SAGE PublicationsSage CA: Los Angeles, CA. pp. 82-87.
- Sawangsurriya, A., Edil, T.B., and Bosscher, P.J. 2009b. Modulus-Suction-Moisture Relationship for Compacted Soils in Postcompaction State. *In* *Journal of Geotechnical and Geoenvironmental Engineering*. American Society of Civil Engineers (ASCE). pp. 1390-1403.
- Schädlich, B., and Schweiger, H.F. 2013. Influence of Anisotropic Small Strain Stiffness on the Deformation Behavior of Geotechnical Structures. *In* *International Journal of Geomechanics*. American Society of Civil Engineers (ASCE). pp. 861-868.
- Schultheiss, P.J. 1981. Simultaneous measurement of P & S wave velocities during conventional laboratory soil testing procedures. *In* *Marine Geotechnology*. pp. 343-367.

- Shanina, M., and McCartney, J.S. 2017. Influence of anisotropic stress states on the thermal volume change of unsaturated silt. *Soils and Foundations*, **57**(2): 252-266. doi:<https://doi.org/10.1016/j.sandf.2016.12.003>.
- Sheng, D., Sloan, S.W., and Gens, A. 2004. A constitutive model for unsaturated soils: thermomechanical and computational aspects. *Computational Mechanics*, **33**(6): 453-465. doi:10.1007/s00466-003-0545-x.
- Simpson, B. 1992. Retaining structures : displacement and design. *Géotechnique*, **42**: 541-576.
- Sivakumar, V., and Wheeler, S.J. 2000. Influence of compaction procedure on the mechanical behaviour of an unsaturated compacted clay Part 1: Wetting and isotropic compression. *In Géotechnique*. Thomas Telford Services Ltd. pp. 359-368.
- Sivakumar, V., Kodikara, J., O'Hagan, R., Hughes, D., Cairns, P., and McKinkey, J.D. 2013. Effects of confining pressure and water content on performance of unsaturated compacted clay under repeated loading. *In Géotechnique*. pp. 628-640.
- Skempton, A.W. 1954. The Pore-Pressure Coefficients A and B. *In Géotechnique*. pp. 143-147.
- Sultan, N., Delage, P., and Cui, Y.J. 2002. Temperature effects on the volume change behaviour of Boom clay. *In Engineering Geology*. Elsevier. pp. 135-145.
- Sun, a., Zhang, J., Gao, Y., and Sheng, D. 2015. Influence of Suction History on Hydraulic and Stress-Strain Behavior of Unsaturated Soils.
- Sun, D.a., You, G., Annan, Z., and Daichao, S. 2016. Soil–water retention curves and microstructures of undisturbed and compacted Guilin lateritic clay. *Bulletin of Engineering Geology and the Environment*, **75**: 781-791. doi:10.1007/s10064-015-0765-2.
- Tang, A.-M., and Cui, Y.-J. 2005. Controlling suction by the vapour equilibrium technique at different temperatures and its application in determining the water retention properties of MX80 clay. *In Canadian Geotechnical Journal*. pp. 287-296.
- Tang, A.-M., Cui, Y.-J., and Barnel, N. 2008. Thermo-mechanical behaviour of a compacted swelling clay. *Géotechnique*, **58**: 45-54. doi:10.1680/geot.2008.58.1.45.
- Tarantino, A. 2011. Unsaturated soils: compacted versus reconstituted states. *In Unsaturated soils*. Edited by EE Alonso and A. Gens. CRC Press, Barcelona, Spain. pp. 113-136.
- Terzaghi, K. The shear strength of saturated soils. *In Proceedings of the first international conference on soil mechanics and foundation engineering*, Cambridge, MA. 1936.
- Tessier, D. 1984. Etude expérimentale de l'organisation des matériaux argileux. Hydratation, gonflement et structuration au cours de la dessiccation et de la réhumectation.
- Tidfors, M., and Sällfors, S. 1989. Temperature effect on yield stress. *In Geotechnical Testing Journal*. pp. 93-97.
- Toll, D.G. 1990. A framework for unsaturated soil behaviour. *In Géotechnique*. Thomas Telford Ltd. pp. 31-44.
- Toll, D.G. 2000. The influence of fabric on the shear behaviour of unsaturated compacted soils. *In Advances in unsaturated geotechnics*. pp. 222-234.
- Tuller, M., Dani, O., and Dudley, L.M. 1999. Adsorption and capillary condensation in porous media: Liquid retention and interfacial configurations in angular pores. *In Water Resources Research*. John Wiley & Sons, Ltd. pp. 1949-1964.
- Uchaipichat, A., and Khalili, N. 2009a. Experimental investigation of thermo- hydro-mechanical behaviour of an unsaturated silt. *Géotechnique*, **59**(4): 339-353. doi:DOI 10.1680/geot.2009.59.4.339.
- Uchaipichat, A., and Khalili, N. 2009b. Experimental investigation of thermo-hydro-mechanical behaviour of an unsaturated silt. pp. 339-353.
- Vahedifard, F., Thota, S.K., Cao, T.D., Samarakoon, R.A., and McCartney, J.S. 2020. Temperature-Dependent Model for Small-Strain Shear Modulus of Unsaturated Soils.

- In Journal of Geotechnical and Geoenvironmental Engineering*. American Society of Civil Engineers (ASCE). p. 04020136.
- Vardanega, P.J., and Bolton, M.D. 2013. Stiffness of clays and silts: Normalizing shear modulus and shear strain. *Journal of Geotechnical and Geoenvironmental Engineering*, **139**: 1575-1589.
- Vassallo, R., Mancuso, C., and Vinale, F. 2007. Effects of net stress and suction history on the small strain stiffness of a compacted clayey silt. *In Canadian Geotechnical Journal*. pp. 447-462.
- Vega, A., and McCartney, J.S. 2015. Cyclic heating effects on thermal volume change of silt. *Environmental Geotechnics*, **2**(5): 257-268. doi:10.1680/envgeo.13.00022.
- Viggiani, G., and Atkinson, J.H. 1995. Interpretation of bender element tests. *In Géotechnique*. pp. 149-154.
- Vucetic, M. 1994. Cyclic threshold shear strains in soils. *Journal of Geotechnical Engineering*, **120**(12): 2208-2228.
- Vucetic, M., and Dobry, R. 1991. Effect of Soil Plasticity on Cyclic Response. *In Journal of Geotechnical Engineering*. pp. 89-107.
- Warren, H., and Dieckmann, W. 1963. Numerical computation of stresses and strains in a multiple-layer asphalt pavement system. International Report, Chevron Research Corporation, Richmond, CA.
- Wheeler, S.J., and Karube, D. 1996. State of the Art Report-Constitutive modelling. *In Proceedings 1st International Conference on Unsaturated Soils, Paris*. pp. Vol. 3, 1323-1356.
- Wheeler, S.J., and Sivakumar, V. 2000. Influence of compaction procedure on the mechanical behaviour of an unsaturated compacted clay. Part 2: Shearing and constitutive modelling. *In Géotechnique*. Thomas Telford Services Ltd. pp. 369-376.
- Wheeler, S.J., Sharma, R.S., and Buisson, M.S.R. 2003. Coupling of hydraulic hysteresis and stress-strain behaviour in unsaturated soils. *In Géotechnique*. pp. 41-54.
- Wongsaroj, J., Soga, K., and Mair, R.J. 2007. Modelling of long-term ground response to tunnelling under St James's Park, London. *In Géotechnique*. pp. 75-90.
- Wu, S., Gray, D.H., and Richart Jr, F.E. 1984. Capillary effects on dynamic modulus of sands and silts. *In Journal of Geotechnical Engineering*. pp. 1188-1203.
- Xu, J. 2011. Experimental study of effects of suction history and wetting-drying on small strain stiffness of an unsaturated soil. Civil Engineering, The Hong Kong University of Science and Technology, Clear Water Bay, Kowloon, Hong Kong.
- Yang, J., and Gu, X.Q. 2013. Shear stiffness of granular material at small strains: does it depend on grain size? *In Géotechnique*. pp. 165-179.
- Yang, S.-R., Lin, H.-D., Kung, J.H.S., and Huang, W.-H. 2008a. Suction-controlled laboratory test on resilient modulus of unsaturated compacted subgrade soils. *In Journal of Geotechnical and Geoenvironmental Engineering*. American Society of Civil Engineers. pp. 1375-1384.
- Yang, S.R., Lin, H.D., Kung, J.H.S., and Liao, J.Y. 2008b. Shear wave velocity and suction of unsaturated soil using bender element and filter paper method. *In Journal of GeoEngineering*. pp. 67-74.
- Yimsiri, S., and Soga, K. 2011a. Cross-anisotropic elastic parameters of two natural stiff clays. *In Géotechnique*. pp. 809-814.
- Yimsiri, S., and Soga, K. 2011b. Cross-anisotropic elastic parameters of two natural stiff clays. pp. 809-814.
- Young, J.F. 1967. Humidity control in the laboratory using salt solutions—a review. *Journal of Applied Chemistry*, **17**(9): 241-245.

- Zeng, X., and Ni, B. 1998. Application of Bender Elements in Measuring G_{max} of Sand Under K_0 Condition. *In Geotechnical Testing Journal*. p. 251.
- Zhang, J., Andrus, R.D., and Juang, C.H. 2005. Normalized Shear Modulus and Material Damping Ratio Relationships. *Journal of Geotechnical and Geoenvironmental Engineering*, **131**(4): 453-464. doi:10.1061/(ASCE)1090-0241(2005)131:4(453).
- Zhang, J., Peng, J., Zheng, J., Dai, L., and Yao, Y. 2019. Prediction of Resilient Modulus of Compacted Cohesive Soils in South China. *In International Journal of Geomechanics*. p. 04019068.
- Zhang, X.W., Kong, L.W., Cui, X.L., and Yin, S. 2016. Occurrence characteristics of free iron oxides in soil microstructure: evidence from XRD, SEM and EDS. *In Bulletin of Engineering Geology and the Environment*. pp. 1493-1503.
- Zhao, C., Liu, Z., Shi, P., Li, J., Cai, G., and Wei, C. 2016. Average Soil Skeleton Stress for Unsaturated Soils and Discussion on Effective Stress. *International Journal of Geomechanics*, **16**(6): D4015006. doi:10.1061/(ASCE)GM.1943-5622.0000610.
- Zhao, C.G., Liu, Y., and Gao, F.P. 2009. Work and energy equations and the principle of generalized effective stress for unsaturated soils. *International Journal for Numerical and Analytical Methods in Geomechanics*: n/a-n/a. doi:10.1002/nag.839.
- Zhou, C. 2014. Experimental study and constitutive modelling of cyclic behaviour at small strains of unsaturated silt at various temperatures. *In Phd thesis, Clear Water Bay, Kowloon, Hong Kong*.
- Zhou, C., and Ng, C.W.W. 2015a. A thermomechanical model for saturated soil at small and large strains. *In Canadian Geotechnical Journal*. pp. 1101-1110.
- Zhou, C., and Ng, C.W.W. 2015b. A thermomechanical model for saturated soil at small and large strains [Article]. *Canadian Geotechnical Journal*, **52**(8): 1101-1110. doi:10.1139/cgj-2014-0229.
- Zhou, C., and Ng, C.W.W. 2016. Simulating the cyclic behaviour of unsaturated soil at various temperatures using a bounding surface model. *In Géotechnique*. pp. 344-350.
- Zhou, C., and Ng, C.W.W. 2018. A new thermo-mechanical model for structured soil [Article]. *Géotechnique*, **68**(12): 1109-1115. doi:10.1680/jgeot.17.T.031.
- Zhou, C., Xu, J., and Ng, C.W.W. 2015a. Effects of temperature and suction on secant shear modulus of unsaturated soil. *In Géotechnique Letters*. pp. 123-128.
- Zhou, C., Ng, C.W.W., and Chen, R. 2015b. A bounding surface plasticity model for unsaturated soil at small strains. *In International Journal for Numerical and Analytical Methods in Geomechanics*. pp. 1141-1164.
- Zur, B. 1966. Osmotic control of the matric soil-water potential: I. Soil-water system. *In Soil Science*. LWW. pp. 394-398.